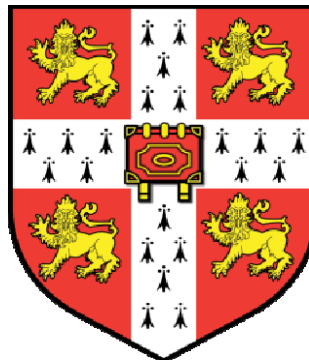


# INDIRECT MEASUREMENT OF THE ELECTROCALORIC EFFECT

---

James Scott Young

SUBMITTED FOR THE DEGREE OF  
DOCTOR OF PHILOSOPHY  
AT THE UNIVERSITY OF CAMBRIDGE



CHURCHILL COLLEGE  
CAMBRIDGE  
DECEMBER 2011

To my mother, who schooled me from an early age and my father, who answered all my questions.

## **DECLARATION**

This dissertation is the result of my own work and includes nothing which is the outcome of work done in collaboration except where specifically indicated in the text. This work has been carried out in the Departments of Materials Science and Metallurgy, Earth Sciences and Physics at the University of Cambridge, UK since October 2007. No part of this dissertation has been submitted previously at Cambridge or any other University for a degree, diploma or other qualification. This dissertation does not exceed 60,000 words.

James Young  
December 2011

## ACKNOWLEDGEMENTS

Producing this thesis has been a long, arduous and extraordinary journey. Reaching this point has been made possible with the help of many people, some disproportionately more helpful than others. I truly owe these friends a great deal indeed. They were under no obligation to lend a hand, yet they did, over and over again. Jim Scott tops the list, accompanied by Pavel Zubko, Gustau Catalán and Karl Sandeman. Outside of immediate academic circles, there were several authors who graciously donated their expertise via e-mail correspondence, or even in person, as was the case with Gerry Carrington. David Griffiths answered question after question of mine, despite not knowing me from Adam. Also, Dan Schroeder, Volker Heine and C.J. Adkins were obliging, from a distance. In the realm of analysis software and precision equipment, the mysterious AG from Wavemetrics and Joe Evans from Radiant Technologies exchanged well over a hundred e-mails with me, all to do with the finer details of their fine products. And Rantej Bali and Ali Hakimi were a great support, both emotionally and intellectually. To all these people, I am very grateful.

That said, there are many others I must thank, such as Leszek Spalek, Paul Nahai-Williamson, Doug Astill, Ken Cooper and Melanie Tribble from the QM and Semiconductor Physics groups at the Cavendish, all kind and generous people. Tatiana Correia, my counterpart at Cranfield, not only fabricated films, she was also a comrade. I would like to thank Casey Israel, Alex Barcza and Sohini Kar-Narayan for their time and practical knowledge in the early days and finally, Neil Mathur, my supervisor, who did his utmost to support me with knowledge and pastoral advice during the first half of this flustering adventure in academia.

## ABSTRACT

In August 2011 at the International Symposium on Integrated Functionalities [1] in Cambridge, a whole session was devoted to the electrocaloric effect, which is undergoing a modest renaissance. Surprisingly, the various reports showed that the indirect method of measuring cooling (described in the following sections) did not usually agree with the direct method (actually measuring temperature change with a thermometer). However, there was no obvious systematic error: sometimes the indirect temperature change was larger and sometimes smaller. The discrepancies were beyond the experimental errors.

The majority of the present thesis is dedicated to careful reexamination of some of the assumptions made in the indirect method, both during measurement and in the subsequent data analysis that leads to inferred temperature changes. Experimentally, I conclude that the most serious systematic error is likely to be the unwarranted assumption that polarization and field measurements, recorded in hysteresis loops that are traced within a millisecond or less, are all taken at the same temperature. In reality, the experience of the material during such loops is neither isothermal nor adiabatic. Other systematic errors relate to data analyses and are discussed in detail.

In some ways, therefore, this thesis has a negative flavour. But it is not designed to criticise prior work. Rather, it is intended to discriminate between reliable experimental procedures and those less convincing. This is a line of research with important technology transfer possibilities, and hence the numerical values of electric cooling must be unusually reliable if we are to avoid unwise capital investment as a country.

## SYMBOLS AND ABBREVIATIONS

$A$	$U - TS + E_0 P_m$ / capacitor electrode area
$A'$	$U - TS - E P_m$
$A_C$	$U_C - TS - E D_m$
$\alpha$	thermal diffusivity
BTO	barium titanate
$C$	heat capacity
$c$	heat capacity per unit volume
$D$	displacement field
$D_{vac}$	displacement field of empty capacitor
$D_m$	$Dv$
$E$	overall field of filled capacitor
$E_0$	field of capacitor due to free charge on electrodes
$E_M$	field of filled capacitor due to bound charge in medium
$E_{vac}$	field of empty capacitor
$\mathcal{E}_F$	field energy of $E$
$\epsilon_0$	permittivity of free space
$F$	Helmholtz free energy
$F'$	Helmholtz free energy based on $U'$
FC	fast cooled
$H$	magnetizing field in absence of medium
$h$	convection heat transfer coefficient
$k$	thermal conductivity
$k_B$	Boltzmann constant
$l$	capacitor thickness
$M$	magnetization
OIP	“over intermediate points”
$P$	polarization
$p$	dipole moment
$P_m$	magnitude of total dipole moment of medium
$\mathcal{P}$	air pressure
$p_i$	probability of system being in given, accessible microstate

$\phi$	electric potential
$\phi_{vac}$	electric potential at empty-capacitor electrode
Poly	polynomial fit
POIP	polynomial fit over intermediate points
PMN-PT	lead magnesium niobate-lead titanate
PST	lead scandium tantalate
P(VDF-TrFE)	poly(vinylidene fluoride-trifluoroethylene)
P(VDF-TrFE-CFE)	poly(vinylidene fluoride-trifluoroethylene-chlorofluoroethylene)
PZ	lead zirconate
PZST	lead zirconate stannate titanate
PZT	lead zirconate titanate
PZT 95/05	$\text{PbZr}_{0.95}\text{Ti}_{0.05}\text{O}_3$
$q$	heat
$\Delta q_{ISO}$	heat change during isothermal process
$Q$	charge
$Q_{vac}$	charge on electrode of empty capacitor
$\rho$	material density / charge density
$\rho_{free}$	free-charge density
$S$	entropy
$s$	entropy per unit volume
$S_C$	configurational entropy
$S_T$	temperature-related entropy
SBT	strontium bismuth tantalate
SC	slow cooled
SEM	scanning electron microscope
Smth	boxcar smoothed
SOIP	smoothed over intermediate points
$\sigma$	surface charge density
$T$	temperature
$T_m^p$	temperature at plane m and moment p (finite-element model)
$t$	time
$U$	internal energy of medium
$U'$	pseudo-internal energy of medium

$U_C$	internal energy of (medium+conductors) system
$v$	volume
$V$	potential difference
$V_{max}$	maximum applied voltage
$W$	total work done in charging / discharging a capacitor
$W_B$	work done by battery in charging / discharging a capacitor
$W_{B_0}$	work done by battery in charging / discharging an empty capacitor
$W_M$	work done by battery on medium in charging / discharging a filled capacitor
$W_{E_0P}$	$\int Qd\phi$
$x$	distance in direction of heat flow
XRD	X-ray diffraction

# TABLE OF CONTENTS

<b>1. INTRODUCTION</b>	<b>1</b>
<b>2. THERMODYNAMICS</b>	<b>9</b>
<b>2.1. FIFTY-FIVE YEARS OF DISAGREEMENT</b>	<b>9</b>
2.1.1. ELECTRICAL WORK	9
2.1.2. WHY IS EdP MISTAKENLY DERIVED?	19
2.1.3. THE MEANING OF EdP	22
2.1.4. WHERE IS THE ENERGY?	23
2.1.5. AN UNCOMPENSATED FERROELECTRIC	27
2.1.6. ANALOGOUS TO THE MAGNETIC CASE?	28
<b>2.2. THE INDIRECT METHOD</b>	<b>30</b>
<b>2.3. MAXWELL RELATIONS</b>	<b>35</b>
<b>2.4. SUMMARY</b>	<b>38</b>
<b>3. TYPICAL ELECTROCALORIC PREDICTIONS</b>	<b>40</b>
<b>3.1. EXPERIMENTAL METHOD</b>	<b>40</b>
<b>3.2. ANALYTICAL METHOD</b>	<b>56</b>
<b>3.3. PZT</b>	<b>81</b>
3.3.1. 1100 NM THICK. FAST COOLED. HOTPLATE.	81
3.3.2. 1050 NM THICK. HIGHER ANNEAL TEMPERATURE. CRYOSTAT.	88
3.3.3. $\Delta T$ PREDICTION COMPARISON BETWEEN THREE PZT 95/05 SAMPLES	102
3.3.4. NEGATIVE ELECTROCALORIC EFFECT	108
3.3.5. PARAMETER VARIATION	117
3.3.6. PEAK $\Delta T$ PREDICTIONS	137
<b>3.4. PMN-PT</b>	<b>142</b>
3.4.1. 225 NM THICK	144
3.4.2. 700 NM THICK	157
3.4.3. PEAK $\Delta T$ PREDICTIONS	169
<b>4. APPLICABILITY OF THERMODYNAMICS</b>	<b>173</b>
<b>4.1. THERMODYNAMIC BEHAVIOUR</b>	<b>173</b>
<b>4.2. A SEARCH FOR VALID DATASETS</b>	<b>178</b>
<b>4.3. ISOTHERMAL OR ADIABATIC?</b>	<b>196</b>

<b>5. FINAL THOUGHTS</b>	<b>223</b>
<b>6. APPENDICES</b>	<b>225</b>
APPENDIX A – ELECTRICAL WORK WITHIN THE MODEL OF AN INFINITE-AREA CAPACITOR	225
APPENDIX B – THE LOCATION OF THE ENERGY OF A CHARGE CONFIGURATION	228
APPENDIX C - IGOR FUNCTIONS FOR TYPICAL ELECTROCALORIC PREDICTIONS	229
APPENDIX D - IGOR FUNCTIONS FOR TESTING P(E,T) SURFACES FOR COMPLIANCE WITH INDIRECT METHOD CONDITIONS	241
APPENDIX E - IGOR FUNCTIONS FOR FINITE-ELEMENT MODEL OF TEMPERATURE EVOLUTION IN SAMPLE	244

# 1. INTRODUCTION

## WHAT IS THE ELECTROCALORIC EFFECT?

The electrocaloric effect is an induced change in temperature of a nominally insulating material, caused by changing its entropy through application or removal of a field across it. This temperature change is largest where the process is adiabatic, i.e. where no heat enters or leaves the system, and reversible. Under these conditions, the process is isentropic, meaning the overall change in entropy is zero, characterised by two types of entropy change occurring simultaneously, that is, there are changes in configurational and temperature-related entropy, but in opposite senses, so the overall change is always zero.

The entropy of a system is defined classically as:

(1.1)

$$S = -k_B \sum_i p_i \ln p_i$$

where  $k_B$  is Boltzmann's constant and  $p_i$ , the probability of an atom in the system being in an accessible microstate of certain position and momentum, summed over all accessible microstates of all atoms. As a field is applied across a polarizable material, the field reduces configurational entropy, as the thermal fluctuations of the atoms or ions and their associated charge, are spatially restricted. Under isentropic conditions, an equal and opposite increase in entropy occurs at the same time, as the lattice vibrates more vigorously, opening its constituents up to states of more possible momenta and thus increasing the temperature of the material. Removing the field causes the configurational entropy to increase and the temperature to drop.

Prior to the existence of an external field, a material may be uncharged, but as a field is applied, positive and negative charge within the material are pulled with ever-greater force, in opposite directions. The small separation of charge at the microscopic level

manifests macroscopically as charged surfaces of the material. The material then has a total dipole moment, where dipole moment is defined as equal and opposite charge separated by a distance and thus expressed in SI units as coulomb-metres. An alternative formulation of this phenomenon is to take the dipole moment accounted for by these microscopic dipoles over unit volume. This is polarization, having SI units of coulombs per square metre. The average polarization of a slab of material is equivalent to the charge per unit area on one of the surfaces [2].

Two types of material that can be readily polarized are dielectrics and ferroelectrics, which are a subset of dielectrics. In the absence of an external field, a dielectric is unpolarized and the larger the applied field, the larger the separation of bound charge in the material. A ferroelectric can have a zero, or finite, average polarization in the absence of an external field. Unit cells of similar configuration are arranged in domains, which are not charge neutral. Each domain can point in one of two opposite directions, that is, the average dipole of the domain can have its positive charge at either end, where the direction of the dipole runs from the negative charge towards the positive charge, as is the convention for dipole moment and polarization. Progressive application of a field causes domains to nucleate and grow. The dipole moment of nucleated domains will point more in the direction of the field than away from it, increasing polarization in the direction of the field. Removal of the field can cause the dipole moment of domains to switch to the opposite direction, though a ferroelectric also behaves like a dielectric with the dipole moments of the domains being stretched or compressed.

The change in configurational entropy and hence the size of the electrocaloric effect in the material, is a function of the polarization of the material and in turn, the applied field.

## THE INDIRECT METHOD

The indirect method takes advantage of the exchange between configurational and temperature-related entropy under isentropic conditions and applies thermodynamics to determine electrocaloric temperature changes from polarization, field and temperature data, which in certain circumstances are much more easily obtainable than direct measurements of temperature.

The electrocaloric effect was first discovered in 1930 by Kobeko and Kurtschatov, in Rochelle Salt [3] and since then, 64 experimental papers have been published. Only half of those, however, were published over the 74-year period from 1930 to 2004. During that time, all electrocaloric temperature change measurement was direct and made on bulk samples and hopes for solid-state cooling via the electrocaloric effect were never fulfilled. No temperature drop greater than 2.6 °C was recorded [4] and this required a large applied voltage of 750 V. Such a small return in cooling for a large investment in power was a likely reason for such little interest in the electrocaloric effect. However, in 2006, Alex Mischenko *et al.* [5] published a paper that made use of the indirect method and suggested cooling in zirconium-rich PZT 95/05 ( $\text{PbZr}_{0.95}\text{Ti}_{0.05}\text{O}_3$ ) of up to 12 °C, starting from 226 °C. This reignited enthusiasm in the topic and the output rate of experimental papers has increased 15-fold since then. At the time of that paper, the indirect method was not new. The idea had been cited in three previous electrocaloric papers [4, 6] and reasonable agreement of 15-20% had been observed between indirect method predictions and direct temperature measurements [4, 7]. The paper by Mischenko was the first to predict large cooling effects, though no direct measurement data was given to support it.

The reason for this is that thin films were being studied, as opposed to bulk. PZT 95/05 was chosen for its high dielectric constant and relatively low bulk Curie temperature, at 242 °C, where the greatest electrocaloric effects are expected due to the large entropy changes of the ferroelectric to paraelectric structural phase transition. It is also similar to the PZST ( $\text{Pb}_{0.99}\text{Nb}_{0.02}(\text{Zr}_{0.75}\text{Sn}_{0.20}\text{Ti}_{0.05})_{0.98}\text{O}_3$ ) studied by Tuttle and Payne in 1981, where the largest cooling thus far, of 2.6 °C had been observed. By using a film only 350 nm thick, large fields of over 700 kV/cm could be applied and removed with 25 V, which compares to 30 kV/cm using 750 V in the case of Tuttle and Payne. Previous experiments on bulk materials had not withstood fields much above 50 kV/cm, but in this thin film, 700 kV/cm had been achieved without suffering breakdown. Speculation at the time suggested high fields had been achieved due to a lack of defects in the film, though the speed of field application and removal, which was considerably higher, was undoubtedly significant. A ferroelectric tester had been employed to measure hysteresis loops from which the necessary polarization and field data, measured at different temperatures, was extracted. Such loops had a period of 0.1 ms, compared to the

20 seconds-per-cycle loops measured by Tuttle and Payne, where direct measurements agreed reasonably with indirect method predictions. Direct measurements on thin films were deemed to be very difficult, given that not only was the film very thin, but small electrodes (circular, 200  $\mu\text{m}$  diameter) were used to apply the field, as larger electrodes can often result in film breakdown or measurement-current overload for precision ferroelectric testers. Thus the volume of material that underwent testing in the work of Mischenko *et al.* was of the order of  $10^{-8} \text{ mm}^3$  and would have experienced, at most, an electrocaloric heat change of the order of microjoules. Measuring such a small heat change in such a small volume is unsurprisingly difficult and prone to inaccuracy.

However, a few very recent papers have reported large electrocaloric temperature changes that have been measured directly [8-11] in ferroelectric polymers and the indirect method will now probably disappear from the electrocaloric literature. Nonetheless, since 2006, 21 of the 32 experimental papers published produced results based on the indirect method.

All papers that have used the indirect method are listed in the table below, alongside several relevant characteristics.

<i>Date</i>	<i>Author and reference</i>	<i>Material</i>	<i>Thickness (<math>\mu\text{m}</math>)</i>	<i>Field change (kV/cm)</i>	<i>Frequency (Hz) / Field removal time (s)</i>	<i><math>\Delta T</math> indirect method (<math>^{\circ}\text{C}</math>)</i>	<i><math>\Delta T</math> measured directly (<math>^{\circ}\text{C}</math>)</i>
Aug 2011	Luo <i>et al.</i> [12]	PMN-PT	600	40	1 / 0.25	1	None
Jun 2011	Feng <i>et al.</i> [13]	PMN-PT/PZT	0.250	600	100 / 0.0025	13.4	None
Mar 2011	Correia <i>et al.</i> [14]	PST	0.200	774	1000 / 0.00025	-6.9	None
Mar 2011	He <i>et al.</i> [15]	PMN-PT	N/A	N/A	N/A	4.25	N/A
Jan 2011	Rozic <i>et al.</i> [16]	P(VDF-TrFE)	N/A	N/A	N/A	N/A	N/A
Nov 2010	Feng <i>et al.</i> [17]	PMN-PT	0.200	600	1000 / 0.00025	14.5	None
Nov 2010	Lu <i>et al.</i> [10]	P(VDF-TrFE-CFE)	5	700	Not specified	0.87	3.6
May 2010	Bai <i>et al.</i> [18]	BTO	1.4	176	Not specified	0.68	$\pm 1.8$
Feb 2010	Liu <i>et al.</i> [19]	P(VDF-TrFE-CFE)	0.090	3500	1000 / 0.00025	21.6	None
Jan 2010	Kar-Narayan <i>et al.</i> [20]	BTO	6.5	300	0.01 / 25	-0.9	-0.5
Nov 2009	Correia <i>et al.</i> [21]	PMN-PT	0.210	723	100 / 0.0025	9	None
Jun 2009	Saranya <i>et al.</i> [22]	PMN-PT	0.240	747	200 / 0.00125	31	None
May 2009	Chen <i>et al.</i> [23]	SBT	0.200	600	10000 / 0.000025	+4.93	None
Jan 2009	Neese <i>et al.</i> [24]	P(VDF-TrFE-CFE)	1	3000	1000 / 0.00025	9	None
Aug 2008	Neese <i>et al.</i> [25]	P(VDF-TrFE)	2	2090	1000 / 0.00025	12	None
July 2008	Parui [26]	PZ	0.7	400	1000 / 0.00025	-11.4	None
Mar 2007	Sebald <i>et al.</i> [27]	PMN-PT	1000	27.5	1 / 0.25	-0.46	-0.65
Dec 2006	Mischenko <i>et al.</i> [28]	PMN-PT	0.260	895	10000 / 0.000025	5	None

Dec 2006	Sebald <i>et al.</i> [29]	PMN-PT	1000	25	1 / 0.25	±0.89	±0.62
Sep 2006	Guyomar <i>et al.</i> [30]	PMN-PT	1000	13.5	1 / 0.25	-0.94	-0.40
Mar 2006	Mischenko <i>et al.</i> [5]	PZT	0.350	481	10000 / 0.000025	12	None
1981	Tuttle & Payne [4]	PZST	250	30	0.05 / 10	2.21-2.99	2.6
1980	Olsen <i>et al.</i> [7]	PZST	250	20	0.04 / 12.5	-2.4	-2.0

**Table 1. Papers that have predicted electrocaloric changes via the indirect method**

Where  $\Delta T$  values in this table are not preceded by a negative or positive sign, it is because neither was specified in the paper. It can be seen that this lack of sign applies to most papers for the indirect  $\Delta T$  data, which is an important omission in relation to the temperature at which these indirect predictions apply and hints at a lack of understanding in the literature, as will be explained in chapter 3. Two papers were unavailable and eight of the rest of the 23 listed papers supply both an indirect peak  $\Delta T$  prediction and a direct measurement, where the larger value ranges from being 15% to over 300% bigger than the smaller value. The best levels of agreement were achieved with relatively slowly recorded polarization data.

Alongside taking a look at new experimental data and potentially adding to this list, it will be suggested that the indirect method should no longer be trusted, until a significant body of experimental evidence can be built up that demonstrates under what conditions it can be regarded as reliable. Not only are scientists now able to measure temperature change directly on robust polymer films, recording even greater cooling than that predicted by the indirect method and rendering the indirect method essentially obsolete [8-11], but the underlying assumptions of the indirect method are generally applied dubiously. This author is of the opinion that these assumptions should not be ignored or dismissed as “negligible”, nor should they conveniently be consumed by referring to such predictions as “approximate”. In fact, a wide range of results can be produced from good quality data measured on the same sample.

This thesis will begin by examining the theoretical foundations of the indirect method, where a long-standing discrepancy in the thermodynamic literature will be resolved. The main body of the thesis will then look at the analysis of experimental data taken on PZT 95/05 and PMN-PT, in continuation of the studies initiated by Alex Mischenko and the present Cambridge group of this author. This will demonstrate a significant variability in temperature change predictions, even when the only reason for such variation is the choice of one of several valid methods of analysis. Thirdly, rules implicit in the theory of the indirect method will be exposed and used to discard temperature change predictions that do not comply; and finally, there will be a thorough estimation of the necessary isothermality of measured  $P(E)$  loops using finite-element modelling.



## 2. THERMODYNAMICS

### 2.1. FIFTY-FIVE YEARS OF DISAGREEMENT

#### 2.1.1. ELECTRICAL WORK

There is a lack of agreement across thermodynamic textbooks as to the identity and definition of the electrical work performed on a capacitor medium during charging and discharging. It is often derived as a simple analogy to magnetic work and rarely is it treated carefully and in detail. In the few textbooks that it is, there are differing approaches and thus the potential for misunderstanding. The predominant conclusion is that the infinitesimal term that describes the work done on a capacitor medium, per unit volume, is  $EdP$ , where  $E$  represents a uniform field across the medium and  $P$ , a uniform polarization throughout the medium (e.g. [31-36]). In several other publications, the work term per unit volume is found to be  $-PdE_0$ , under the same uniform conditions, where  $E_0$  represents the “applied” field, meaning the field one would find between the plates of a capacitor, were all charge to be frozen in their position and the medium then removed from the capacitor [37-43]. The difference between  $-PdE_0$  and  $EdP$  is quite profound, as they differ in sign. The former means that the medium does work, while the latter does not. This discrepancy has existed ever since the original proposition of  $-PdE_0$  in 1956 by Volker Heine [41] without any attempt since, at reconciliation with  $EdP$ .

The majority of the experimental findings in the electrocaloric literature of the last five years, when activity has been most fervent, employ the indirect method, which is based on the work term being  $EdP$ . This chapter presents a logical and detailed case for  $-PdE_0$ , with special consideration for uncompensated ferroelectrics. It also explains how  $EdP$  has been mistakenly derived, identifies its physical meaning and hence resolves this long-standing disagreement. In addition, the indirect method gains alternative equations for predicting temperature change, where all temperature changes predicted would be the same for each equation, for an ideal dataset, i.e. data that describe reversible processes. Fortunately, both work terms can be used indiscriminately in the indirect method. However, the fundamental character of this discrepancy warrants a clear resolution.

If one takes a polarizable medium, sandwiches it between two parallel plates and creates a charged capacitor, we have the following situation:

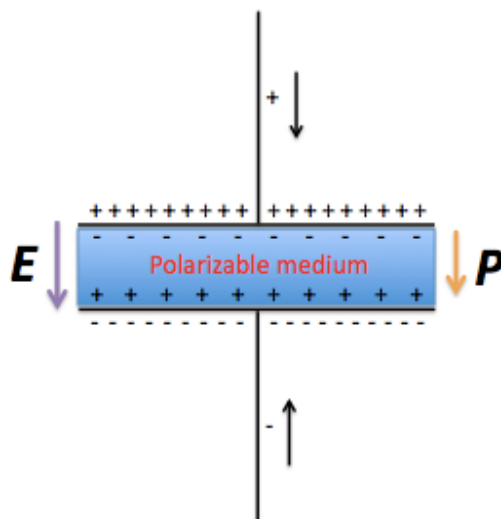


**Figure 2-1. A snapshot of a charging capacitor, showing charge, the field,  $E$ , across the capacitor and the polarization,  $P$ , of the medium.**

A charged capacitor containing a polarizable medium implies a macroscopic field across it, referred to here as  $E$ . This is the superposition of the field due to the charges on the electrodes,  $E_0$ , and the field due to the polarized medium,  $E_M$  (see fig. 2-2). The external field,  $E_0$ , must not be mistaken for being the field across an empty capacitor, though that is possible. When the capacitor is empty, the field across it,  $E = E_0$ , but when the capacitor contains a medium,  $E = E_0 + E_M$ , i.e.  $E_0$  is the field due to the free charge that reside on the capacitor electrodes, whether the capacitor is empty or not. When one measures the voltage across the capacitor to establish the field across the capacitor, one is measuring  $E$ , which is due to both the free charge on the electrodes and the bound charge in the medium. The following figure shows the medium outside the capacitor, but this is just for clarity. One is to imagine the medium sitting between the capacitor electrodes with  $E_0$  and  $E_M$  combining to give  $E$ , as is the situation in fig. 2-1.

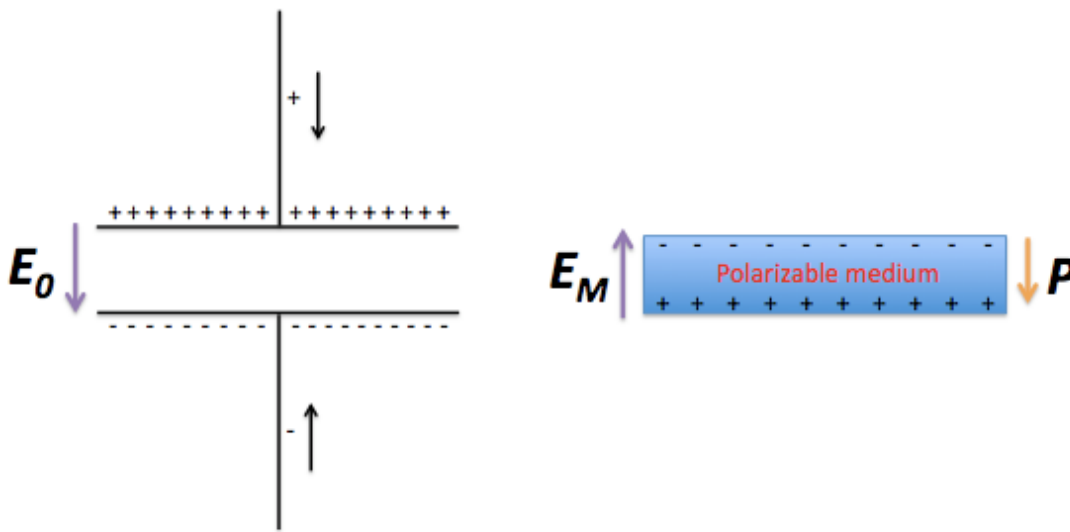
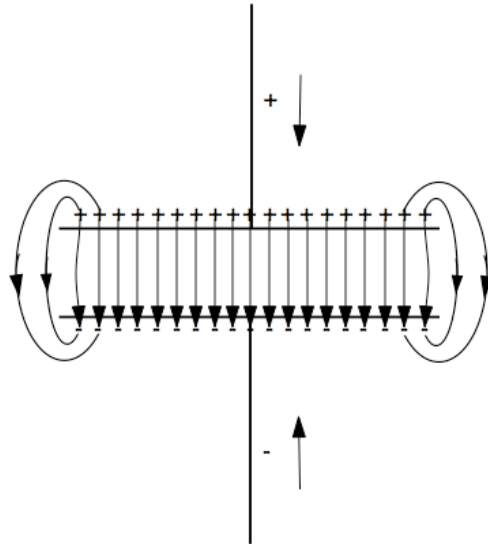


Figure 2-2. The constituent fields of  $E$  ( $E_0$  and  $E_M$ ) across a charging capacitor.

As free charge is forced onto the plates, bound charge within the medium, of opposite polarity, is attracted to this charge, causing the surfaces of the medium to become charged as it is polarized.  $E$  and  $P$  come together to form the definition of the displacement field,  $D = \epsilon_0 E + P$ . It should be noted that the two figures above, present an instructive picture, but they lack accuracy, describing uniform fields and polarization between the capacitor plates. This approximation excludes fringing fields, taking the capacitor as an imagined section of a capacitor that is infinite in  $x$  and  $y$ , i.e. its thickness is finite, but the electrode areas are infinite. A lack of material homogeneity would also destroy uniformity, but in all real cases, the surface charge density on the electrodes is larger at the edges, so none of these vectors is uniform at the capacitor edges.



**Figure 2-3. The field,  $E=E_0$ , represented by field lines, across an empty, charging capacitor. Fringing fields exist at the capacitor edges.**

The infinitesimal work done by the voltage source, hereon referred to as “the battery”, in placing charge on the plates can be determined, as for every negative charge that is placed on the negative plate, a positive charge is placed on the positive plate. An equivalent interpretation would be to move a positive charge from the lower-potential plate to the higher-potential plate. Hence, a small amount of positive charge,  $dQ$ , is moved through the potential difference between the plates, so:

(2.1)

$$\delta W_B = VdQ$$

An alternative, but equal, view of moving charge through the potential difference,  $V$ , starts with the same idea that the work is done in placing free charge on both electrodes, this time being brought in from zero potential at infinity [44]. Then one begins with:

(2.2)

$$\delta W_B = \phi dQ = \int_{all\ space} \phi(d\rho_{free}) \delta v$$

where  $\rho_{free}$  is the free charge density, i.e. that which is not bound charge.  $\delta v$  here represents a small volume element and  $\phi$  is the electric potential. Now:

$$\int_{all\ space} \nabla \cdot d\mathbf{D} = d\rho_{free} \quad (2.3)$$

Then, as  $\nabla \cdot (\phi d\mathbf{D}) = \phi(\nabla \cdot d\mathbf{D}) + (\nabla\phi) \cdot d\mathbf{D}$ :

$$\delta W_B = \int_{all\ space} [\nabla \cdot (\phi d\mathbf{D}) - (\nabla\phi) \cdot d\mathbf{D}] \delta v \quad (2.4)$$

and as  $-\nabla\phi = \mathbf{E}$ ,

$$\delta W_B = \int_{all\ space} \nabla \cdot (\phi d\mathbf{D}) \delta v + \int_{all\ space} \mathbf{E} \cdot d\mathbf{D} \delta v \quad (2.5)$$

The first term on the right-hand side can be turned into a surface integral by the divergence theorem, which disappears when integrated over all space, as the potential is zero at infinity. So, one has:

$$\delta W_B = \int_{all\ space} \mathbf{E} \cdot d\mathbf{D} \delta v = \phi dQ \quad (2.6)$$

Another energy change is now introduced:

(2.7)

$$\delta W_{E_0P} = Qd\phi = \int_{all\ space} \rho_{free} d\phi \delta v = \int_{all\ space} (\nabla \cdot \mathbf{D}) d\phi \delta v$$

Similarly, as  $\nabla \cdot (\mathbf{D} d\phi) = (\nabla \cdot \mathbf{D})d\phi + (\nabla d\phi)\mathbf{D}$ :

(2.8)

$$\begin{aligned} \delta W_{E_0P} &= \int_{all\ space} [\nabla \cdot (\mathbf{D} d\phi) - (\nabla d\phi)\mathbf{D}]d\phi \delta v \\ &= \int_{all\ space} \nabla \cdot (\mathbf{D} d\phi)\delta v + \int_{all\ space} d\mathbf{E} \cdot \mathbf{D} \delta v \end{aligned}$$

Again, if the first term is turned into a surface integral and integrated over all space, it vanishes, as  $d\phi$  is zero at infinity. One has:

(2.9)

$$\delta W_{E_0P} = \int_{all\ space} \mathbf{D} \cdot d\mathbf{E} \delta v = Qd\phi$$

The subscript of  $\delta W_{E_0P}$  makes reference to  $\int_{all\ space} -\mathbf{E}_0 \cdot d\mathbf{P} \delta v$ , which can be shown to be equivalent to  $\int_{all\ space} \mathbf{D} \cdot d\mathbf{E} \delta v$  when  $\mathbf{E}_0$  is constant. This work is part of an internal redistribution of energy within the medium in a process where only the potential of the electrodes changes and the free charge remains constant, such as when a charged capacitor is disconnected from the battery and heated or cooled. As the medium changes its polarization in a fixed, external field, the dipoles' potential energy changes by  $\int_{all\ space} -\mathbf{E}_0 \cdot d\mathbf{P} \delta v$ , which, combined with the field energy of the medium, is compensated for by the opposite change in energy due to internal forces.

These two energy changes,  $\delta W_B$  and  $\delta W_{E_0P}$ , form the basis of determining the work done by the battery on the medium in charging or discharging a capacitor. This is the work

done in changing the free charge on the electrodes of an empty capacitor, subtracted from that done on a filled capacitor [38]:

(2.10)

$$\delta W_M = \int_{\text{all space}} \mathbf{E} \cdot d\mathbf{D} \delta v - \int_{\text{all space}} \mathbf{E}_{vac} \cdot d\mathbf{D}_{vac} \delta v$$

For an empty capacitor, there is no polarization and hence  $\mathbf{D}_{vac} = \epsilon_0 \mathbf{E}_{vac}$ , so:

(2.11)

$$\delta W_M = \int_{\text{all space}} \mathbf{E} \cdot d\mathbf{D} \delta v - \int_{\text{all space}} \mathbf{D}_{vac} \cdot d\mathbf{E}_{vac} \delta v = \phi dQ - Q_{vac} d\phi_{vac}$$

As the charging process is the same in both the filled and empty cases,  $Q = Q_{vac}$  and  $dQ = dQ_{vac}$ , hence:

(2.12)

$$\begin{aligned} \delta W_M &= \phi dQ_{vac} - Q d\phi_{vac} = \int_{\text{all space}} \mathbf{E} \cdot d\mathbf{D}_{vac} \delta v - \int_{\text{all space}} \mathbf{D} \cdot d\mathbf{E}_{vac} \delta v \\ &= \int_{\text{all space}} (\epsilon_0 \mathbf{E} - \mathbf{D}) \cdot d\mathbf{E}_{vac} \delta v = - \int_{\text{all space}} \mathbf{P} \cdot d\mathbf{E}_0 \delta v \end{aligned}$$

or:

(2.13)

$$W_B - W_{B_0} = - \int_{\text{medium}} \left( \int_{E_{01}}^{E_{02}} \mathbf{P} \cdot d\mathbf{E}_0 \right) \delta v$$

where  $W_B$  and  $W_{B_0}$  represent the total work done by the battery on a filled and empty capacitor, respectively, so:

(2.14)

$$W_B = \int_{all\ space} \left( \epsilon_0 \int_{\mathbf{E}_{0_1}}^{\mathbf{E}_{0_2}} \mathbf{E}_0 \cdot d\mathbf{E}_0 \right) \delta v - \int_{medium} \left( \int_{\mathbf{E}_{0_1}}^{\mathbf{E}_{0_2}} \mathbf{P} \cdot d\mathbf{E}_0 \right) \delta v$$

It should be noted that values of  $\mathbf{E}_0$ , such as the limits in the above integrals,  $\mathbf{E}_{0_1}$  and  $\mathbf{E}_{0_2}$ , do not refer to a single field, rather, the macroscopic field in each volume element for a given state. The second term here need only be integrated over the medium, as outside this volume, there is no polarization.

A simplified version of this derivation can be carried out if one begins with the approximate model of a section from an infinite-area capacitor. This model is necessary for the indirect method and its ramifications are explained in detail in appendix A.

An implication of equation 2.14 is that:

(2.15)

$$\delta W_B = \int_{all\ space} (\epsilon_0 \mathbf{E}_0 - \mathbf{P}) \cdot d\mathbf{E}_0 \delta v = \int_{all\ space} \mathbf{E} \cdot d\mathbf{D} \delta v$$

where the middle expression of the above equation is an abbreviation of the infinitesimal version of equation 2.14 and the final expression is a restatement of equation 2.6. So even though it is known that  $\mathbf{D} \neq \epsilon_0 \mathbf{E}_0$  (see appendix A), in the case of a charging or discharging capacitor,  $\int_{all\ space} \mathbf{D} \delta v = \int_{all\ space} \epsilon_0 \mathbf{E}_0 \delta v = \int_{all\ space} (\epsilon_0 \mathbf{E} + \mathbf{P}) \delta v$  must be true for equation 2.15 to hold.

$$\text{As } \mathbf{E} = \mathbf{E}_0 + \mathbf{E}_M, \text{ then } \int_{all\ space} \epsilon_0 (\mathbf{E}_0 - \mathbf{E}) \delta v = - \int_{all\ space} \epsilon_0 \mathbf{E}_M \delta v = \int_{all\ space} \mathbf{P} \delta v.$$

The medium sits in the  $\mathbf{E}_0$ -field and is influenced by it, but the energy of this field does not constitute part of the internal energy of the medium. For an empty capacitor, the work done by the battery in moving free charge around the external circuit is the total work performed and is stored as the energy of the  $\mathbf{E}_0$ -field. For a filled capacitor, the

work done by the battery causes work to be done by the medium, which can either be seen as reducing the potential difference against which the battery works, or in “pulling” charge on to the electrodes. So the battery and the medium perform this collaborative work in moving charge. Hence, for both cases:

(2.16)

$$W = W_{B_0} = W_B - W_M$$

where  $W$  is the total work done,  $W_{B_0}$  is the work done to create the  $\mathbf{E}_0$ -field, which is therefore the energy of this field and  $W_M$  is the work done on the medium by the battery. The energy of the  $\mathbf{E}_0$ -field is built up as work is done against itself through the movement of free charge.

When one thinks of the work done in charging a capacitor, it is natural to assume that this is the work done by the battery in moving free charge around the external circuit. However, both the battery and the medium collaborate to move the free charge and hence, the work done in charging the capacitor is the sum of their contributions, which is equal to the energy of the external field. Though the battery does work by forcing charge onto the electrodes, which attract bound charge in the medium, the bound charge attracts the free charge in the external circuit as much as the free charge attracts the bound charge in the medium.

Thus, the battery can be seen to be *responsible* for the increase in energy of the external field and the drop in energy of the medium, while the actual energy of the external field comes from the battery and the medium. Once again, the drop in energy of the medium can be interpreted either as reducing the potential through which the battery moves charge or in “pulling” free charge onto the electrodes. This is further supported here, by recognising that:

(2.17)

$$\delta W_B = \int_{all\ space} \mathbf{E} \cdot d\mathbf{D} \delta v = \int_{all\ space} \mathbf{E}_0 \cdot d\mathbf{D} \delta v + \int_{all\ space} \mathbf{E}_M \cdot d\mathbf{D} \delta v$$

the final term of which, is the work done by the battery in moving free charge through potential differences in the external circuit, due to the field of the medium alone. As  $\int_{all\ space} \mathbf{D} \delta v = \int_{all\ space} \epsilon_0 \mathbf{E}_0 \delta v$  and  $\int_{all\ space} \epsilon_0 \mathbf{E}_M \delta v = -\int_{all\ space} \mathbf{P} \delta v$ , then  $\int_{all\ space} \mathbf{E}_M \cdot d\mathbf{D} \delta v = \int_{all\ space} (-\mathbf{P} \cdot d\mathbf{E}_0) \delta v$ . By restating the work done by the medium,  $\int_{all\ space} (\mathbf{P} \cdot d\mathbf{E}_0) \delta v$ , as  $\int_{all\ space} (-\epsilon_0 \mathbf{E}_M \cdot d\mathbf{E}_0) \delta v$  and simplifying for the infinite-area capacitor model, one has an equivalent thermodynamic term to  $vPdE_0$ , which is  $v\epsilon_0 E_M dE_0$  ( $v$  is the volume of the medium). Note as with all expressions of work in thermodynamics, this term is the product of a force and the change that is effected by that force.  $v\epsilon_0 E_M$  is the magnitude of a force per unit charge, multiplied by a constant, causing a change,  $dE_0$ , in the external field, as it pulls charge towards the medium.

The definition of  $dW_M = -\int_{medium} (\mathbf{P} \cdot d\mathbf{E}_0) \delta v$  has only been derived by a few authors<sup>1</sup>, through a variety of methods. These authors, in chronological order, are Heine [41], Landau and Lifshitz [39], Leupold [42], Böttcher [37], Howard [43], Waldram [40] and Carrington [38].

---

<sup>1</sup> The earliest presentation of this term, in the paper by Volker Heine [41], is derived by considering the entropy of the medium, as opposed to its energy. As an interesting side note, at the time it was published, Heine had recently completed his master's degree at the University of Otago, New Zealand (Gerald Carrington later wrote his aforementioned book on thermodynamics there) and was working on his PhD at the Royal Society Mond Laboratory within the Cavendish, at Cambridge. Heine thanks Brian Pippard, later Sir Brian Pippard and Cavendish Professor of Physics between 1971 and 1984, for encouragement and advice, at the end of this paper. In 1957, Pippard published a seminal book entitled "Classical Thermodynamics" [45] in which the paper by Heine is referred to. The treatment Pippard provides for electrical work arrives at a slightly different answer by claiming an analogous relationship between electrical work and magnetic work, though with a little consideration, one can see where the discrepancy lies (explained in the following section). In 1958, Pippard supervised a student named John Waldram, who went on to become a member of the Cavendish and later published "The Theory of Thermodynamics" [40] in 1985, which also concludes  $\delta W_M = -\int_{medium} (\mathbf{P} \cdot d\mathbf{E}_0) \delta v$ , this time via a quantum mechanical approach. These three distinguished scientists spent the vast majority of their careers at the Cavendish and John Waldram and Volker Heine are currently Cavendish emeritus professors. Brian Pippard passed away in 2008.

### 2.1.2. WHY IS $EdP$ MISTAKENLY DERIVED?

$EdP$  is often derived as the work done, per unit volume, by the battery on the medium. This term only comprises the magnitudes of the overall field and polarization vectors because it originates from a treatment that considers the model of an imagined section from an infinite-area capacitor, where all field and polarization vectors are uniform and normal to the capacitor electrodes (see appendix A). Hence, only vector magnitudes are required. Furthermore, all fields are confined to the volume of the medium ( $v$ ), so the work done on the medium becomes  $vEdP$ . The derivation starts from equation 2.1, reproduced and expanded upon, below:

(2.18)

$$\delta W_B = VdQ = Eld(DA) = vEdD$$

where  $A$  is electrode area and  $l$  is capacitor thickness.  $D$  is equivalent to the surface charge density on one electrode [2]. As  $D = \epsilon_0 E + P$ , then:

(2.19)

$$\delta W_B = v\epsilon_0 EdE + vEdP$$

As the voltage of the battery is changed, this potential difference is passed to the capacitor, created by the progressive change of charge on the electrodes. The work done on the capacitor is then:

(2.20)

$$W_B = v\epsilon_0 \int_{E_1}^{E_2} EdE + \int_{P_{m_1}}^{P_{m_2}} E dP_m$$

The derivation reaches equation 2.19 and states that the first term exists whether or not there is a medium present in the capacitor, therefore the second term represents the work done on the medium by the battery. At first sight, this may seem logical, but equation 2.20 reveals this is not correct.

The limits of the integrals in this equation are those that represent field and polarization values that correspond to the initial and final charge state of the electrodes, so:

(2.21)

$$W_B = \int_{Q_1}^{Q_2} V dQ = v\epsilon_0 \int_{E_1}^{E_2} E dE + \int_{P_{m_1}}^{P_{m_2}} E dP_m$$

If one wishes to compare the work done by the battery in charging an empty and filled capacitor, claiming the difference in this work to be the work done on the medium when charging a filled capacitor, then one must perform these comparative-charging processes between the same charge limits. Then the work done on the medium by the battery is  $-\int_{E_{01}}^{E_{02}} P_m dE_0$  (see appendix A).

When charging is performed from  $Q_1$  to  $Q_2$  without the medium in the capacitor, i.e. when there is a vacuum between the electrodes, the limits  $E_1$  (except where  $E_1 = 0$ ) and  $E_2$  will be larger than in the case where a medium is present. The field energy of a filled capacitor is smaller than that of an empty one, for the same amount of charge on the electrodes. Thus, when considering the work done in changing the charge on an empty, then filled capacitor from  $Q_1$  to  $Q_2$ , the first term of  $W_B$  in equation 2.21 is not the same and the difference in work is not equal to  $\int_{P_{m_1}}^{P_{m_2}} E dP_m$ .

The overall field,  $E$ , is due to the superposition of the field due to the charge on the capacitor electrodes and the field of the polarized medium, so the energy of  $E$ , which is the first term of equation 2.21, includes part of the energy of the medium, i.e. the field energy due to bound charge in the medium. For  $\int_{P_{m_1}}^{P_{m_2}} E dP_m$  to be the work done by the battery on the medium,  $v\epsilon_0 \int_{E_1}^{E_2} E dE$  would have to be independent of the energy of the medium, which it is not.

It has been suggested [46] that it is just as logical to say that the work done by the battery on the medium is the difference in work done in the comparative charging processes

(empty and filled capacitor) where the change in potential difference across the capacitor is the same in each case. The integral limits,  $E_1$  and  $E_2$ , are the same in both cases and the difference in work done in those two processes is  $\int_{P_{m_1}}^{P_{m_2}} E dP_m$ . However, this does not represent the work done by the battery on the medium. In order for the limits,  $E_1$  and  $E_2$ , to be identical in both the filled and empty capacitor cases, the external field due to the charge on the plates,  $E_0$ , must be different in the two charging processes. Hence, the energy of the  $E_0$  field is different in each process.

The only part of the work done by the battery that is independent of the medium, is in building  $E_0$ . If one breaks down the actual field,  $E$ , into its constituent parts,  $E_0$  is the only part that cannot be described in terms of the properties of the medium.  $E_0$  is due to the charge on the electrodes, which reside outside of the medium and it exists whether or not there is a medium between the electrodes. Subtracting the changing energy of  $E_0$  from the work done by the battery, results in  $-P_m dE_0$ , showing the medium moves to a lower energy state in the presence of  $E_0$ . It should be noted that in quantum mechanics, the energy of a body due to its charge configuration in an external field, such as the field of the medium in  $E_0$ , is as described here, including the energy of its own field and the interaction energy, but excluding the energy of the external field [40].

For an ideal, non-dissipative, closed system of battery-conductors-medium, when charging a filled capacitor, the work done by the battery on the medium is the difference between the total work done by the battery and the energy of the  $E_0$  field. The work done by the battery is not all done on the medium, it is all done in moving the free charge. This results in a change of polarization of the medium and an  $E$ -field. These changes represent an energy increase in the conductors-medium subsystem, transferred from the battery subsystem, within the overall closed battery-conductors-medium system. There is no energy change in the overall system, but the energy of the battery drops, while the energy of the conductors-medium subsystem increases by the same amount. Of the energy changes in the conductors-medium subsystem, only the energy of the  $E_0$ -field can be considered to not be part of the internal energy of the medium. The battery transfers energy in creating the  $E_0$ -field and the medium responds to this field. Only when the same amount of energy is transferred into the  $E_0$ -field in each of the two comparative processes (1. filled capacitor, 2. empty capacitor), can one deduce that the difference in

work done by the battery in the two processes represents the work done by the battery on the medium in charging a filled capacitor. This turns out to be a negative quantity, that is, the work the battery did not need to do, instead, done by the medium, when charging a filled capacitor. The medium contributes energy to the  $E_0$ -field. If one performs the two processes between  $E_1$  and  $E_2$  and thus creates a different  $E_0$ -field change in each process, it cannot be said that the difference in work done by the battery in these two cases is equal to the work it does on the medium.

### 2.1.3. THE MEANING OF $E dP$

Returning to the general description of work performed by the battery in charging a filled capacitor (equation 2.6) and noting that  $\mathbf{D} = \epsilon_0 \mathbf{E} + \mathbf{P}$ :

(2.22)

$$\begin{aligned} W_B &= \int_{\text{all space}} \left( \int_{\mathbf{D}_1}^{\mathbf{D}_2} \mathbf{E} \cdot d\mathbf{D} \right) \delta v \\ &= \int_{\text{all space}} \left( \epsilon_0 \int_{\mathbf{E}_1}^{\mathbf{E}_2} \mathbf{E} \cdot d\mathbf{E} \right) \delta v + \int_{\text{medium}} \left( \int_{\mathbf{P}_1}^{\mathbf{P}_2} \mathbf{E} \cdot d\mathbf{P} \right) \delta v \end{aligned}$$

In accordance with the observation made on equation 2.14, the values  $\mathbf{E}_{01}$ ,  $\mathbf{E}_{02}$ ,  $\mathbf{P}_1$  and  $\mathbf{P}_2$ , refer to each volume element for a given state.  $W_B$ , as seen in the last expression of this equation, accounts for all the field energy and an extra term,  $\int_{\text{medium}} \left( \int_{\mathbf{P}_1}^{\mathbf{P}_2} \mathbf{E} \cdot d\mathbf{P} \right) \delta v$ . This  $\mathbf{E} \cdot d\mathbf{P}$  term refers to the work done by the battery that is not stored in the overall field. By elimination, this energy must be that which is stored in the medium due to restorative internal forces between charged particles. As free charge is forced to accumulate on the electrodes, work is done in pulling at bound charge in the medium against forces that give the medium its form in the first place. These forces exist in addition to the electrostatic forces that account for the energy of the charge configuration and in the energetically conservative scenario, this “spring” energy is recovered upon capacitor discharge.

#### 2.1.4. WHERE IS THE ENERGY?

The energy of an overall field,  $\mathbf{E}_2$ , due to a given charge configuration is:

(2.23)

$$\mathcal{E}_F = \int_{all\ space} \frac{1}{2} \epsilon_0 \mathbf{E}_2^2 \delta v$$

$\mathbf{E}_2$  is the vector sum of  $\mathbf{E}_{0_2}$  and  $\mathbf{E}_{M_2}$ , where  $\mathbf{E}_{M_2}$  is the field due to the polarized medium alone. These extra subscripts (the number “2”) denote a specific value of the variables.

So:

(2.24)

$$\mathcal{E}_F = \int_{all\ space} \frac{1}{2} \epsilon_0 (\mathbf{E}_{0_2} + \mathbf{E}_{M_2})^2 \delta v$$

and

(2.25)

$$\mathcal{E}_F = \int_{all\ space} \frac{1}{2} \epsilon_0 (\mathbf{E}_{0_2}^2 + 2\mathbf{E}_{0_2} \cdot \mathbf{E}_{M_2} + \mathbf{E}_{M_2}^2) \delta v$$

The middle term refers to the energy required to bring together the two charge distributions of  $\mathbf{E}_{0_2}$  and  $\mathbf{E}_{M_2}$ . As  $\mathbf{E}_{M_2}$  is due to a collection of dipoles and the work required to place a dipole in a fixed external field is  $-\mathbf{p} \cdot \mathbf{E}_0$ , then this middle term can be re-written as  $\int_{all\ space} (-\mathbf{P}_2 \cdot \mathbf{E}_{0_2}) \delta v$ , so:

(2.26)

$$\begin{aligned} \mathcal{E}_F = & \int_{\text{all space}} \left( \varepsilon_0 \int_{\mathbf{E}_{01}}^{\mathbf{E}_{02}} \mathbf{E}_0 \cdot d\mathbf{E}_0 \right) \delta v - \int_{\text{medium}} \left( \int_{\mathbf{E}_{01}}^{\mathbf{E}_{02}} \mathbf{P} \cdot d\mathbf{E}_0 \right) \delta v \\ & - \int_{\text{medium}} \left( \int_{\mathbf{P}_1}^{\mathbf{P}_2} \mathbf{E}_0 \cdot d\mathbf{P} \right) \delta v + \int_{\text{all space}} \left( \varepsilon_0 \int_{\mathbf{E}_{M1}}^{\mathbf{E}_{M2}} \mathbf{E}_M \cdot d\mathbf{E}_M \right) \delta v \end{aligned}$$

the infinitesimal change of which, is:

(2.27)

$$\begin{aligned} d\mathcal{E}_F = & \int_{\text{all space}} \varepsilon_0 (\mathbf{E}_0 \cdot d\mathbf{E}_0 + \mathbf{E}_M \cdot d\mathbf{E}_M) \delta v - \int_{\text{medium}} (\mathbf{P} \cdot d\mathbf{E}_0 + \mathbf{E}_0 \cdot d\mathbf{P}) \delta v \\ = & \int_{\text{all space}} (\varepsilon_0 \mathbf{E} \cdot d\mathbf{E}) \delta v \end{aligned}$$

The infinitesimal work done by the battery is (after equation 2.22):

(2.28)

$$\delta W_B = \int_{\text{all space}} (\varepsilon_0 \mathbf{E} \cdot d\mathbf{E} + \mathbf{E} \cdot d\mathbf{P}) \delta v$$

and combining it with equation 2.27:

(2.29)

$$\begin{aligned} \delta W_B = & \int_{\text{all space}} \varepsilon_0 (\mathbf{E}_0 \cdot d\mathbf{E}_0 + \mathbf{E}_M \cdot d\mathbf{E}_M) \delta v - \int_{\text{medium}} (\mathbf{P} \cdot d\mathbf{E}_0 + \mathbf{E}_0 \cdot d\mathbf{P}) \delta v \\ & + \int_{\text{medium}} (\mathbf{E} \cdot d\mathbf{P}) \delta v \end{aligned}$$

or:

(2.30)

$$\delta W_B = \int_{all\ space} (\epsilon_0 \mathbf{E}_0 \cdot d\mathbf{E}_0 + \epsilon_0 \mathbf{E}_M \cdot d\mathbf{E}_M + \mathbf{E} \cdot d\mathbf{P}) \delta v + \int_{medium} (d(-\mathbf{P} \cdot \mathbf{E}_0)) \delta v$$

This equation shows how the work done is stored in various forms. There is the energy of the external field,  $\int_{all\ space} (\epsilon_0 \mathbf{E}_0 \cdot d\mathbf{E}_0) \delta v$ , the energy of the field due to the polarization of the medium,  $\int_{all\ space} (\epsilon_0 \mathbf{E}_M \cdot d\mathbf{E}_M) \delta v$ , the “spring” energy stored between charged particles in the medium ( $\int_{medium} (\mathbf{E} \cdot d\mathbf{P}) \delta v$ ) and the change in potential energy of the total dipole moment of the medium,  $\int_{medium} (d(-\mathbf{P} \cdot \mathbf{E}_0)) \delta v$ , first referred to as the “interaction energy” by Charles Kittel (magnetic context) [47].

During charging, the battery, via  $\mathbf{E}_0$ , does work on the medium by polarizing it, which in turn gives the medium its own field,  $\mathbf{E}_M$  and there is an amount of energy stored in the medium due to the charge being pulled apart, that is equal to  $\int_{medium} (\mathbf{E} \cdot d\mathbf{P}) \delta v$ , passed from the battery to the medium. However, as  $\mathbf{E}_0$  is built up by the battery, there is an energy saving provided to the battery by the polarizing medium due to the falling potential energy of the bound charge in the medium, as it sits in an increasing  $\mathbf{E}_0$ . This can be seen by considering the remaining energy:

(2.31)

$$\begin{aligned} \delta W_B - \int_{all\ space} (\epsilon_0 \mathbf{E}_0 \cdot d\mathbf{E}_0 + \mathbf{E} \cdot d\mathbf{P}) \delta v \\ = \int_{all\ space} (\epsilon_0 \mathbf{E}_M \cdot d\mathbf{E}_M - \mathbf{P} \cdot d\mathbf{E}_0 - \mathbf{E}_0 \cdot d\mathbf{P}) \delta v \end{aligned}$$

In the last expression here, the first and last terms combine to give:

(2.32)

$$\int_{all\ space} (-\mathbf{P} \cdot d\mathbf{E}_0 - \mathbf{E} \cdot d\mathbf{P}) \delta v$$

as  $\int_{all\ space} \epsilon_0 d\mathbf{E}_M \delta v = - \int_{all\ space} d\mathbf{P} \delta v$  and  $-\mathbf{E}_0 - \mathbf{E}_M = -\mathbf{E}$ .

The term for the changing energy density of the field of the medium,  $\epsilon_0 \mathbf{E}_M \cdot d\mathbf{E}_M = -\mathbf{E}_M \cdot d\mathbf{P}$ , is a positive quantity and mitigates the drop in potential energy,  $\int_{medium} (d(-\mathbf{P} \cdot \mathbf{E}_0)) \delta v = \int_{medium} (-\mathbf{P} \cdot d\mathbf{E}_0 - \mathbf{E}_0 \cdot d\mathbf{P}) \delta v$ . In equation 2.31,  $-\mathbf{E}_M \cdot d\mathbf{P}$  combines with  $-\mathbf{E}_0 \cdot d\mathbf{P}$  to give  $-\mathbf{E} \cdot d\mathbf{P}$  in equation 2.32, which is a negative quantity, but less negative than  $-\mathbf{E}_0 \cdot d\mathbf{P}$ . The second term of equation 2.32 is then equal and opposite to the  $\int_{medium} (\mathbf{E} \cdot d\mathbf{P}) \delta v$  work done on the medium by the battery, leaving an overall drop in energy of the medium,  $\int_{all\ space} (-\mathbf{P} \cdot d\mathbf{E}_0) \delta v$ .

As the battery drops its energy by  $\int_{all\ space} (\epsilon_0 \int_{E_{01}}^{E_{02}} \mathbf{E}_0 \cdot d\mathbf{E}_0) \delta v - \int_{medium} (\int_{E_{01}}^{E_{02}} \mathbf{P} \cdot d\mathbf{E}_0) \delta v$  and the energy of the medium drops by  $\int_{medium} (\int_{E_{01}}^{E_{02}} \mathbf{P} \cdot d\mathbf{E}_0) \delta v$ , one can see that energy from these two sources accounts for the energy of  $\mathbf{E}_0$ , or in other words, the work done by the battery and the medium in moving free charge around the circuit. In this sense, one can intuitively see that the positive and negative bound charge of the polarizing medium, that moves towards electrodes of opposite polarity, reduces the workload on the battery.

One could say that the energy of the total charge configuration, comprising both the bound charge in the medium and the free charge on the electrodes, belongs to the configuration as a whole and that it is unreasonable to assign any portion of the energy to any specific part of this configuration. First of all, this idea negates the argument for  $vEdP$  being the work done on the medium, as it must exclude the energy of the whole charge configuration that is due, in part, to the presence of the bound charge, which is clearly part of the medium. Furthermore, though the energy of a charge configuration is well defined, the location of that energy is not. It is just as reasonable to say the energy of a charge configuration is located in the space occupied by the charge, as it is in the space occupied by the field. This is well explained by David Griffiths [48] and reproduced in appendix B. Hence, the energy of the charge configuration that is responsible for  $\mathbf{E}_0$  can be said to be located outside of the medium and the problem of ascertaining the work done by the battery on the medium simply and clearly reduces to

the total work done by the battery, less the energy of  $\mathbf{E}_0$ , which of course, is

$$- \int_{medium} \left( \int_{E_{01}}^{E_{02}} \mathbf{P} \cdot d\mathbf{E}_0 \right) \delta v.$$

### 2.1.5. AN UNCOMPENSATED FERROELECTRIC

Now consider an uncompensated ferroelectric. It has been shown that a thin-film ferroelectric can self-pole when cooled through its Curie temperature in a vacuum [49, 50]. Were the vacuum to be broken, free charge in the surroundings of the ferroelectric would be attracted to its charged surface. The work done by the ferroelectric, via its field,  $\mathbf{E}_M$ , is again,  $\int_{medium} \left( \int_{E_{01}}^{E_{02}} \mathbf{P} \cdot d\mathbf{E}_0 \right) \delta v$ . The difference between this situation and that of a dielectric or a compensated ferroelectric in a capacitor that is worked upon by a battery, is that here there is only an uncompensated ferroelectric and its surroundings. There is neither a battery, nor electrodes and the ferroelectric leads the work process.

Free charge of opposite polarity to that on a given surface of the ferroelectric, is pulled onto that surface by  $\mathbf{E}_M$  and so the ferroelectric does work on its surroundings. In doing so, an  $\mathbf{E}_0$ -field is built up, against which the free charge must work as they approach the surface of the ferroelectric. Even though the free charge in the surroundings gain the energy  $\int_{medium} \left( \int_{E_{01}}^{E_{02}} \mathbf{P} \cdot d\mathbf{E}_0 \right) \delta v$ , they also convert some of it into the energy of the  $\mathbf{E}_0$ -field. At the beginning of this process, the infinitesimal of the work done by the ferroelectric on its surroundings is much larger than that which the free charge do in building the  $\mathbf{E}_0$ -field, but as the  $\mathbf{E}_0$ -field increases, more work is done by the free charge for the same change,  $d\mathbf{E}_0$ , against an increasing  $\mathbf{E}_0$ . Equation 2.14 describes the work done by the free charge and as  $\int_{all\ space} (\varepsilon_0 \mathbf{E}_0 - \mathbf{P}) \delta v = \int_{all\ space} \varepsilon_0 \mathbf{E} \delta v$ :

(2.33)

$$\begin{aligned} & \int_{all\ space} \left( \varepsilon_0 \int_{E_{01}}^{E_{02}} \mathbf{E}_0 \cdot d\mathbf{E}_0 \right) \delta v - \int_{all\ space} \left( \int_{E_{01}}^{E_{02}} \mathbf{P} \cdot d\mathbf{E}_0 \right) \delta v \\ &= \int_{all\ space} \left( \int_{E_{01}}^{E_{02}} (\varepsilon_0 \mathbf{E}_0 - \mathbf{P}) \cdot d\mathbf{E}_0 \right) \delta v = \int_{all\ space} \left( \int_{E_{01}}^{E_{02}} \varepsilon_0 \mathbf{E} \cdot d\mathbf{E}_0 \right) \delta v \end{aligned}$$

Throughout the compensation process,  $\mathbf{E}$  acts in the opposite direction to  $\mathbf{E}_0$ , so this final integral gives a negative quantity, showing the compensation proceeds naturally, as the ferroelectric does work on its surroundings. A final point of equilibrium is reached when the work that the ferroelectric would have to do on its surroundings against  $d\mathbf{E}_0$ , would be equal to the corresponding drop in energy of the free charge to increase the energy of  $\mathbf{E}_0$ . At this point, all forces balance,  $\mathbf{E}_0 = -\mathbf{E}_M$ , there is no macroscopic field present and no further work is done.

If  $\mathbf{P}$  were to remain constant during this process,  $\mathbf{E}_M$  would also remain constant and no work would be done by internal forces in the ferroelectric ( $\int_{medium} (\mathbf{E} \cdot d\mathbf{P}) \delta v$ ). Thus the only change in the energy of the ferroelectric would be that due to the change in potential energy of its dipoles in the  $\mathbf{E}_0$ -field. This is  $\int_{medium} d(-\mathbf{E}_0 \cdot \mathbf{P}) \delta v = \int_{medium} (-\mathbf{P} \cdot d\mathbf{E}_0 - \mathbf{E}_0 \cdot d\mathbf{P}) \delta v = \int_{medium} (-\mathbf{P} \cdot d\mathbf{E}_0) \delta v$ . If  $\mathbf{P}$  were to change, the work done by internal forces would be balanced by part of the change in the potential energy of the dipoles and the change in the energy of  $\mathbf{E}_M$ :  $\int_{all\ space} (\mathbf{E} \cdot d\mathbf{P} - \mathbf{E}_0 \cdot d\mathbf{P} + \epsilon_0 \mathbf{E}_M \cdot d\mathbf{E}_M) \delta v = 0$ . Hence, in all these cases, the ferroelectric does  $\int_{medium} \left( \int_{E_{01}}^{E_{02}} \mathbf{P} \cdot d\mathbf{E}_0 \right) \delta v$  work on its surroundings.

### 2.1.6. ANALOGOUS TO THE MAGNETIC CASE?

In “Classical Thermodynamics” [51], published in 1957, the electrical analogue to the magnetic scenario described consists of a battery doing work both in creating  $\mathbf{E}_0$  and against the polarizing medium<sup>2</sup>, the infinitesimal term for which is concluded as being  $\int_{medium} (\mathbf{E}_0 \cdot d\mathbf{P}) \delta v$ .

The treatment models the magnetizing field as that produced by a solenoid and the magnetic moment of a magnetic material placed in the solenoid as the sum of elementary

---

<sup>2</sup> This argument is soon adopted by Callen [52] and later, in large part, by Adkins [53], a contemporary of Waldram and Heine and currently an emeritus professor alongside John Waldram in the Quantum Matter group at the Cavendish, Cambridge.

magnetic dipoles modelled as small current loops of a certain area. The mutual induction between the solenoid and one of these current loops is considered to ascertain the work done by the battery against the back emf in the solenoid due to the changing current in the loop, i.e. the changing magnetic moment. This is then summed over all elementary magnetic dipoles and added to the work done by the battery against the back emf due to the self-inductance of the solenoid as the magnetizing field is built up. By this method, the work done by the battery is concluded to be:

(2.34)

$$\delta W_B = \int_{all\ space} (\epsilon_0 \mathbf{H} \cdot d\mathbf{H} + \mathbf{H} \cdot d\mathbf{M}) \delta v$$

where  $\mathbf{H}$  is the field in the solenoid in the absence of the magnetic material, i.e. in a vacuum, and  $\mathbf{M}$  is the magnetization of the magnetic material, both of which can vary with position. The work done on the magnetic material alone is then  $\int_{medium} \mathbf{H} \cdot d\mathbf{M} \delta v$ . The book moves on by stating that the corresponding case for electric fields leads to the work done on a polarizable medium in a capacitor being  $\int_{medium} \mathbf{E}_0 \cdot d\mathbf{P} \delta v$ .

However, if one moves back a couple of steps in this argument, the work done on the medium is said to be that which is performed against the back emf due to the medium. In the electrical analogue, this is the work the battery does against the change in potential difference across the capacitor, due to the presence of the medium. If one separates equation 2.6 into its constituent fields:

(2.35)

$$\delta W_B = \int_{all\ space} \mathbf{E} \cdot d\mathbf{D} \delta v = \int_{all\ space} \mathbf{E}_0 \cdot d\mathbf{D} \delta v + \int_{all\ space} \mathbf{E}_M \cdot d\mathbf{D} \delta v$$

then the final term is this work done against the changing potential difference due to the medium and is equal to  $-\int_{medium} \mathbf{P} \cdot d\mathbf{E}_0 \delta v$ , as  $\int_{all\ space} \mathbf{D} \delta v = \int_{all\ space} \epsilon_0 \mathbf{E}_0 \delta v$  and  $\int_{all\ space} \epsilon_0 \mathbf{E}_M \delta v = -\int_{all\ space} \mathbf{P} \delta v$ . Hence this approach produces the same result proposed in this chapter and not that proposed by Pippard ( $\int_{medium} \mathbf{E}_0 \cdot d\mathbf{P} \delta v$ ), which

seems to have been arrived at by merely substituting analogous variables. That is,  $\mathbf{H}$  is the magnetic field in the solenoid in the absence of the magnetic medium, while  $\mathbf{E}_0$  is the electric field in the capacitor in the absence of a polarizable medium. Similarly, magnetization  $\mathbf{M}$  and polarization  $\mathbf{P}$ , of the media, are analogous. Thus,  $\mathbf{E}_0 \cdot d\mathbf{P}$  is the equivalent of  $\mathbf{H} \cdot d\mathbf{M}$  when one considers the analogous variables alone. However, if Pippard had applied the same logic and reasoning to the electric case, as he did for the magnetic case, he would have arrived at  $-\int_{medium} \mathbf{P} \cdot d\mathbf{E}_0 \delta v$  as the work done by the battery on the medium. Interestingly, the second edition of the aforementioned book by Callen, published in 1985, retains the same argument for magnetic systems used by Pippard, but omits the electrical system version.

## 2.2.THE INDIRECT METHOD

The electrocaloric temperature change inference of the indirect method is based on the following derived equation:

(2.36)

$$dT = -\left(\frac{T}{c}\right)_E \left(\frac{\partial P}{\partial T}\right)_E dE$$

Where  $P$  is polarization in the direction of the field,  $T$  is the temperature in Kelvin,  $E$  is the field and  $c_E$ , the heat capacity per unit volume at  $E$ .  $P$  is a charge per unit area of the capacitor electrode, normal to the electric field and is equivalent to the polarization in the capacitor medium [2]. At the root of this equation, lies a work term that is derived within the infinite-area capacitor model. The infinitesimal change in temperature the equation describes would be attained under isentropic conditions and comes from the initial and reasonable supposition that the entropy of the polarizing medium is only affected by a change in its temperature and / or changes in the field across the medium, which in turn, changes the dipole moment of the medium and thus its configurational entropy. Hence, one begins with:

(2.37)

$$dS = \left(\frac{\partial S}{\partial T}\right)_E dT + \left(\frac{\partial S}{\partial E}\right)_T dE$$

Then, under reversible, adiabatic conditions the change in entropy,  $dS = 0$  and:

(2.38)

$$-\left(\frac{\partial S}{\partial T}\right)_E dT = \left(\frac{\partial S}{\partial E}\right)_T dE$$

As  $dS = dq/T$  where  $q$  is heat:

(2.39)

$$-\left(\frac{C}{T}\right)_E dT = \left(\frac{\partial S}{\partial E}\right)_T dE$$

Where  $C_E = dq/dT$  is heat capacity. Thus:

(2.40)

$$dT = -\left(\frac{T}{C}\right)_E \left(\frac{\partial S}{\partial E}\right)_T dE$$

At this point, the following Maxwell relation is introduced:

(2.41)

$$\left(\frac{\partial S}{\partial E}\right)_T = \left(\frac{\partial P_m}{\partial T}\right)_E$$

where  $P_m$  is the total dipole moment of the medium. By using this relation and taking both the total dipole moment and the heat capacity over unit volume, equation 2.40 becomes equation 2.36, reproduced here:

(2.42)

$$dT = -\left(\frac{T}{c}\right)_E \left(\frac{\partial P}{\partial T}\right)_E dE$$

This refers to a change in temperature from a given field and temperature, i.e. in the limit as  $dE$  tends to zero. The constraint of this being an isentropic process introduces reversibility and thus equilibrium states and their  $P(E, T)$  data surface. The inclusion of a Maxwell relation is then possible.

An alternative to this  $dT$  equation is to start with an entropy dependence on temperature and total dipole moment, as opposed to field:

(2.43)

$$dS = \left(\frac{\partial S}{\partial T}\right)_{P_m} dT + \left(\frac{\partial S}{\partial P_m}\right)_T dP_m$$

and employ the alternative Maxwell relation:

(2.44)

$$\left(\frac{\partial E}{\partial T}\right)_{P_m} = -\left(\frac{\partial S}{\partial P_m}\right)_T$$

which leads to:

(2.45)

$$dT = \left(\frac{T}{c}\right)_P \left(\frac{\partial E}{\partial T}\right)_P dP$$

where  $c_P$  is the heat capacity per unit volume at  $P$ .

The Maxwell relations originate from the thermodynamic equation for the internal energy of a system and thermodynamic potentials that follow from that. The common description of the infinitesimal change in the internal energy of a capacitor medium (e.g.

[31-36]) mistakenly considers  $EdP_m$  to be the electrical work done on the medium and takes the form:

(2.46)

$$dU' = TdS + EdP_m$$

where  $dU'$  is the change in internal energy<sup>3</sup>.  $TdS$  is the heat gained by the medium. This equation could include further energy terms such as the pressure-volume work and stress-strain work, but they are left out here, considered negligible.

At first sight, it could be considered simpler to derive useful Maxwell relations for the indirect method by starting with the internal energy of a different system to that of the medium, i.e. the system that is everything outside the battery. Then as it is known that the work done by the battery, within the infinite-area capacitor model, is  $\delta W_B = vEdD$ , then the change in internal energy of this system is:

(2.47)

$$dU_c = TdS + EdD_m$$

where  $D_m = Dv$ . A thermodynamic potential can then be defined:

(2.48)

$$A_c \equiv U_c - TS - ED_m$$

and so the infinitesimal change in this energy is:

---

<sup>3</sup> If one follows the  $dT$  equations along the trail of referenced papers back from Mischenko *et al.* [5], it leads to the 1968 paper by Thacher [54], which refers to the textbooks by Nye [35] and Cady [32], where the expression for internal energy of the system is as described in equation 2.46, except in terms of unit volume, i.e.  $EdP$  is the work term.

(2.49)

$$dA_C = -SdT - D_m dE$$

Via the equivalence of second derivatives, which in this case, is:

(2.50)

$$\frac{d^2 A_C}{dT dE} = \frac{d^2 A_C}{dE dT}$$

the following Maxwell relation is established:

(2.51)

$$-\left(\frac{\partial S}{\partial E}\right)_T = -\left(\frac{\partial D_m}{\partial T}\right)_E$$

This modifies equation 2.36 to become:

(2.52)

$$dT = -\left(\frac{T}{C}\right)_E \left(\frac{\partial D}{\partial T}\right)_E dE$$

The system to which this equation refers is the capacitor as a whole, comprising the medium and the conductors. Note that this system includes electrodes and wires and only excludes the battery from the larger battery-conductor-medium system. Work is done by the battery to create a potential difference by charging the conductors. In considering the ideal, non-dissipative case, that energy is stored in the field change due to the new charge configuration and as potential energy due to the internal restorative forces of the polarized medium. The charge configuration includes free charge on the conductors and bound charge in the medium. Considering this system has an important drawback, as there are four variables in the internal energy expression that are required, by thermodynamics, to be invariant with position throughout the system. They are  $T$ ,  $S$ ,  $E$  and  $D$  (see equation 2.47), where  $D$  is a function of  $E$  and  $P$ . Even if it were experimentally possible to pass the conductor-medium subsystem (medium, electrodes and wires that lead right up to the

battery), upon which the battery works, through a series of quasi-static equilibrium states where  $T$  was invariant with position throughout the system,  $S$ ,  $E$  and  $P$  cannot be positionally invariant throughout this system.  $S$  in the medium is different to  $S$  in the electrodes and wires; and  $E$  and  $P$  do not even exist outside the medium. There is an illusion created here when  $VdQ$  is reformulated as  $vEdD$ , as  $E$  and  $D$  are both entirely located at the medium in this model, but it must be remembered that this is actually the work done by the battery on its surroundings, which includes the conductors of the external circuit. This issue is thus avoided by considering work done on the medium alone.

Only by both using the model of an imagined section within an infinite-area capacitor and by considering the medium alone as the relevant system, can one apply thermodynamics to predict temperature changes due to the electrocaloric effect. This is because all the relevant variables,  $T$ ,  $S$ ,  $E$ ,  $E_0$ ,  $E_M$ ,  $P$  and  $D$ , are invariant over the volume of the medium in this model, at each state the medium passes through during a quasi-static process.

## 2.3. MAXWELL RELATIONS

Four useful Maxwell relations are now established. For the error incurred by the infinite-area capacitor model to be considered negligible, the capacitor must be much wider than it is thick. Experiments presented in the following chapter comply with this requirement. Some energy functions related to the medium are now summarised.

(2.53)

$$F \equiv U - TS$$

(2.54)

$$A \equiv U - TS + E_0 P_m$$

(2.55)

$$F' \equiv U' - TS$$

(2.56)

$$A' \equiv U' - TS - EP_m$$

The first function is clearly the Helmholtz free energy. The rest are energy expressions.

The corresponding infinitesimal energy changes are:

(2.57)

$$dF = -SdT - P_m dE_0$$

(2.58)

$$dA = -SdT + E_0 dP_m$$

(2.59)

$$dF' = -SdT + E dP_m$$

(2.60)

$$dA' = -SdT - P_m dE$$

Each of these last four equations leads to a Maxwell relation, all of which apply to the medium. They are:

(2.61)

$$-\left(\frac{\partial P_m}{\partial T}\right)_{E_0} = -\left(\frac{\partial S}{\partial E_0}\right)_T$$

(2.62)

$$\left(\frac{\partial E_0}{\partial T}\right)_{P_m} = -\left(\frac{\partial S}{\partial P_m}\right)_T$$

(2.63)

$$\left(\frac{\partial E}{\partial T}\right)_{P_m} = -\left(\frac{\partial S}{\partial P_m}\right)_T$$

(2.64)

$$-\left(\frac{\partial P_m}{\partial T}\right)_E = -\left(\frac{\partial S}{\partial E}\right)_T$$

The above Maxwell relations provide four different expressions for electrocaloric temperature change, all of which would be equivalent when integrated between the corresponding limits and starting from the same temperature, providing the data employed represent equilibrium states in reversible processes. These expressions are:

(2.65)

$$dT = -\left(\frac{T}{c}\right)_{E_0} \left(\frac{\partial P}{\partial T}\right)_{E_0} dE_0$$

(2.66)

$$dT = \left(\frac{T}{c}\right)_P \left(\frac{\partial E_0}{\partial T}\right)_P dP$$

(2.67)

$$dT = \left(\frac{T}{c}\right)_P \left(\frac{\partial E}{\partial T}\right)_P dP$$

(2.68)

$$dT = -\left(\frac{T}{c}\right)_E \left(\frac{\partial P}{\partial T}\right)_E dE$$

The equivalence of these equations will be put to use in chapter 4, to investigate the validity of applying the indirect method to real data.

## 2.4. SUMMARY

- When measuring the voltage across a filled capacitor, to establish the field across it, one is measuring a potential difference due to both the free charge on the electrodes and bound charge within the medium. The field thus measured is  $E = V/l$ , where  $V$  is the voltage and  $l$  the thickness of the capacitor. It is also possible to consider  $E_0$ , which is the field due only to the free charge on the electrodes and calculated from  $D = \epsilon_0 E_0$ , where  $D$  is the surface charge density of one electrode. There is also  $E_M$ , which is the field due to the bound charge in the medium, where  $E = E_0 - E_M$ .
- The work done by a battery on the polarizable medium of a capacitor during charging or discharging, in a non-dissipative process, is:

$$- \int_{medium} \left( \int_{E_{01}}^{E_{02}} \mathbf{P} \cdot d\mathbf{E}_0 \right) \delta v$$

or, within the infinite-area capacitor model,  $-P_m dE_0$ , where  $P_m$  is the total dipole moment of the medium. It is not  $E dP_m$ , which is only part of the story, being energy stored in the medium due to internal restorative forces. Though it may not seem so at first glance,  $-P_m dE_0$ , like all thermodynamic work terms, is the product of a force causing a change, evident in reformulation:  $-P_m dE_0 = -v \epsilon_0 E_M dE_0 = -E_M l dQ$ .

- As the work done by the battery on the medium is negative, this actually means the medium does work on its surroundings. It collaborates with the battery to move the free charge around the circuit and create  $E_0$ .
- $\int_{all\ space} \epsilon_0 \mathbf{E}_M \delta v = - \int_{all\ space} \mathbf{P} \delta v$
- The indirect method uses thermodynamics to generate expressions for  $dT$ , which are functions of easily measured variables. An important part in their derivation is the inclusion of Maxwell relations, which come from energy expressions relevant to the system and defined in terms of system variables.

It is not possible to use Maxwell relations derived from energy expressions that have a  $vEdD$  term, as this refers to the work done by the battery on both the medium and the conductors that join the battery and medium. This is a larger system than the medium alone, across which, the system variables are not invariant with position. Such invariance is required by thermodynamics.

### 3. TYPICAL ELECTROCALORIC PREDICTIONS

This chapter will present predictions for electrocaloric temperature change using the indirect method. It will also draw attention to the possible variation of such predictions, where different methods of analysis, measurement and material processing are involved.

#### 3.1. EXPERIMENTAL METHOD

The majority of the thin films of lead zirconium titanate (PZT) presented here, were fabricated at Cranfield University by Tatiana Correia using a sol-gel method. Two samples, a 1.1  $\mu\text{m}$  thick “fast cooled” film and a 1  $\mu\text{m}$  “slow cooled” film (details to follow) were fabricated by Silvana Corkovic, also at Cranfield university. All films were of the same composition, containing a ratio of zirconium to titanium ions of 95:5 ( $\text{PbZr}_{0.95}\text{Ti}_{0.05}\text{O}_3$ ). The films fabricated by Tatiana Correia began with the substrate. A 700 nm layer of silicon dioxide was grown on a silicon wafer by heating the wafer at 1200 °C for 11 hours in air. An 8 nm layer of titanium was then RF sputtered onto the  $\text{SiO}_2$  surface in vacuum and then annealed in air at 550 °C for 15 minutes to oxidise the titanium. A second 8 nm titanium layer was then sputtered to improved adhesion of the subsequent 100 nm platinum layer, which was sputter deposited. The final substrate structure was then Si/ $\text{SiO}_2$ / $\text{TiO}_2$ /Ti/Pt.

The film solution consisted of lead acetate trihydrate, zirconium n-propoxide and titanium butoxide, mixed in a solution of methanol and acetic acid. Lead acetate trihydrate was first dissolved in methanol by stirring while heating. The zirconium n-propoxide and titanium butoxide were then mixed together with acetic acid and this solution was diluted with methanol. The lead based solution was then heated and mixed, under reflux, with the zirconium-titanium solution, for 2 hours. This mixture was then allowed to cool to room temperature, at which point ethylene glycol was added to stabilise the sol. An excess of 10 mol% lead was added to the solution to compensate for lead loss during later pyrolysis.

After cleaning the platinum surface of the substrate with acetone and isopropanol, a few drops of the sol were deposited onto a small piece of the substrate using a 0.2 micron

filter. The substrate was then spun at 3000 rpm for 30 seconds. During spinning, the moisture in the air allowed hydrolysis of the precursor to occur and a gel was formed. A subsequent pyrolysis step took place at 300 °C for 1 minute, which is below the crystallisation temperature of the gel, evaporating organic residuals. This formed an intermediate pyrochlore phase<sup>4</sup>. The film and substrate were then placed on a hotplate at 530 °C for a further 10 minutes. The film thus crystallized from pyrochlore to perovskite. In this way, a layer of PZT of ~70 nm was fabricated and the process repeated for subsequent layers, to build up the thickness of the film and create samples having a range of thicknesses.

When the film and substrate had cooled to room temperature, the PZT surface was cleaned with acetone and isopropanol and an array of square, chromium / gold electrodes, measuring 350 microns along one side, were deposited onto the surface, via evaporation, through a lithographically produced mask. The chromium (similarly high work function to gold) was deposited to 10 nm to improve the adhesion of the 60 nm of gold on top. Access to the underlying layer of platinum was gained by using a 5% solution of fluoridic acid and a 10% solution of nitric acid, to etch away a corner portion of the film. A cross section of the final sample is shown below:

---

<sup>4</sup> Pyrochlore phases have the composition  $A_2B_2O_7$ , where A is a large trivalent cation and B is a smaller tetravalent cation, as opposed to the  $ABO_3$  composition of perovskites, such as PZT.



**Figure 3-1. Cross section of PZT 95/05 sample mounted on sapphire disc.**

X-ray diffraction measurements show the lack of pyrochlore, which would be apparent from a peak around  $29^\circ$ .

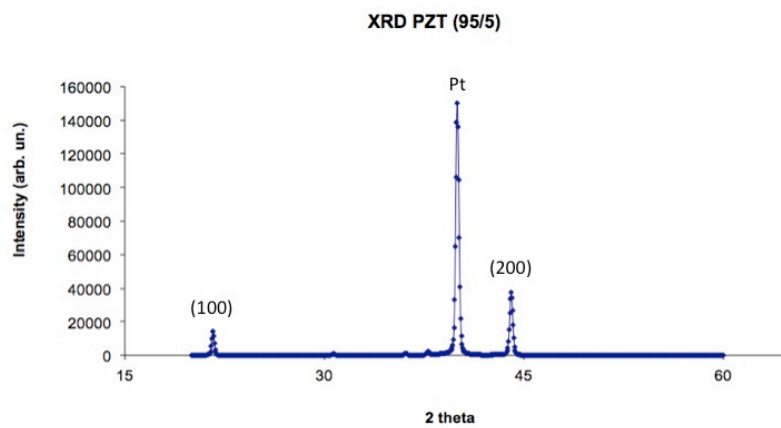


**Figure 3-2. XRD measurements on PZT 95/05**

The large peak at  $40^\circ$  is due to the platinum bottom electrode, whereas the peaks at  $21^\circ$  and  $45^\circ$  indicate PZT (100) and (200), respectively. Energy-dispersive X-ray spectroscopy was employed to confirm composition.

For the two films fabricated by Silvana Corkovic, there was a slight difference in the annealing process after pyrolysis, where the samples were annealed for 5 minutes at 450 °C and then a further 5 minutes at 530 °C. Following this, the “slow cooled” sample was placed on a hotplate, which had been pre-heated to 200 °C, for 1 minute, before finally placing the sample on a metal block at room temperature. The “fast cooled” sample was placed directly on the metal block after annealing. Additional SEM images of the cross-section of these films were obtained:

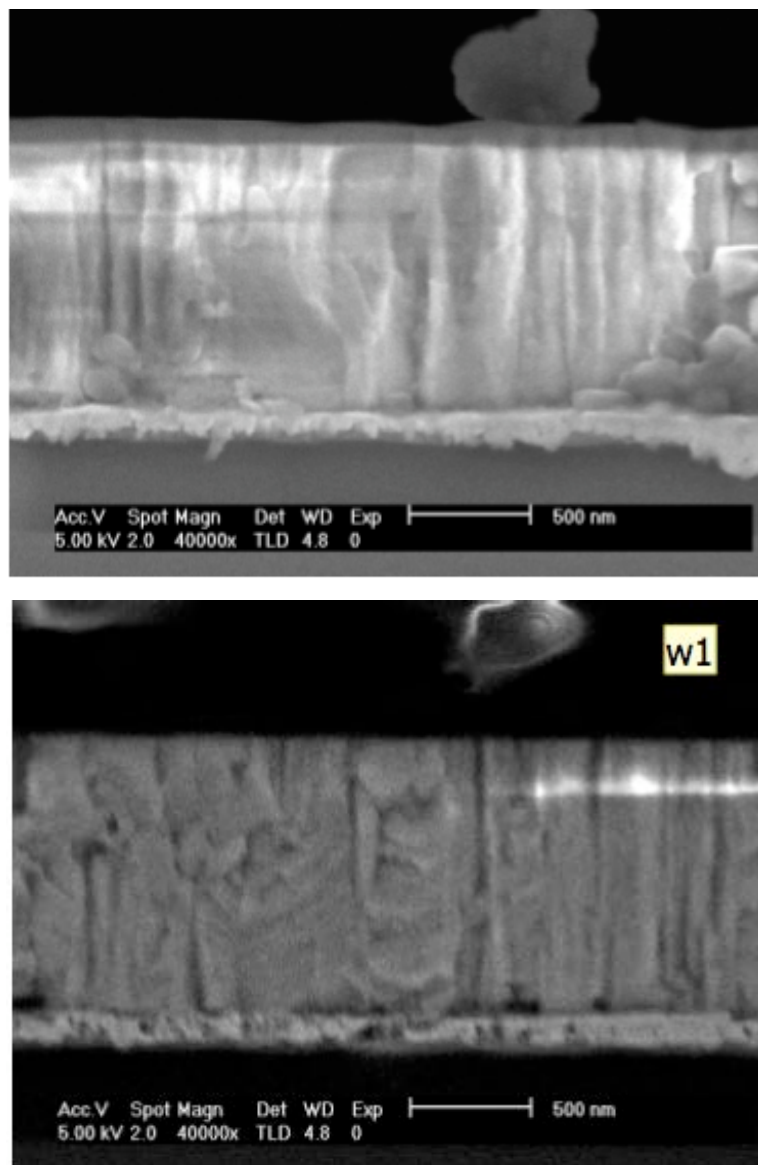


**Figure 3-3. The top SEM image is of the “slow cooled”, 1000 nm PZT film and the bottom SEM image of the “fast cooled” 1100 nm PZT film.**



trihydrate, magnesium ethoxide, titanium n-butoxide and niobium ethoxide. The lead acetate trihydrate was dissolved in acetic acid and methanol, while the magnesium and niobium ethoxides were mixed in a solution of acetic acid, methanol and acetylacetone. Titanium n-butoxide was then added to the latter solution and stirred at room temperature for one hour. The dissolved lead acetate trihydrate in solution was then slowly added to the magnesium-niobium-titanium mixture. A 20 mol% excess of lead was ensured to allow for loss of lead during annealing. Finally, ethylene glycol was added to the solution to prevent film cracking during later crystallisation. This solution was stirred for four hours.

As with the PZT 95/05 fabrication, the PMN-PT sol was spin-coated at 3000 rpm, for 30 seconds, to form a 70 nm layer and the process repeated to create the desired final film thickness. In this case, however, the Si/SiO<sub>2</sub>/TiO<sub>2</sub>/Ti/Pt substrate was initially spin-coated with a 15 nm thick “seed layer” of PZT 30/70, which proved to improve film crystallisation and assured elimination of any pyrochlore phase. The pyrolysis step was performed at 350 °C for one minute and then the film was annealed at 650 °C for 5 minutes.

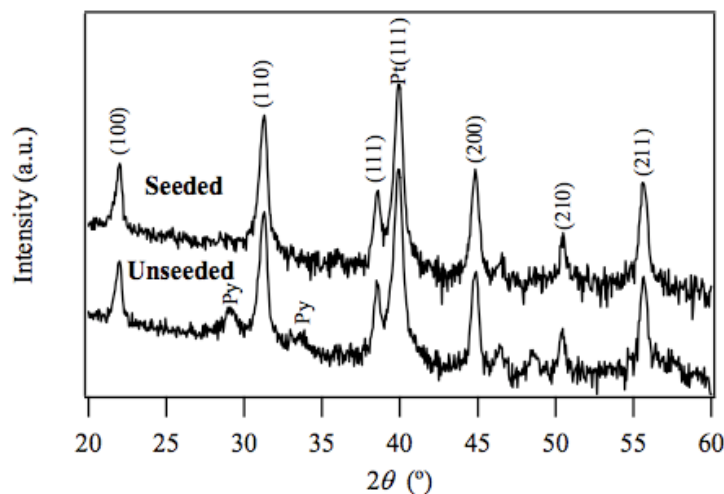


**Figure 3-5. XRD of 0.93PMN-0.07PT films.**

The XRD data shows pyrochlore reflections at 29° and 33° for the unseeded film, which are eliminated in the case of the seeded film.

For  $P(E, T)$  measurements, there were two experimental set-ups used. In the main one, the sample was connected into a simple circuit consisting of a Radiant Premier Precision ferroelectric tester and a Janis CCS-400H/204N high temperature cryostat. This cryostat is a closed circuit refrigerator, cooled via helium pumped through it from an external compressor; and the sample stage temperature is controlled externally by a Lakeshore 331S temperature controller. It has an operating temperature range from 800 K down to around 10 K. The ferroelectric tester houses an internal motherboard and is controlled via an external keyboard and monitor.

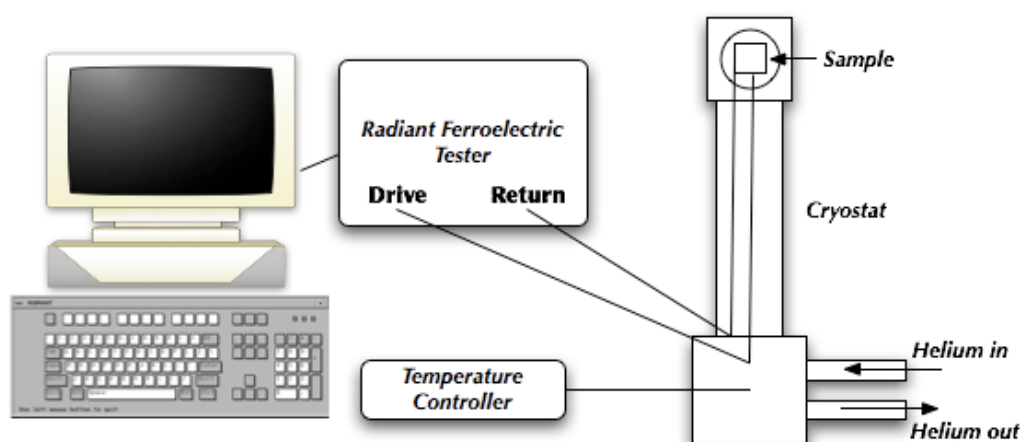


**Figure 3-6. Equipment set-up.**

The cryostat has two cold stages made from copper, the first attaches to and cools a radiation shield and the second cools the sample holder, which is thermally distanced from the second stage, via columns, to allow for gradual heat transfer. Just below the sample holder, a 50 W electrical heater is housed to heat the sample holder while the second cold stage cools it, the competing efforts of which, set the temperature of the sample stage. A diagram is shown here:

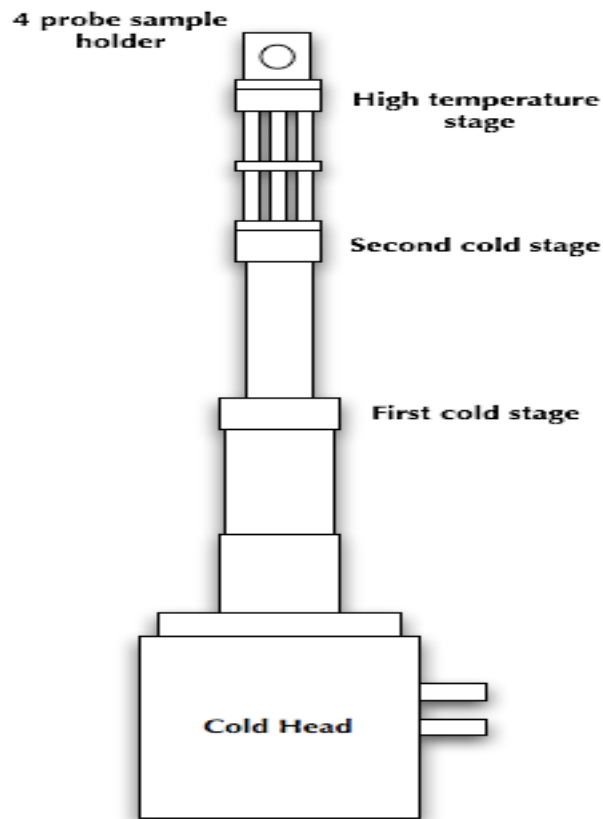


Figure 3-7. Beneath external shroud of cryostat.

The temperature of the sample stage is measured by an E-type thermocouple, which is recommended for measurements above room temperature. An optional silicon diode thermometer can be installed for low temperature measurements, where it is more accurate. Calibration of the thermometers was performed at Janis and the system delivered to Cambridge in August 2009. The precision of the temperature measurement due to the resistance of the E-type thermocouple is 0.01 K.

The following photograph shows how the cryostat is positioned vertically, when in operation:



**Figure 3-8. Cryostat on table top.**

Just to the right of centre, one can see the cryostat standing upright. Over to the left, next to the stack of three pieces of equipment, the uppermost of which is the ferroelectric tester, there is the temperature controller, which is connected to the cryostat via a multi-pin connector situated on the front of the cryostat.

The base of the cryostat is the cold head, where it is possible to see the send and return lines of the helium compressor entering the right-hand side, just behind the more obvious vacuum pump line that enters the photograph from the bottom-right corner. At the same height as the multi-pin connector, one can see BNC connectors and cables attached on the left and right. These connect probes at the sample stage in the cryostat, with the drive and return ports on the ferroelectric tester.

The upper part of the cryostat is the shroud. It sits over a radiation shield, which in turn, covers the second cold stage and the sample stage. It is clamped on to the cold head at its base, where a rubber o-ring, lightly covered in high vacuum grease, ensures the vacuum of the evacuated shroud. Four windows at the top of the shroud allow the experimenter to see the radiation shield and sample inside. The compressor sat on the floor, next to the table on which the cryostat stood:



**Figure 3-9. Compressor and vacuum pump.**

One can also see the basic rotary pump on the right of the photograph. The silver-coloured helium braided flex-hoses connect to the cold head of the cryostat, while the black hoses supply recirculated laboratory water for the cooling needs of the compressor. The black power cable is visible and the lighter grey cable is connected to the cryostat cold head to control valves within the cold head that open and close during the helium pump cycle.



**Figure 3-10. Shroud removed.**

With the shroud removed, one can see the o-ring, the radiation shield, which is firmly held against the first cold stage by six screws; and in the area below the radiation shield, insulated wires are visible. These run from the BNC ports to tungsten probes at the sample stage. There are two holes at the top of the radiation shield – one can be seen here at the front and there is another on the opposite side, to allow views of the sample.



**Figure 3-11. Cold stages and sample stage.**

With the radiation shield removed, this photograph shows the first cold stage, at the bottom of the picture. Insulated wires run around the shaft protruding from this first cold stage and a metal tube is screwed onto the second cold stage. This tube houses a J-type thermocouple which is connected to an external breaker circuit that disconnects the cryostat heater to prevent the second cold stage from rising above 325 K, which could damage the cryostat. There is a four-pin connector between the shaft and the metal tube, which is used to connect the optional silicon-diode thermometer.

On the second cold stage sits a thick copper disc, upon which there are four columns, then another copper disc and a further four columns and finally a copper section, or high temperature stage, in which two holes are visible. The heater is housed inside this copper section and its two wires are seen leaving from the hole on the right. This structure,

comprising copper discs and columns, allows for a more gradual thermal link between the heated and cooled sections of the cryostat.

The final block of copper is the sample stage:



**Figure 3-12. Sample holder.**

The probes pass through copper blocks that are screwed to the vertical section of the sample stage. There are a total of four probes that can be used, but in this picture, the two unused probes are screwed to the opposite side to allow for more space. They can be held in position at various heights by the spring loaded adjusters in the copper blocks. The circular recessed area in the middle allows for a 0.5 mm thick sapphire disc to sit comfortably, held tight against the copper block by the washers of four screws. At the bottom of the circular feature, one of these washers can be seen. The sample is then stuck to the sapphire disc by covering its bottom surface with silver dag and curing at 160 °C for 10 minutes.

The sapphire disc has a thermal conductivity that varies from ~20 to ~45 W/mK [55], across the temperature range used in the experiments presented here, which is similar to that of 20% chrome steel at our temperatures of greatest interest (22 W/mK at 200-300 °C) and about an order of magnitude smaller than that of copper at ~372 W/mK

[56]. This may be relevant as all experiments attempted to measure  $P(E)$  at given temperatures, so the intention was for the process to be isothermal. This means that as the film changes its temperature due to the change in its entropy, heat must flow into and out of the film fast enough to maintain the film at the same temperature. The degree to which the process is isothermal can be estimated with thermal modelling, though for the moment, it is to be assumed that the process is isothermal, as has been the case in all the electrocaloric literature that uses the indirect method.

The unfortunate characteristic of this cryostat is that the manipulation of the probes is rather awkward and imprecise. Electrical contact with the bottom, platinum electrode, which covers the whole area of the film, was simple. The probe was either held down on an exposed area of the electrode, due to previous chemical etching of the film, or against the lightly-sanded side of the sample where silver dag had been applied. In the case of the exposed electrode, silver dag was also applied to ensure good electrical contact. When the cryostat was running at temperatures of around 200 °C or more, if the probe contacting the top electrode rested there, applying light pressure so as not to damage the electrode and film, it was able to move and nearly always slipped off, onto the sample surface.

For this reason, it was decided to make contact between the electrode on the top of the film and the probe with a wire. Wire bonding to the top electrode proved ineffective as subsequent  $P(E)$  measurements gave distorted hysteresis loops and eventual conduction through the film, thought to be due to a damaged film surface, due to the force applied during wire bonding. To solve this problem, a 25  $\mu\text{m}$  thick platinum wire was stuck to the electrode at one end and the probe at the other. At the probe, silver dag was sufficient to keep the wire in place and provide good conduction, but sticking the wire to an electrode was a different matter.

Not only was it a very fiddly business, but also, not any silver-based adhesive would do. Silver dag would not form a small enough drop to remain only on the electrode. It would spread beyond the edges of the electrode and cause conduction through the film. Standard silver-epoxy adhesives were more promising in this respect and by bending the very end of the wire at 90° to the rest of the wire, it was possible to dip this “foot” of the wire into the epoxy mix and lightly stick it to the electrode, within the electrode area.

This provided enough adhesion to be able to move the sample to a hotplate for curing. Unfortunately, at temperatures of around 200 °C and higher, conduction through the film was occurring, evident from capacitor measurements as a function of temperature and greatly enlarged and rounded  $P(E)$  loops.

The solution came from a silver epoxy designed for high temperature applications, EPO-TEK H21D. The epoxy was cured for 30 minutes at 150 °C. This allowed for experiments where the sample temperature was cycled from room temperature up to nearly 300 °C, and back again, twice a day, over a two to three day period, without suffering the suspected silver migration and resulting conduction through the film.

After evacuating the chamber within the shroud for 30 minutes, the compressor was switched on and the cryostat cooled until the second cold stage reached a safe operating temperature to be used in conjunction with the heater, below 275 K. The sample stage could then be heated via the temperature controller until a given temperature was reached, at which  $P(E)$  measurements were performed by the ferroelectric tester. As the sample stage is brought to a desired temperature, this is initially overshoot, then brought back, also passing the set temperature, though to a lesser degree and this continued oscillation is gradually brought to near rest. The procedure in all experiments, except where indicated in the results section, was to wait until the oscillation reduced to  $\pm 0.01$  K and then to wait one minute, before measuring  $P(E)$ .

The second experimental method, which applies to just two datasets presented in this thesis, fixed the sample to the centre of a hotplate with Kapton tape and used tungsten probes mounted in micro-adjusters. Temperature measurement was less precise, using a K-type thermocouple and hand-held reader. The thermocouple was held against the hotplate, next to the sample, using Kapton tape; and it was observed that the difference between the temperature measured in this position and with the thermocouple held against the sample surface, was about  $\pm 1$  K. It was possible to stabilise the measured temperature to  $\pm 0.1$  K around room temperature and  $\pm 0.5$  K at 250 °C.

$P(E)$  measurements were taken by applying a bi-polar voltage over a given period, resulting in a hysteresis loop. For example:

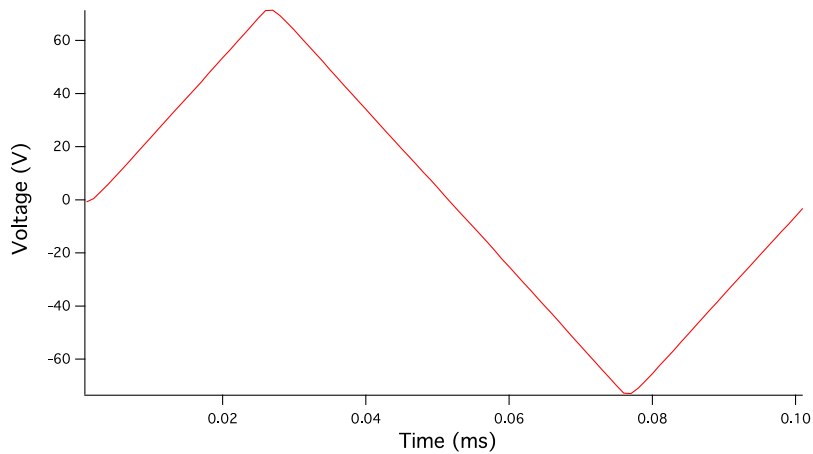


**Figure 3-13. Bipolar voltage applied by the ferroelectric tester.**

The maximum voltage in both directions and the period of the voltage excursion is set by the user. The tester ramps the voltage up and down in steps. For a 0.1 ms excursion, there are 100 steps, whereas for a 1 ms excursion or longer, 1000 steps. Thus there is 1  $\mu$ s between each step in these cases and the charge on one electrode is measured simultaneously with the voltage just before the next voltage step is executed. This is ample time for the polarization to adjust, which takes place over the nanosecond timescale, while reducing any leakage (partial conduction through the film) to a minimum. Should leakage affect the hysteresis loops, this can be easily seen, as the sharply pointed ends of the loop begin to round off. This is where even the smallest amount of leakage is evident.

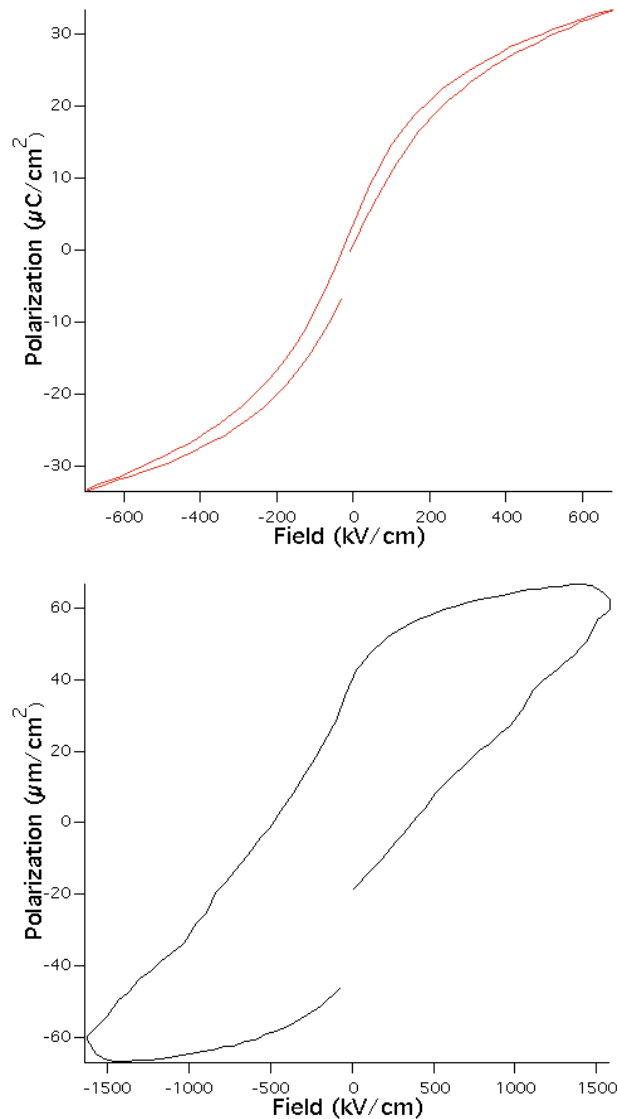


**Figure 3-14. Two P(E) loops. The top loop shows negligible leakage, the bottom loop is very significantly affected by leakage.**

### 3.2. ANALYTICAL METHOD

To illustrate the methods used in the analysis of raw data, the data measured on the  $1\ \mu\text{m}$  thick, “slow cooled”, PZT 95/05 sample, fabricated by Silvana Corkovic, will be used. The raw data supplies a  $P(E, T)$  surface, across which one predicts an adiabatic temperature change due to a changing field. As this is a prediction that employs thermodynamics, the data points that constitute the surface are implicitly taken to represent equilibrium states and that any process that moves from one state on the surface

to another, must be reversible. Thus, any adiabatic process across this surface would also be isentropic. This condition introduces the derived  $dT$  equations presented in chapter 2, which predict isentropic temperature changes.

Data is assumed to be taken isothermally and as a result of the applied bipolar voltage, takes the form of a loop:

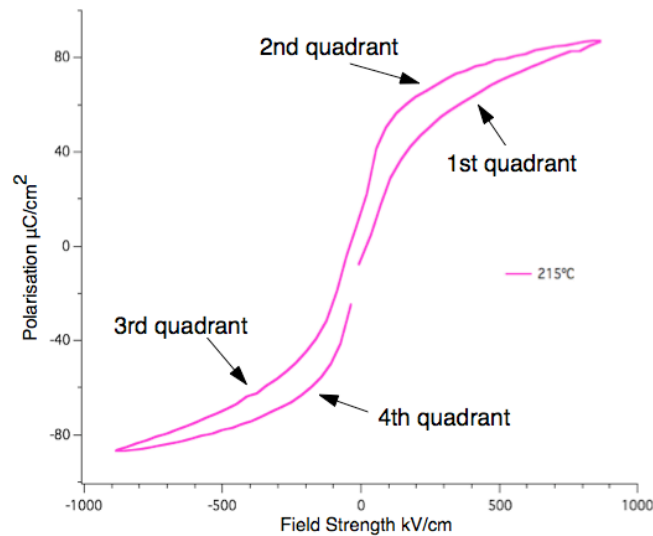


**Figure 3-15.  $P(E)$  loop at  $215^\circ\text{C}$ .**

The measured polarization as a function of field is therefore hysteretic and strictly, one cannot apply thermodynamics to hysteretic systems. However, all samples measured and presented in this thesis, are ferroelectrics, which nominally have two equilibrium states for every field value, separated by an energy barrier.

Figure 3-15 indicates a division of a typical  $P(E)$  loop, into four parts. Before applying the bipolar voltage, the ferroelectric is set to its negative remnant state, either because the last measured loop at an adjacent temperature left it in this state, or this is the first measurement in a dataset and a preset bipolar voltage is applied before taking loop data. The first quadrant, then, is measured from zero volts up to the maximum voltage, and thus, field, stipulated in the ferroelectric tester control panel. The second quadrant is the one of interest, as the voltage is stepped back down to zero volts. If the measurement of the second quadrant were performed adiabatically, rather than isothermally, the  $P(E)$

states measured along this quadrant would be at different temperatures, where a lower voltage would correspond to a lower temperature. This is electrocaloric cooling. The data in the fourth quadrant of all measured loops could equally be used.

The idea is that all the states measured in the second quadrant represent equilibrium states of the ferroelectric at the temperature at which the voltage excursion began, as we assume the loop to have been measured isothermally. By reducing the loops to just their second quadrants and joining up the data points in the temperature dimension, the desired  $P(E, T)$  surface is obtained. As the field is decreased and the material experiences an isentropic change, it is assumed that the equilibrium states through which the material would pass lie on this  $P(E, T)$  surface built from second quadrant data, as it is highly unlikely that the material would cross the energy barrier to its alternative equilibrium state for any given field. Having said that, if one were to measure loops where the maximum voltage were slightly reduced, the top-right end of this minor loop would trace out metastable states, so the predicted isentropic cooling path may well pass through metastable states, rather than equilibrium states. The principal  $dT$  equation that has been used in the electrocaloric literature is:

(3.1)

$$dT = - \left( \frac{T}{c} \right)_E \left( \frac{\partial P}{\partial T} \right)_E dE$$

To predict isentropic cooling, one would then choose a starting temperature and field and move across the  $P(E, T)$  surface according to equation 3.1. The following figure shows the second quadrant data for the 1  $\mu\text{m}$  thick, “slow cooled” PZT 95/05:

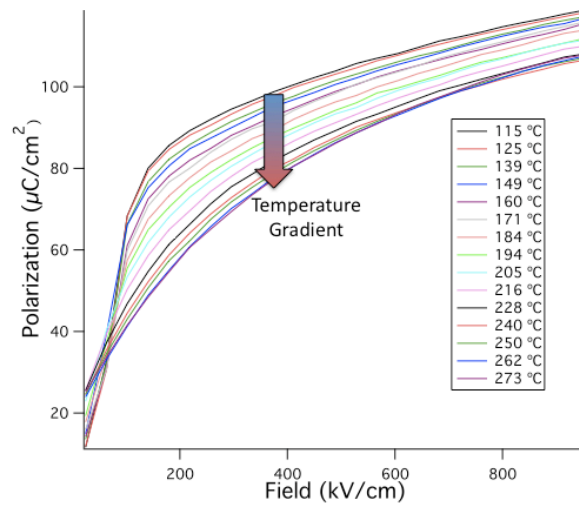


**Figure 3-16. Second quadrant data from P(E) loops measured on 1 $\mu$ m thick PZT 95/05. The lower polarization curves were measured at higher temperatures.**

When the data from these curves are presented in a three dimensional format, one has:

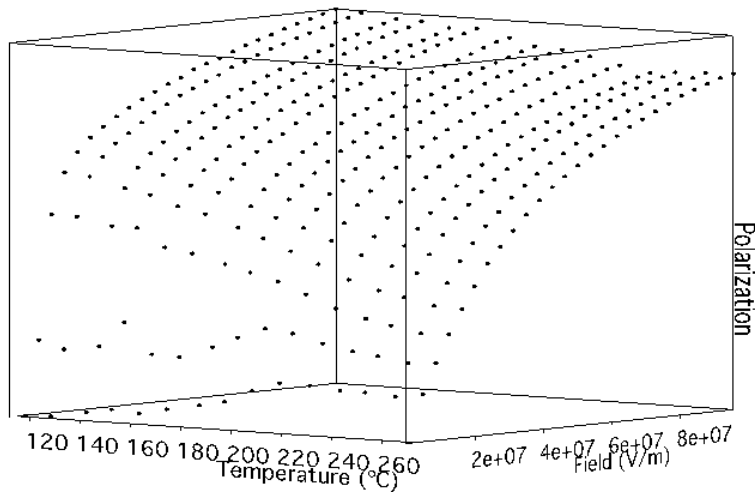


**Figure 3-17. P(E,T) data points measured on 1 $\mu$ m thick PZT 95/05.**

Each black dot is a single data point and one can see how the three dimensional plot shows the second quadrant curves spread along the temperature dimension.

The  $dT$  calculation is then applied to this discrete data, which of course, implies an approximate temperature change prediction, as  $dT$  should be calculated in the limit as  $dE$  tends to zero, when in practice,  $dE$  must be finite. The other approximation that is consistently applied in the electrocaloric literature is in the value of the specific heat capacity, which is taken as constant throughout the field and isentropic temperature change, though estimations of maximum possible variance in heat capacity suggest a reduction in cooling of no more than around 3% of the predicted temperature drop (based on [81]).

The ferroelectric tester is designed to measure polarization and voltage values at equal time intervals. This means that when comparing data from loops taken at different temperatures, such as on the  $P(E, T)$  surface constructed, the voltage values can differ very slightly and hence the calculated field values. The heart of the  $dT$  calculation, is  $\left(\frac{\partial P}{\partial T}\right)_E dE$ , so one can start on the surface at some measured point and calculate the difference between the polarization value at that point and at the same field on the second quadrant curve of the next temperature up, giving  $\left(\frac{\partial P}{\partial T}\right)_E$ .

This implies the necessity for linear interpolation between two points on the higher temperature second quadrant, thus slightly deviating from actual measured points. This deviation is unavoidable and it is simpler to linearly interpolate each of the second quadrant curves, using an equal number of points, so that all their data points occur at the same field values and then transpose  $P(E)$  at a set of  $T$  values, to give  $P(T)$  at a set of  $E$  values. From this, one can differentiate and transpose again to gain  $\left(\frac{\partial P}{\partial T}\right)_E(E)$  at the original set of  $T$  values, i.e. the temperatures at which the loops were taken. Stepwise integration then completes the analysis to give the predicted temperature change. Interpolation and transposition of the second quadrant data for the 1  $\mu\text{m}$  thick PZT 95/05 sample, leads to the following  $P(T)$  graph:

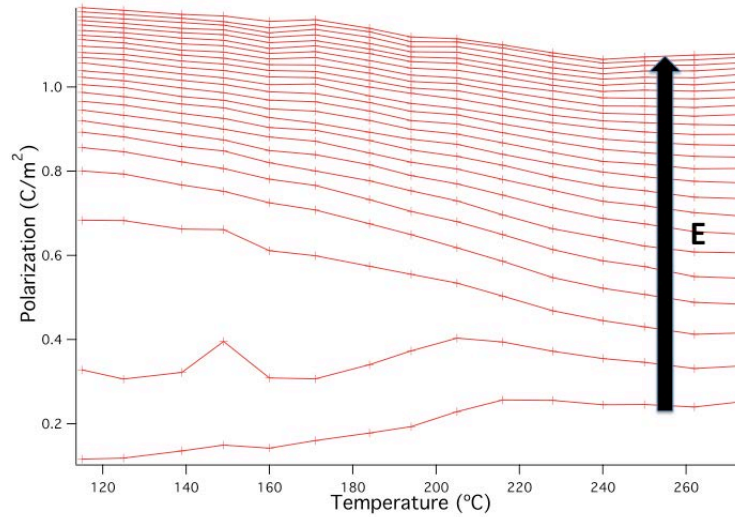


**Figure 3-18.  $P(T)$  at a set of field values. Points at the same field ( $E$ ) are joined to give a set of curves, where those higher up the graph correspond to larger fields.**

The red crosses in the above figure mark the linearly interpolated data points and one can see those that were measured at the same temperature. In the electrocaloric literature, there are examples of predicted temperature changes, where it is not clear whether the predictions are for electrocaloric cooling or heating [4, 5, 10, 12, 13, 17-19, 21, 22, 24, 25, 28]. Where any  $\Delta T$  calculations are presented, they are often displayed as a function of temperature and field change, such as the following graph from D. Saranya *et al.*:

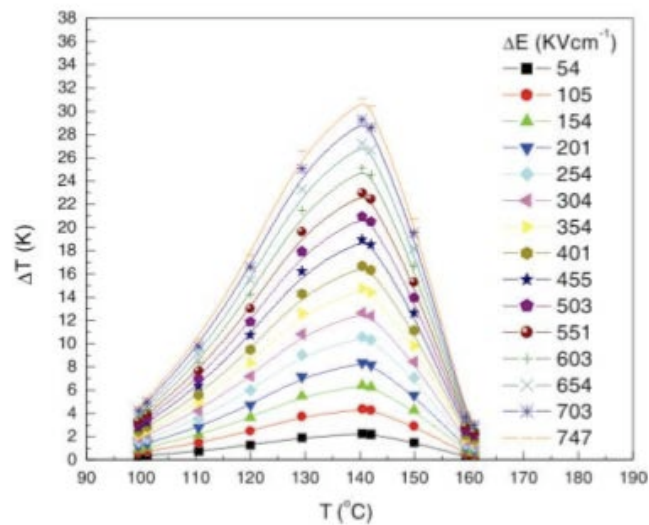


**Figure 3-19. From D. Saranya *et al.* [22]. Temperature change predictions from applied / withdrawn voltage.**

In this case, it was not made clear as to whether the  $\Delta T$  curves refer to an application or release of electric field, but in general, it must be made clear that when calculating  $\Delta T$  for a given field change across some  $P(E, T)$  surface, that the temperature referred to along the bottom axis is a starting temperature and that for any given  $\Delta E$ , there will be one  $\Delta T$  curve that corresponds to electrocaloric cooling and another that corresponds to heating. As the thermodynamic nature of these calculations implies a reversible  $P(E, T)$  surface, then if the curve representing  $\Delta E=747$  kV/cm in fig. 3-19, refers to cooling, there will be a heating curve that peaks at around 31 °C below the peak of the cooling curve. The heating and cooling curves will have data points at the same  $\Delta T$  values and these corresponding data points will be separated horizontally by their  $\Delta T$  value. It is equally important to recognise that when stepping across the  $P(E, T)$  surface according to  $dT$  calculations over small  $dE$  steps, that  $\left(\frac{\partial P}{\partial T}\right)_E$  varies from point to point and one must take this into account.

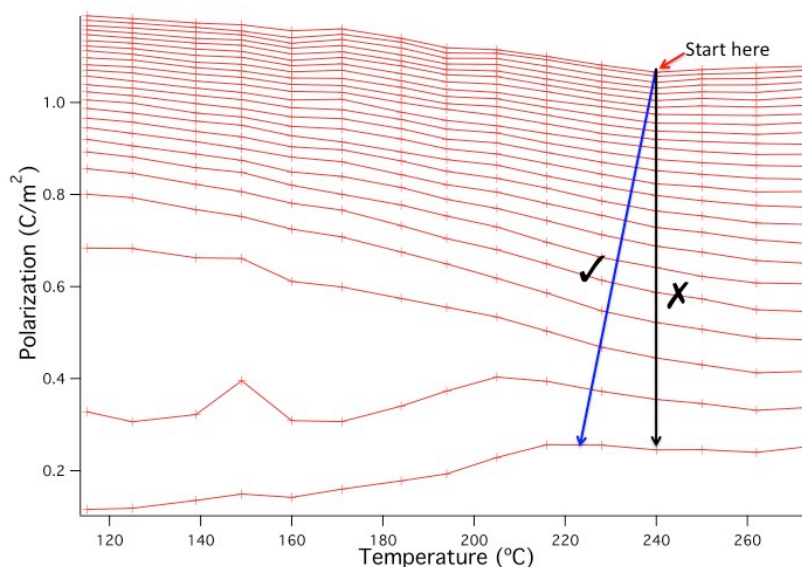


**Figure 3-20. Blue arrow represents electrocaloric temperature change, starting at high field at 240 °C and cooling by releasing the field.**

The above figure illustrates this quite well, as one can imagine starting at high field at 240 °C and releasing the field under isentropic conditions to cause the material to cool.

The blue line represents an approximation to the electrocaloric cooling, along which, one can see that the  $\left(\frac{\partial P}{\partial T}\right)_E$  values are quite different to those along the black line at 240 °C, which refers to an isothermal change.

Once the  $P(T)$  data has been differentiated and transposed, the final graph is obtained, from which  $\Delta T$  predictions are obtained:

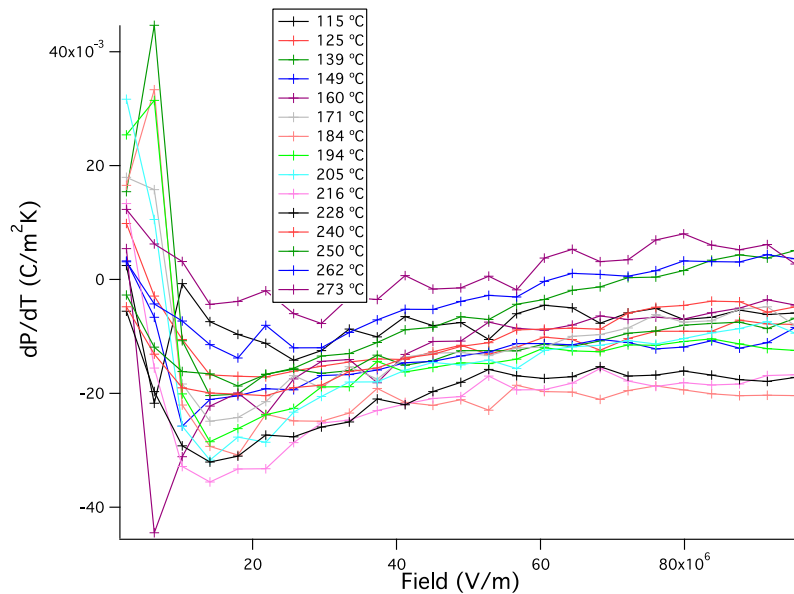


**Figure 3-21.  $dP/dT$  vs  $E$  at different  $T$ .**

The cooling calculation starts at a given temperature, represented by one of the curves in the above graph, and the maximum field value. By gradually increasing the field range over which one integrates this curve, i.e. by gradually decreasing the lower limit of the integration, the calculated  $dT$  increases to a point where one must change to another curve, representing an adjacent temperature. At this point, the field is lower and integration continues with the new curve, from this field downwards, moving from one temperature curve to another and so on, until the minimum field. In this case,  $\Delta E=929$  kV/cm. As the differentiation of  $P(T)$  was performed with a forward difference method, a given temperature curve in fig. 3-21 covers all temperatures between its own and the next highest temperature. This  $\Delta T$  calculation follows an adiabatic temperature change path, albeit a rather coarse one, due to the discrete nature of the data and large intervals between temperatures. By inserting intermediate curves between those in fig.

3-21, one gains finer calculations, though of course, this does not represent finer data in the temperature dimension, but merely the artificial insertion of intermediate points between adjacent temperature curves. All analysis was performed in Igor Pro, via user defined functions, which are included in appendix C. The resulting electrocaloric cooling and heating predictions are presented here:

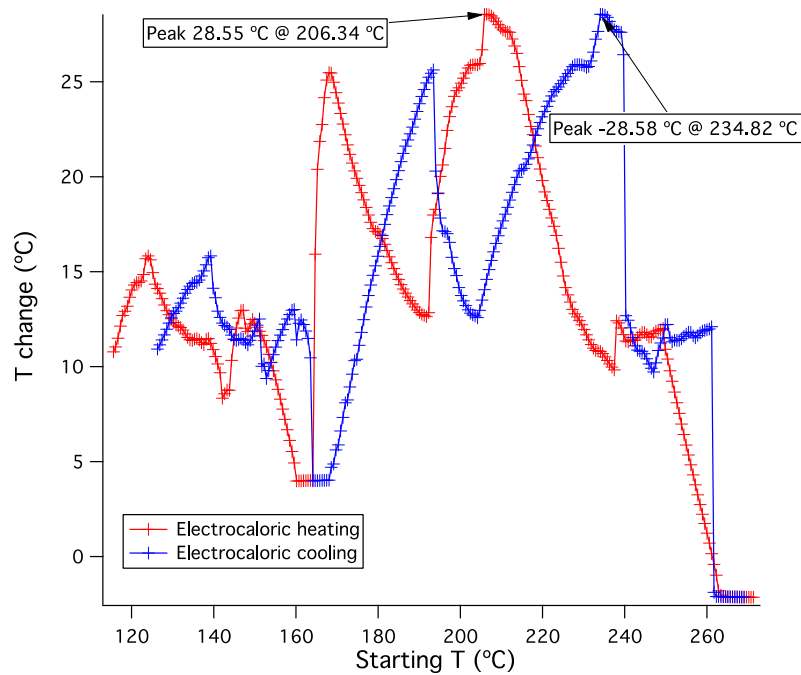


**Figure 3-22. Electrocaloric cooling and heating calculated from  $P(E,T)$  measurements on a 1  $\mu\text{m}$  thick film of PZT 95/05. Data points are joined by lines.  $\Delta E=929$  kV/cm.**

The  $\Delta T$  values of the electrocaloric cooling curve in the above figure, have been multiplied by -1 and the vertical axis renamed “T change”, to allow for an easier visual comparison between heating and cooling curves. Perhaps the most surprising characteristic of these curves is the degree to which they fluctuate, not following a smooth progression as one might hope for and expect. This highlights the large effect that minor deviations in the smooth progression of  $P(E, T)$ , can have on the final electrocaloric predictions. For this reason, predictions from raw  $P(E, T)$  data have generally not been presented in the electrocaloric literature and attempts have been made at drawing smooth lines through  $P(T)$  curves derived from the raw data.

What is evident, however, is how heating and cooling predictions trace out different curves, where logically, the larger the change in temperature, the greater the separation between cooling and heating curves. This relationship, where the separation of the curves would be equal to their height at any given point, is not represented exactly here, due to the discrete nature of the data, but one can see how the peak cooling and heating values calculated here turn out to be identical, though their separation differs from these peak values by about a degree Celsius.

Three methods have been used in the literature to draw smoother lines through imperfectly smooth  $P(T)$  data. These have been via polynomial regression (e.g. [5, 12, 13, 18, 28]), boxcar smoothing [20] and cubic spline interpolation [21]. The first attempts to fit a mathematical expression to the data while the second redefines the  $P$  value at a given  $T$  and  $E$ , by taking an average of itself and its neighbours along the temperature axis, at the same  $E$ . Such data manipulation may assume that the smoother data more accurately represents the data one would gain by taking an average of a large amount of  $P(E, T)$  data measured identically, on identical samples. It is clear from ferroelectric hysteresis measurements, that no two loops are identical, though they can be very similar.

More fundamentally, one would hope that the manipulated data more closely represents equilibrium points on a reversible surface, so that the thermodynamic treatment of the electrocaloric effect becomes more, rather than less, of an approximation. This theme will be explored in the following chapter.

In what remains of this section, various forms of data smoothing will be presented and the electrocaloric prediction results compared. These will initially be the polynomial fit and boxcar smoothing, as previously mentioned, plus a surface smoothing, where the whole of the  $P(E, T)$  surface is smoothed, not just data in the  $P(T)$  planes. As temperature change predictions utilise the three dimensions of the  $P(E, T)$  surface, as opposed to the two dimensions of a  $P(T)$  curve, it would perhaps seem more appropriate to smooth the whole surface, rather than just  $P(T)$  at different  $E$ .

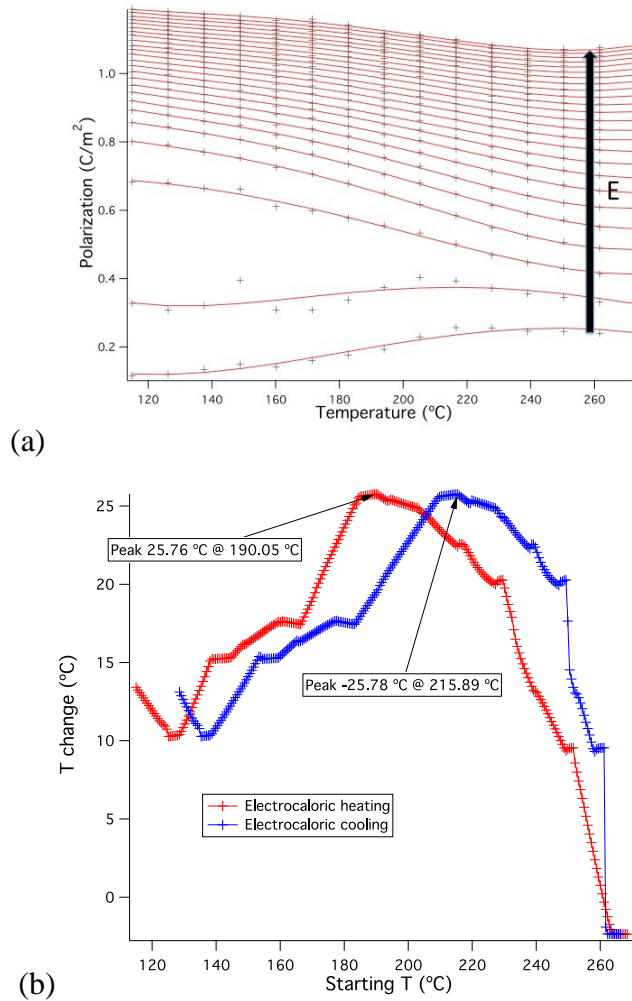


**Figure 3-23. 1  $\mu\text{m}$  thick PZT 95/05. (a)  $P(T)$  at various  $E$ . The red curves are 4<sup>th</sup> order polynomial fits through isofield, black data points. (b) Heating and cooling predictions.  $\Delta E=929$  kV/cm.**

The polynomial curves in the graph (a) of the above figure fit very closely to the field curves, with the exception of the bottom two or three, principally, the second curve from the bottom. In this case it is not clear whether or not the raw data point at 149 °C, is an outlier. The calculated cooling and heating curves show less fluctuating predictions of temperature change with starting temperature, compared with the calculations based on raw data. The peak changes are slightly smaller and the peak cooling starting temperature is about 20 °C lower than in the raw data case.

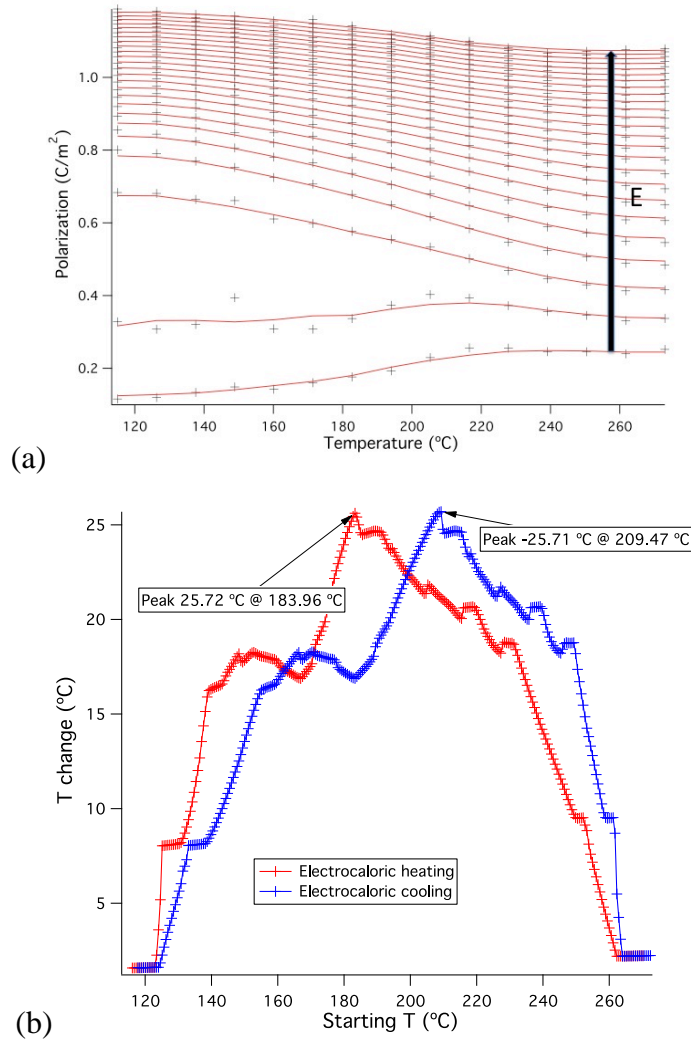


**Figure 3-24. 1  $\mu\text{m}$  thick PZT 95/05. (a)  $P(T)$  at various  $E$ . Red lines join boxcar smoothed (five point averaging) black data points at a specific  $E$ . (b) Heating and cooling predictions.  $\Delta E=929 \text{ kV/cm}$ .**

The smoothed data in the graph (a) in the above figure, represented by the red lines, joins points that are averages of the data points along each field curve. Here, this boxcar smoothing is performed over five points, so the polarization for every raw data point on a field curve is replaced with the average of the polarization values of itself and those of the two raw data to its left and two to its right. This is five point boxcar smoothing, a moving-average method. At the ends of the field curves, imaginary data points are created to determine averages. The points along a curve are numbered from zero to  $n$ , so  $n$  will be one less than the number of points on the curve. Then the imaginary points beyond the ends of the curve are created by setting the polarization value of curve point  $-i$  equal to that of curve point  $i$ , at the beginning of the curve; and curve point  $n+i$  takes on

the polarization value of point n-i, at the end of the curve. This is appropriately referred to as the “bounce” method. The temperature change predictions, in this case, are very similar to those from the polynomial fit data, though the peak cooling starting temperature is around 6 °C lower.

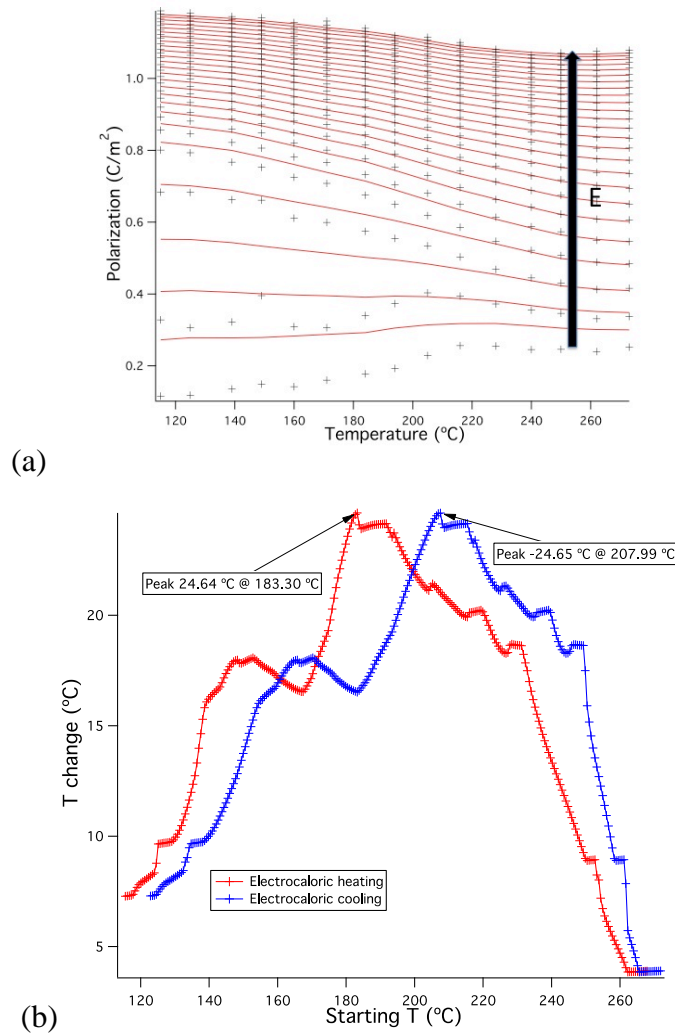


**Figure 3-25. 1  $\mu\text{m}$  thick PZT 95/05. (a)  $P(T)$  at various  $E$ . Red isofield curves are extracted from surface smoothing of data. (b) Heating and cooling predictions.  $\Delta E=929$  kV/cm.**

In this case of surface smoothing a kernel moves across the raw  $P(E, T)$  surface, taking a similar five-point average as in the boxcar smoothing example, except here, the average is over an extra dimension, making it an average of 25 points. The kernel is a 5x5 square matrix and it centres on each data point on the surface, replacing the polarization value of that data point with the average of all 25 points in the matrix. This is another moving-

average method, where calculations at the edges of the surface are dealt with by replicating the edge data to artificially extend the surface. It is clear from the graph (a), in the above figure that this method unfortunately results in field curves that deviate very significantly from the raw data at lower fields. However, the gradients of these curves, which are the key elements in the temperature change predictions, are rather similar to those in the boxcar smoothing case. Hence, heating and cooling peaks in graph (b) of the above figure, are only about a degree lower than in the boxcar smoothing analysis.

A summary of  $\Delta T$  predictions are presented below:

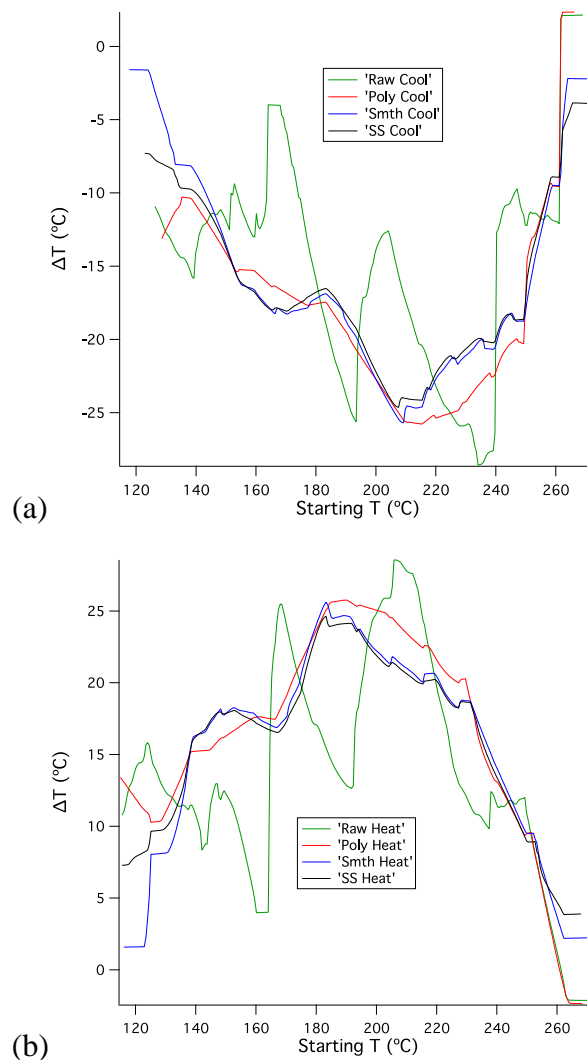


**Figure 3-26. A summary of (a) electrocaloric cooling and (b) electrocaloric heating predictions, calculated from raw data and P(T) data that was smoothed in various ways – by fitting a polynomial curve (poly), by applying a five point moving average (smth) and by using a 5x5 square matrix averaging across the P(E,T) surface (SS).**

$$\Delta E = 929 \text{ kV/cm.}$$

There seems to be a common, general shape to all the curves in fig. 3-26 and the three  $P(T)$  data smoothing methods have produced similar  $\Delta T$  results. Predictions based on raw data, however, vary greatly and oscillate about this general shape. Despite the surface smoothing giving a bad fit to the data, the  $\Delta T$  curves from the  $P(T)$  smoothing and  $P(E, T)$  surface smoothing methods are almost identical. The peak cooling values vary from  $-24.63$  °C to  $-28.56$  °C, which is a difference of just under 4 °C. The starting temperatures at which these peak cooling predictions are calculated to occur, range from  $207.54$  °C to  $234.06$  °C, a spread of  $26.52$  °C. If one excludes the predictions from raw data, peak cooling varies from  $-24.63$  °C to  $-25.77$  °C, just over 1 °C of difference. This seems negligible in light of the difference between heating and cooling calculations, where the discrete nature of the data can cause such variation. The starting temperatures, however, range from  $207.54$  °C to  $215.44$  °C, which is a difference of  $7.9$  °C. The following table summarises the results:

	COOLING		HEATING	
	<i>Peak change</i> (°C)	<i>At</i> (°C)	<i>Peak change</i> (°C)	<i>At</i> (°C)
Raw data	-28.58	234.82	28.55	206.34
Polynomial fit	-25.78	215.89	25.76	190.05
Smoothed	-25.71	209.47	25.72	183.96
Surface Smoothed	-24.65	207.99	24.64	183.30

**Table 2. Peak electrocaloric cooling and heating predictions in 1µm thick, “slow cooled” PZT 95/05.  $\Delta E=929$  kV/cm.**

When calculating how the isentropic temperature change progresses over the  $P(E, T)$  surface, it is necessary to make certain assumptions. By manipulating the raw  $P(T)$  values at each  $E$ , to give fit or smoothed data, the number of points nor the temperature of those points on the  $P(T)$  curves was changed. In the final integration of  $\left(\frac{\partial P}{\partial T}\right)_E$ , assumptions must be made about the  $\left(\frac{\partial P}{\partial T}\right)_E$  values between the  $\left(\frac{\partial P}{\partial T}\right)_E$  curves at different

temperatures, that have been extracted from the  $P(T)$  data. The simplest assumption, which is the one made here, is that  $P(T)$  isofield data points are joined by straight lines.

The above calculations, illustrating the relationship between heating and cooling curves, were made by inserting equidistant points along those straight lines that join  $P(T)$  points and hence, no further assumptions are made by doing so. By calculating temperature changes from many temperature starting points, it has been possible to demonstrate how the starting temperatures of the electrocaloric heating and cooling curves are separated by their  $\Delta T$  values at any given starting temperature. Any  $\Delta T$  versus starting temperature graph must be clear about whether it represents heating or cooling predictions. However, if one chooses to calculate  $\Delta T$  only from the starting temperatures where data was measured, the results can differ significantly to those where intermediate values are inserted. This can be seen in the following figures and table, where calculations were performed only at the measurement temperatures. The peak temperature changes seen from the raw data are over 3 °C less (over 10%) than in the previous data and the peak-change starting temperatures differ by up to ~6 °C. This excludes the surface smoothed calculations, which have only been presented here to illustrate how little difference one can find in the  $\Delta T$  predictions, despite significant manipulation of the raw data.

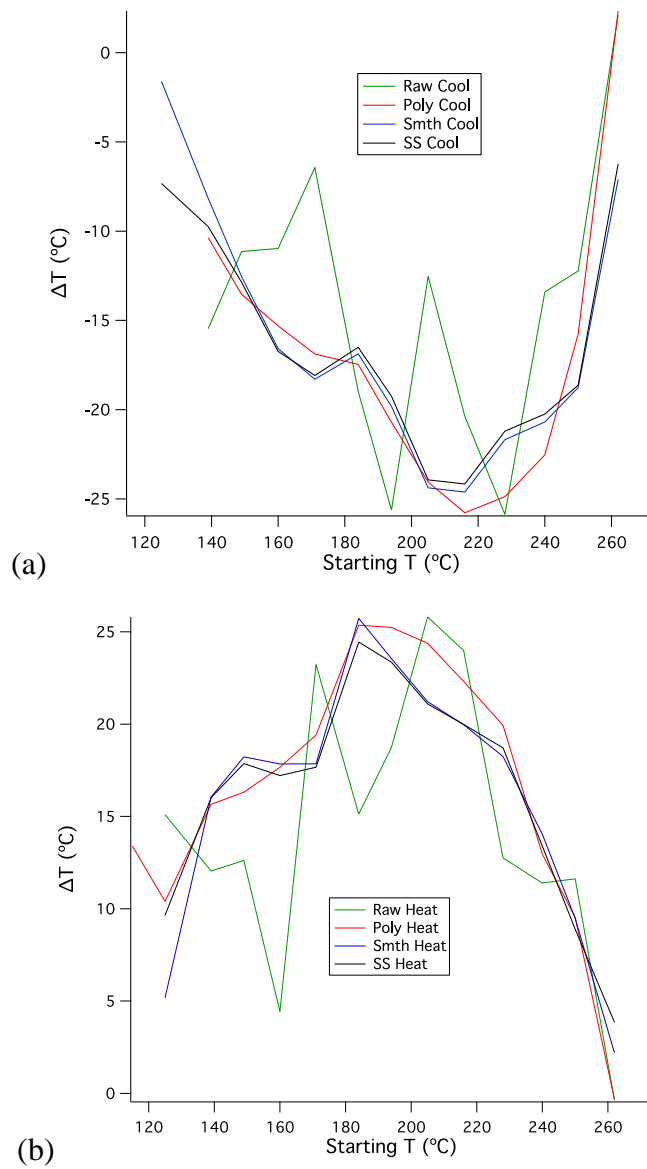
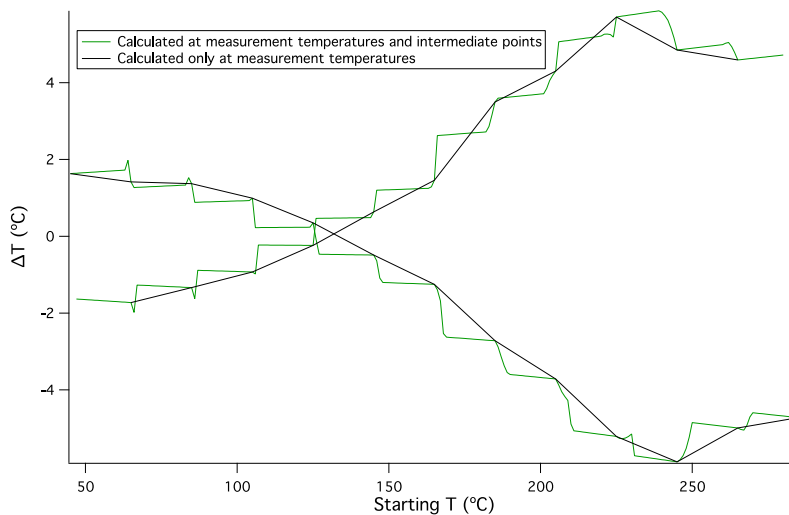


Figure 3-27. As fig. 3-26, except calculations made at measurement temperatures only.

	COOLING		HEATING	
	Peak change (°C)	At (°C)	Peak change (°C)	At (°C)
Raw data	-25.86	228.00	25.80	205.00
Polynomial fit	-25.78	216.00	25.36	184.00
Smoothed	-24.62	216.00	25.73	184.00
Surface Smoothed	-24.17	216.00	24.44	184.00

**Table 3.** As table 2, , except calculations made at measurement temperatures only.

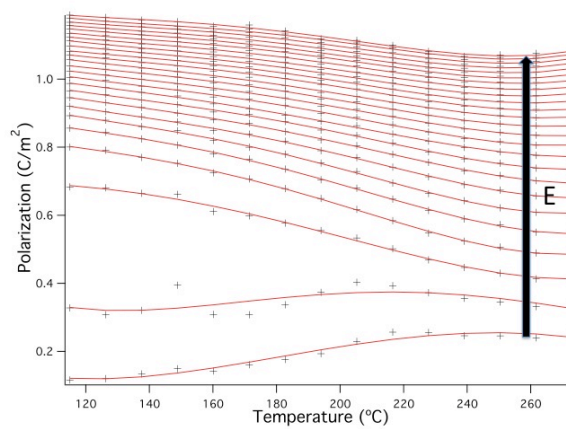
These variations between the peak temperature change predictions, depending on whether one includes the implicit intermediate  $P(T)$  data or only calculates at the measurement temperatures, are merely due to that simple difference. Temperature change calculations return the exact same result at the measurement temperatures, regardless of whether the calculation is performed across twenty  $\left(\frac{\partial P}{\partial T}\right)_E$  curves, or two hundred, for example. The following figure shows the  $\Delta T$  calculations for such a dataset:



**Figure 3-28.** Comparison of predictions (field applied or released) from data at measurement temperatures and that from the same, plus intermediate  $P(T)$  data. Dataset measured from 285 °C to 45 °C in 20 °C steps, on 1.05 $\mu\text{m}$  thick PZT 95/05.  $\Delta E=440$  kV/cm.

The calculations from the denser data are stepped. This is due to the artificial insertion of data along straight lines joining  $P(T)$  points and particular to a dataset where data is measured at temperature intervals that are large compared to the calculated temperature changes. Though  $\Delta T$  calculations are thus made at many intermediate  $P(T)$  points, those points are nonetheless taken to exist when  $\Delta T$  calculations are only made at the measurement temperatures.

One could argue that if  $P(T)$  data is to be manipulated at all, then the line that would be drawn through any set of isofield  $P(T)$  data should consist of a large number of points and follow the curvature of the surface, which is evident to the eye, between measured data. This can be attempted either by using a polynomial fit with many points or by linearly interpolating each isofield curve and then boxcar smoothing over many points. The following figure shows how  $P(T)$  graphs can vary, depending on how one decides to draw a line through raw data.



(a)

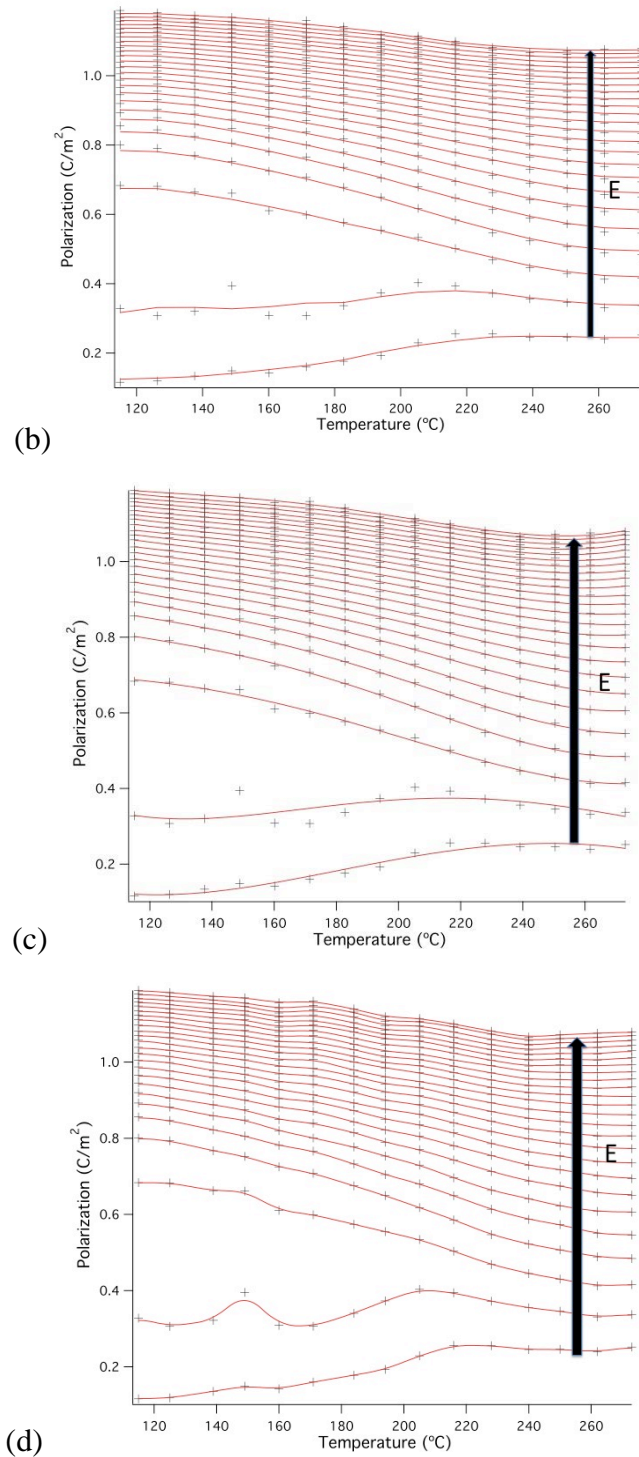
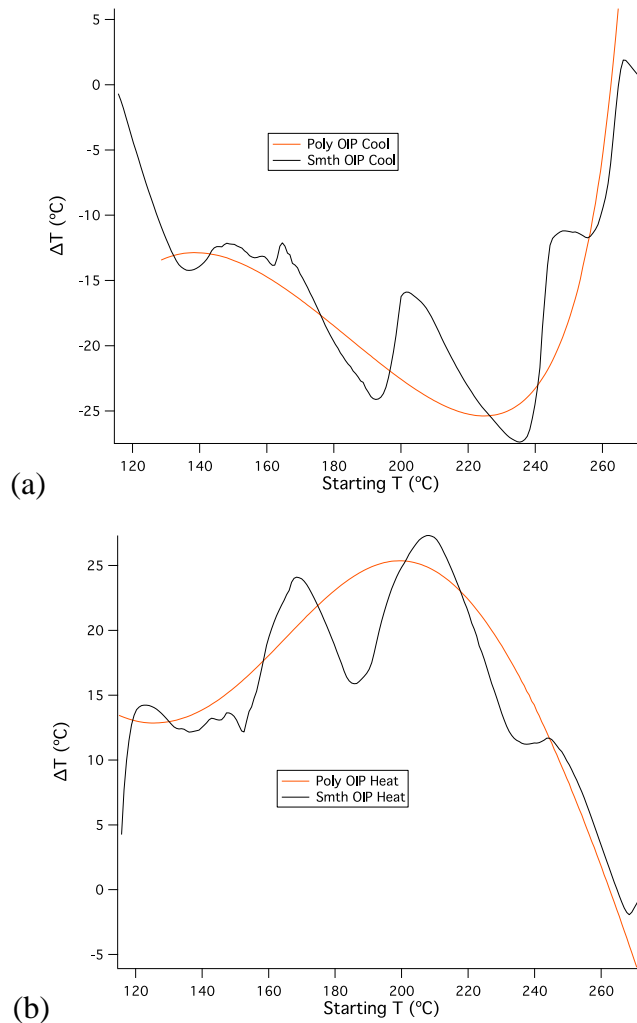


Figure 3-29. 1  $\mu\text{m}$  thick PZT 95/05.  $P(T)$  at various  $E$ . Red lines are isofield alternatives to raw data (black crosses). Graphs (a) and (b) are reproduced from fig. 3-23 and fig. 3-24. (a) Red lines are 4<sup>th</sup> order polynomial fits, joining 15 points at the same temperatures as raw data. (b) Red lines join five-point boxcar smoothed raw data (15 points). (c) Red lines are 4<sup>th</sup> order polynomial fits, joining 211 points. These correspond to points at the same temperatures as raw data, plus 14 intermediate points between each pair of raw data points. (d) Red lines join 15-point boxcar smoothed data, which are the linear interpolation of raw data (14 intermediate points per raw data pair).

All four of the alternative isofield curves in the above figure are nominally good fits. It is debatable as to which of the four represents the better alternative. Graph (d) seems to most closely follow the raw data, but the best choice would be that which most closely represents equilibrium states through which the material should pass, were this whole thermodynamic approach valid. Essentially, one is taking blind guesses by drawing lines through raw data and the above alternatives are just as good as each other. Despite seemingly smoothly varying  $P(T)$  data, analyses using raw data often result in the violently oscillating  $\Delta T$  predictions shown in this section and though drawing lines through  $P(T)$  data is guesswork, it is arguably an improvement over the use of raw data for  $\Delta T$  predictions, producing smoother varying  $\Delta T$  predictions over a given field and temperature range. Looking past the small lumps and bumps on the measured  $P(E, T)$  surface, one can plainly see how the surface undulates smoothly and hence, should provide smoothly varying  $\Delta T$  predictions. The difficulty lies in finding the best way to remove the imperfections on the surface and this topic has not been dealt with in the electrocaloric literature. The rest of this chapter intends to demonstrate the extent of the variation in  $\Delta T$  predictions, depending on whether raw data or some reasonable alternative is used; and how that variation is amplified when more than one dataset measured on the same piece of material is considered. This variation can be further extended when data is measured on the same film, but at different locations and tiny changes in film processing can make quite startling differences.

The  $\Delta T$  predictions from polynomial fits and boxcar smoothing of raw  $P(T)$  data, over an increased number of points (fig. 3-29, graphs (c) and (d)) , are presented below:



**Figure 3-30. (a) Cooling and (b) heating predictions from polynomial fits to and smoothing of many points per  $P(T)$  isofield curve, i.e. an extra 14 intermediate points per pair of  $P(T)$  raw data points.**

At this point, it may be useful to clarify the difference between the  $\Delta T$  predictions in the above figure and those made in fig. 3-26. For predictions made from polynomial fits to  $P(T)$  data, in one case, the fits are made using the same number of points as there are isofield, raw data points to which one is fitting. Then straight lines are drawn between these new fit points and an additional 14 points introduced at equidistant positions along each of these straight lines. Each new point will be at a different temperature. To create fig. 3-26,  $\Delta T$  calculations were made at all of these temperatures, which are those where raw data was measured, plus all the intermediate temperatures. In the second case, polynomial fits to  $P(T)$  data are made using a larger number points than the number of measurement temperatures, specifically, 14 more points between each pair of isofield,

raw  $P(T)$  data points. So in this second case, the fit also applies to the intermediate temperatures, whereas in the first case, the fit is over the raw data points alone.  $\Delta T$  calculations from this method are shown in the above figure, where “OIP” is used in the graph legend to indicate that the polynomial fits to  $P(T)$  data from which these  $\Delta T$  predictions have been made, were fits that were also made Over Intermediate Points.

For predictions made from boxcar smoothed data, the first case smooths the isofield, raw data and straight lines are drawn between the smoothed points. Then 14 intermediate points, per pair of adjacent smoothed points, are introduced at equidistant positions. Figure 3-26 shows  $\Delta T$  calculations made from all of these temperatures. In the second case, straight lines are drawn between isofield, raw  $P(T)$  data points, the 14 intermediate points introduced and then smoothing is performed over 15 points. This results in  $P(T)$  curves that weave their way from one measured  $P(T)$  point to the next. The more uneven the raw data, the more the  $\Delta T$  predictions from such data will oscillate in a similar way to  $\Delta T$  predictions from raw data, as is the case for this dataset. OIP smoothing results in  $\Delta T$  predictions that are more distinctive than those from raw data where raw data are smoother in  $P(T)$  and measured at larger temperature intervals.

The difference between the  $P(T)$  curves is shown in the following figure over several raw, isofield data points:

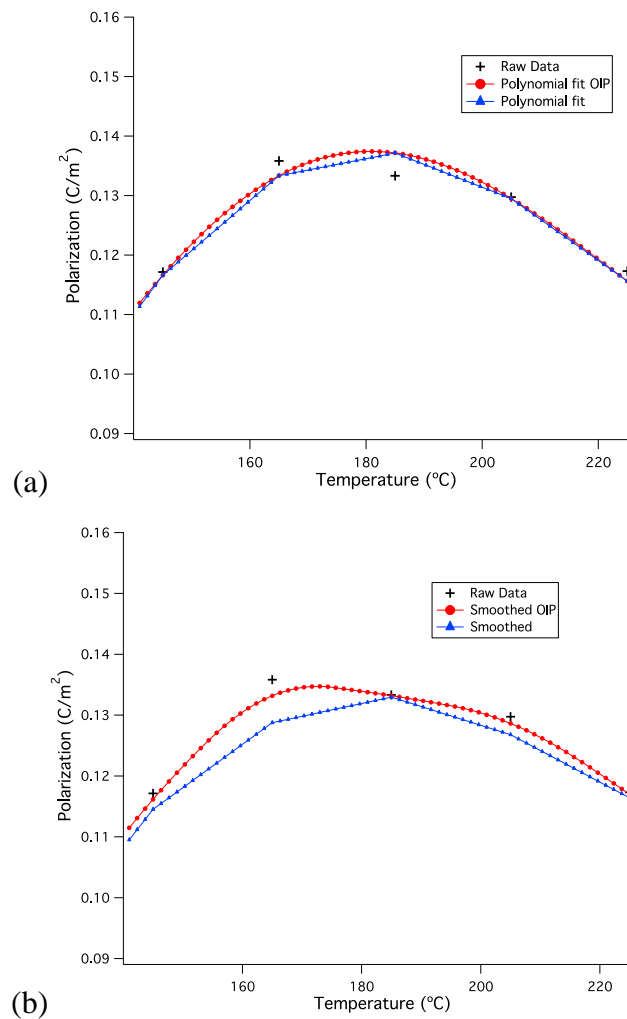


**Figure 3-31. (a) Two types of polynomial fits to raw data (b) Two types of smoothing of raw data.**

It should be noted that, in general, temperature change predictions due to the isentropic application, as opposed to release of a field, result in the material getting warmer due to the electrocaloric effect. Isentropic release of a field would generally cool the material due to the electrocaloric effect. Hence the usual reference to cooling and heating predictions relating to the release and application of a field, respectively. However, across certain field ranges at certain temperatures, the indirect method suggests that the opposite occurs. This is the negative electrocaloric effect and where it is evident, the  $\Delta T$  curves will be referred to as those due to application or release of a field (see fig. 3-28). In fig. 3-30, more clearly than any graph so far, it could be construed that there is a negative electrocaloric effect at the highest temperatures. This usually occurs with

predictions from polynomial fits to  $P(T)$  data, at the extremes of the temperature range and is due to the nature of the polynomial curves curling slightly at the ends. It can also be seen in predictions from raw data, where  $\left(\frac{\partial P}{\partial T}\right)_E$  can change from being positive to negative, along the  $P(T)$  isofield curves, which are commonly uneven. In both cases, the  $\Delta T$  predictions are to be considered appropriately.

	COOLING		HEATING	
	<i>Peak change</i> (°C)	<i>At</i> (°C)	<i>Peak change</i> (°C)	<i>At</i> (°C)
Polynomial fit OIP	-25.38	224.85	25.37	199.27
Smoothed OIP	-27.38	235.38	27.32	208.30

**Table 4. Peak cooling and heating predictions from fig. 3-30.**

### 3.3. PZT

#### 3.3.1. 1100 NM THICK. FAST COOLED. HOTPLATE.

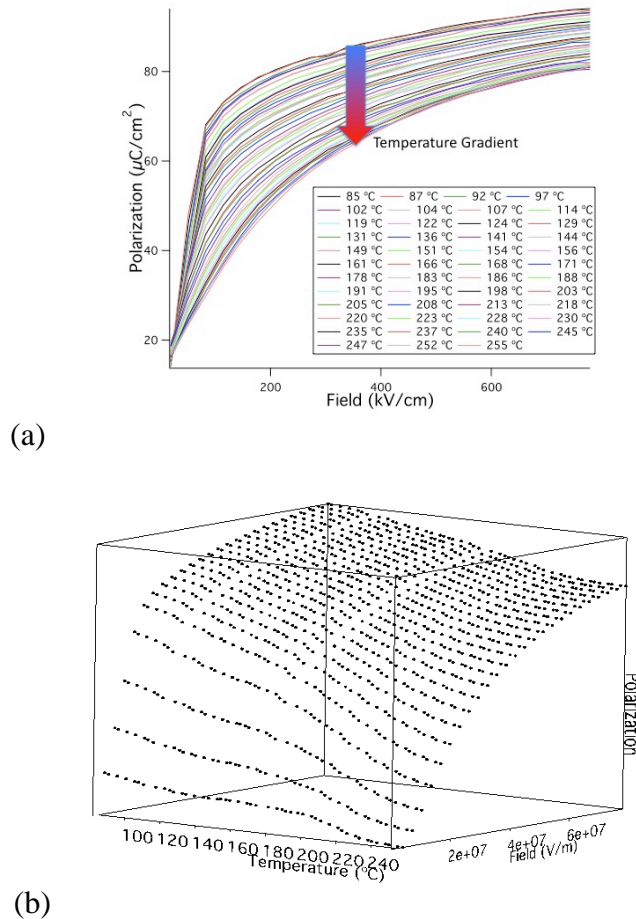
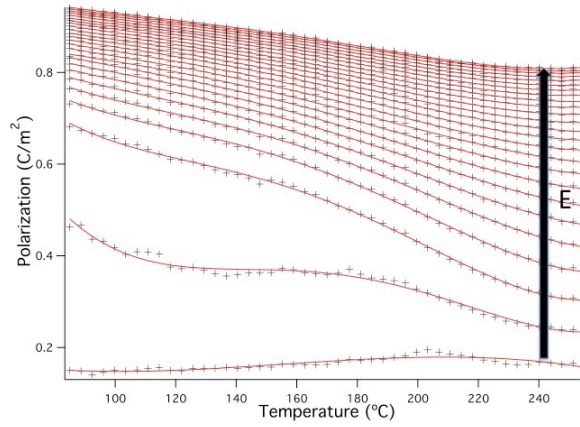


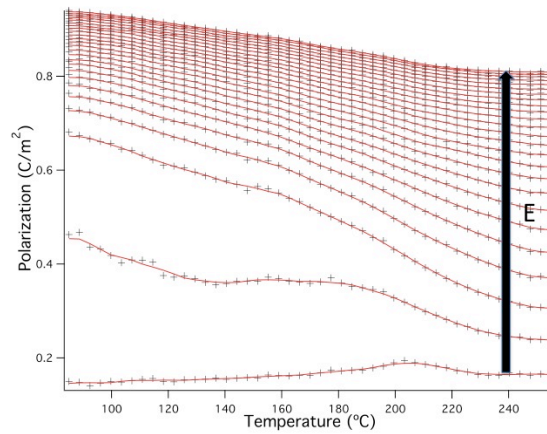
**Figure 3-32. 1.1µm thick PZT 95/05. (a) Second quadrant data from P(E) loops. (b) P(E,T). 3D view of the same data.**

The data in the above figure was measured on a 1100 nm thick film of PZT 95/05. This is the second sample fabricated by Silvana Corkovic at Cranfield University. It differs from the 1000 nm sample presented in the previous section, as a guinea pig for the explanation of the analytical method, only in that it is slightly thicker and during its fabrication, was cooled from its annealing process in one swift step. Whereas the 1000 nm sample was taken from its 530 °C hotplate annealing step and placed on a pre-heated 200 °C hotplate for one minute before finally placing it on a metal block at room temperature, this 1100 nm sample was placed directly onto the metal block from the

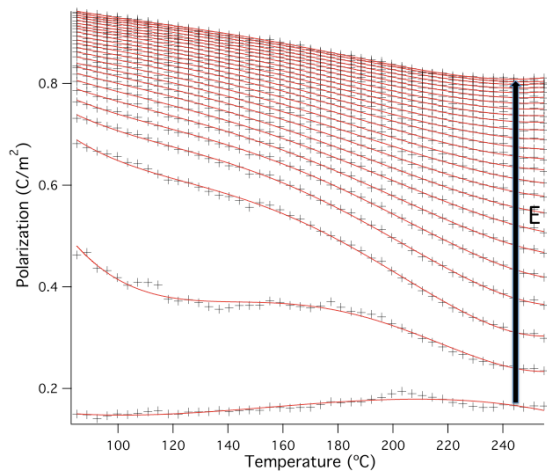
530 °C hotplate. Measurement was performed on a hotplate, using a thermocouple and reader for temperature determination and loops were taken at 47 temperature points between 255 °C and 85 °C at intervals varying between 3 °C and 5 °C.



(a)



(b)



(c)

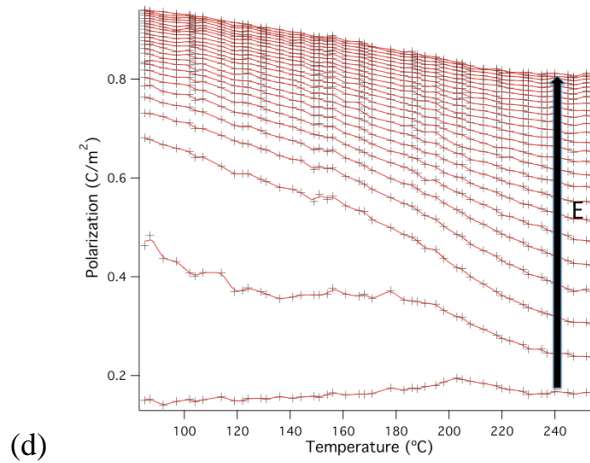


**Figure 3-33. 1.1  $\mu\text{m}$  thick PZT 95/05.  $P(T)$ . Red lines represent alternatives to isofield, black data points. (a) 4<sup>th</sup> order polynomial fit. (b) Five-point boxcar smoothing (c) 4<sup>th</sup> order polynomial fit OIP (d) 15-point boxcar smoothing OIP.**

Figure 3-33 shows fits to raw data. Graphs (a) and (c) seem identical to the eye at this resolution. However, the red lines in graph (c) join 691 points, whereas graph (a) shows red isofield curves that join 47 measured data points. The smoothed data in graph (b) is very similar to (a) and (c), but graph (d) stands out as being different. This is because the isofield raw data oscillates along its trajectory from low to high temperature and the 15-point smoothing of 691 points does little to change that. The temperature change calculations are presented below:

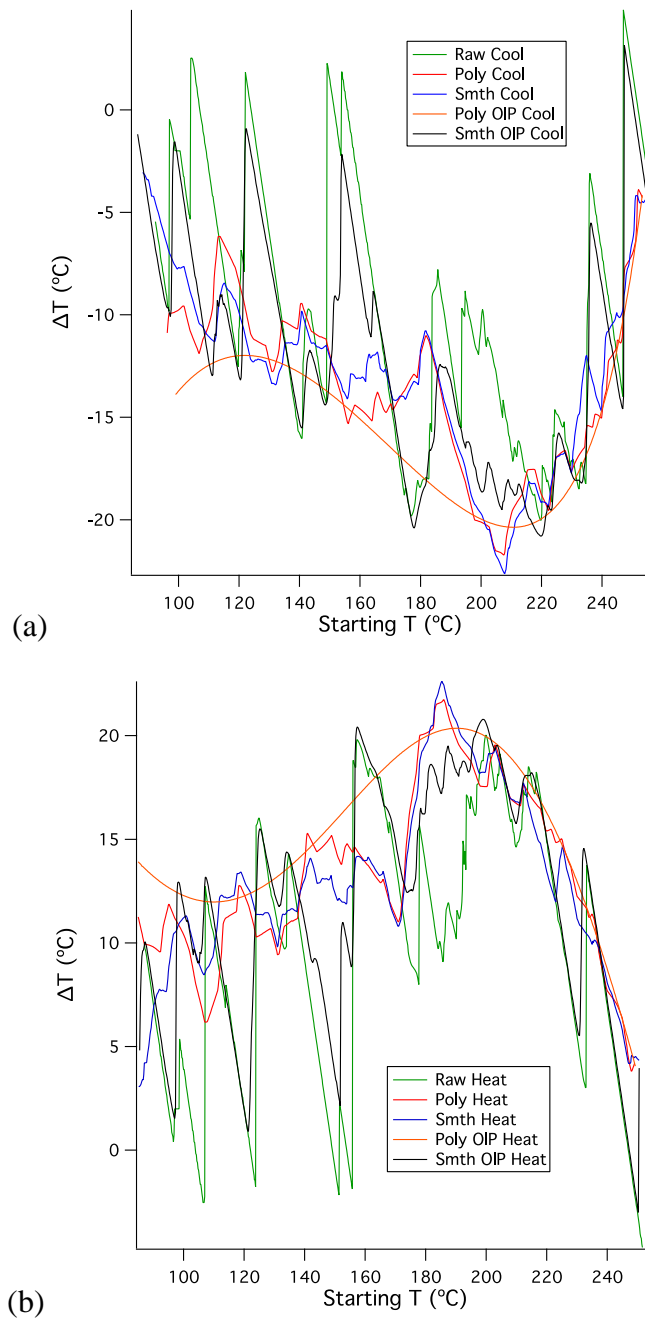


**Figure 3-34. 1.1 $\mu$ m thick PZT 95/05. (a) Electrocaloric cooling and (b), heating predictions. Each graph shows calculations from raw data and four alternatives.  $\Delta E=759$  kV/cm.**

As with the 1000 nm sample, the raw data is erratic and in general, the  $\Delta T$  predictions are substantially lower, by up to nearly 8 °C (nearly 30%) lower than in the 1000 nm sample case. This sample was subjected to a field change that was 18% smaller than that experienced by the 1000 nm sample.

	COOLING		HEATING	
	<i>Peak change (°C)</i>	<i>At (°C)</i>	<i>Peak change (°C)</i>	<i>At (°C)</i>
Raw data	-20.02	219.71	20.03	199.94
Polynomial fit	-21.72	207.51	21.73	185.89
Smoothed	-22.63	207.88	22.62	185.34
Polynomial fit OIP	-20.37	210.65	20.36	190.20
Smoothed OIP	-20.80	219.77	20.78	199.07

**Table 5. Peak electrocaloric cooling and heating predictions in 1.1 $\mu$ m thick, “fast cooled” PZT 95/05.  
 $\Delta E=759$  kV/cm.**

Peak temperature changes calculated at measurement temperatures only, are shown below:

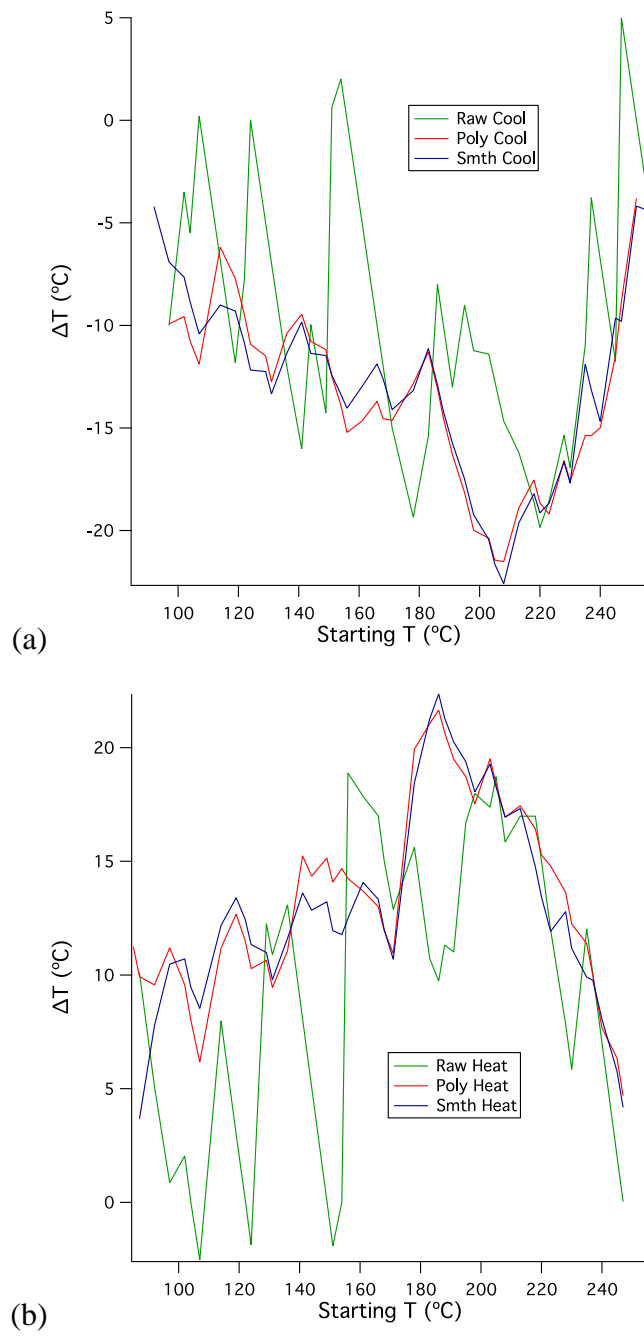


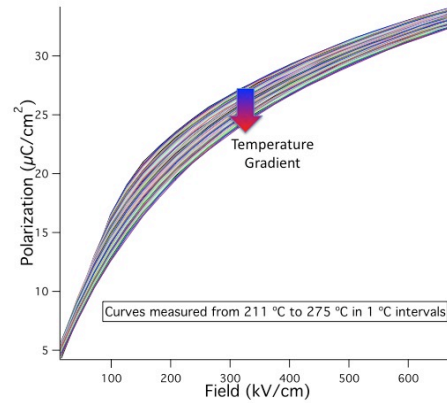
Figure 3-35. As fig. 3-34, except calculations made at measurement temperatures only.

	COOLING		HEATING	
	<i>Peak change (°C)</i>	<i>At (°C)</i>	<i>Peak change (°C)</i>	<i>At (°C)</i>
Raw data	-19.85	220.00	18.88	156.00
Polynomial fit	-21.52	208.00	21.65	186.00
Smoothed	-22.59	208.00	22.36	186.00

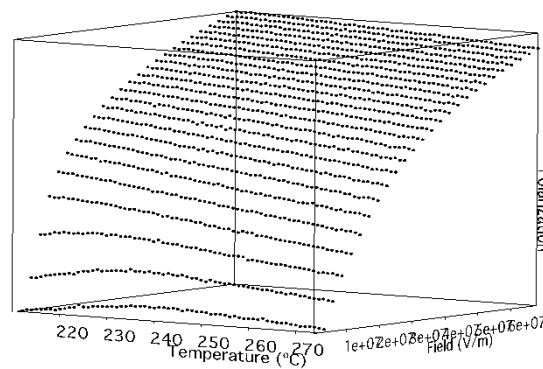
**Table 6.** As table 5, except calculations made at measurement temperatures only.

### 3.3.2. 1050 NM THICK. HIGHER ANNEAL TEMPERATURE. CRYOSTAT.

*LOOPS MEASURED FROM 211 °C TO 275 °C AT 1 °C INTERVALS*



(a)

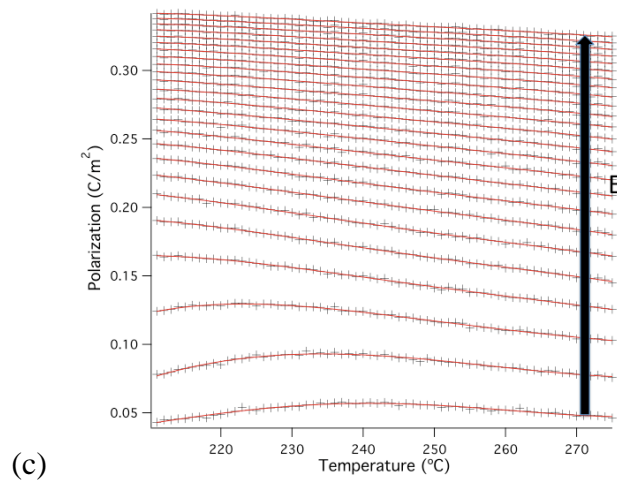
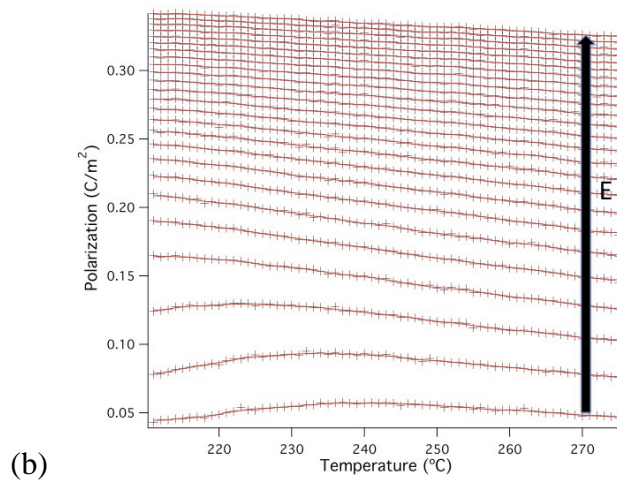
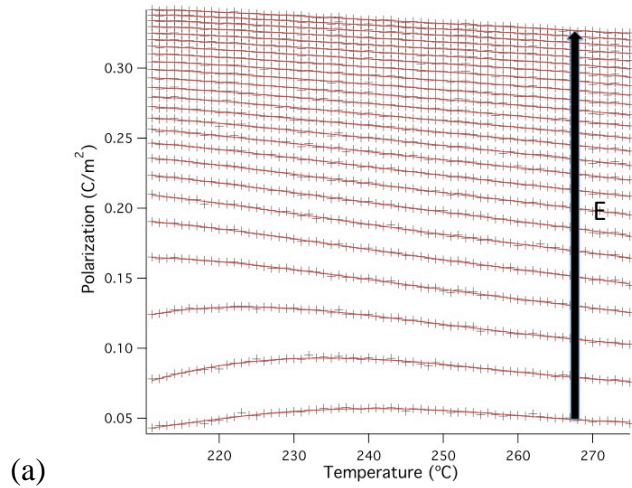


(b)

**Figure 3-36. 1.05  $\mu\text{m}$  thick PZT 95/05. (a) Second quadrant data from  $P(E)$  loops measured from 211 °C to 275 °C in 1 °C steps. (b)  $P(E,T)$ . 3D view of the same data.**

This dataset is the first presented here that was measured in the cryostat. The highly precise temperature control afforded by this environment ( $\pm 0.01$  °C) allows for confident  $P(E)$  loop measurement at starting temperatures that differ by only 1 °C. This sample is of very similar thickness to the previous two films, at 1050 nm and the only difference between its fabrication and that of the previous two samples, is that it was annealed at 530 °C for 10 minutes, as opposed to five minutes at 430 °C, followed by 530 °C for five

minutes. It was also made by Tatiana Correia, as opposed to Silvana Corkovic, so there are possible, subtle differences in the processing that would not be recognised between the two experimentalists.



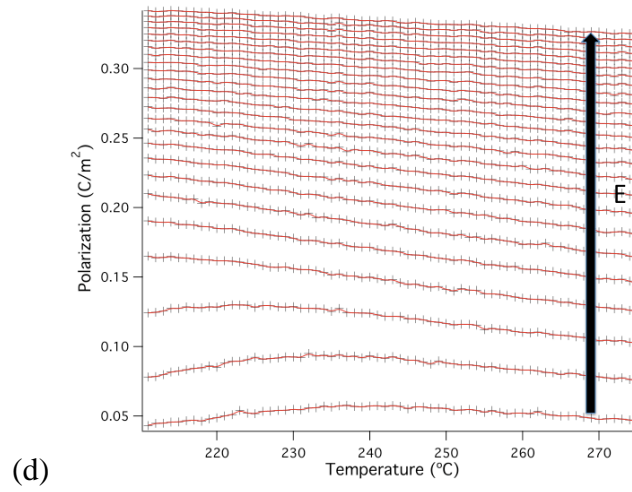


**Figure 3-37. 1.05  $\mu\text{m}$  thick PZT 95/05.  $P(T)$ . Red lines represent alternatives to the isofield, black data points. (a) 4<sup>th</sup> order polynomial fit. (b) Five-point boxcar smoothing. (c) 4<sup>th</sup> order polynomial fit OIP (d) 15-point boxcar smoothing OIP. Data measured as  $P(E)$  from 211  $^{\circ}\text{C}$  to 275  $^{\circ}\text{C}$  in 1  $^{\circ}\text{C}$  steps.**

The  $\Delta T$  predictions are shown below:

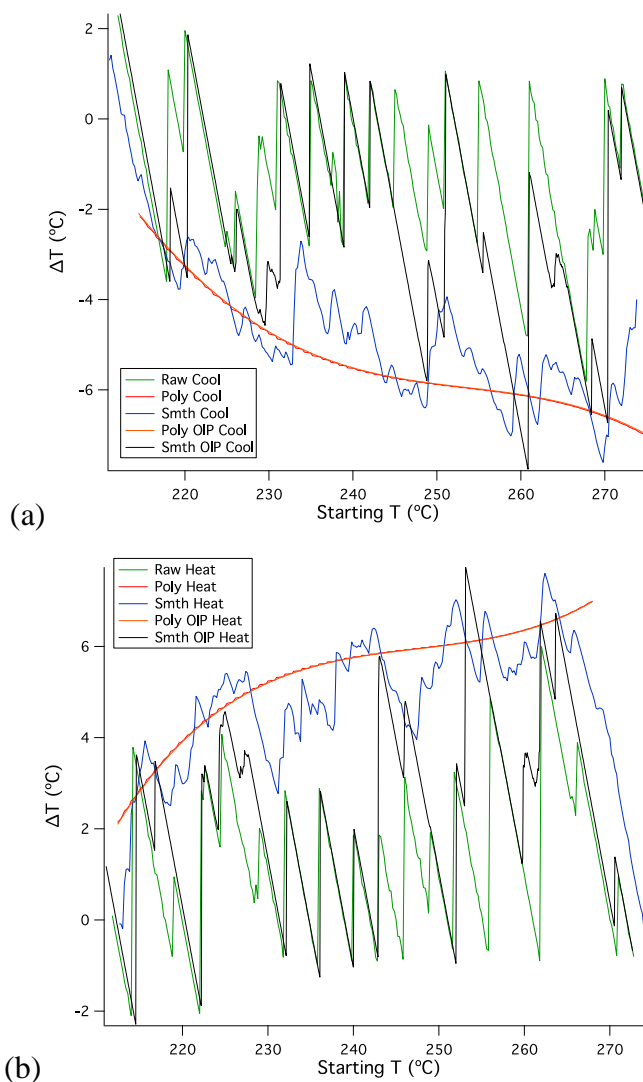


**Figure 3-38. 1.05  $\mu\text{m}$  thick PZT 95/05 measured from 211  $^{\circ}\text{C}$  to 275  $^{\circ}\text{C}$  in 1  $^{\circ}\text{C}$  steps. (a) Electrocaloric cooling and (b), heating predictions. Each graph shows calculations from raw data and four alternatives.**

$$\Delta E = 662 \text{ kV/cm.}$$

As is seemingly standard in the electrocaloric literature that utilises the indirect method to date, the heat capacity for PZT 95/05 was taken as constant throughout its temperature and field excursion. It was based on a specific heat capacity of 330 J/K.kg and material density of  $8.3 \times 10^3 \text{ kg/m}^3$  [5], giving a volumetric specific heat capacity of  $2.739 \times 10^6 \text{ J/K.m}^3$ .

Surprisingly, both sets of polynomial fit data returned  $\Delta T$  curves without a peak over this temperature range, but what is most startling is the difference in peak temperatures compared to the previous two samples. The thicknesses of these three samples are similar (1000 nm, 1100 nm and 1050 nm), though it must be acknowledged that the field range is about one third wider in the previous two datasets. Even so, peak temperature change calculations here do not rise above 8 °C, whereas in the previous two datasets, they start at around 24 °C. This is a stark difference considering the principal differences are the fabricator and the extra 80 °C over five minutes, during annealing. The two types of polynomial fits to  $P(T)$  returned nearly identical  $\Delta T$  predictions, due to the small temperature interval between raw  $P(T)$  data and relatively small  $\Delta T$  predictions compared to the previous two datasets.

One could decide to reject the results from this dataset, as it suggests the peak temperature change, taken from polynomial  $P(T)$  fits, can be achieved by starting somewhere above 275 °C, which is a long way from the bulk ferroelectric to paraelectric phase transition temperature of 242 °C. This is the temperature around which one would expect the largest electrocaloric changes, as the structural phase transition will constitute a large entropy change by itself. Then again, the second-order nature of thin-film phase transitions spreads the transition temperature over a temperature range and the application of these large fields will also shift  $T_c$  up in temperature [57]. The fact remains that we still do not know whether peak electrocaloric changes necessarily take place from starting temperatures that are close to  $T_c$ , so such  $\Delta T$  predictions will continue to be considered a possibility. Dielectric constant measurements taken on the same day at the same electrode, suggest a broad, zero-bias transition temperature range around 245 °C:

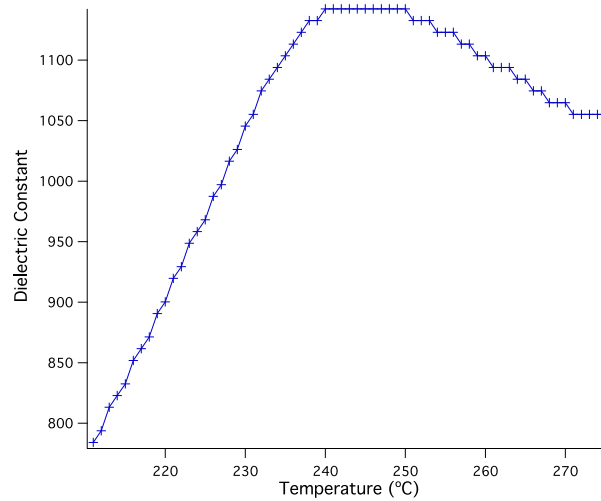


**Figure 3-39. Dielectric constant as a function of temperature and zero-voltage bias, taken from capacitance measurements as a function of temperature. Lines join data points.**

	COOLING		HEATING	
	<i>Peak change (°C)</i>	<i>At (°C)</i>	<i>Peak change (°C)</i>	<i>At (°C)</i>
Raw data	-5.81	267.80	6.00	262.00
Polynomial fit	-6.99	274.80	6.99	268.00
Smoothed	-7.61	269.80	7.60	262.40
Polynomial fit OIP	-6.99	275.00	6.99	268.00
Smoothed OIP	-7.76	260.87	7.74	253.13

**Table 7. Peak electrocaloric cooling and heating predictions in 1.05µm thick PZT 95/05 measured from 211 °C to 275 °C in 1 °C steps.  $\Delta E=662$  kV/cm.**

It can be seen in the following figure and table that the difference between the above temperature change predictions and those calculated at the measurement temperatures only differs by up to two tenths of a degree Celsius. The smaller the difference in temperature between measured data points, the less the temperature change predictions differ when calculating from the measured temperatures, compared to when including intermediate temperatures.

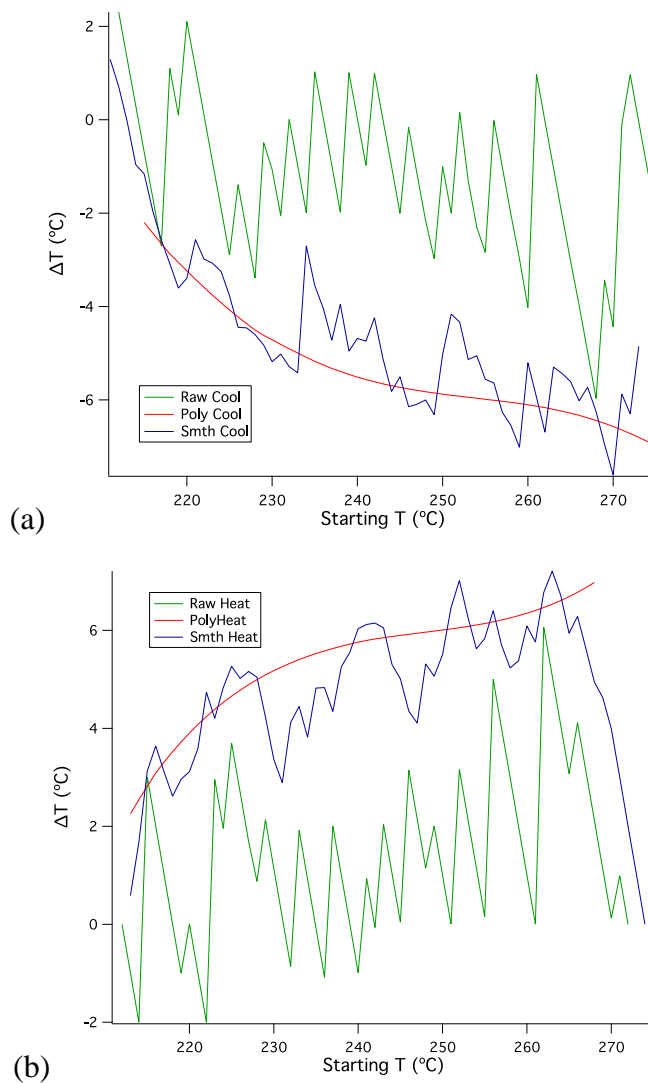
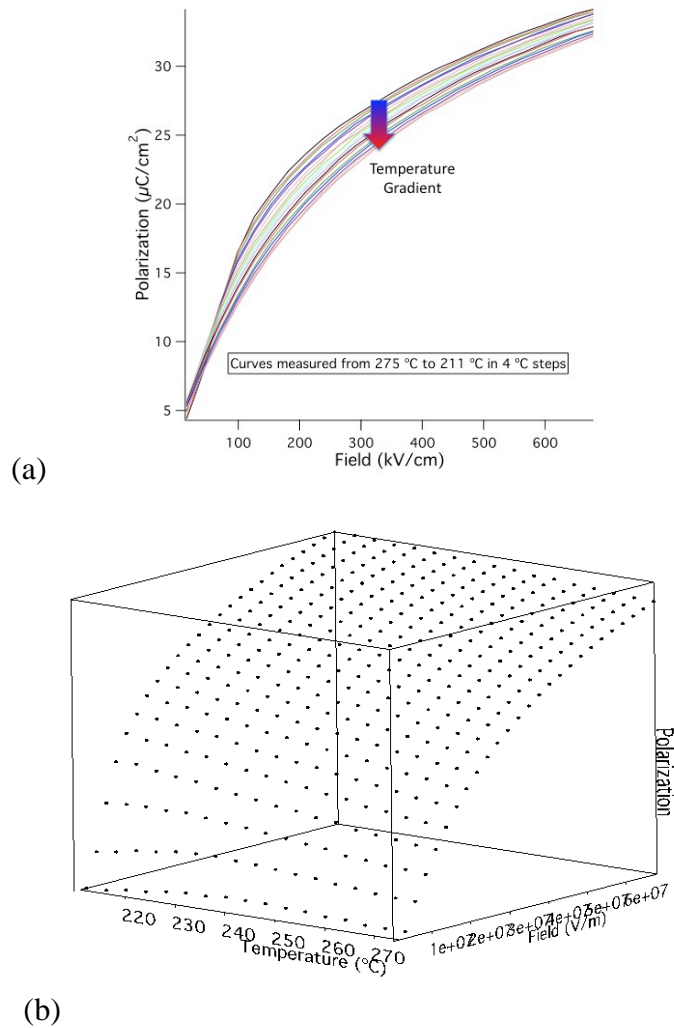


Figure 3-40. As fig. 3-38, except calculations made at measurement temperatures only.

	COOLING		HEATING	
	<i>Peak change</i> (°C)	<i>At</i> (°C)	<i>Peak change</i> (°C)	<i>At</i> (°C)
Raw data	-5.97	268.00	6.06	262.00
Polynomial fit	-6.98	275.00	6.98	268.00
Smoothed	-7.60	270.00	7.60	263.00

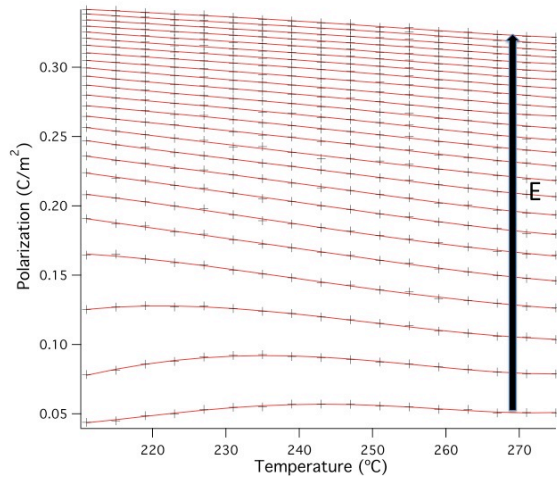
Table 8. As table 7, except calculations made at measurement temperatures only.

*LOOPS MEASURED FROM 275 °C TO 211 °C AT 4 °C INTERVALS*

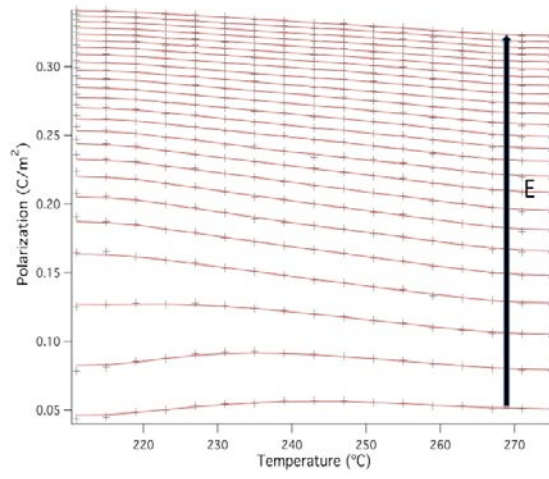


**Figure 3-41. 1.05 $\mu\text{m}$  thick PZT 95/05. (a) Second quadrant data from P(E) loops measured from 275 °C to 211 °C in 4 °C steps. (b) P(E,T). 3D view of the same data.**

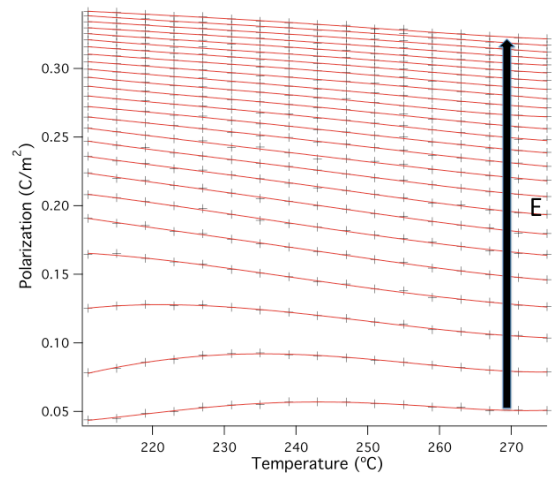
The dataset in the above figure was taken on the same 1.05 $\mu\text{m}$  thick PZT 95/05 film just presented. It was measured between the same temperature limits and at the same electrode, on consecutive days. First, the previous dataset was measured, the cryostat then cooled to room temperature and the sample exposed to the laboratory atmosphere. The shroud was then replaced, shielding the sample, though air could freely move in and out of the chamber. This was left overnight and the dataset in fig. 3-41 was measured the following day. The principal difference here is that the data was taken from high to low temperature and the temperature measurement interval was 4 °C.



(a)



(b)



(c)

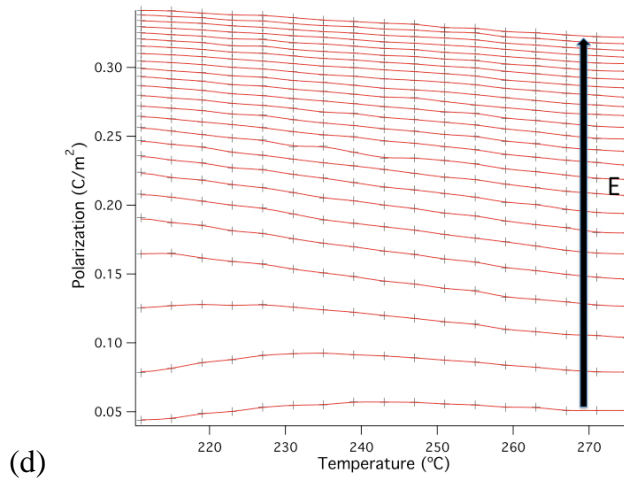


**Figure 3-42. 1.05  $\mu\text{m}$  thick PZT 95/05.  $P(T)$ . Red lines represent alternatives to isofield, black data points. (a) 4<sup>th</sup> order polynomial fit. (b) Five-point boxcar smoothing. (c) 4<sup>th</sup> order polynomial fit OIP (d) 15-point boxcar smoothing OIP. Data measured as  $P(E)$  from 275 °C to 211 °C in 4 °C steps.  $\Delta E=662$  kV/cm.**

It has been suggested that indirect data for electrocaloric predictions be taken only from high to low temperatures, to avoid pronounced  $\left(\frac{\partial P}{\partial T}\right)_E$  gradients due to ferroelectric fatigue [5], but fatigue is seen only to set in after many repeated hysteresis loop measurements, of the order of  $10^6$  cycles or more [58, 59] and these films are likely to never see more than a 100 cycles, so data that varies imperceptibly in  $P(T)$  graphs of measurements on robust films such as these, are not expected to return distinctive  $\Delta T$  predictions. However,  $\Delta T$  values do differ by nearly a degree Celsius; and the starting temperatures can differ by around 10 °C. Most remarkably, the imperceptible difference between this dataset and the last has resulted in a polynomial fit to  $P(T)$  data that led to  $\Delta T$  predictions that had a peak over the temperature measurement range, where the previous dataset did not.

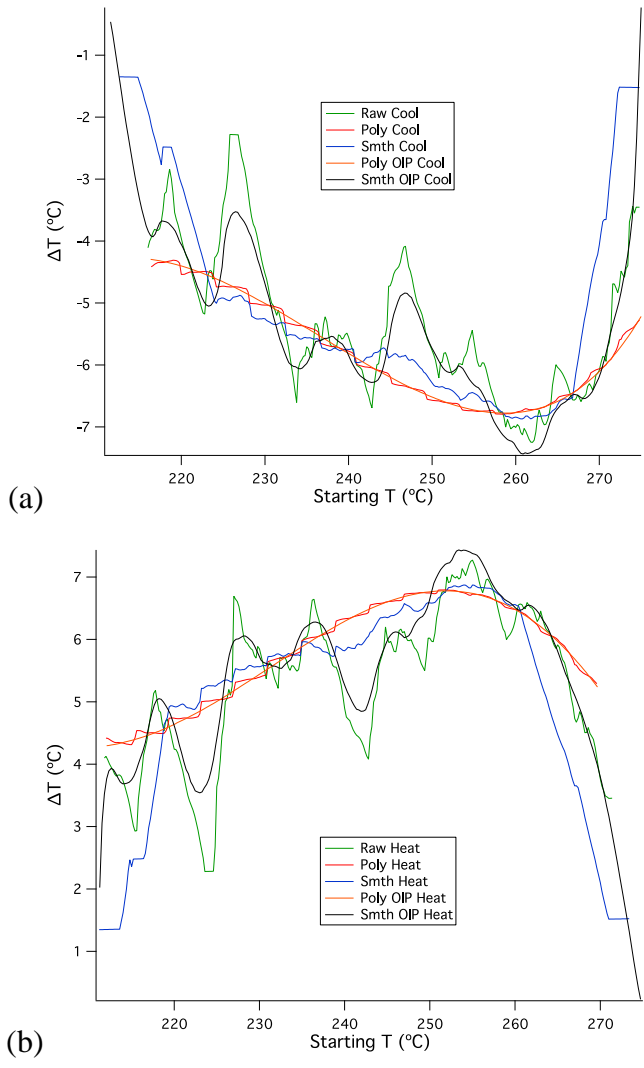


**Figure 3-43. 1.05 $\mu$ m thick PZT 95/05 measured from 275  $^{\circ}$ C to 211  $^{\circ}$ C in 4  $^{\circ}$ C steps. (a) Electrocaloric cooling and (b), heating predictions. Each graph shows calculations from raw data and four alternatives.  $\Delta E=662$  kV/cm.**

	COOLING		HEATING	
	Peak change (°C)	At (°C)	Peak change (°C)	At (°C)
Raw data	-7.25	262.00	7.27	255.00
Polynomial fit	-6.79	258.40	6.79	251.80
Smoothed	-6.87	260.80	6.87	255.00
Polynomial fit OIP	-6.78	258.73	6.78	251.80
Smoothed OIP	-7.44	260.87	7.44	253.40

**Table 9. Peak electrocaloric cooling and heating predictions in 1.05µm thick PZT 95/05 measured from 275 °C to 211 °C in 4 °C steps. ΔE=662 kV/cm.**

The difference in  $P(T)$  data that led to these distinct results is displayed in the following figure:

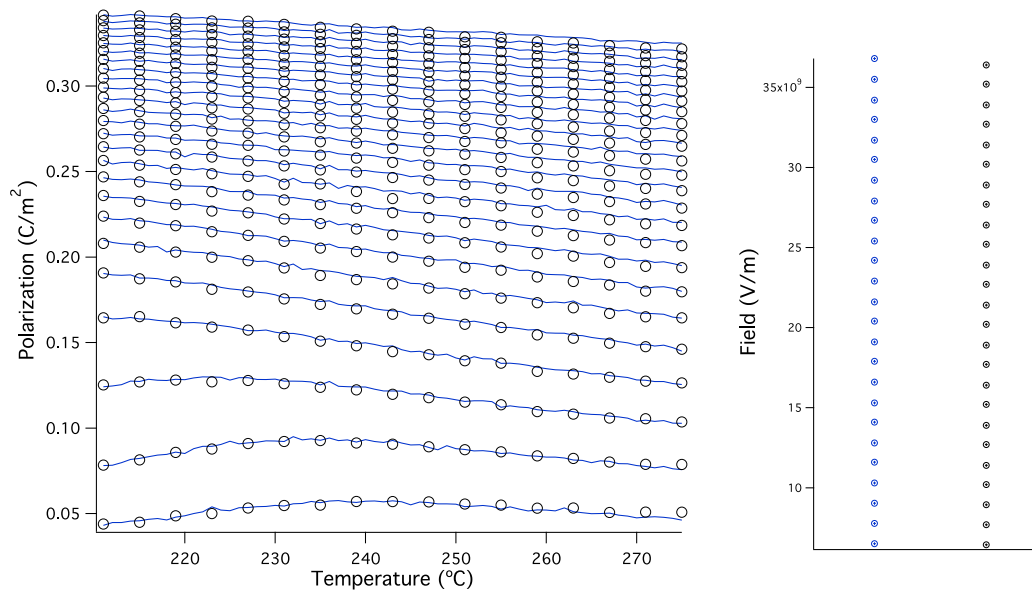


**Figure 3-44. Comparison of raw  $P(T)$  data between (a) that measured as  $P(E)$  from 211 °C to 275 °C in 1 °C steps and (b) that measured as  $P(E)$  from 275 °C to 211 °C in 4 °C steps. The blue lines join isofield points in dataset (a) and the black circles lie on isofield curves of dataset (b). The right-hand graph compares the isofield values from the two datasets.**

One can see in the left-hand graph in the above figure, how the data points represented by the black circles, i.e. the measurements on the film while reducing the temperature in 4 °C intervals, closely follow the blue lines of 1 °C spaced data taken while increasing the temperature of the film in 1 °C steps. Though the set field range of the tester was identical for both datasets, it can be seen that the data taken downward in temperature was subject to lower voltages, earlier in the voltage descent, which persisted for about half of the voltage release range. This would suggest larger  $\left(\frac{\partial P}{\partial T}\right)_E$  values overall and larger calculated temperature changes, for the dataset represented by black circles, i.e. 275 °C to 211 °C in 4 °C steps, yet this is only supported by the peak  $\Delta T$  predictions from raw data. Comparisons between the  $\Delta T$  predictions calculated from the polynomial fits in each dataset are unreliable, as the fits to  $P(T)$  data in the 211 °C to 275 °C dataset did not produce peaks. Those  $\Delta T$  predictions calculated from smoothed  $P(T)$  data in the 211 °C to 275 °C dataset are susceptible to larger values merely due to the greater number of raw data points along the temperature axis inducing greater variability in  $\Delta T$  calculations, evident in comparison of fig. 3-38 and fig. 3-43.

The calculations made only at measurement temperatures are presented below and the differences in  $\Delta T$  are limited to tenths of a degree, while starting temperatures differ by about a degree Celsius, akin to the small differences seen for the same sample measured upwards in temperature and consistent with the similar values of  $\left(\frac{\partial P}{\partial T}\right)_E$  across the two datasets.

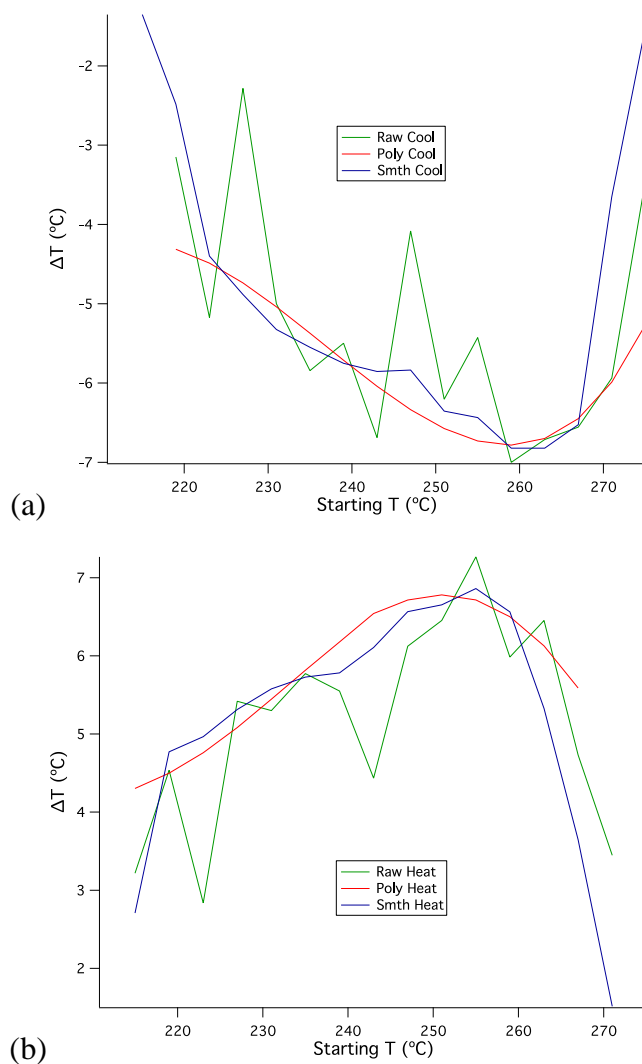


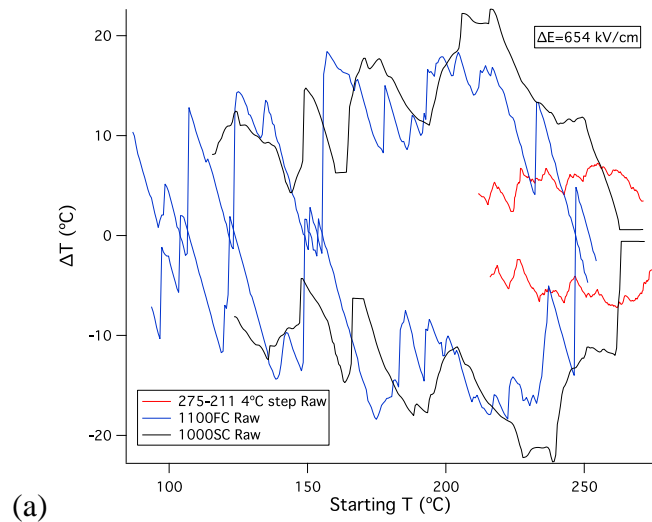
Figure 3-45. As fig. 3-43, except calculations made at measurement temperatures only.

	COOLING		HEATING	
	<i>Peak change</i> (°C)	<i>At</i> (°C)	<i>Peak change</i> (°C)	<i>At</i> (°C)
Raw data	-7.00	259.00	7.27	255.00
Polynomial fit	-6.78	259.00	6.78	251.00
Smoothed	-6.82	263.00	6.86	255.00

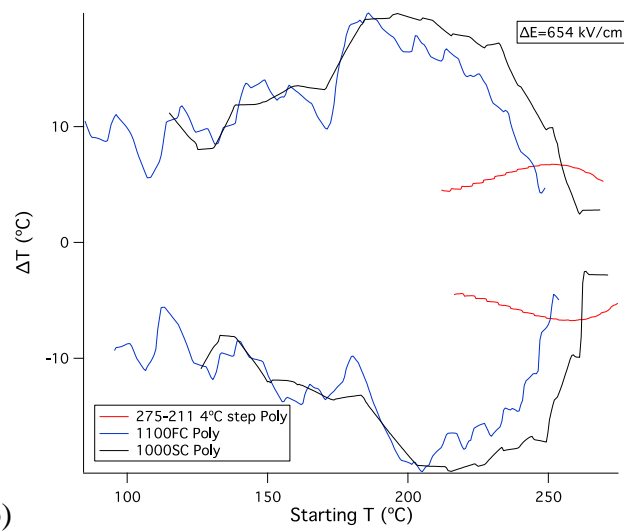
Table 10. As table 9, except calculations made at measurement temperatures only.

### 3.3.3. $\Delta T$ PREDICTION COMPARISON BETWEEN THREE PZT 95/05 SAMPLES

The first two datasets presented here, those measured on the 1000 nm thick and the 1100 nm thick PZT 95/05 samples, returned temperature change predictions that were around three times larger than those calculated on the 1050 nm thick PZT 95/05 sample. The three film thicknesses are very similar, but the field application/release ranges employed were quite different. The 1000 nm thick sample was subjected to 929 kV/cm, the 1100 nm sample, 759 kV/cm and the 1050 nm sample, 662 kV/cm. Though it would seem that such differences in field range would not account for the much smaller  $\Delta T$  predictions from the 1050 nm sample dataset, it would be interesting to compare  $\Delta T$  predictions for the three datasets between the same field limits. The results from such calculations, using raw data and the four approximations to raw  $P(T)$  data explained so far, are presented below.



(a)



(b)

**Figure 3-46. Electrocaloric heating and cooling predictions from (a) raw data in three datasets and (b) polynomial fits to raw  $P(T)$  data in the same three datasets, between the same field limits.**

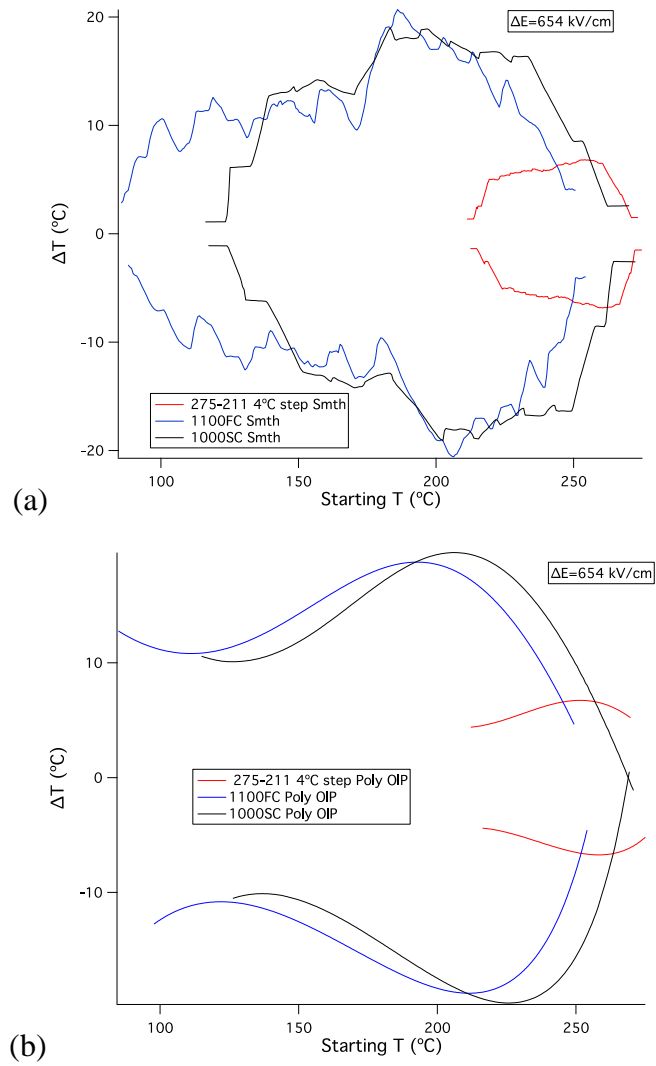


**Figure 3-47. Electrocaloric heating and cooling predictions from same three datasets as previous figure, using (a) five-point boxcar smoothing of and (b) polynomial fits OIP to raw P(T) data.**

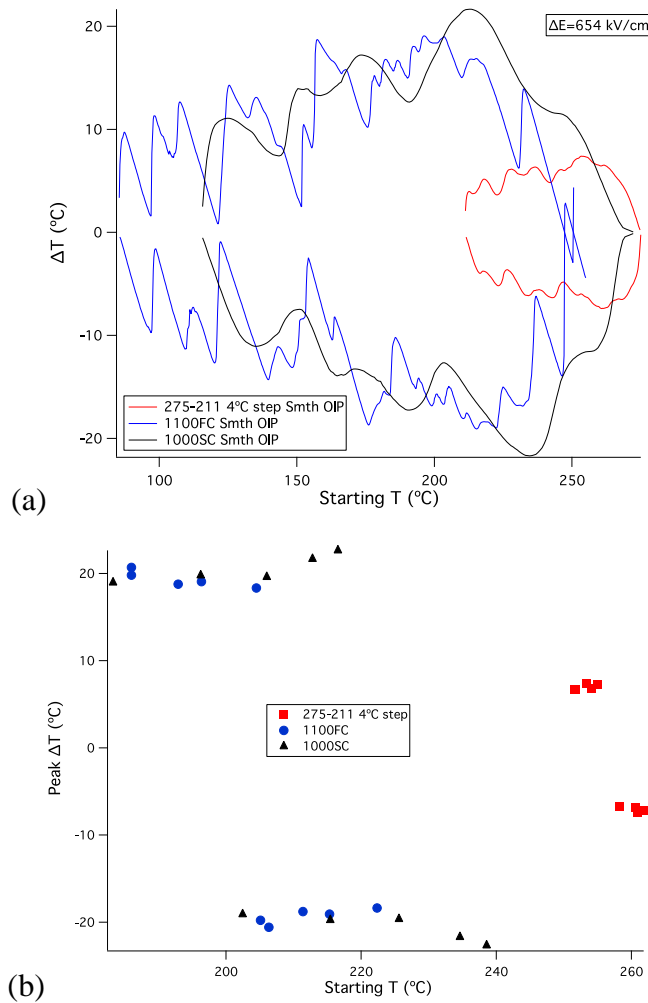


**Figure 3-48. (a) Electrocaloric heating and cooling predictions for same three datasets as previous two figures, using 15-point smoothing OIP to raw P(T) data. (b) Peak heating and cooling predictions for each dataset.**

In the above three figures, 1100FC refers to the 1100 nm thick film, which was “fast cooled”, as described in the experimental method section and 1000SC, refers to the 1000 nm “slow cooled” film. “275-211 4 $^{\circ}\text{C}$  step”, refers to the second of the datasets presented here that was measured on the 1050 nm thick film.

Even when temperature changes are calculated using the indirect method, over the same field range, between the same field limits, the 1000SC and 1100FC datasets suggest temperature changes that are approximately three times larger than those in the 1050 nm thick film. When looking at the results in peak temperature changes, as shown in the table below, the 1000SC  $\Delta T$  predictions show larger peak values in general. However, if one takes the view that the predictions that oscillate most along the starting temperature

axis are unreliable and ignores those predictions from raw or smoothed OIP data, then it is the 1100FC dataset that shows the highest  $\Delta T$  predictions, at  $-20.58\text{ }^{\circ}\text{C}$  for cooling and  $20.69\text{ }^{\circ}\text{C}$  for heating.

Curiously, comparing the peak  $\Delta T$  predictions from the 1050 nm film with those from the other two films, i.e. the 1000SC and 1100FC datasets, not only is there an approximately three-fold difference, but the maximum polarization values for roughly equal applied fields differs by the same factor. Specifically, the ‘275-211  $4^{\circ}\text{C}$  step’ dataset gives a  $0.34\text{ C/m}^2$  polarization at  $683\text{ kV/cm}$  at the lowest measured temperature, compared to  $1.11\text{ C/m}^2$  in the 1000SC dataset and  $0.93\text{ C/m}^2$  in the 1100FC dataset, for an approximately equal field. As this means, in an average sense, that  $\left(\frac{\partial P}{\partial T}\right)_E$  is roughly three times larger for the 1000 nm and 1100 nm film datasets, compared to the ‘275-211  $4^{\circ}\text{C}$  step’ dataset measured on the 1050 nm film, there is the possibility of explaining this as a three-fold difference in domain density per unit volume.

The spread of  $\Delta T$  predictions is displayed in graph (b) of fig. 3-48. The 1050 nm thick film dataset shows relatively less variation in starting temperature, compared to the other two films. The peak changes differ, at most, by  $0.67\text{ }^{\circ}\text{C}$ , which is 9.1% of the largest change of  $-7.40\text{ }^{\circ}\text{C}$ . If those predictions from raw and smoothed OIP data are ignored, the spread of changes reduces to a mere  $0.10\text{ }^{\circ}\text{C}$ , which is only 1.5% of the peak change of  $-6.83\text{ }^{\circ}\text{C}$ . The starting temperatures at which these peaks are predicted vary by only two or three degrees Celsius.

In the case of the 1100FC dataset, there is a variation in peak changes of  $2.35\text{ }^{\circ}\text{C}$ , which is 11.4% of the largest change,  $20.69\text{ }^{\circ}\text{C}$ . Ignoring the predictions from raw and smoothed OIP data, the peak change variation drops to  $1.92\text{ }^{\circ}\text{C}$ , which is 9.3% of the largest peak change. Starting temperatures then vary by  $6.9\text{ }^{\circ}\text{C}$ .

Looking across all predictions made on the 1000SC dataset, variation in peak  $\Delta T$  is  $3.68\text{ }^{\circ}\text{C}$ , which is 16.2% of the largest change,  $22.65\text{ }^{\circ}\text{C}$ . However, ignoring predictions from raw and smoothed OIP data leaves only a small variation of  $0.81\text{ }^{\circ}\text{C}$ , which is 4.1% of the largest change,  $22.76\text{ }^{\circ}\text{C}$ . The most striking variation in predictions from this

dataset is in the starting temperatures, which even when ignoring the results calculated from raw and smoothed OIP data, vary by 23.14 °C.

	COOLING		HEATING	
	<i>Peak change (°C)</i>	<i>At (°C)</i>	<i>Peak change (°C)</i>	<i>At (°C)</i>
<i>275-211°C 1050nm</i>				
Raw data	-7.22	261.82	7.22	255.00
Polynomial fit	-6.74	258.29	6.74	251.71
Smoothed	-6.83	260.65	6.83	254.06
Polynomial fit OIP	-6.73	258.20	6.73	251.53
Smoothed OIP	-7.40	260.87	7.39	253.40
<i>255-85°C 1100nm</i>				
Raw data	-18.37	222.36	18.34	204.49
Polynomial fit	-19.78	205.11	19.81	186.01
Smoothed	-20.58	206.34	20.69	186.01
Polynomial fit OIP	-18.78	211.39	18.77	192.91
Smoothed OIP	-19.08	215.33	19.07	196.36
<i>273-115°C 1000nm</i>				
Raw data	-22.66	238.58	22.65	216.57
Polynomial fit	-19.76	215.44	19.78	196.26
Smoothed	-19.09	202.46	18.97	183.28
Polynomial fit OIP	-19.63	225.60	19.60	206.04
Smoothed OIP	-21.70	234.63	21.66	212.81

**Table 11. Peak heating and cooling predictions for three datasets measured on three different films.**  
 $\Delta E=654$  kV/cm.

### 3.3.4. NEGATIVE ELECTROCALORIC EFFECT

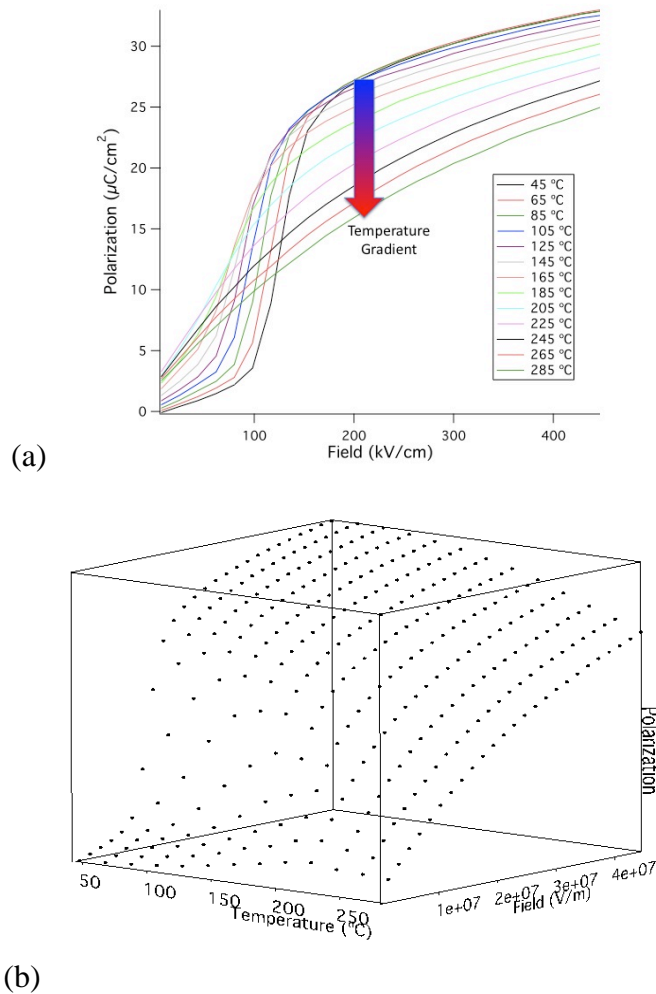
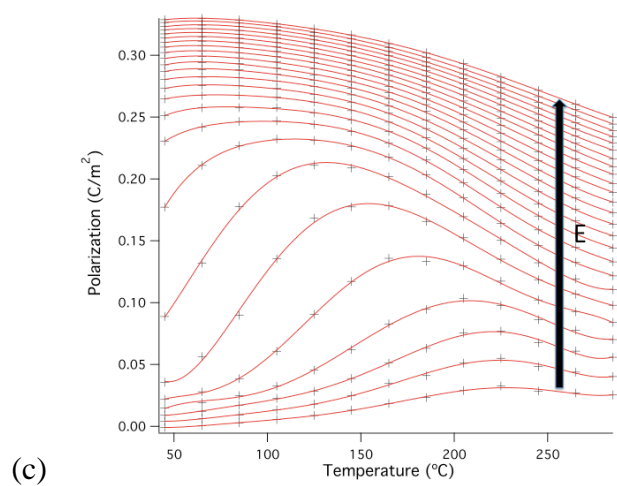
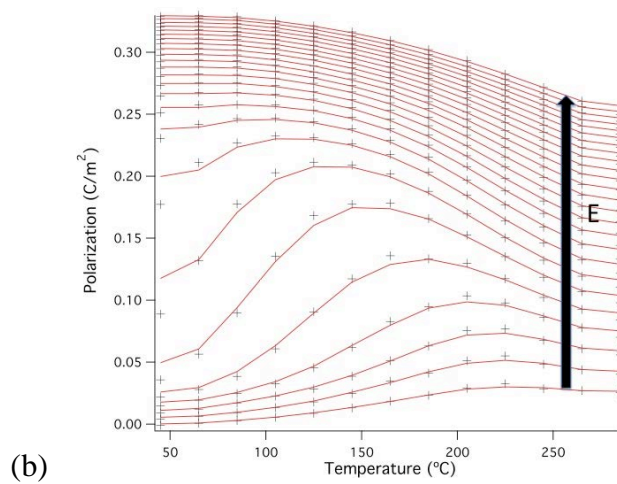
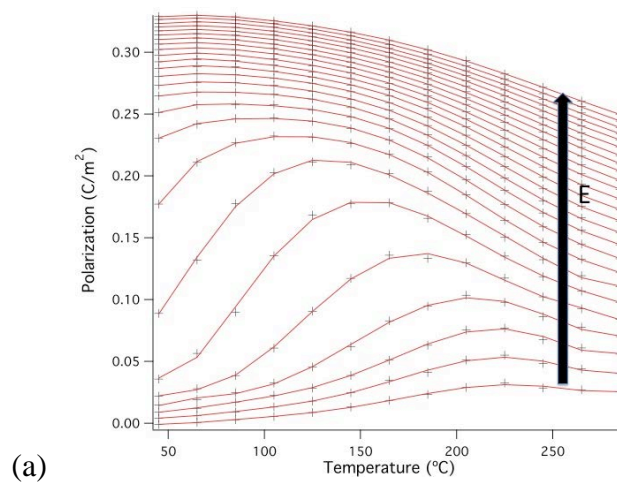


**Figure 3-49. 1.05 $\mu$ m thick PZT 95/05. (a) Second quadrant data from P(E) loops measured from 285 °C to 45 °C in 20 °C steps. (b) P(E,T). 3D view of the same data.**

This dataset and all remaining datasets measured on PZT to be presented in this chapter, bar one, were measured on the same 1050 nm thick film, using a bipolar voltage profile rising to a maximum of 50 V, which is the equivalent of 476 kV/cm.

In this case, as shown in the above figure, measurements were performed from 285 °C down to 45 °C, in 20 °C steps. This section has been entitled the “negative electrocaloric effect” as from around 50 °C to 140 °C, in the lower half of the field range,  $\left(\frac{\partial P}{\partial T}\right)_E$  is positive, so  $dT$  calculations in that region will suggest positive temperature changes when considering the release of a field. It will suggest the contrary, negative temperature

change when considering application of the field. This behaviour is known as the negative electrocaloric effect.



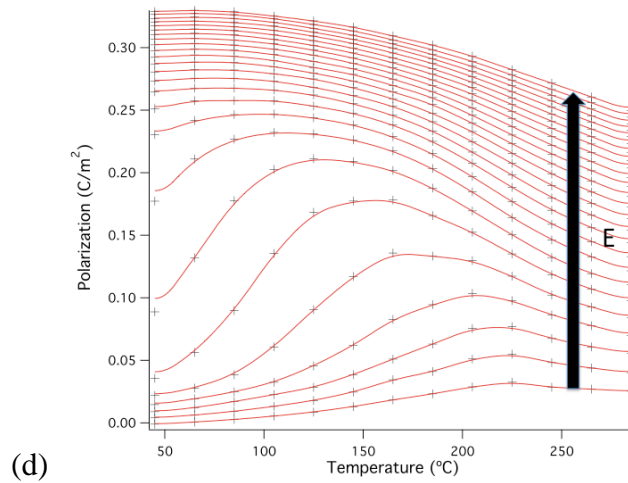


**Figure 3-50. 1.05  $\mu\text{m}$  thick PZT 95/05.  $P(T)$ . Red lines represent alternatives to isofield, black data points. (a) 6<sup>th</sup> order polynomial fit. (b) Three-point boxcar smoothing. (c) 6<sup>th</sup> order polynomial fit OIP (d) 15-point boxcar smoothing OIP. Data measured as  $P(E)$  from 285 °C to 45 °C in 20 °C steps.**

It seems the “OIP” fits in graphs (c) and (d) of the above figure are more smoothly varying alternatives to the raw data than the polynomial fits and smoothed  $P(T)$  data in graphs (a) and (b). It can also be seen that at the very lowest temperatures,  $\left(\frac{\partial P}{\partial T}\right)_E$  is positive right up to the highest fields and the negative electrocaloric effect prediction should be at its largest there. None of the  $P(T)$  approximations in the above figure appears to give a satisfactory fit at this minimum extreme of the temperature range, so the raw data will give the most reliable temperature change predictions in this region.

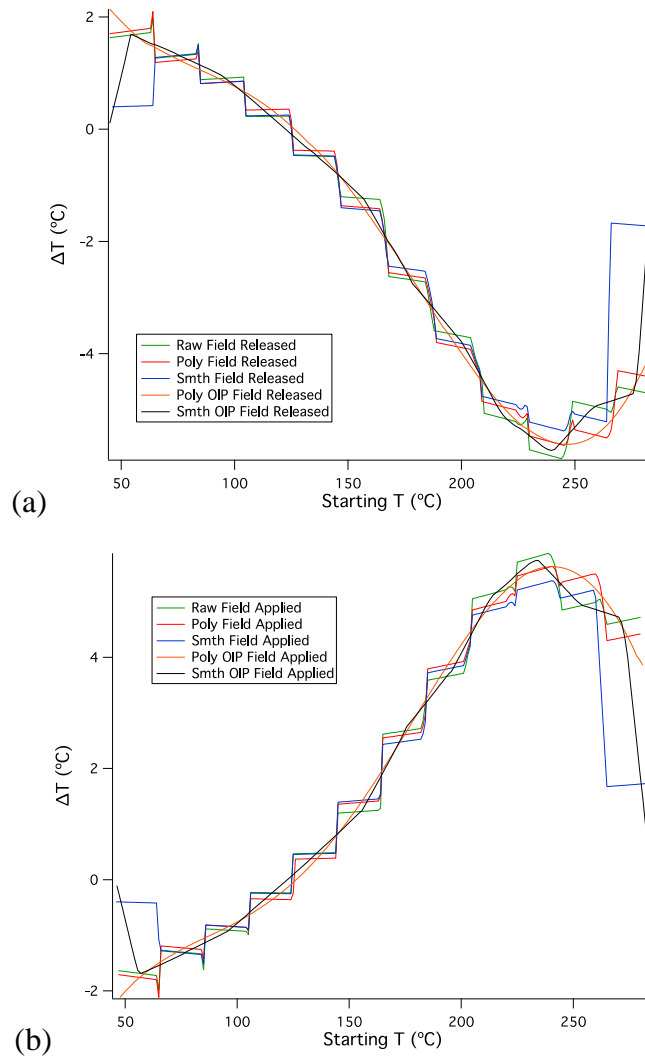


**Figure 3-51. 1.05 $\mu\text{m}$  thick PZT 95/05 measured from 285  $^{\circ}\text{C}$  to 45  $^{\circ}\text{C}$  in 20 $^{\circ}\text{C}$  steps. (a) Electrocaloric predictions based on releasing and (b) applying a field. Each graph shows calculations from raw data and four alternatives.**

Initially, this is to be examined in terms of peak cooling and heating predictions.

	COOLING		HEATING	
	<i>Peak change (°C)</i>	<i>At (°C)</i>	<i>Peak change (°C)</i>	<i>At (°C)</i>
Raw data	-5.87	244.00	5.87	239.00
Polynomial fit	-5.63	245.00	5.63	240.00
Smoothed	-5.38	245.00	5.37	240.00
Polynomial fit OIP	-5.62	246.33	5.63	241.00
Smoothed OIP	-5.72	239.67	5.74	234.33

**Table 12. Peak electrocaloric cooling and heating predictions in 1.05  $\mu\text{m}$  thick PZT 95/05 measured from 285 °C to 45 °C in 20 °C steps.**

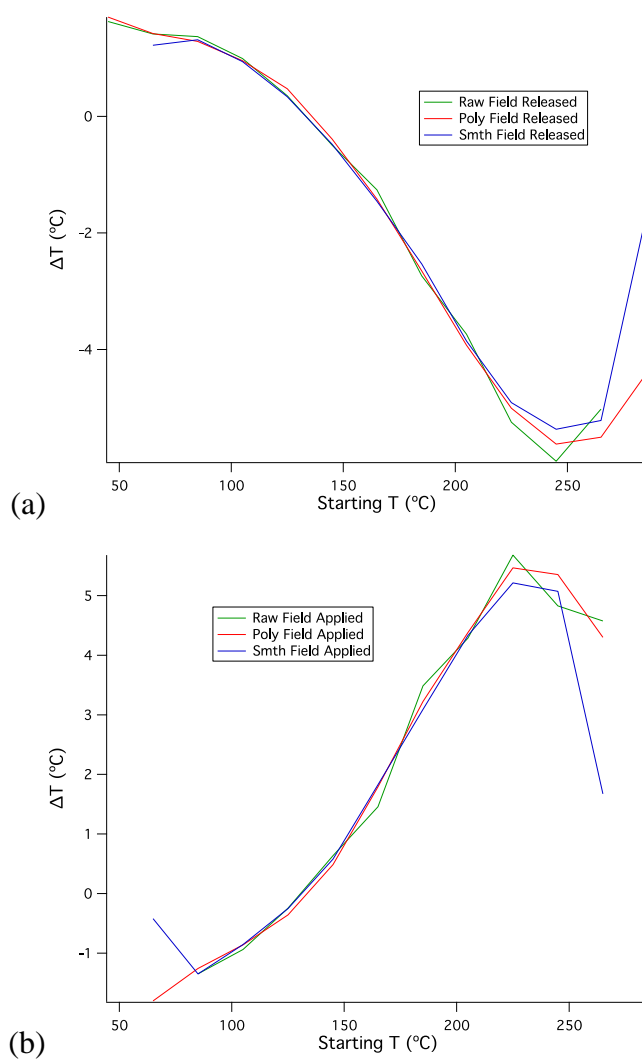
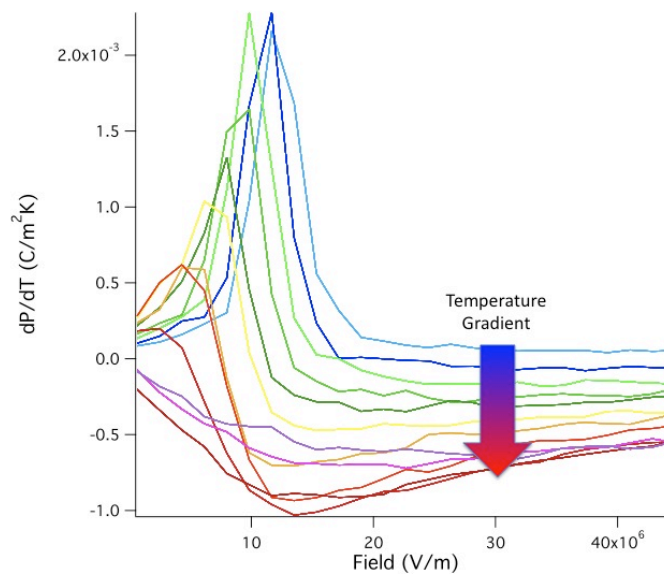


Figure 3-52. As fig. 3-51, except calculations made at measurement temperatures only.

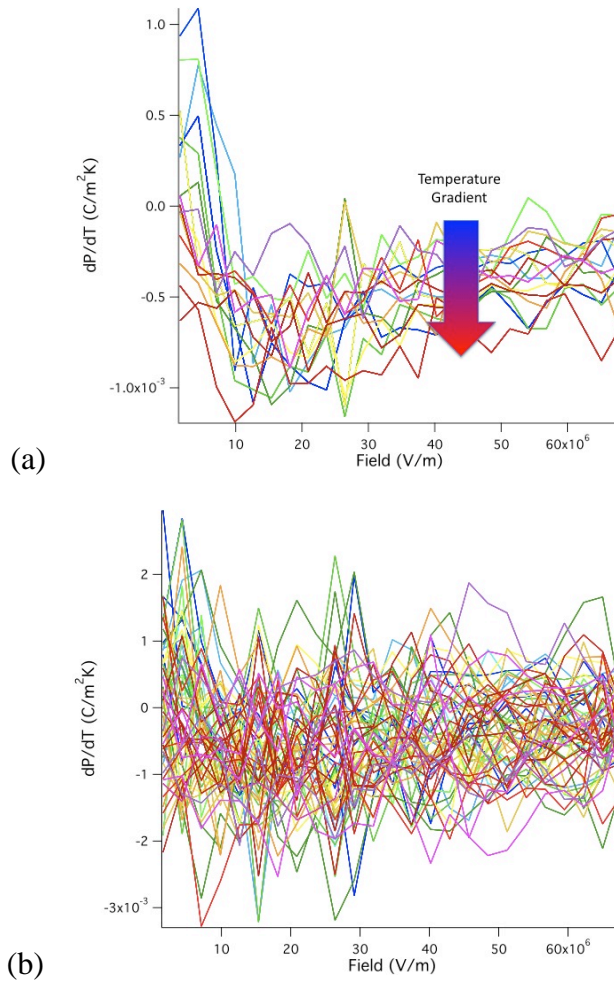
	COOLING		HEATING	
	Peak change (°C)	At (°C)	Peak change (°C)	At (°C)
Raw data	-5.92	245.00	5.68	225.00
Polynomial fit	-5.62	245.00	5.46	225.00
Smoothed	-5.37	245.00	5.21	225.00

Table 13. As table 12, except calculations made at measurement temperatures only.

Some of the predictions described in fig. 3-51 were originally displayed in the earlier section of this chapter that explained the analysis methods and it was remarked upon how the temperature change predictions have a stepped characteristic as a function of starting temperature. It was mentioned that this feature would be revisited. In contrast to the  $\Delta T$  calculations made on the two datasets measured between 211 °C and 275 °C on the same film, their progression as a function of starting temperature is far smoother and for the first time here, the raw data lead to predictions that do not fluctuate along the starting temperature axis. This is because the temperature interval between data measurement points is a lot larger, resulting in a relatively smoother  $P(T)$  relationship. This is illustrated by the following three graphs, which show the final sets of  $\left(\frac{\partial P}{\partial T}\right)_E$  curves extracted from raw data that are then integrated over the relevant field range to calculate  $\Delta T$  from each starting temperature.



**Figure 3-53. 1.05  $\mu\text{m}$  thick PZT 95/05.  $dP/dT$  vs.  $E$  from raw data measured from 285 °C to 45 °C in 20 °C steps.**



**Figure 3-54. 1.05  $\mu\text{m}$  thick PZT 95/05.  $dP/dT$  vs.  $E$  from raw data measured (a) from 275 °C to 211 °C in 4 °C steps and (b) from 211 °C to 275 °C in 1 °C steps.**

As can be seen in the above two figures, the larger the temperature interval between measured data, the less erratic these pivotal  $\left(\frac{\partial P}{\partial T}\right)_E$  versus  $E$  graphs become and the smoother the progression of  $\Delta T$  predictions with starting temperature. The stepping feature of fig. 3-51 occurs due to the small predicted temperature changes, of up to nearly 6 °C, relative to the temperature interval of raw data, which is 20 °C. For the calculations from raw data and those from  $P(T)$  fit and smoothed data, the intermediate temperatures between raw data temperature points, lie on a straight line joining isofield, raw  $P(T)$  points, so  $\left(\frac{\partial P}{\partial T}\right)_E$  is the same for these intermediate points at a given field. Hence, when starting the series of  $dT$  calculations from one of these intermediate temperatures, many  $\Delta T$  results will have seen a very similar set of  $dT$  components in their integration and will

be virtually identical for many of the starting temperatures in the 20 °C intervals between raw data measurement temperatures. As the polynomial fit OIP and smoothed OIP alternatives will provide  $\left(\frac{\partial P}{\partial T}\right)_E$  values that change gradually over the 20 °C intervals, their  $\Delta T$  curves vary much more smoothly as a function of starting temperature.

With respect to the negative electrocaloric effect, peak values are recorded in the table below:

	COOLING (FIELD APPLIED)		HEATING (FIELD RELEASED)	
	<i>Peak change</i> (°C)	<i>At</i> (°C)	<i>Peak change</i> (°C)	<i>At</i> (°C)
<i>Calculated from many starting temperatures</i>				
Raw data	-1.98	65.00	1.98	64.00
Polynomial fit	-2.12	65.00	2.10	64.00
Smoothed	-1.51	85.00	1.49	84.00
Polynomial fit OIP	-2.11	47.67	2.14	45.00
Smoothed OIP	-1.69	57.00	1.69	54.33
<i>Calculated from measurement temperatures only</i>				
Raw data	-1.35	85.00	1.63	45.00
Polynomial fit	-1.80	65.00	1.70	45.00
Smoothed	-1.35	85.00	1.31	85.00

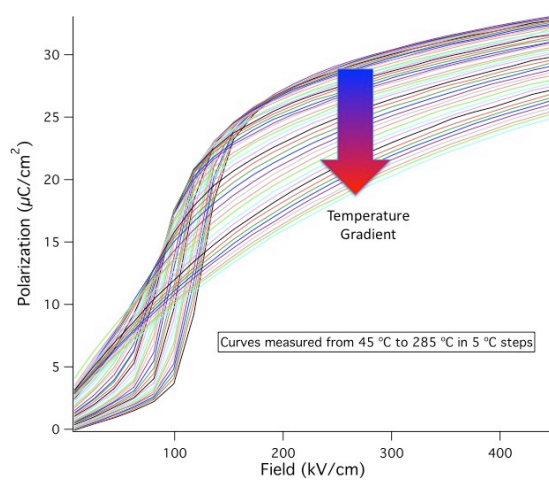
**Table 14. Peak negative electrocaloric effect predictions in 1.05µm thick PZT 95/05 measured from 285 °C to 45 °C in 20 °C steps.**

The variation in peak  $\Delta T$  predictions and their starting temperatures here, is larger than in previous results. The largest range of peak changes are in heating calculations, from 1.31 °C to 2.14 °C. This is a spread of 0.83 °C, which is 38.8% of the largest change, 2.14 °C. The starting temperatures also vary most for the heating calculations, from 45.00 °C to 85.00 °C. This is due to a combination of smoothing and polynomial fits to  $P(T)$  diverging in their approximations at the end of the temperature range of the dataset and the odd  $\Delta T$  calculation running off the  $P(E, T)$  surface and thus not being recorded,

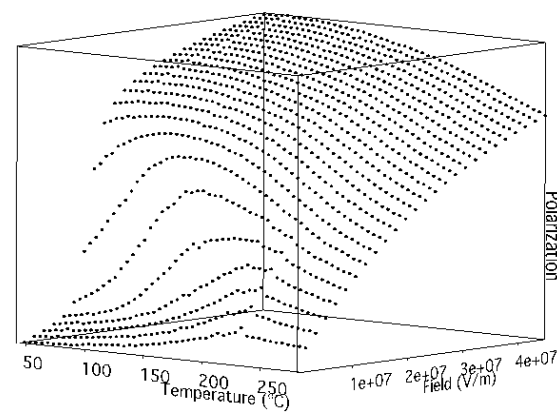
as the calculation was not possible over the entire field range. As noted earlier, the raw data should give the most reliable predictions in light of the poor fits and smoothing alternatives. Unfortunately, calculations on raw data from measurement temperatures only, have suffered from  $\Delta T$  calculations running off the  $P(E, T)$  surface and the only remaining noteworthy predictions are  $-1.98\text{ }^\circ\text{C}$  cooling from application of a field of  $476\text{ kV/cm}$  and  $1.98\text{ }^\circ\text{C}$  of heating from the release of the same field.

### 3.3.5. PARAMETER VARIATION

Five of the following six datasets were measured on the same  $1.05\text{ }\mu\text{m}$  thick PZT 95/05 sample, over  $50\text{ V}$ . These include three datasets that were measured from  $45\text{ }^\circ\text{C}$  and  $285\text{ }^\circ\text{C}$ , where hysteresis loops were taken every  $5\text{ }^\circ\text{C}$ ,  $20\text{ }^\circ\text{C}$  and  $30\text{ }^\circ\text{C}$ , respectively. Data were recorded in these three cases, as in all examples so far, in  $10\text{ kHz}$  hysteresis loops ( $1\text{ ms}$  period). This equates to second quadrant data comprising  $25$  points, each measured  $1\text{ }\mu\text{s}$  apart. The other two datasets of the five measured across  $50\text{ V}$ , were measured from  $230\text{ }^\circ\text{C}$  to  $280\text{ }^\circ\text{C}$  in  $5\text{ }^\circ\text{C}$  steps and  $275\text{ }^\circ\text{C}$  to  $215\text{ }^\circ\text{C}$  in  $3\text{ }^\circ\text{C}$  steps, using  $1\text{ kHz}$  hysteresis loops ( $0.1\text{ ms}$  period), where data are also recorded every  $1\text{ }\mu\text{s}$ , hence there are  $250$  points per second quadrant. There was no evidence of leakage in any of the hysteresis loops. The sixth dataset was measured from  $300\text{ }^\circ\text{C}$  to  $200\text{ }^\circ\text{C}$  in  $10\text{ }^\circ\text{C}$  steps, in  $10\text{ kHz}$  loops, on the same film, but over  $75\text{ V}$ .  $\Delta T$  calculations were then performed over  $50\text{ V}$  for comparison with the other five datasets, by setting the upper field limit accordingly. Additionally, the sample was left for an extra ten minutes at each measurement temperature, before taking a loop for this dataset.

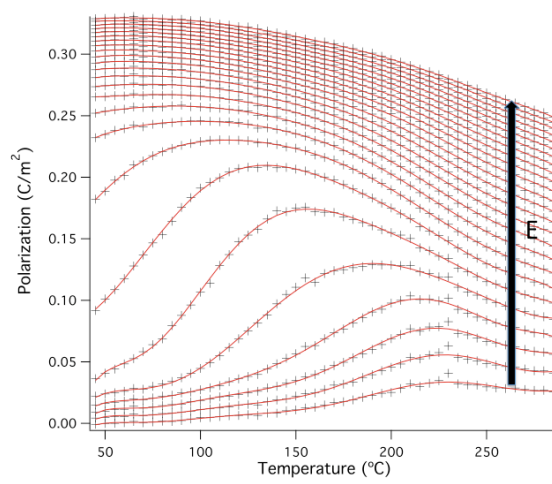


(a)



(b)

Figure 3-55. 1.05  $\mu\text{m}$  thick PZT 95/05. (a) Second quadrant data from P(E) loops measured from 45 °C to 285 °C in 5 °C steps. (b) P(E,T). 3D view of the same data.



(a)

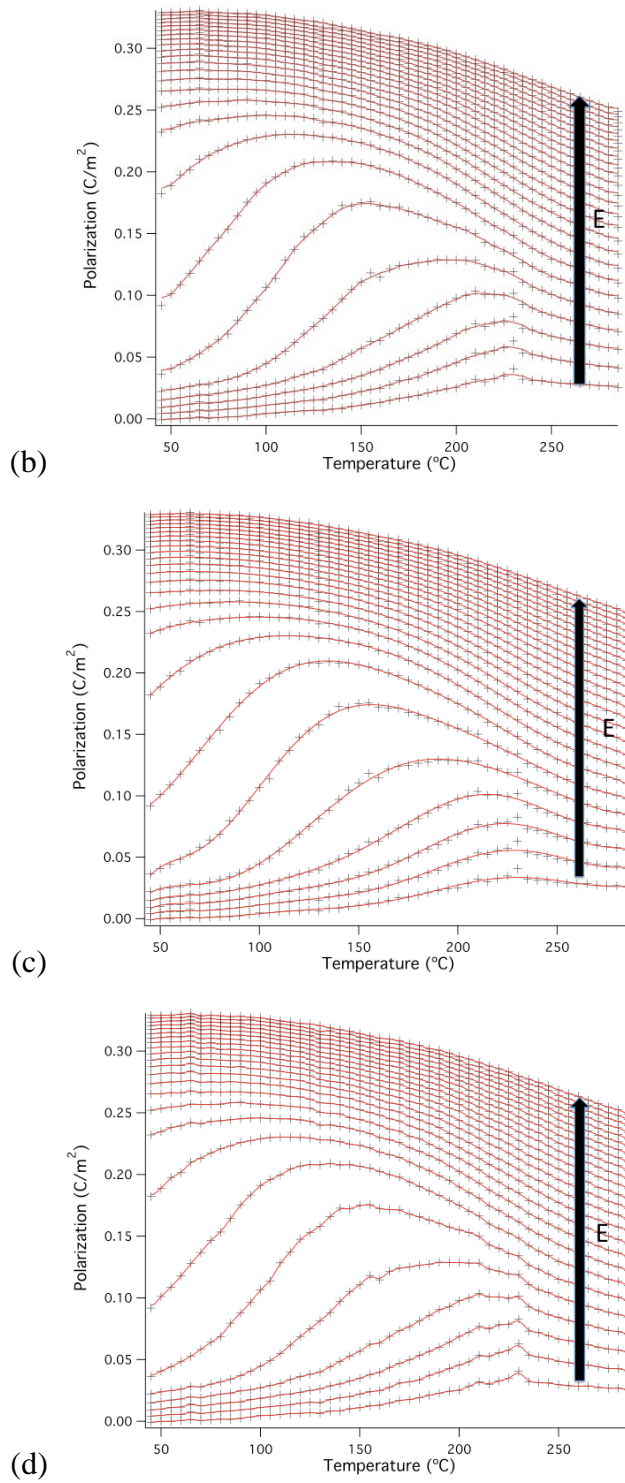
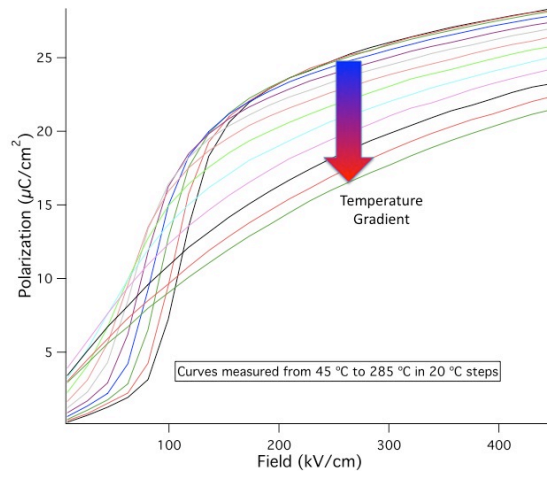
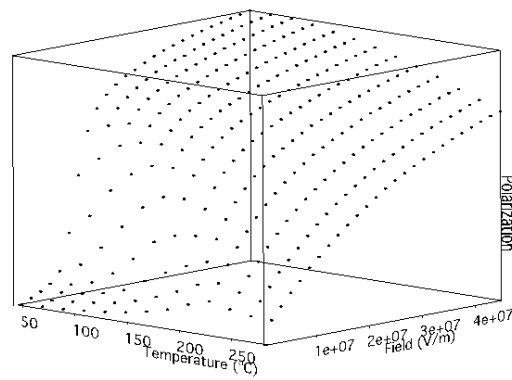


**Figure 3-56. 1.05  $\mu\text{m}$  thick PZT 95/05.  $P(T)$ . Red lines represent alternatives to isofield black data points. (a) 8<sup>th</sup> order polynomial fit. (b) Three-point boxcar smoothing. (c) 8<sup>th</sup> order polynomial fit OIP (d) 15-point boxcar smoothing OIP. Data measured as  $P(E)$  from 45  $^{\circ}\text{C}$  to 285  $^{\circ}\text{C}$  in 5  $^{\circ}\text{C}$  steps.**

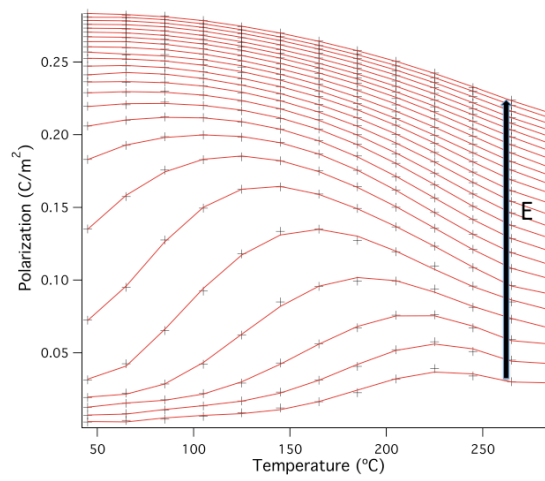


(a)



(b)

**Figure 3-57. 1.05  $\mu\text{m}$  thick PZT 95/05. (a) Second quadrant data from P(E) loops measured from 45  $^{\circ}\text{C}$  to 285  $^{\circ}\text{C}$  in 20  $^{\circ}\text{C}$  steps. (b) P(E,T). 3D view of the same data.**



(a)

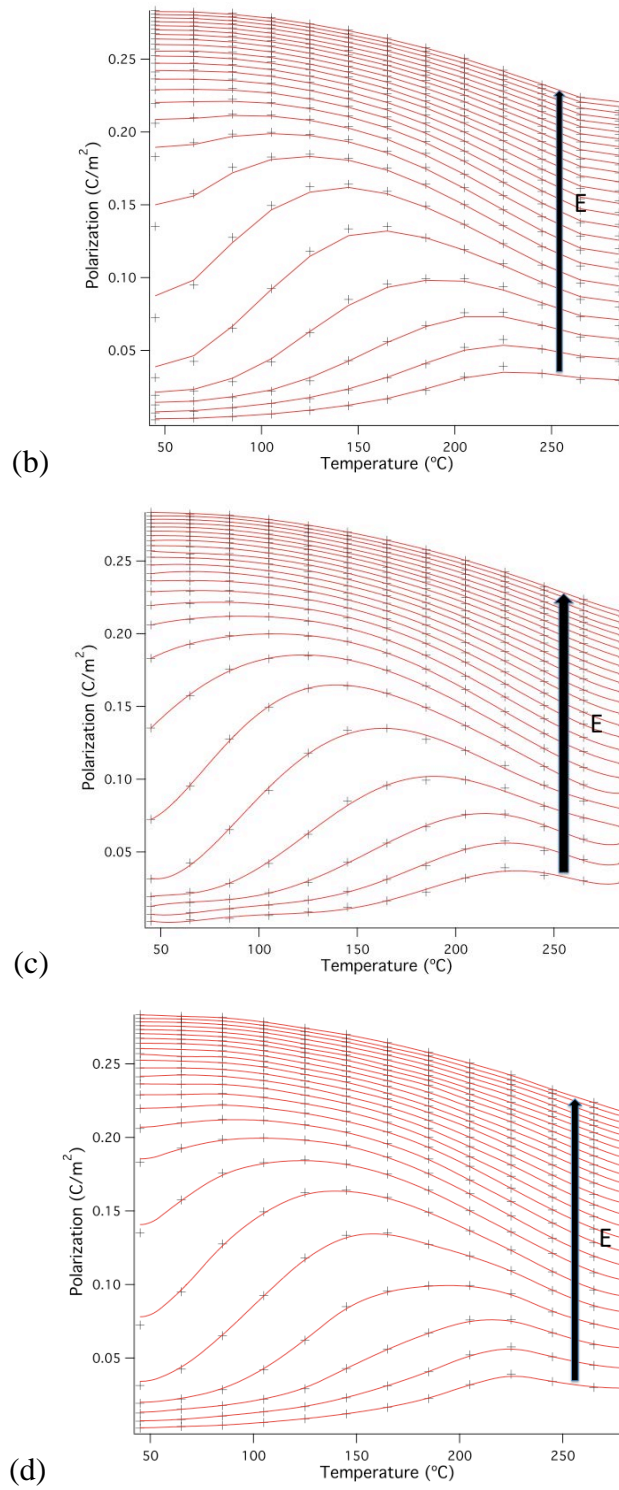


**Figure 3-58. 1.05  $\mu\text{m}$  thick PZT 95/05.  $P(T)$ . Red lines represent alternatives to isofield black data points. (a) 6<sup>th</sup> order polynomial fit. (b) Three-point boxcar smoothing. (c) 6<sup>th</sup> order polynomial fit OIP (d) 15-point boxcar smoothing OIP. Data measured as  $P(E)$  from 45  $^{\circ}\text{C}$  to 285  $^{\circ}\text{C}$  in 20  $^{\circ}\text{C}$  steps.**

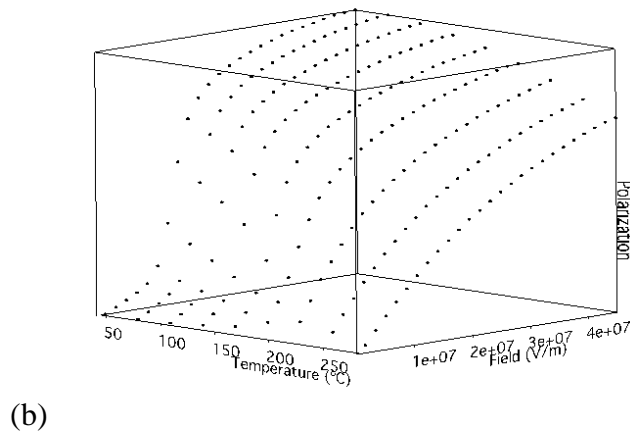
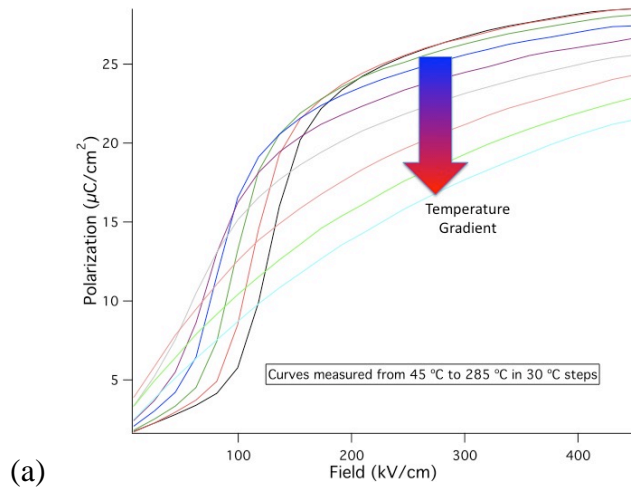
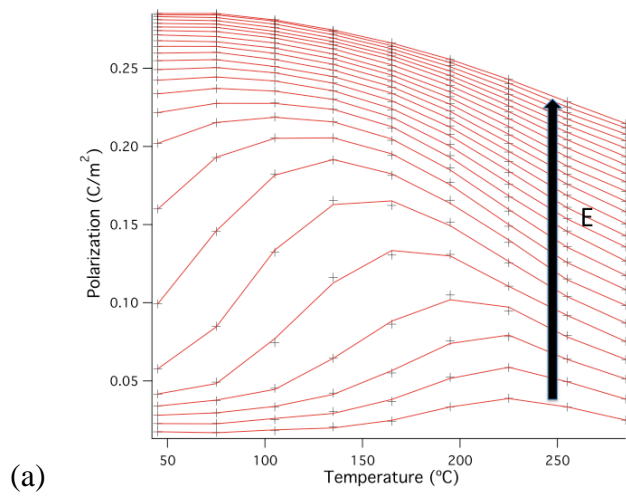
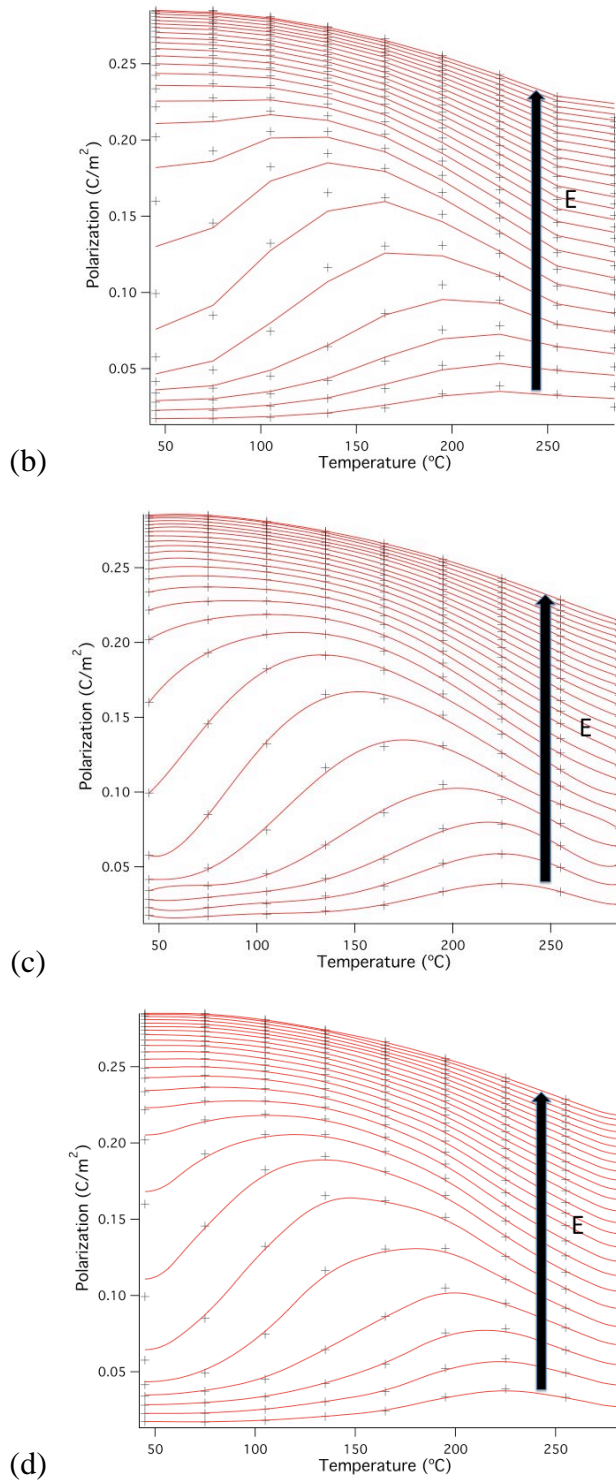
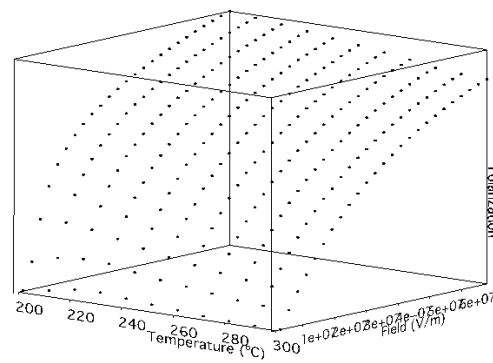
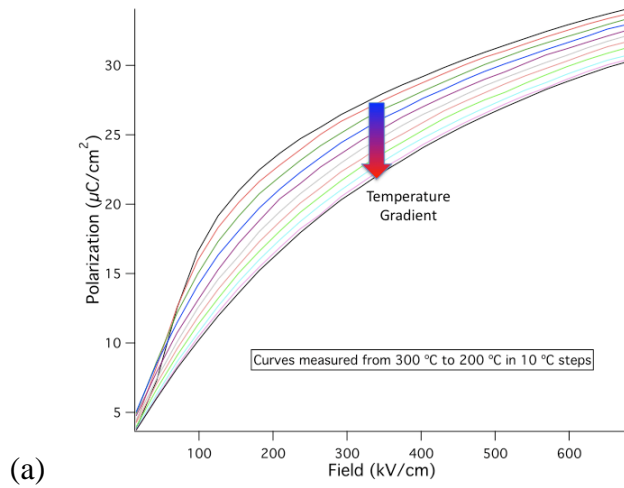


Figure 3-59. 1.05  $\mu\text{m}$  thick PZT 95/05. (a) Second quadrant data from P(E) loops measured from 45  $^{\circ}\text{C}$  to 285  $^{\circ}\text{C}$  in 30  $^{\circ}\text{C}$  steps. (b) P(E,T). 3D view of the same data.

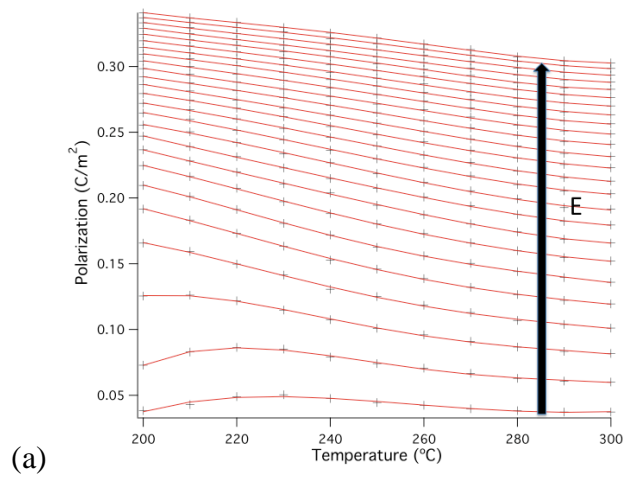




**Figure 3-60. 1.05  $\mu\text{m}$  thick PZT 95/05.  $P(T)$ . Red lines represent alternatives to isofield black data points. (a) 6<sup>th</sup> order polynomial fit. (b) Three-point boxcar smoothing. (c) 6<sup>th</sup> order polynomial fit OIP (d) 15-point boxcar smoothing OIP. Data measured as  $P(E)$  from 45  $^{\circ}\text{C}$  to 285  $^{\circ}\text{C}$  in 30  $^{\circ}\text{C}$  steps.**



**Figure 3-61. 1.05  $\mu\text{m}$  thick PZT 95/05. (a) Second quadrant data from P(E) loops measured from 300 °C to 200 °C in 10 °C steps, where settling time at each temperature was increased to 10 minutes. (b) P(E,T). 3D view of the same data.**



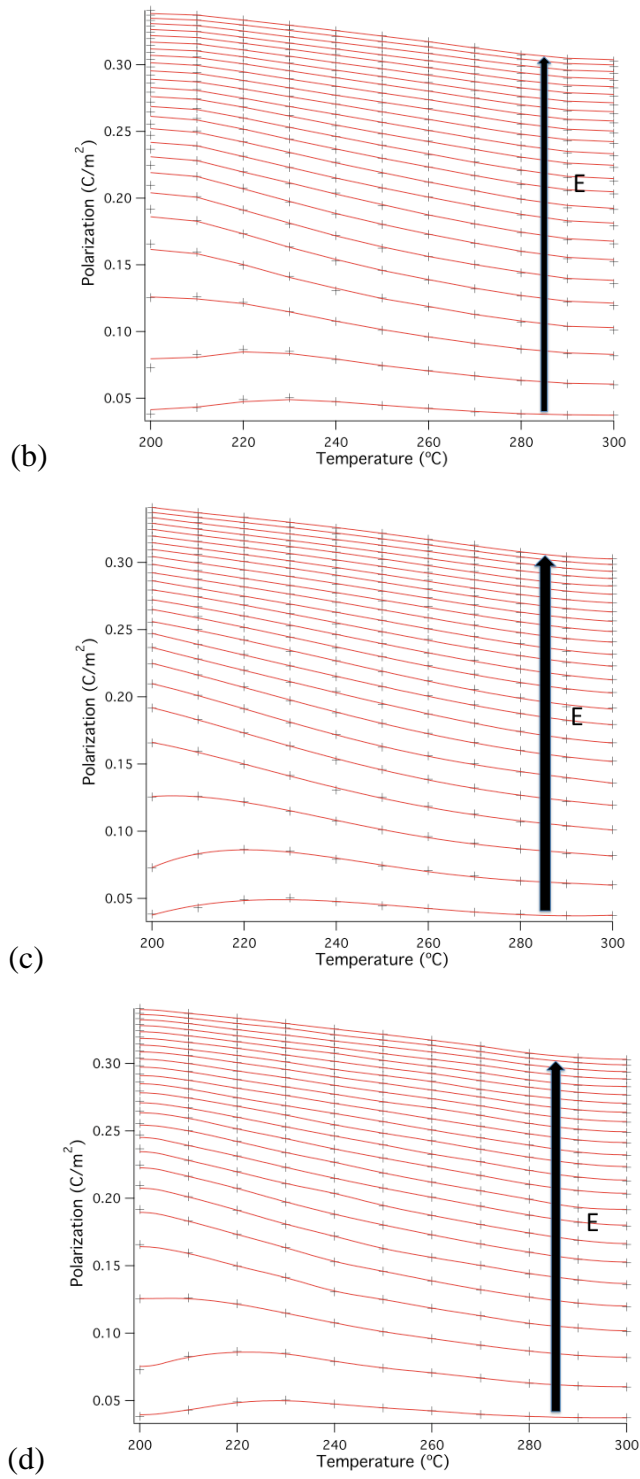
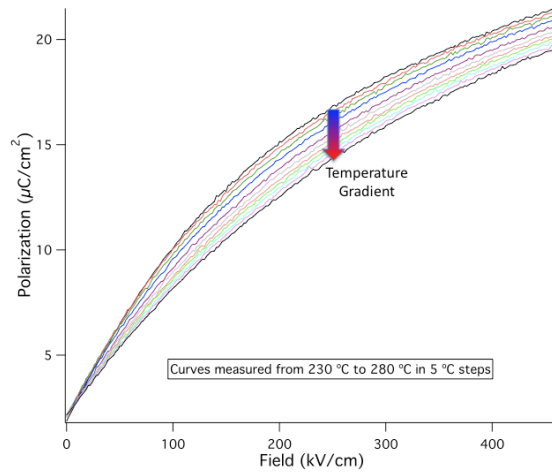
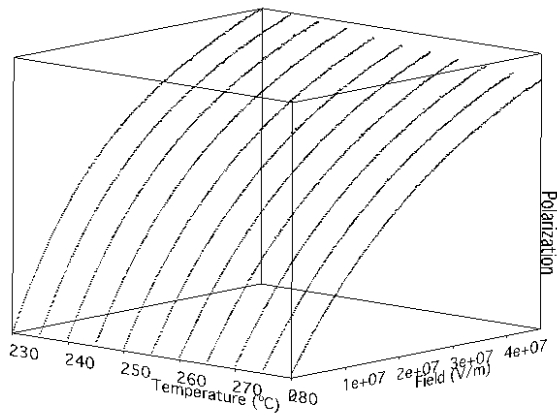


**Figure 3-62. 1.05  $\mu\text{m}$  thick PZT 95/05. P(T). Red lines represent alternatives to isofield black data points. (a) 4<sup>th</sup> order polynomial fit. (b) Three-point boxcar smoothing. (c) 4<sup>th</sup> order polynomial fit OIP (d) 15-point boxcar smoothing OIP. Data measured as P(E) from 300  $^{\circ}\text{C}$  to 200  $^{\circ}\text{C}$  in 10  $^{\circ}\text{C}$  steps.**

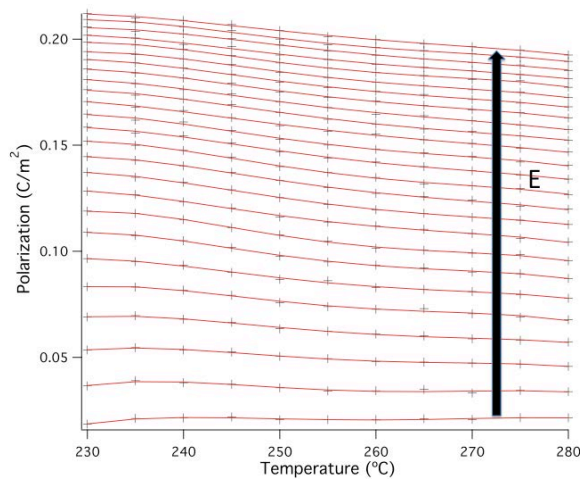


(a)

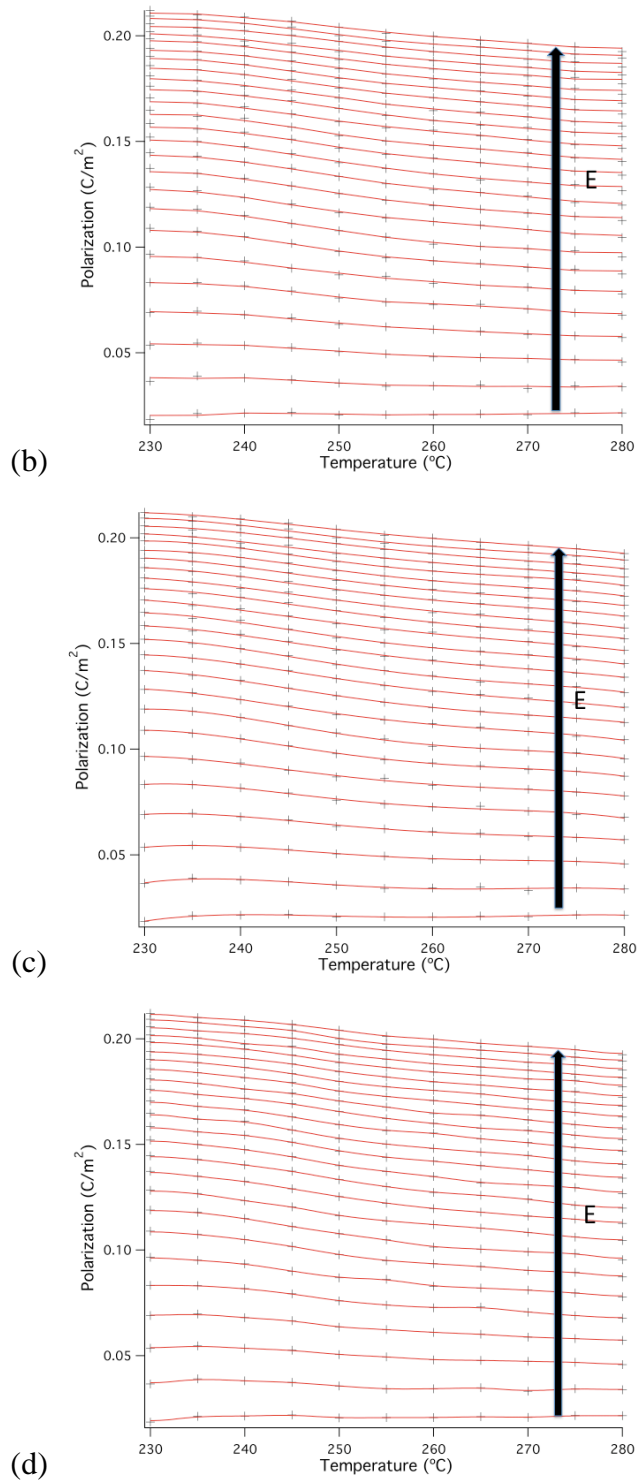


(b)

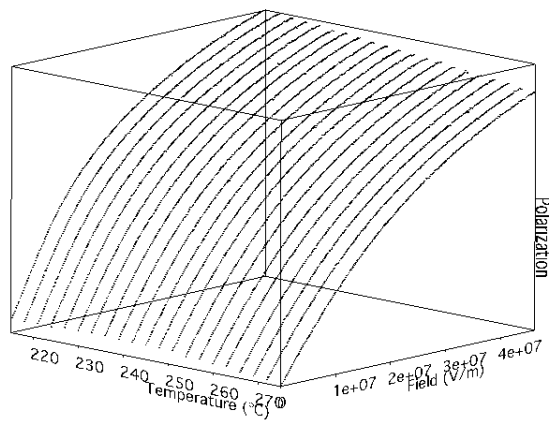
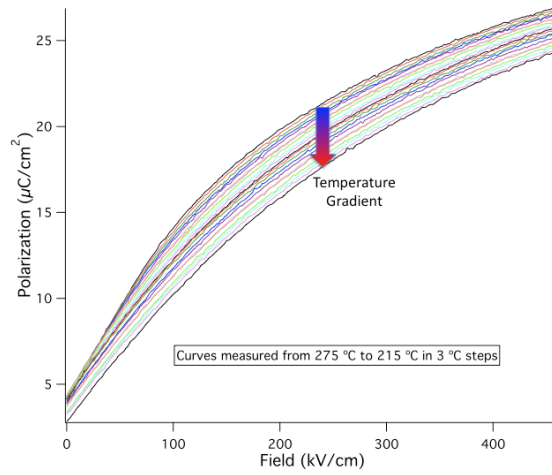
**Figure 3-63. 1.05  $\mu\text{m}$  thick PZT 95/05. (a) Second quadrant data from P(E) loops (250 points) measured from 230 °C to 280 °C in 5 °C steps. (b) P(E,T). 3D view of the same data.**



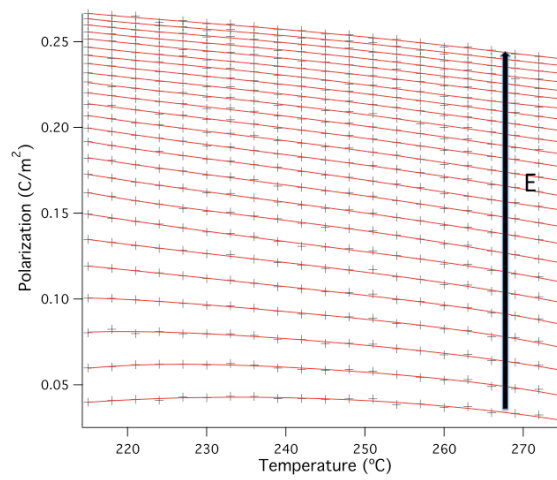
(a)



**Figure 3-64. 1.05  $\mu\text{m}$  thick PZT 95/05. P(T). Red lines represent alternatives to isofield black data points. (a) 4<sup>th</sup> order polynomial fit. (b) Three-point boxcar smoothing. (c) 4<sup>th</sup> order polynomial fit OIP (d) 15-point boxcar smoothing OIP. Data measured as P(E) from 230  $^{\circ}\text{C}$  to 280  $^{\circ}\text{C}$  in 5  $^{\circ}\text{C}$  steps.**



**Figure 3-65. 1.05  $\mu\text{m}$  thick PZT 95/05. (a) Second quadrant data from P(E) loops (250 points) measured from 275  $^{\circ}\text{C}$  to 215  $^{\circ}\text{C}$  in 3  $^{\circ}\text{C}$  steps. (b) P(E,T). 3D view of the same data.**



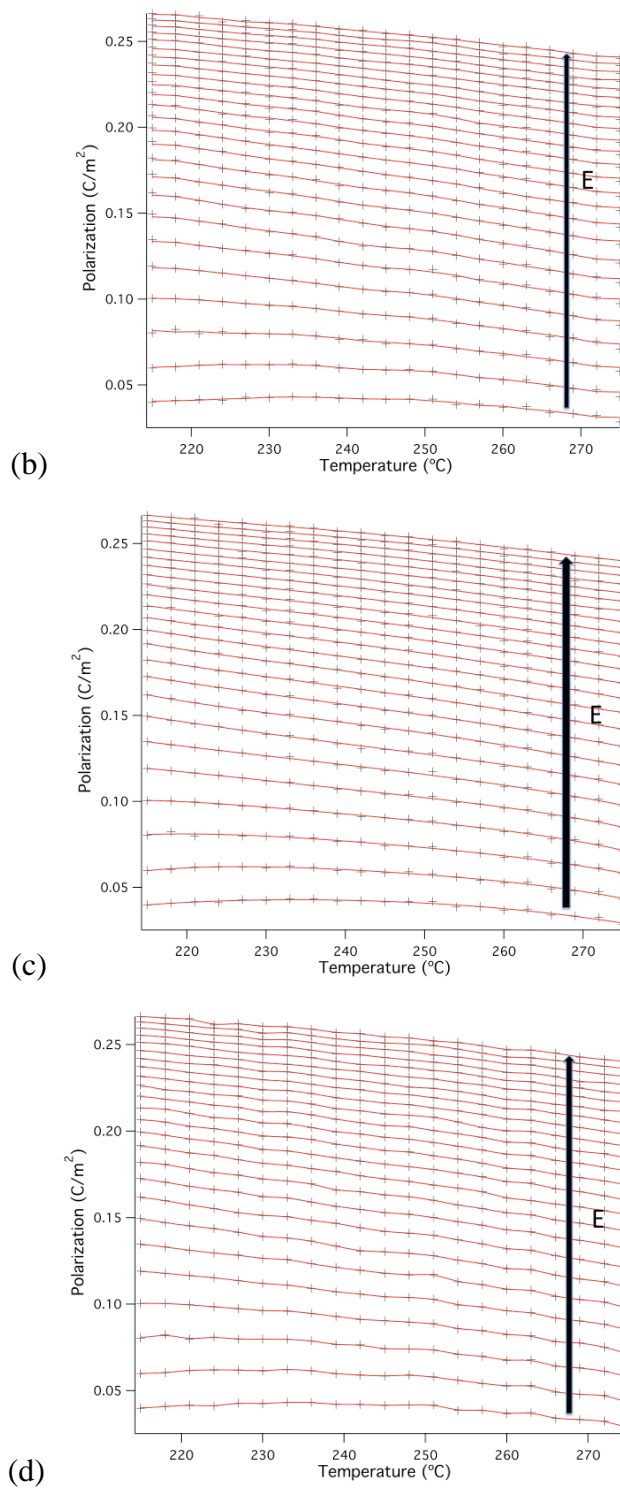


**Figure 3-66. 1.05  $\mu\text{m}$  thick PZT 95/05.  $P(T)$ . Red lines represent alternatives to isofield black data points. (a) 4<sup>th</sup> order polynomial fit. (b) Three-point boxcar smoothing. (c) 4<sup>th</sup> order polynomial fit OIP (d) 15-point boxcar smoothing OIP. Data measured as  $P(E)$  from 275  $^{\circ}\text{C}$  to 215  $^{\circ}\text{C}$  in 3  $^{\circ}\text{C}$  steps.**

Another notable feature is that the 45 °C to 285 °C datasets that were measured at 20 °C and 30 °C intervals used the same top electrode, on the same day. The sample and electrical connections were not disturbed between measurement runs, nor was the vacuum in the cryostat broken. The same applies to the 230 °C to 280 °C and 275 °C to 215 °C datasets.

A comparison between the  $\Delta T$  predictions follows:

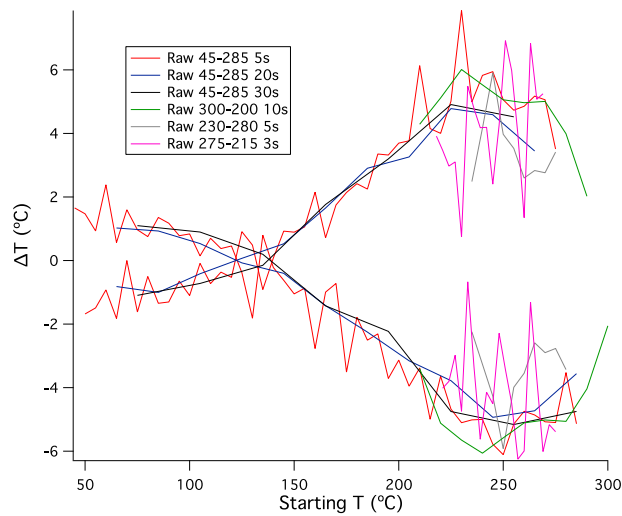


**Figure 3-67. 1.05  $\mu\text{m}$  thick PZT 95/05. Electrocaloric heating and cooling predictions for six datasets from raw data. Calculations from measurement temperatures only.**

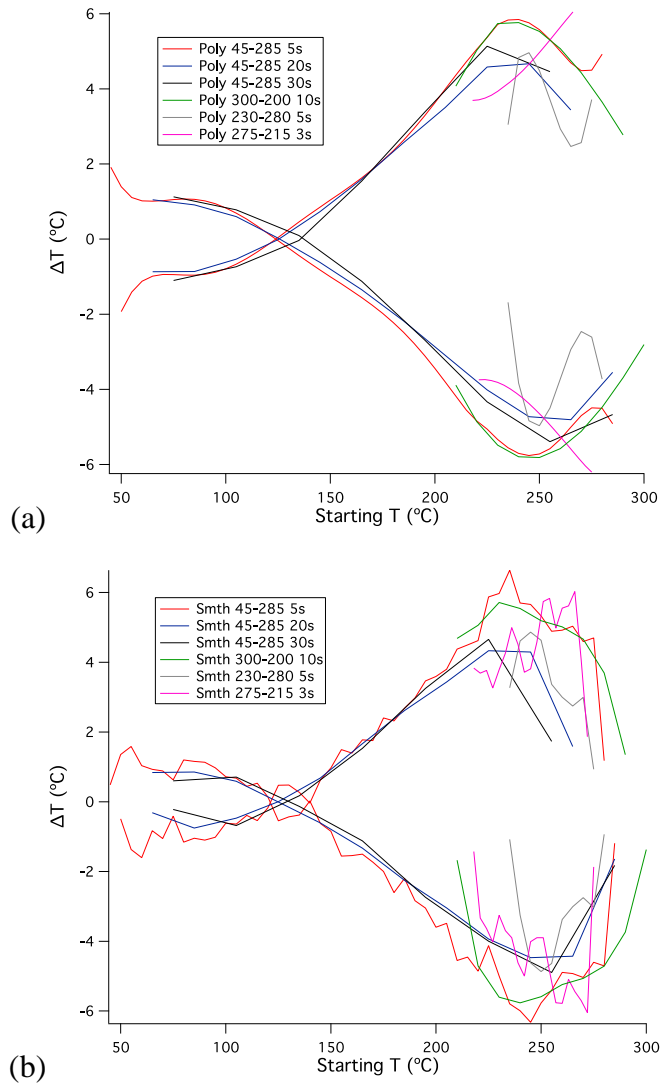


**Figure 3-68. 1.05  $\mu\text{m}$  thick PZT 95/05. Electrocaloric heating and cooling predictions for six datasets from (a) polynomial fits to and (b) boxcar smoothing of raw P(T) data. Calculations from measurement temperatures only.**

	COOLING		HEATING	
	<i>Peak change (°C)</i>	<i>At (°C)</i>	<i>Peak change (°C)</i>	<i>At (°C)</i>
<i>45-285 °C in 5 °C steps</i>				
Raw data	-6.11	250.00	7.87	230.00
Polynomial fit	-5.76	245.00	5.85	240.00
Smoothed	-6.32	245.00	6.64	235.00
<i>45-285 °C in 20 °C steps</i>				
Raw data	-4.93	245.00	4.78	225.00
Polynomial fit	-4.81	265.00	4.67	245.00
Smoothed	-4.47	245.00	4.33	225.00
<i>45-285 °C in 30 °C steps</i>				
Raw data	-5.16	255.00	4.91	225.00
Polynomial fit	-5.39	255.00	5.14	225.00
Smoothed	-4.90	255.00	4.66	225.00
<i>300-200 °C in 10 °C steps</i>				
Raw data	-6.06	240.00	6.01	230.00
Polynomial fit	-5.82	250.00	5.77	240.00
Smoothed	-5.77	241.33	5.72	230.00
<i>230-280 °C in 5 °C steps</i>				
Raw data	-5.92	250.00	5.91	245.00
Polynomial fit	-4.97	250.00	4.96	245.00
Smoothed	-4.87	250.00	4.87	245.00
<i>275-215 °C in 3 °C steps</i>				
Raw data	-6.25	257.00	6.92	251.00
Polynomial fit	-6.20	275.00	6.05	266.00
Smoothed	-6.05	272.00	6.03	266.00

**Table 15. Peak electrocaloric cooling and heating predictions in 1.05  $\mu\text{m}$  thick PZT 95/05 from six datasets, where calculations were made from measurement temperatures only.**

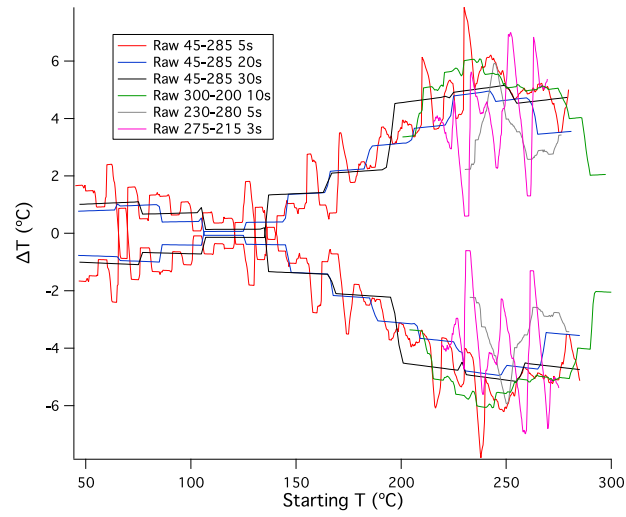


**Figure 3-69. 1.05  $\mu\text{m}$  thick PZT 95/05. Electrocaloric heating and cooling predictions for six datasets from raw data. Calculations from measurement temperatures and additional intermediate temperatures.**

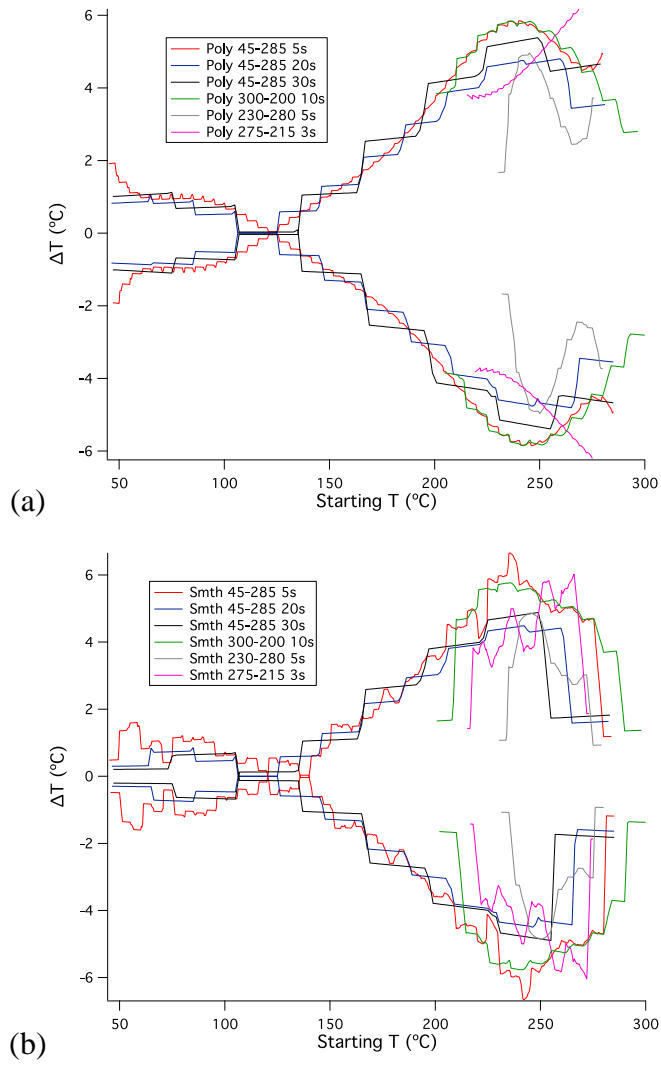


**Figure 3-70. 1.05  $\mu\text{m}$  thick PZT 95/05. Electrocaloric heating and cooling predictions for six datasets from (a) polynomial fits to and (b) boxcar smoothing of raw P(T) data. Calculations from measurement temperatures and additional intermediate temperatures.**

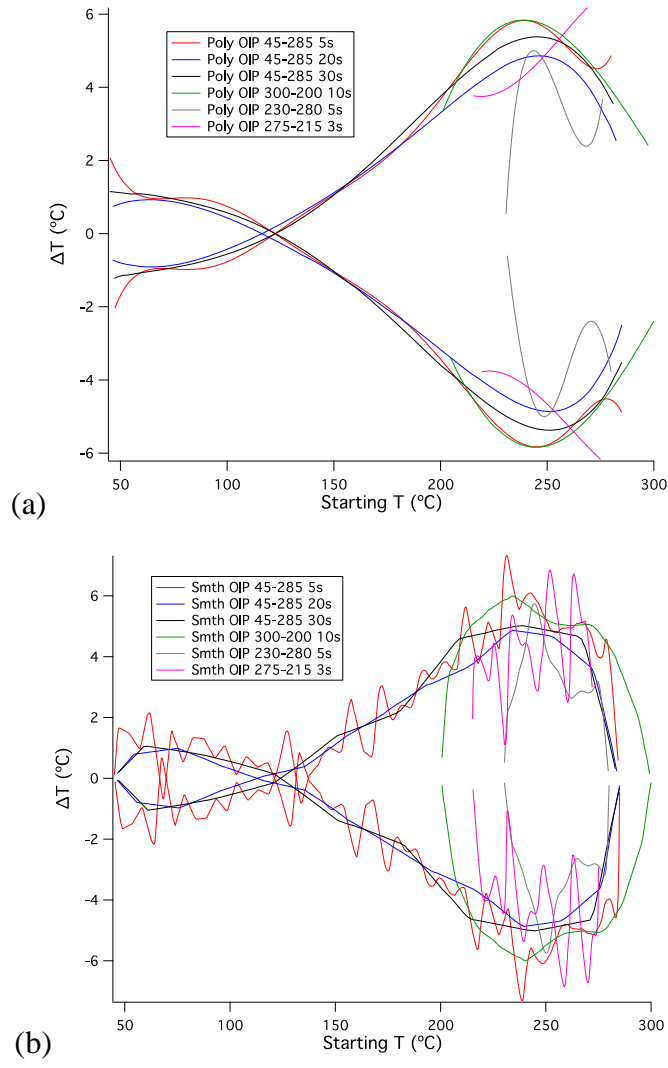


**Figure 3-71. 1.05  $\mu\text{m}$  thick PZT 95/05. Electrocaloric heating and cooling predictions for six datasets from (a) polynomial OIP fits to and (b) boxcar smoothing OIP of raw P(T) data. Calculations from measurement temperatures and additional intermediate temperatures.**

	COOLING		HEATING	
	<i>Peak change (°C)</i>	<i>At (°C)</i>	<i>Peak change (°C)</i>	<i>At (°C)</i>
<i>45-285 °C in 5 °C steps</i>				
Raw data	-7.82	238.00	7.87	230.00
Polynomial fit	-5.85	246.00	5.85	240.33
Smoothed	-6.65	242.33	6.66	235.67
Polynomial fit OIP	-5.83	245.00	5.82	239.33
Smoothed OIP	-7.31	238.67	7.32	231.33
<i>45-285 °C in 20 °C steps</i>				
Raw data	-4.95	246.33	4.95	242.33
Polynomial fit	-4.81	265.00	4.76	242.33
Smoothed	-4.50	246.33	4.49	242.33
Polynomial fit OIP	-4.86	251.67	4.86	246.33
Smoothed OIP	-4.87	239.67	4.86	234.33
<i>45-285 °C in 30 °C steps</i>				
Raw data	-5.16	255.00	5.15	249.00
Polynomial fit	-5.39	255.00	5.38	249.00
Smoothed	-4.90	255.00	4.88	249.00
Polynomial fit OIP	-5.37	251.00	5.38	245.00
Smoothed OIP	-5.01	245.00	5.02	239.00
<i>300-200 °C in 10 °C steps</i>				
Raw data	-6.07	243.33	6.07	237.33
Polynomial fit	-5.85	242.00	5.84	236.67
Smoothed	-5.77	241.33	5.77	235.33
Polynomial fit OIP	-5.84	244.67	5.84	238.67
Smoothed OIP	-6.00	240.00	6.00	234.00

<i>230-280 °C in 5 °C steps</i>				
Raw data	-5.95	250.33	5.93	244.33
Polynomial fit	-4.97	250.00	4.96	245.00
Smoothed	-4.87	250.00	4.87	245.33
Polynomial fit OIP	-5.00	248.67	5.00	243.67
Smoothed OIP	-5.75	250.33	5.74	244.67
<i>275-215 °C in 3 °C steps</i>				
Raw data	-6.92	258.20	6.99	252.20
Polynomial fit	-6.20	275.00	6.18	268.60
Smoothed	-6.05	272.00	6.03	266.00
Polynomial fit OIP	-6.18	275.00	6.18	268.80
Smoothed OIP	-6.85	258.80	6.85	252.00

**Table 16. Peak electrocaloric cooling and heating predictions in 1.05 $\mu$ m thick PZT 95/05 from six datasets, where calculations were made from measurement temperatures and additional intermediate temperatures.**

### 3.3.6. PEAK $\Delta T$ PREDICTIONS

It is now possible to compare the extent of variations in peak  $\Delta T$  predictions and their starting temperatures, across many datasets measured on the same film. The greatest difference between the data procured is that some were measured using different top electrodes on the sample, with either 25 or 250 points per second loop quadrant, where loops were taken at varying temperature intervals, over different temperature ranges. Even so, the starting temperature region where peak temperature changes are predicted, was included in every dataset.  $\Delta T$  predictions were calculated from five reasonable sets of  $P(T)$  data, at measurement temperatures only, or by including intermediate temperatures in three ways.

This comparison covers the six datasets shown in the last section, the ‘285 °C to 45 °C in 20 °C steps’ dataset presented in the section including the negative electrocaloric effect and the two datasets measured between 211 °C and 275 °C. These last two were

measured over 75 V, but have been analysed here over 50 V, by reducing the upper field limit for  $\Delta T$  calculation.

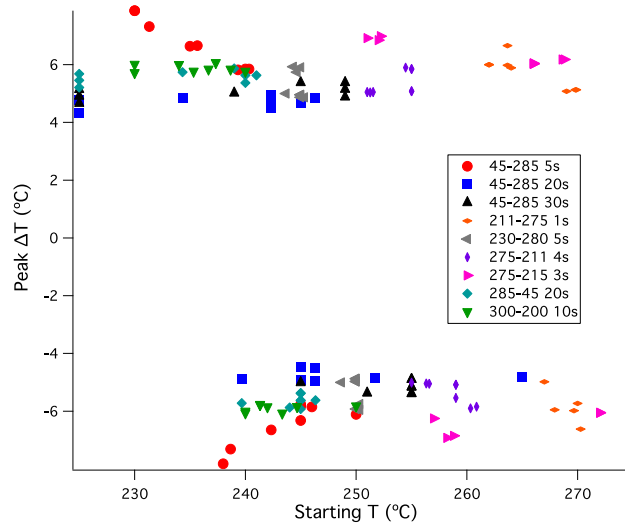


**Figure 3-72. Peak  $\Delta T$  as a function of starting temperature, for nine datasets.**

The peak predictions shown in the above figure are for both heating and cooling. The nine datasets have sixteen predictions each, eight for cooling and eight for heating, as presented in peak  $\Delta T$  tables such as table 15 and table 16.

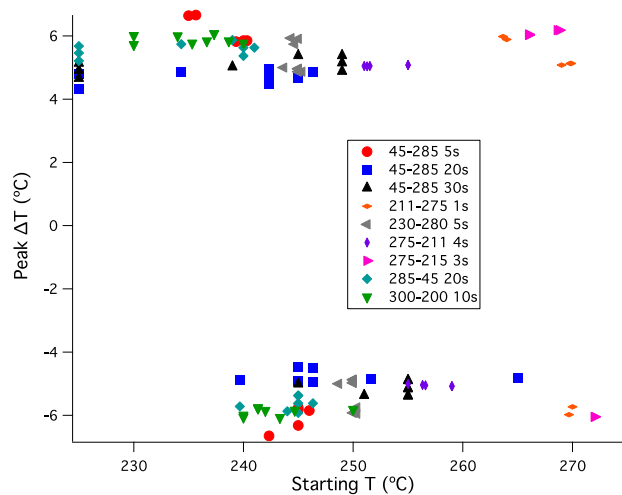


**Figure 3-73. As above figure, excluding peaks from erratic  $\Delta T$  curves.**

Figure 3-73 contains fewer data points than the previous figure, having excluded those values that came from  $\Delta T$  prediction curves that varied erratically as a function of starting temperature. As it can be seen that all measured  $P(E, T)$  surfaces follow a generally smooth curvature, the  $\Delta T$  prediction results using any one method, that fluctuate as a function of starting temperature more than they actually follow a trend, could be regarded as invalid. It is obviously a subjective decision as to which  $\Delta T$  results this would include, but here the excluded  $\Delta T$  sets are those calculated from raw data and  $P(T)$  smoothing OIP in the following datasets: '45 °C to 285 °C in 5 °C steps', '275 °C to 215 °C in 3 °C steps', '211 °C to 275 °C in 1 °C steps' and '275 °C to 211 °C in 4 °C steps'. The following tables summarise the extent to which  $\Delta T$  predictions vary.

	<i>Largest peak <math>\Delta T</math> spread (°C)</i>	<i>Largest peak <math>\Delta T</math> spread in % terms of its largest peak <math>\Delta T</math></i>	<i>Largest peak <math>\Delta T</math> starting temperature spread (°C)</i>	<i>Average peak <math>\Delta T</math> spread (°C)</i>	<i>Average peak <math>\Delta T</math> spread in % terms of its largest peak <math>\Delta T</math></i>	<i>Average peak <math>\Delta T</math> starting temperature spread (°C)</i>
<i>Considering all individual datasets</i>						
Eight alternative sets of predictions	3.74	26.3	43.94	1.51	14.3	14.52
Smoothly varying predictions	2.26	18.2	25.33	0.72	8.1	8.76

**Table 17. Peak  $\Delta T$  prediction variation. PZT 95/05.**

Prediction results per individual dataset vary whether one decides to calculate from measurement temperatures alone, or whether to include intermediate temperature points. All  $\Delta T$  results are encompassed by the second method when intermediate points are established along straight lines joining  $P(T)$  data points, but the first method gives less precise starting temperature predictions and either approach is reasonable.

In the above table, the first row considers all predictions per dataset, whereas the second excludes erratic  $\Delta T$  curves, i.e. it considers values presented in fig. 3-73. Each individual dataset will have a range of peak  $\Delta T$  predictions, one range for heating predictions and

one range for cooling predictions. The widest of these ranges is shown in the first data column. The width of each range, expressed as a percentage of its largest peak  $\Delta T$  prediction, is then compared with the other ranges and the largest value is recorded in the second data column. These peak  $\Delta T$  predictions have corresponding starting temperatures, so the starting temperature ranges are also compared and the largest recorded in the third data column. The average peak  $\Delta T$  spread size is recorded in the fourth data column. The fifth data column shows the average of the percentages considered for the second data column and the final column shows the average of the starting temperature ranges considered for the third data column.

**Even when omitting dubious  $\Delta T$  predictions, it can be seen that the analysis method alone accounts for a variation in peak  $\Delta T$  results that can represent up to 18.2% of its largest peak  $\Delta T$  prediction, over a 25.33 °C range of starting temperatures.**

	<i>Peak <math>\Delta T</math> spread (<math>^{\circ}\text{C}</math>)</i>	<i>Peak <math>\Delta T</math> spread in % terms of its largest peak <math>\Delta T</math></i>	<i>Peak <math>\Delta T</math> starting temperature spread (<math>^{\circ}\text{C}</math>)</i>
<i>Over two datasets: 45-285 <math>^{\circ}\text{C}</math> 20s &amp; 45-285 <math>^{\circ}\text{C}</math> 30s. Same electrode, measured same day.</i>			
Eight alternative sets of predictions	1.05	19.5	24.00
Smoothly varying predictions	1.05	19.5	24.00
<i>Over two datasets: 230-280 <math>^{\circ}\text{C}</math> 5s &amp; 275-215 <math>^{\circ}\text{C}</math> 3s. Same electrode, measured same day.</i>			
Eight alternative sets of predictions	2.12	30.3	26.33
Smoothly varying predictions	1.33	21.5	26.33
<i>Over two datasets: 211-275 <math>^{\circ}\text{C}</math> 1s &amp; 275-211 <math>^{\circ}\text{C}</math> 4s. Same electrode, consecutive days.</i>			
Eight alternative sets of predictions	1.64	24.8	20.00
Smoothly varying predictions	0.97	16.2	20.00
<i>Over all 50 V range calculations. Same film, some different electrodes, mostly different days.</i>			
Eight alternative sets of predictions	3.54	45.0	44.87
Smoothly varying predictions	2.33	35.0	44.87

**Table 18. Peak  $\Delta T$  prediction variation. PZT 95/05.**

Table 18 groups together peak  $\Delta T$  predictions from more than one dataset and looks at the variation of these values as a whole. The first three sets of results look at all peak  $\Delta T$  values from datasets that were measured using the same top electrode. The largest variation is seen from values calculated from the two datasets measured from 230  $^{\circ}\text{C}$  to 280  $^{\circ}\text{C}$ , in 5  $^{\circ}\text{C}$  steps and 275  $^{\circ}\text{C}$  to 215  $^{\circ}\text{C}$  in 3  $^{\circ}\text{C}$  steps. **This increases the variation in reliable peak  $\Delta T$  results, compared to individual datasets, that can represent up to**

**21.5% of its largest peak  $\Delta T$  prediction, over a 26.33 °C range of starting temperatures.**

**Finally, when pooling all peak  $\Delta T$  predictions for the same sample, over the same voltage range, the reliable peak  $\Delta T$  results can cover up to 35.0% of the largest peak  $\Delta T$  prediction, over a 44.87 °C range of starting temperatures.**

### **3.4.PMN-PT**

PMN-PT here, refers to  $0.93\text{PbMg}_{1/3}\text{Nb}_{2/3}-0.07\text{PbTiO}_3$ . Two films were studied, one of 225 nm and another of 700 nm in thickness. They were fabricated by Tatiana Correia at Cranfield University as described in the experimental method section. Three datasets are presented here for each sample. The datasets taken on the 225 nm thick sample were measured over a voltage range of 14 V, equivalent to 622 kV/cm, whereas the datasets of the 700 nm thick sample were taken over 50 V, equivalent to 714 kV/cm. None of the datasets was measured at the same electrode. The volumetric heat capacity was based on a specific heat capacity of 371 J/K.kg and a density of 8080 kg/m<sup>3</sup> [28].

PMN-PT is an unexpected candidate for the indirect method, as it is a relaxor ferroelectric and it is known that relaxors can vary in their polarization response to a voltage sweep depending on the speed at which that sweep is carried out. One could measure significantly varying  $P(E)$  loops as a result.

The benefit of applying the indirect method to ferroelectrics is their generally larger polarization response to given fields and thus, larger entropy change. The down side is that for nearly every field there are nominally, two equilibrium states, where the indirect method formally requires just one. When applying the indirect method to ferroelectrics, the thought is that, for example, every time a field is released from a given maximum, at which the polarization of the material is saturated, the material passes through the same set of equilibrium states represented by the second quadrant data of hysteresis loops and the use of thermodynamics is perhaps justified, or at least, represents an approximation under these conditions.

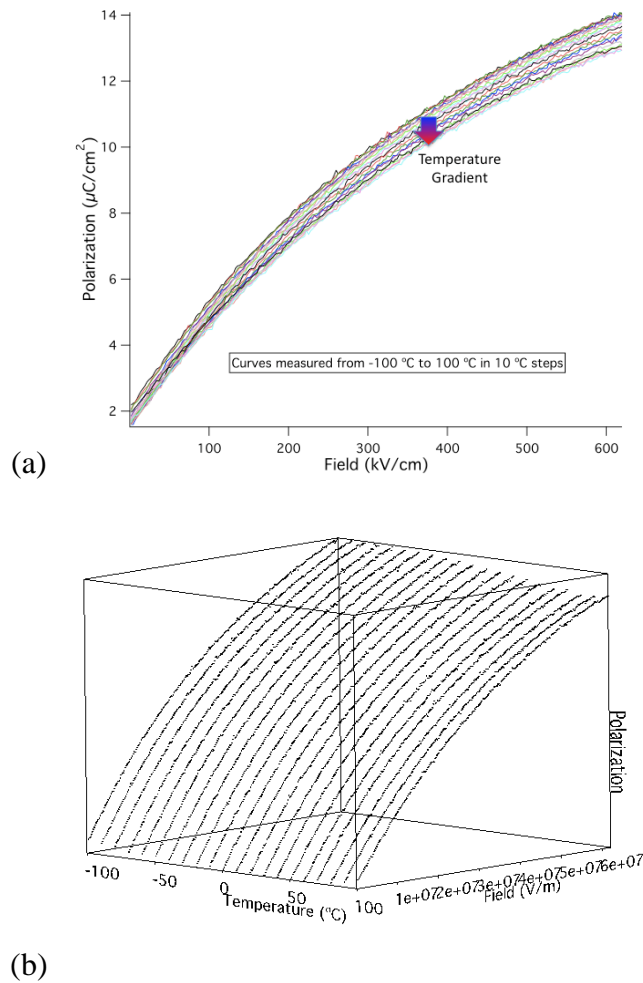
When considering frequency-dependent relaxors, one could try measuring  $P(E)$  loops at ever lower frequencies with the hope that leakage does not become significant and that the resulting  $P(E, T)$  surfaces at sufficiently slow speeds differ negligibly. Then the slowest surface would be taken to represent equilibrium states. However, the literature suggests that relaxors are never in equilibrium [60-62]. Nonetheless, of the 23 papers to date that include the indirect method, 16 refer to experiments on relaxor ferroelectrics, i.e. over two-thirds of the total.

Several of these papers make no mention at all of this frequency dependence [19, 22, 24, 28]. Others show dielectric constant measurements as a function of frequency [12, 13, 17, 21, 25], over a temperature range, but still make no link to the equilibrium issue. A few of those papers [12, 13, 17] show that over several decades of loop frequency, there is no perceptible difference in the dielectric constant over the temperature range of interest, but that is no case for a single, equilibrium  $P(E, T)$  surface on field release, as dielectric constants are measured with the application of a small, oscillating voltage over the relevant temperature range and reveal nothing of the polarization response at those frequencies when the applied bipolar voltage is responsible for fields of several hundred kilovolts per centimetre.

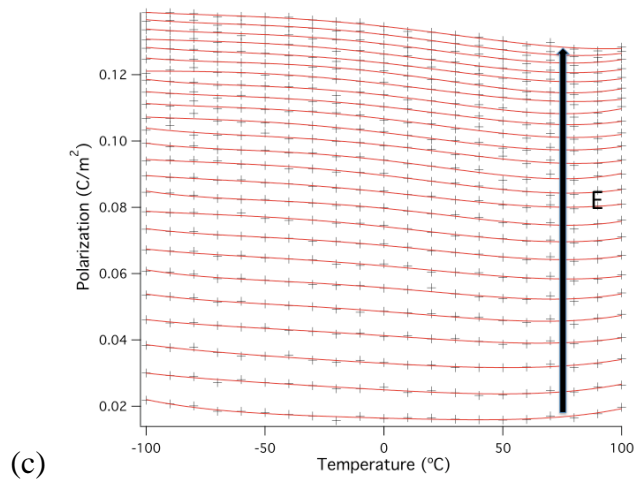
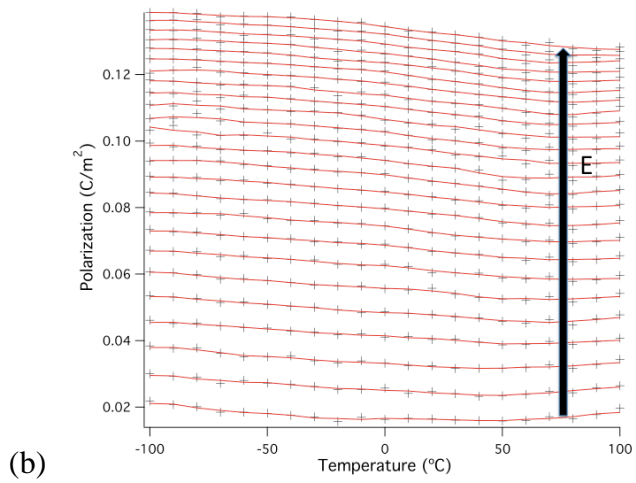
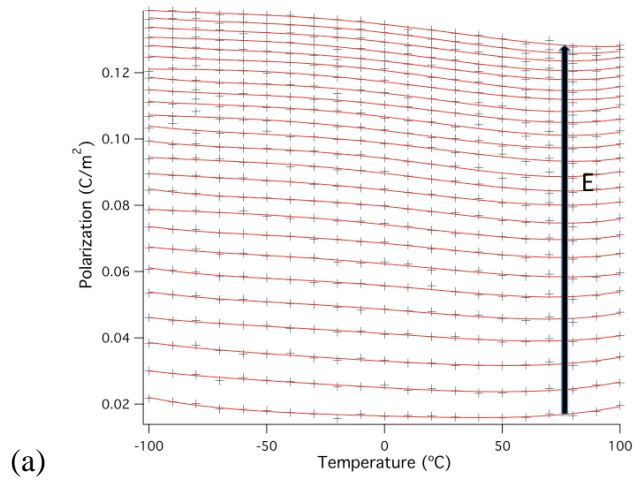
Guyomar *et al.* published reservations towards the indirect method in 2006 [30], but despite this, the same group found indirect method predictions to “reasonably” agree (within  $\sim 40\%$ ) with direct calorimetry measurements for PMN-PT [27, 29]. It may be worth noting that their loops were relatively slow, at 1 Hz, compared to the majority of loop frequencies quoted in the literature, which are most often at 1 kHz. Good agreement between indirect method predictions and direct measurements was also seen by Luo *et al.* [12] comparing their indirect results with one of the aforementioned papers by Sebald *et al.* [27]. Two papers [14, 21] recognise the equilibrium issue, but suggest possible validity of  $\Delta T$  predictions, including ergodicity in one case, despite there being no evidence to support that. Lu *et al.* [10] found that their direct measurements and indirect method predictions on ferroelectric polymers differed greatly, concluding a lack of ergodicity and that the indirect method was ineffective.

The indirect method applied to the two PMN-PT samples studied here, results in a significantly wider variation in  $\Delta T$  predictions, compared to the earlier results on PZT, where variations reach 79.4% of the maximum, reliable  $\Delta T$  predictions, for that sample.

### 3.4.1. 225 NM THICK



**Figure 3-74. 225 nm thick PMN-PT. (a) Second quadrant data from P(E) loops (250 points) measured from -100 °C to 100 °C in 10 °C steps. Loop frequency, 100 Hz (10 ms period). (b) P(E,T). 3D view of the same data.**



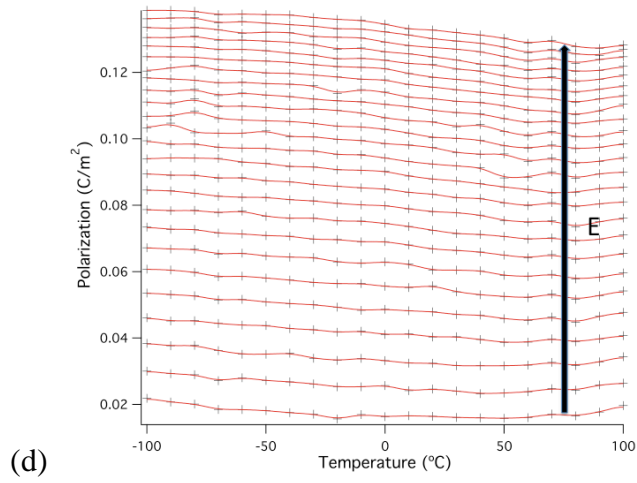
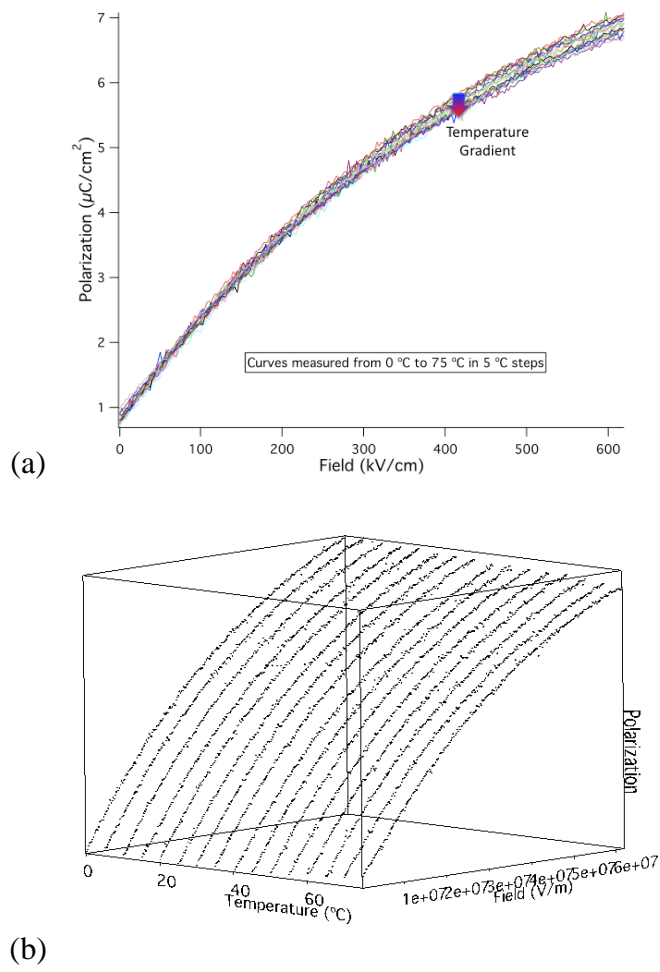
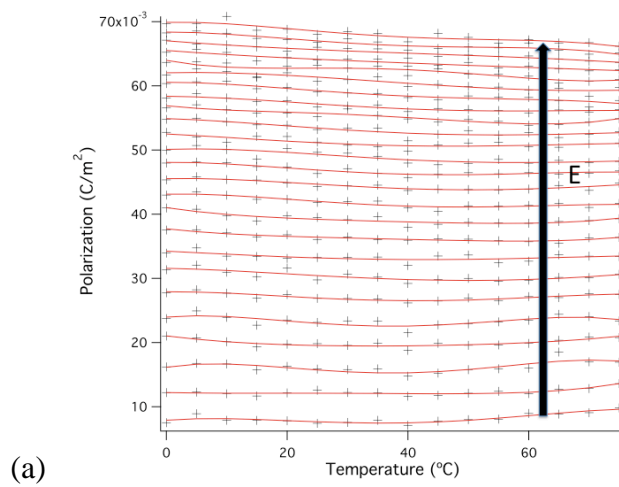
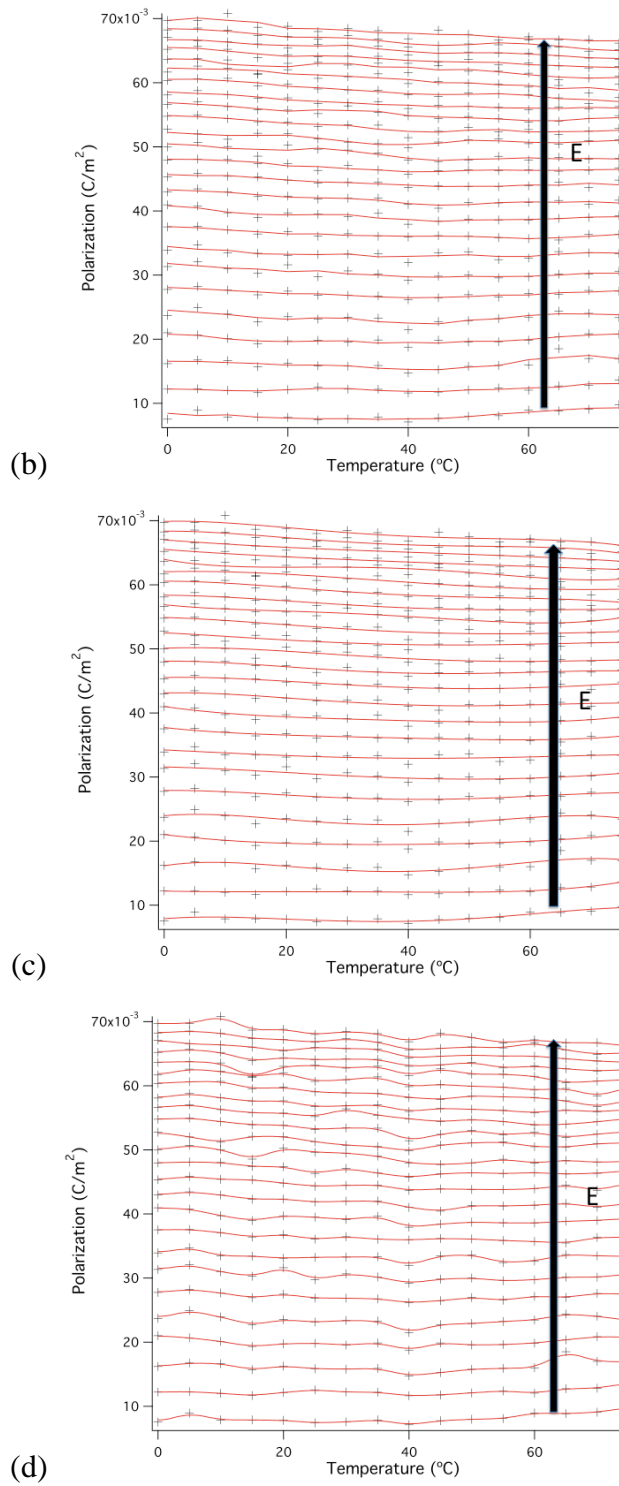


Figure 3-75. 225 nm thick PMN-PT.  $P(T)$ . Red lines represent alternatives to isofield black data points. (a) 4<sup>th</sup> order polynomial fit. (b) Three-point boxcar smoothing. (c) 4<sup>th</sup> order polynomial fit OIP (d) 15-point boxcar smoothing OIP. Data measured as  $P(E)$  from -100 °C to 100 °C in 10 °C steps.

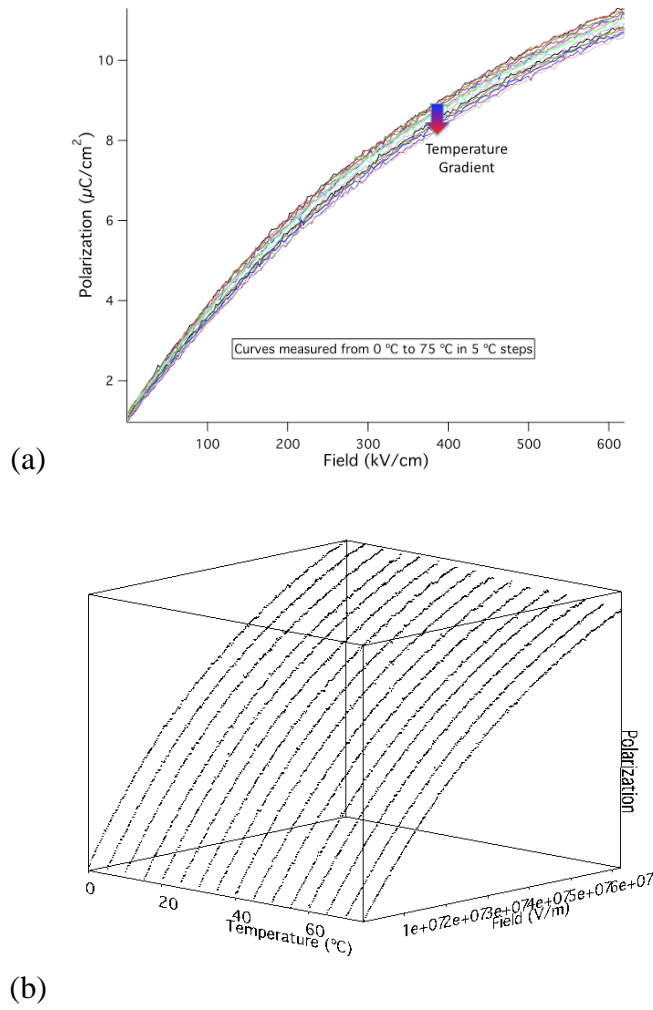


**Figure 3-76. 225 nm thick PMN-PT. (a) Second quadrant data from P(E) loops (250 points) measured from 0 °C to 75 °C in 5 °C steps. Loop frequency, 1kHz (1 ms period). (b) P(E,T). 3D view of the same data.**

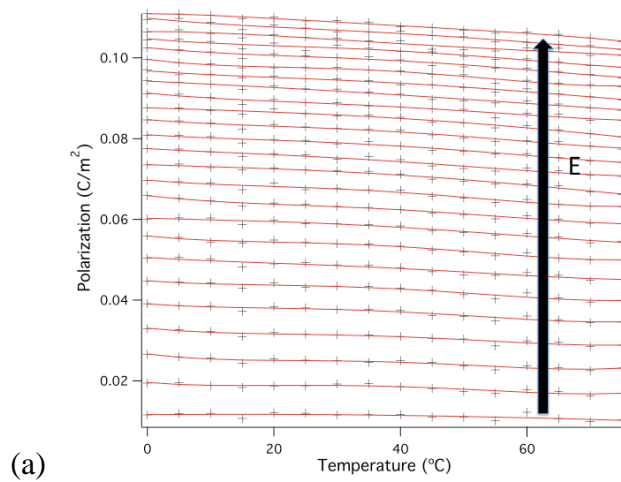




**Figure 3-77. 225 nm thick PMN-PT.  $P(T)$ . Red lines represent alternatives to isofield black data points. (a) 4<sup>th</sup> order polynomial fit. (b) Three-point boxcar smoothing. (c) 4<sup>th</sup> order polynomial fit OIP. (d) 15-point boxcar smoothing OIP. Data measured as  $P(E)$  from 0 °C to 75 °C in 5 °C steps.**



**Figure 3-78. 225 nm thick PMN-PT. (a) Second quadrant data from P(E) loops (250 points) measured from 0 °C to 75 °C in 5 °C steps. Between each loop measurement, the sample was taken up to 200 °C before being cooled to the next measurement temperature. Loop frequency, 1kHz (1 ms period). (b) P(E,T). 3D view of the same data.**



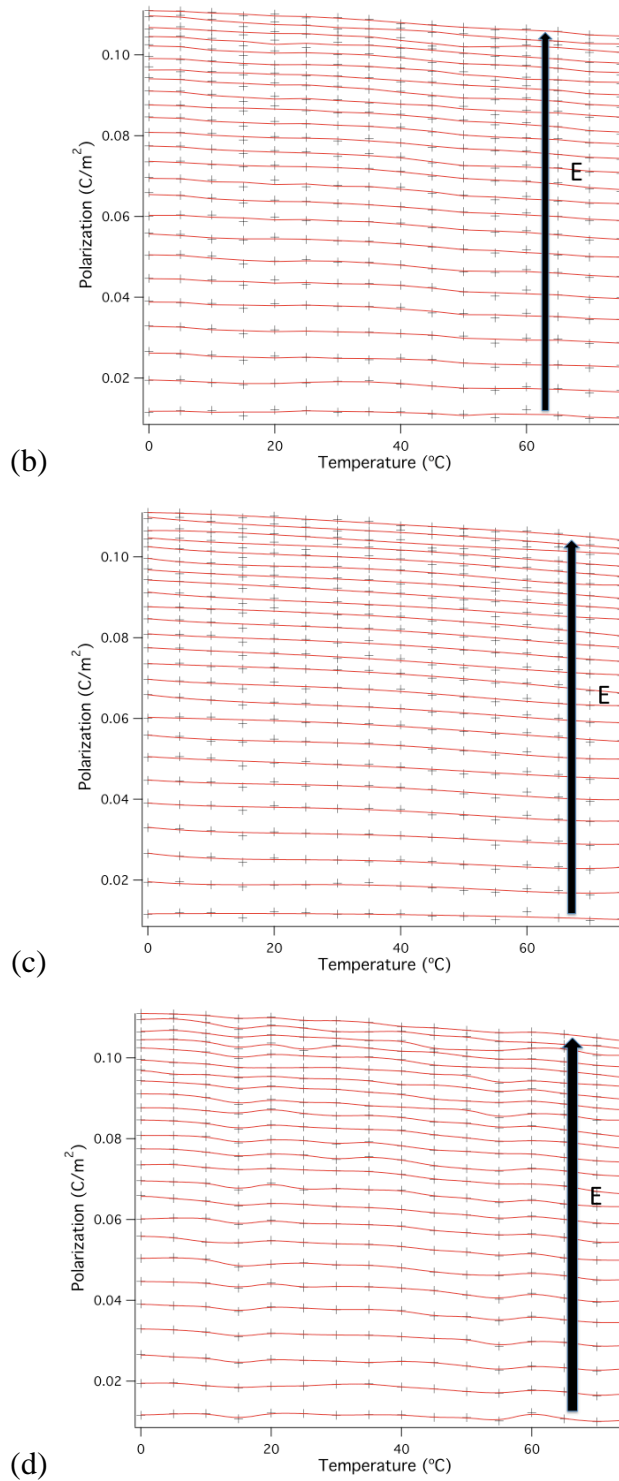


**Figure 3-79. 225 nm thick PMN-PT.  $P(T)$ . Red lines represent alternatives to isofield black data points. (a) 4<sup>th</sup> order polynomial fit. (b) Three-point boxcar smoothing. (c) 4<sup>th</sup> order polynomial fit OIP. (d) 15-point boxcar smoothing OIP. Data measured as  $P(E)$  from 0 °C to 75 °C in 5 °C steps. Between each loop measurement, the sample was taken up to 200 °C before being cooled to the next measurement temperature.**

The difference between the last two datasets is indicated in the above figure caption. In the last dataset, the first loop was measured at 0 °C, as in the previous dataset, but then the sample was heated to 200 °C and subsequently cooled to the next highest measurement temperature and the process of heating to 200 °C and cooled repeated, with the idea that this may remove thermal hysteresis effects. For this reason, this dataset is referred to as ‘0-75Hyst 1kHz’ in the following graphs.

A comparison between the  $\Delta T$  predictions follows:

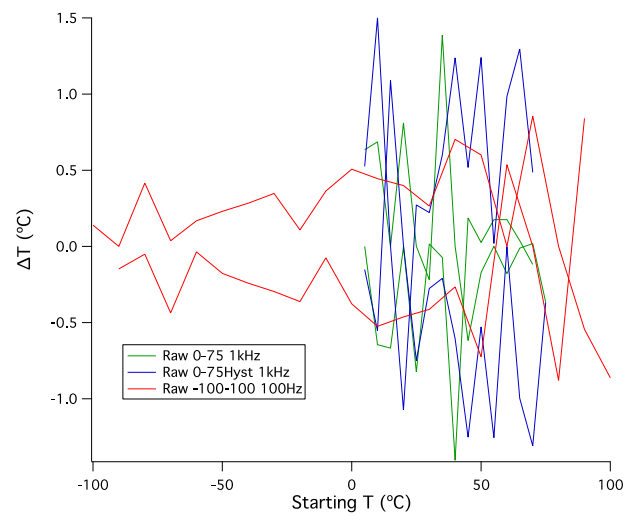


**Figure 3-80. 225 nm thick PMN-PT. Electrocaloric heating and cooling predictions for three datasets from raw data. Calculations from measurement temperatures only.**

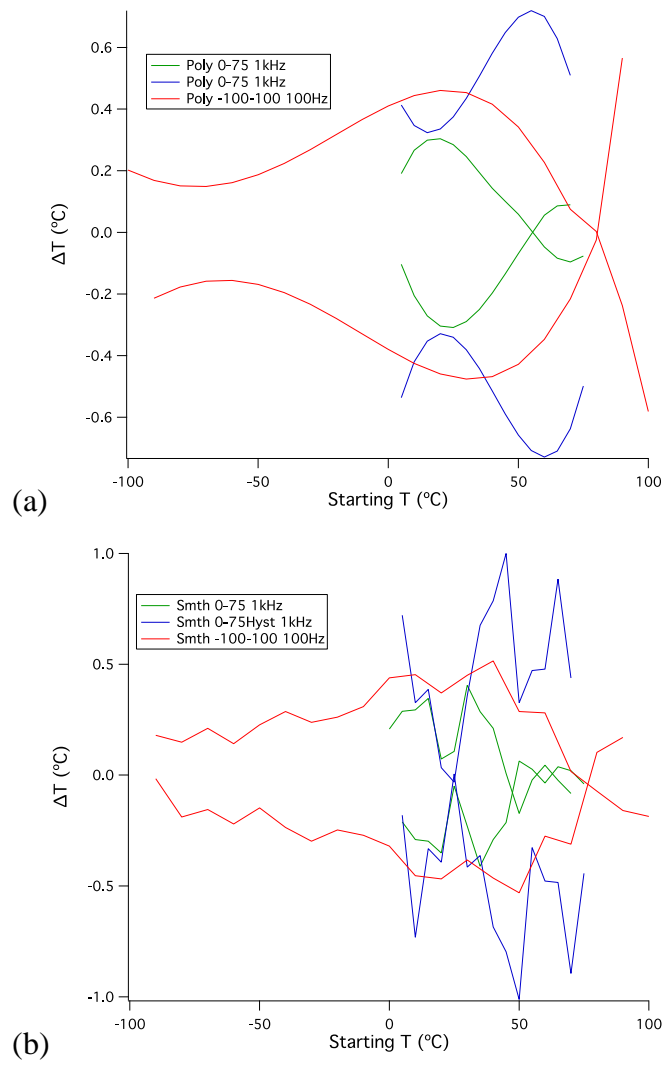


**Figure 3-81. 225 nm thick PMN-PT. Electrocaloric heating and cooling predictions for three datasets from (a) polynomial fits to and (b) boxcar smoothing of raw P(T) data. Calculations from measurement temperatures only.**

	COOLING		HEATING	
	Peak change (°C)	At (°C)	Peak change (°C)	At (°C)
<i>0-75 °C in 5 °C steps. 1 kHz.</i>				
Raw data	-1.40	40.00	1.39	35.00
Polynomial fit	-0.31	25.00	0.30	20.00
Smoothed	-0.41	35.00	0.41	30.00
<i>0-75 °C in 5 °C steps – excursion to temperatures above <math>T_c</math> between each measurement. 1 kHz.</i>				
Raw data	-1.31	70.00	1.50	10.00
Polynomial fit	-0.73	60.00	0.72	55.00
Smoothed	-1.01	50.00	1.00	45.00
<i>-100-100 °C in 10 °C steps. 100 Hz.</i>				
Raw data	-0.88	80.00	0.86	70.00
Polynomial fit	-0.48	30.00	0.46	20.00
Smoothed	-0.53	50.00	0.51	40.00

**Table 19. Peak electrocaloric cooling and heating predictions in 225 nm thick PMN-PT from three datasets, where calculations were made from measurement temperatures only.**

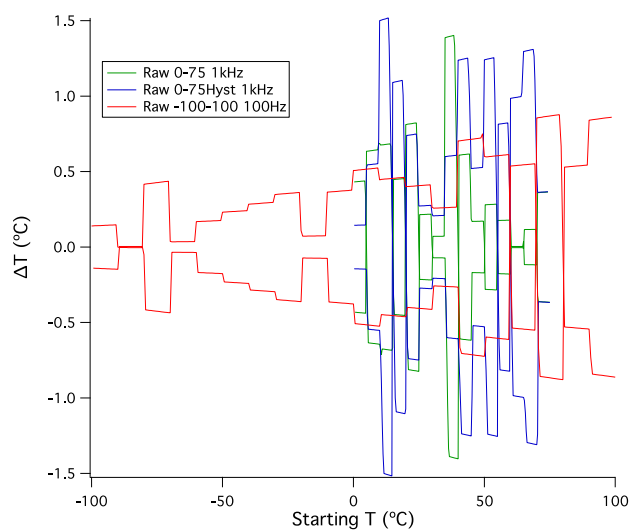


**Figure 3-82. 225 nm thick PMN-PT. Electrocaloric heating and cooling predictions for three datasets from raw data. Calculations from measurement temperatures and additional intermediate temperatures.**

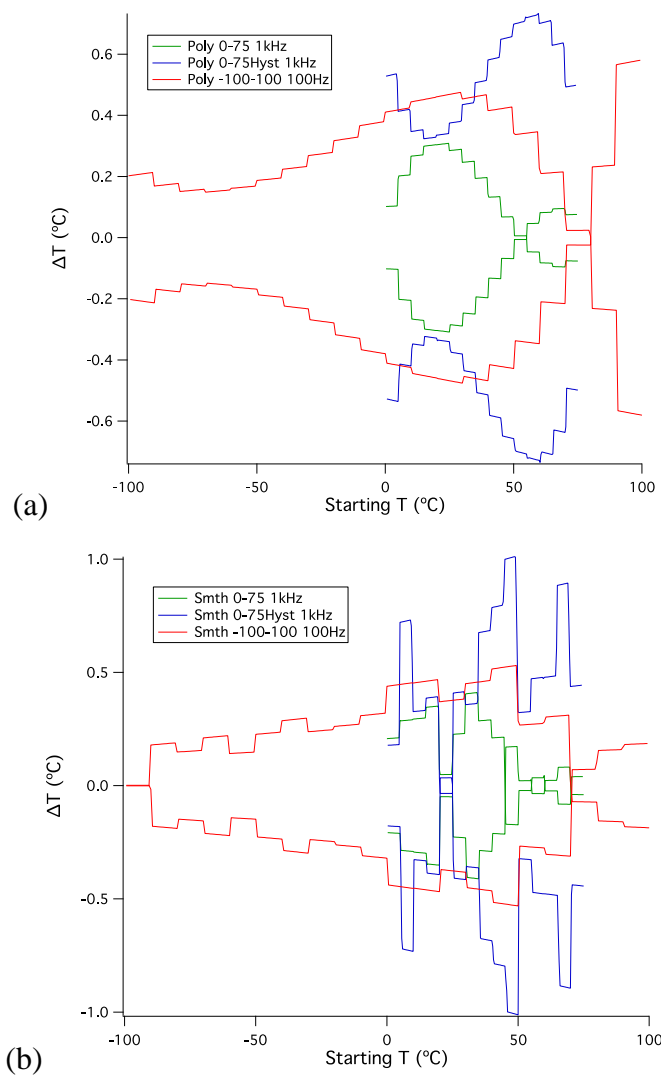


**Figure 3-83. 225 nm thick PMN-PT. Electrocaloric heating and cooling predictions for three datasets from (a) polynomial fits to and (b) boxcar smoothing of raw P(T) data. Calculations from measurement temperatures and additional intermediate temperatures.**

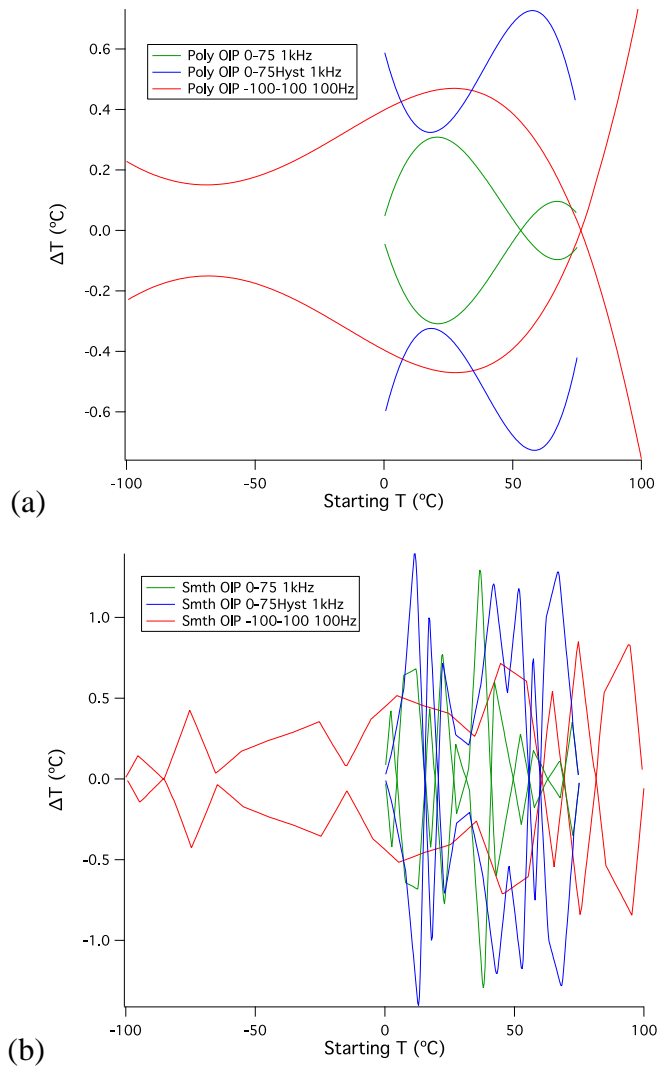
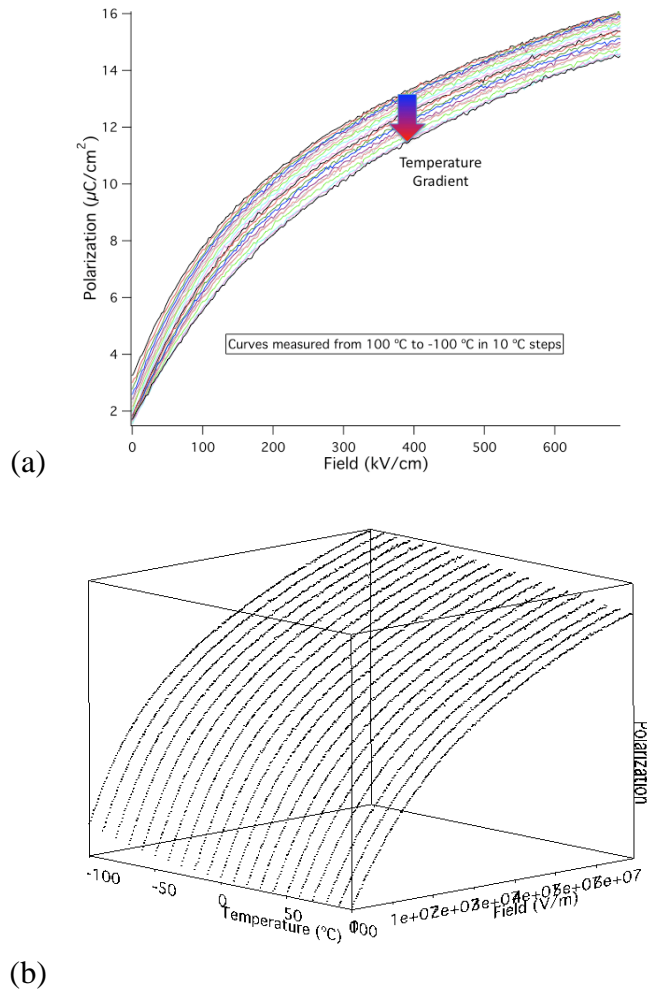


**Figure 3-84. 225 nm thick PMN-PT. Electrocaloric heating and cooling predictions for three datasets from (a) polynomial OIP fits to and (b) boxcar smoothing OIP of raw P(T) data. Calculations from measurement temperatures and additional intermediate temperatures.**

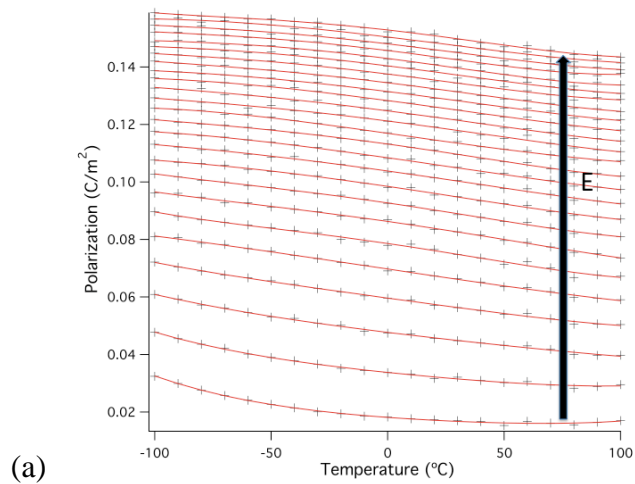
	COOLING		HEATING	
	<i>Peak change (°C)</i>	<i>At (°C)</i>	<i>Peak change (°C)</i>	<i>At (°C)</i>
<i>0-75 °C in 5 °C steps. 1 kHz.</i>				
Raw data	-1.40	40.00	1.40	38.33
Polynomial fit	-0.31	25.00	0.31	24.67
Smoothed	-0.41	35.00	0.41	34.33
Polynomial fit OIP	-0.31	21.00	0.31	20.67
Smoothed OIP	-1.29	38.00	1.29	36.67
<i>0-75 °C in 5 °C steps – excursion to temperatures above <math>T_c</math> between each measurement. 1 kHz.</i>				
Raw data	-1.52	14.67	1.52	13.33
Polynomial fit	-0.74	60.33	0.73	59.67
Smoothed	-1.01	50.00	1.01	48.67
Polynomial fit OIP	-0.73	58.33	0.73	57.67
Smoothed OIP	-1.40	13.00	1.40	11.67
<i>-100-100 °C in 10 °C steps. 100 Hz.</i>				
Raw data	-0.88	80.00	0.88	78.67
Polynomial fit	-0.48	30.00	0.48	29.33
Smoothed	-0.53	50.00	0.53	49.33
Polynomial fit OIP	-0.47	28.00	0.47	27.33
Smoothed OIP	-0.84	95.33	0.85	74.67

**Table 20. Peak electrocaloric cooling and heating predictions in 225 nm thick PMN-PT from three datasets, where calculations were made from measurement temperatures and additional intermediate temperatures.**

### 3.4.2. 700 NM THICK



**Figure 3-85. 700 nm thick PMN-PT. (a) Second quadrant data from P(E) loops (250 points) measured from 100 °C to -100 °C in 10 °C steps. Loop frequency, 1kHz (1 ms period). (b) P(E,T). 3D view of the same data.**



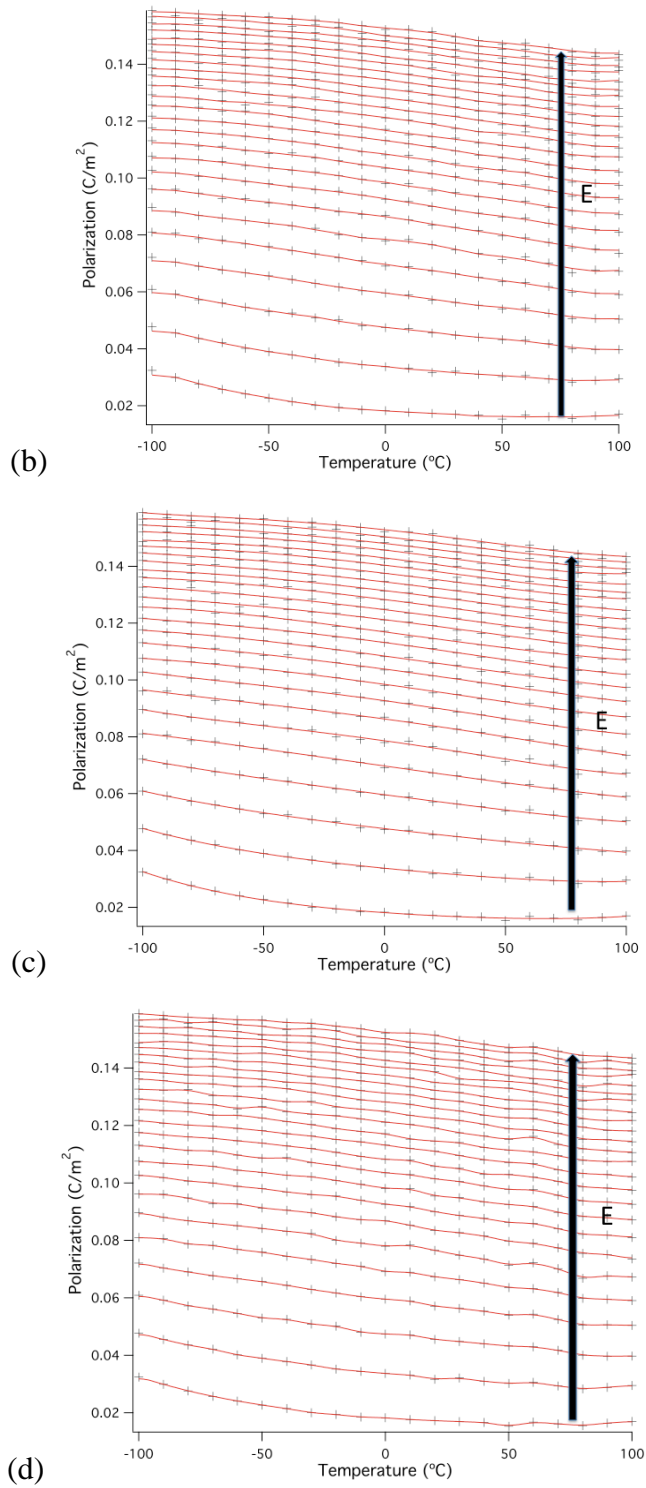


**Figure 3-86. 700 nm thick PMN-PT.  $P(T)$ . Red lines represent alternatives to isofield black data points. (a) 4<sup>th</sup> order polynomial fit. (b) Three-point boxcar smoothing. (c) 4<sup>th</sup> order polynomial fit OIP. (d) 15-point boxcar smoothing OIP. Data measured as  $P(E)$  from 100 °C to -100 °C in 10 °C steps.**

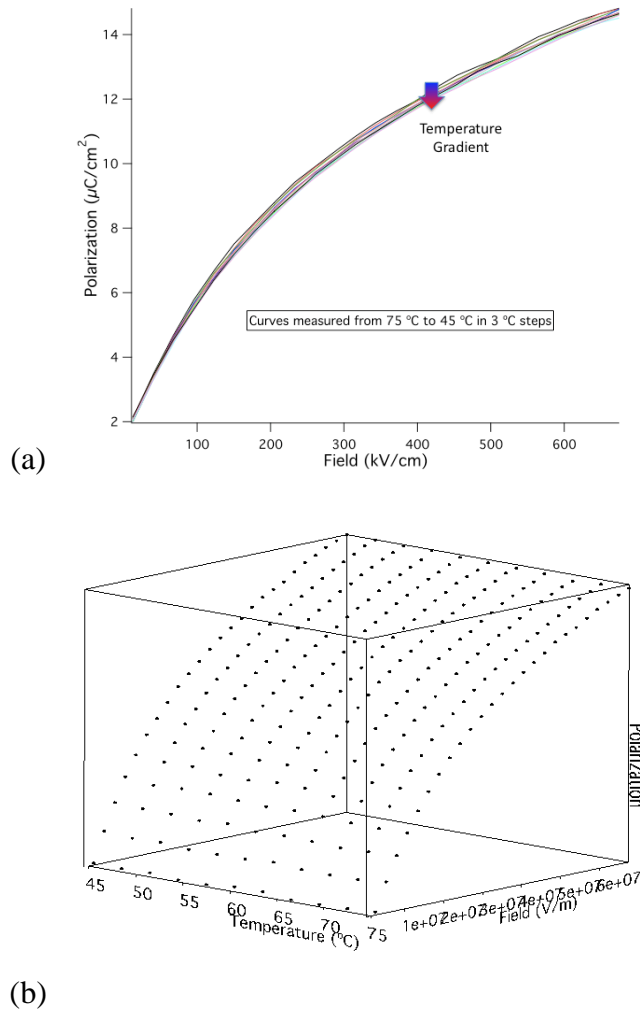
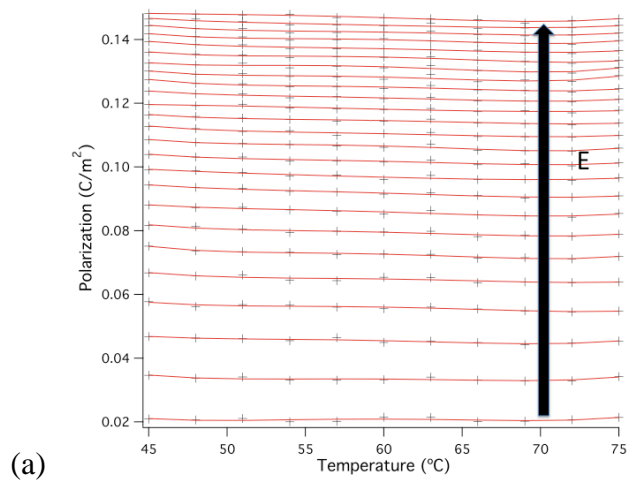
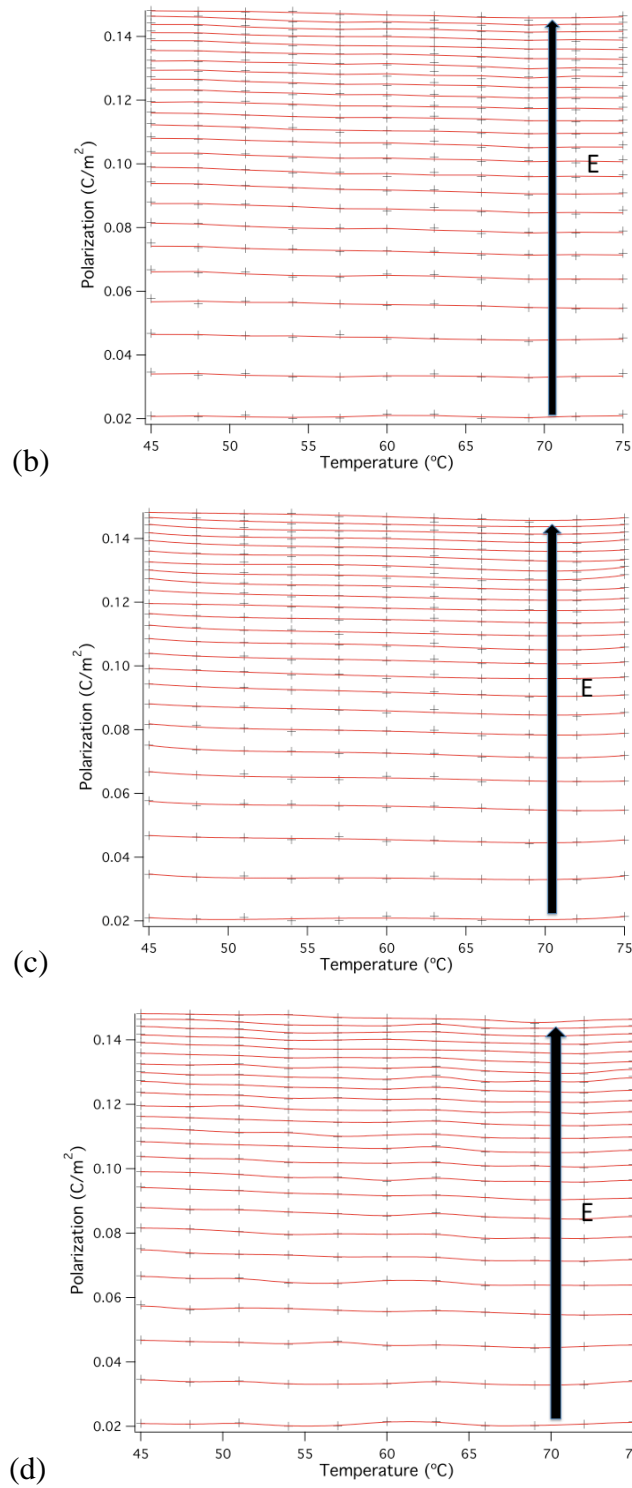
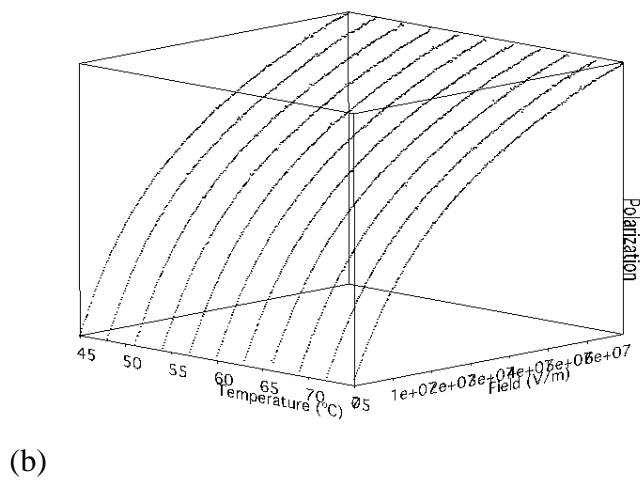
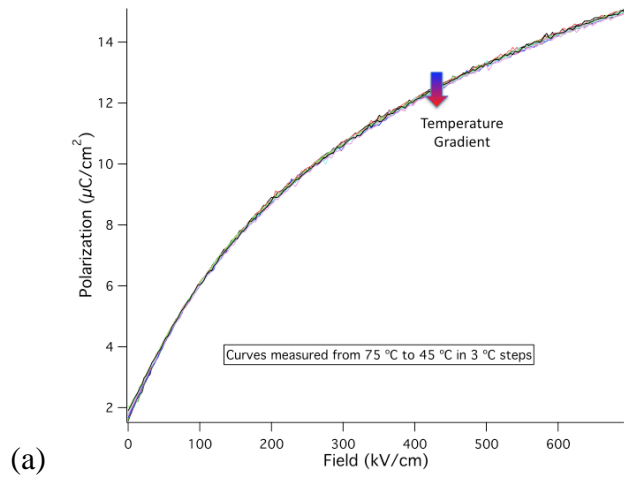


Figure 3-87. 700 nm thick PMN-PT. (a) Second quadrant data from P(E) loops (25 points) measured from 75 °C to 45 °C in 5 °C steps. Loop frequency, 10kHz (0.1 ms period). (b) P(E,T). 3D view of the same data.

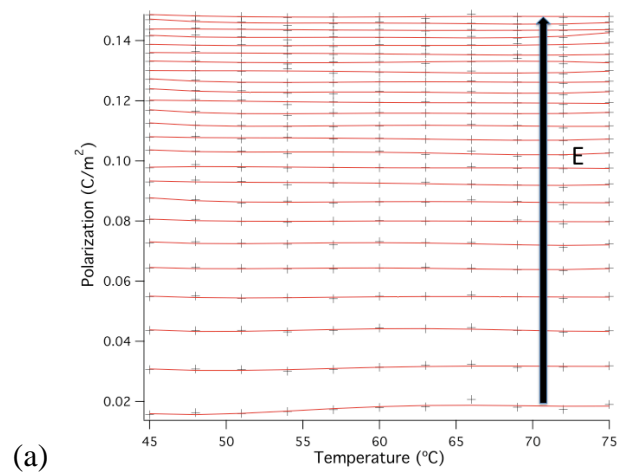




**Figure 3-88. 700 nm thick PMN-PT. From 10 kHz loops.  $P(T)$ . Red lines represent alternatives to isofield black data points. (a) 4<sup>th</sup> order polynomial fit. (b) Three-point boxcar smoothing. (c) 4<sup>th</sup> order polynomial fit OIP. (d) 15-point boxcar smoothing OIP. Data measured as  $P(E)$  from 75 °C to 45 °C in 5 °C steps.**



**Figure 3-89. 700 nm thick PMN-PT. (a) Second quadrant data from P(E) loops (250 points) measured from 75 °C to 45 °C in 5 °C steps. Loop frequency, 1kHz (1 ms period). (b) P(E,T). 3D view of the same data.**



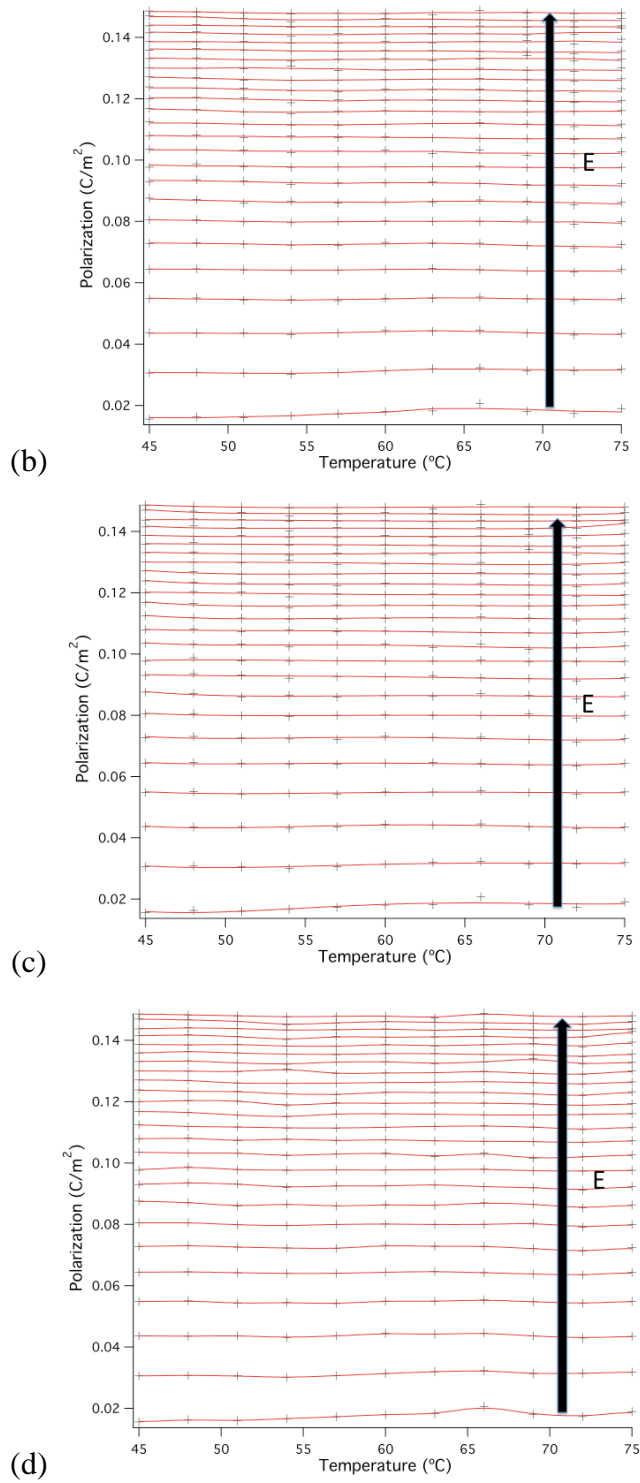


**Figure 3-90. 700 nm thick PMN-PT. From 1 kHz loops.  $P(T)$ . Red lines represent alternatives to isofield black data points. (a) 4<sup>th</sup> order polynomial fit. (b) Three-point boxcar smoothing. (c) 4<sup>th</sup> order polynomial fit OIP. (d) 15-point boxcar smoothing OIP. Data measured as  $P(E)$  from 75 °C to 45 °C in 5 °C steps.**

A comparison between the  $\Delta T$  predictions follows:

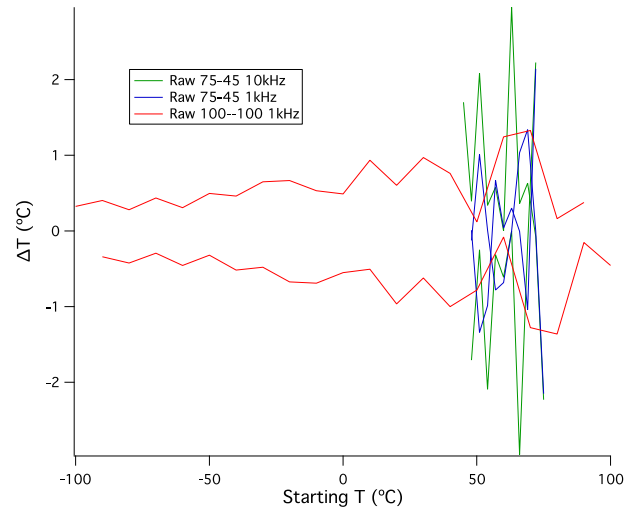


**Figure 3-91. 700 nm thick PMN-PT. Electrocaloric heating and cooling predictions for three datasets from raw data. Calculations from measurement temperatures only.**

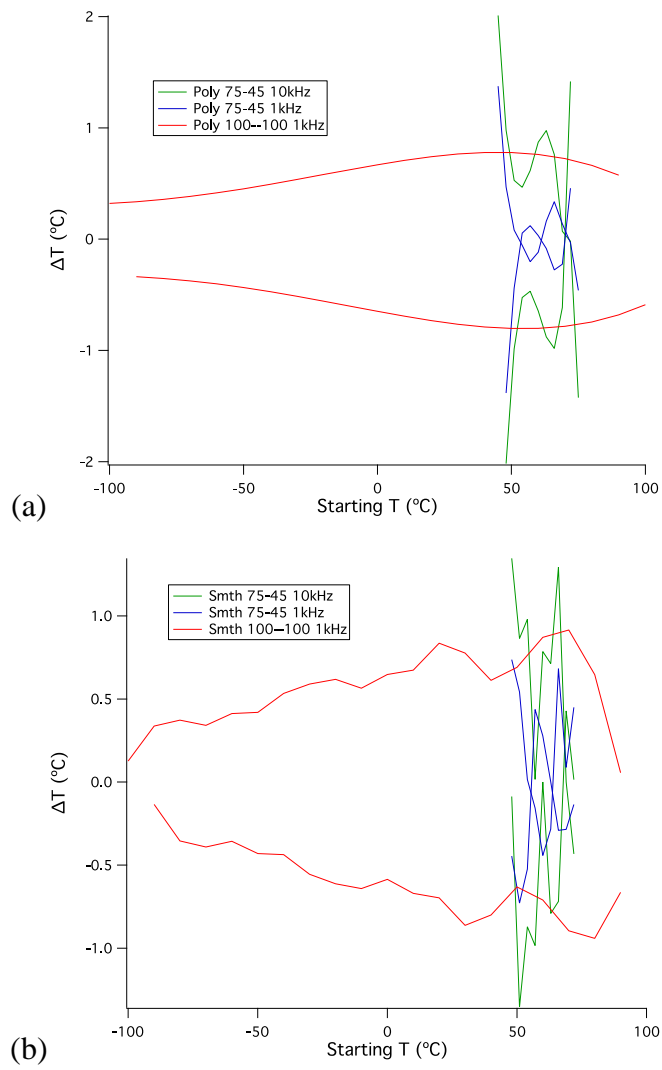


**Figure 3-92. 700 nm thick PMN-PT. Electrocaloric heating and cooling predictions for three datasets from (a) polynomial fits to and (b) boxcar smoothing of raw P(T) data. Calculations from measurement temperatures only.**

	COOLING		HEATING	
	Peak change (°C)	At (°C)	Peak change (°C)	At (°C)
<i>75-45 °C in 3 °C steps. 10 kHz.</i>				
Raw data	-2.96	66.00	2.96	63.00
Polynomial fit	-0.98	66.00	0.98	63.00
Smoothed	-1.35	51.00	1.35	48.00
<i>75-45 °C in 3 °C steps. 1 kHz.</i>				
Raw data	-1.34	51.00	1.34	69.00
Polynomial fit	-0.28	66.00	0.34	66.00
Smoothed	-0.73	51.00	0.74	48.00
<i>100 to -100 °C in 10 °C steps. 1 kHz.</i>				
Raw data	-1.36	80.00	1.33	70.00
Polynomial fit	-0.80	50.00	0.78	40.00
Smoothed	-0.94	80.00	0.92	70.00

**Table 21. Peak electrocaloric cooling and heating predictions in 700 nm thick PMN-PT from three datasets, where calculations were made from measurement temperatures only.**

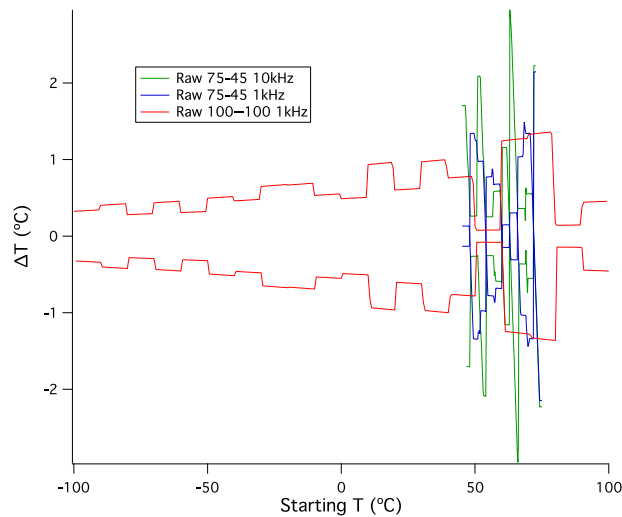


**Figure 3-93. 700 nm thick PMN-PT. Electrocaloric heating and cooling predictions for three datasets from raw data. Calculations from measurement temperatures and additional intermediate temperatures.**

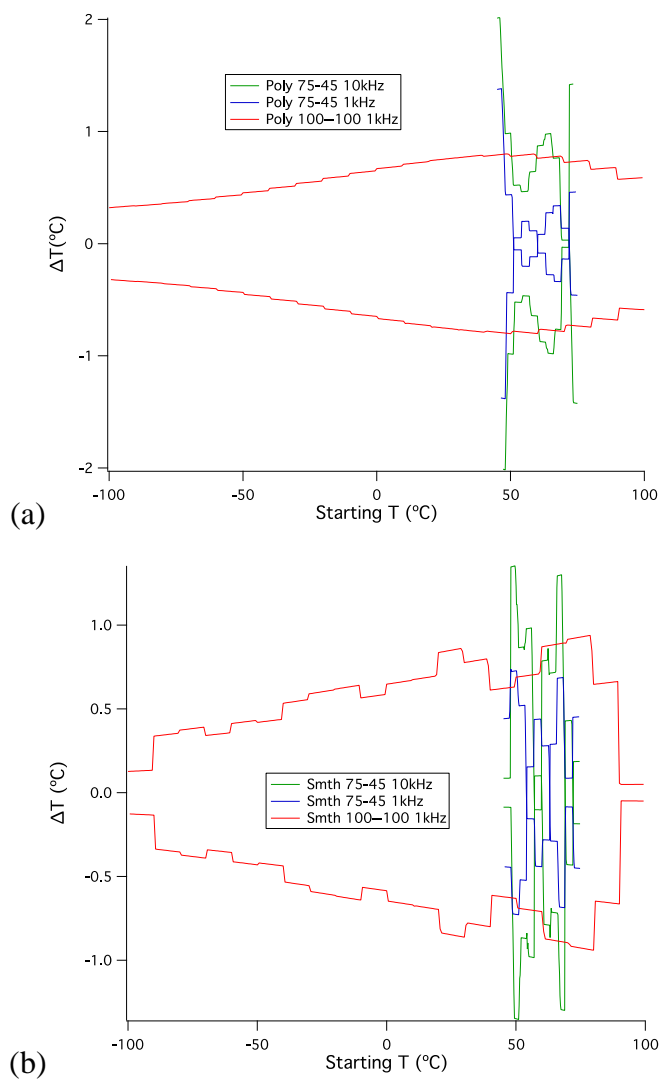


**Figure 3-94. 700 nm thick PMN-PT. Electrocaloric heating and cooling predictions for three datasets from (a) polynomial fits to and (b) boxcar smoothing of raw P(T) data. Calculations from measurement temperatures and additional intermediate temperatures.**

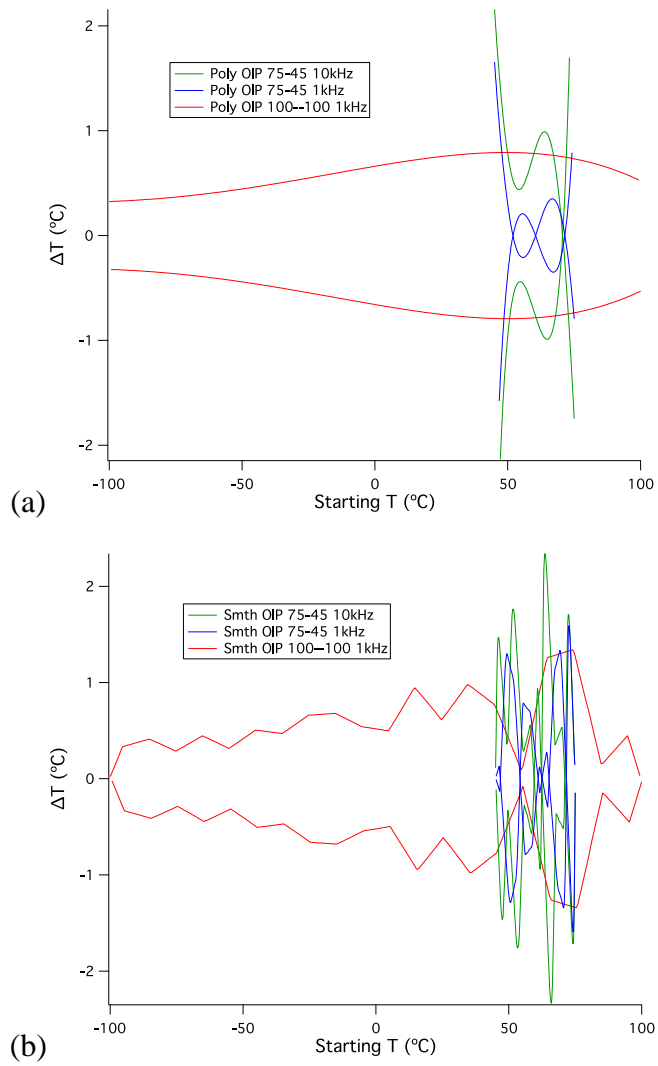


**Figure 3-95. 700 nm thick PMN-PT. Electrocaloric heating and cooling predictions for three datasets from (a) polynomial fits OIP to and (b) boxcar smoothing OIP of raw P(T) data. Calculations from measurement temperatures and additional intermediate temperatures.**

	COOLING		HEATING	
	<i>Peak change (°C)</i>	<i>At (°C)</i>	<i>Peak change (°C)</i>	<i>At (°C)</i>
<i>75-45 °C in 3 °C steps. 10 kHz.</i>				
Raw data	-2.96	66.00	2.96	63.00
Polynomial fit	-0.93	66.20	0.98	65.00
Smoothed	-1.35	51.00	1.35	49.60
Polynomial fit OIP	-0.99	64.80	0.99	63.80
Smoothed OIP	-2.34	66.00	2.34	63.60
<i>75-45 °C in 3 °C steps. 1 kHz.</i>				
Raw data	-1.44	69.80	1.49	68.40
Polynomial fit	-0.34	68.80	0.34	68.60
Smoothed	-0.73	51.00	0.74	48.00
Polynomial fit OIP	-0.35	67.20	0.35	66.80
Smoothed OIP	-1.59	74.20	1.71	72.40
<i>100 to -100 °C in 10 °C steps. 1 kHz.</i>				
Raw data	-1.36	80.00	1.36	78.00
Polynomial fit	-0.80	50.00	0.80	48.67
Smoothed	-0.94	80.00	0.94	78.67
Polynomial fit OIP	-0.79	50.00	0.79	49.33
Smoothed OIP	-1.34	75.33	1.34	74.00

**Table 22. Peak electrocaloric cooling and heating predictions in 700 nm thick PMN-PT from three datasets, where calculations were made from measurement temperatures and additional intermediate temperatures.**

### 3.4.3. PEAK $\Delta T$ PREDICTIONS

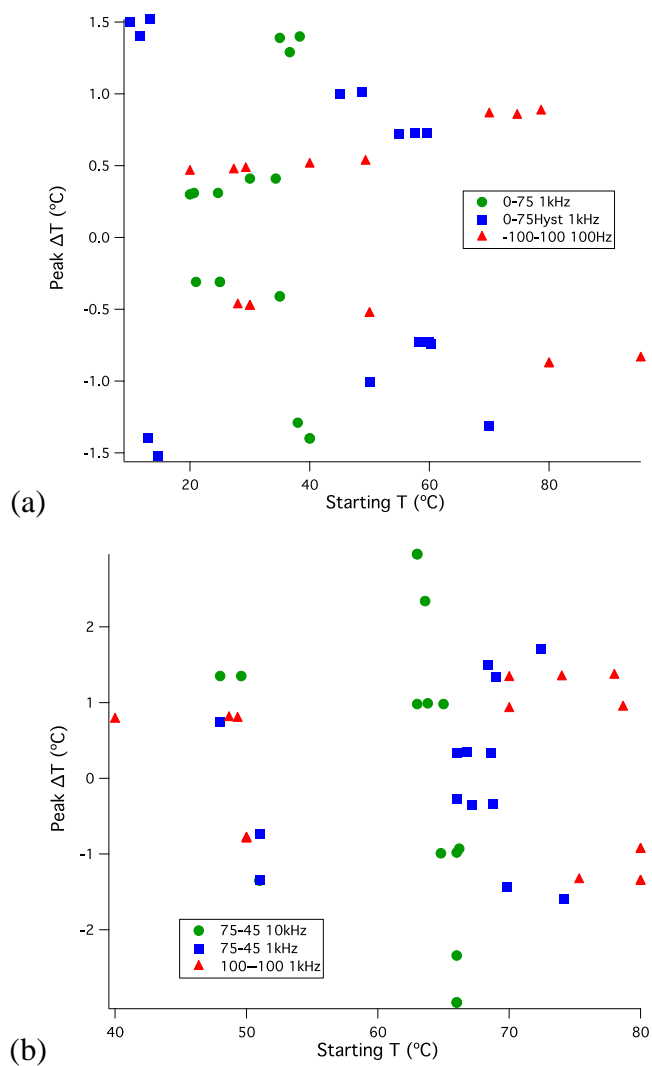
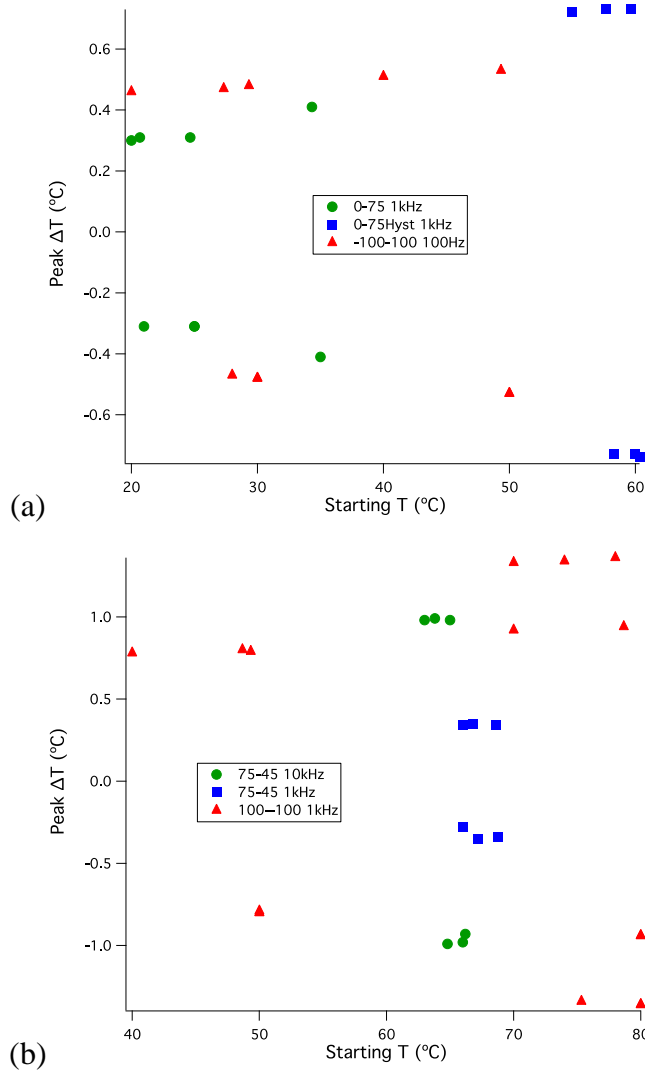


Figure 3-96. Peak  $\Delta T$  as a function of starting temperature, for (a) three 225 nm sample datasets and (b) three 700 nm sample datasets.



**Figure 3-97. As above figure, excluding values from erratic  $\Delta T$  curves.**

The data measured on the two PMN-PT sample were less well-behaved compared to the PZT data and the isofield progression of  $P(T)$  was less clear. Hence, there were more alternative  $P(T)$  options that led to  $\Delta T$  results that fluctuated greatly as a function of starting temperature and could be considered dubious. The excluded  $\Delta T$  sets for the 225 nm PMN-PT sample are all those from raw data, all from smoothed OIP data and from standard smoothing in the '0-75 kHz' and '0-75Hyst 1kHz' datasets. In the case of the 700 nm sample,  $\Delta T$  calculations from raw data and all smoothing operations were ignored from the '75-45 10kHz' and '75-45 1kHz' datasets. The following tables summarise the extent to which  $\Delta T$  predictions vary.

	<i>Largest peak <math>\Delta T</math> spread (°C)</i>	<i>Largest peak <math>\Delta T</math> spread in % terms of its largest peak <math>\Delta T</math></i>	<i>Largest peak <math>\Delta T</math> starting temperature spread (°C)</i>	<i>Average peak <math>\Delta T</math> spread (°C)</i>	<i>Average peak <math>\Delta T</math> spread in % terms of its largest peak <math>\Delta T</math></i>	<i>Average peak <math>\Delta T</math> starting temperature spread (°C)</i>
<i>225 nm sample: considering the three individual datasets</i>						
Eight alternative sets of predictions	1.10	78.6	67.33	0.77	59.2	45.00
Smoothly varying predictions	0.11	26.8	30.00	0.06	13.1	15.72

**Table 23. Peak  $\Delta T$  prediction variation. 225 nm PMN-PT.**

	<i>Largest peak <math>\Delta T</math> spread (°C)</i>	<i>Largest peak <math>\Delta T</math> spread in % terms of its largest peak <math>\Delta T</math></i>	<i>Largest peak <math>\Delta T</math> starting temperature spread (°C)</i>	<i>Average peak <math>\Delta T</math> spread (°C)</i>	<i>Average peak <math>\Delta T</math> spread in % terms of its largest peak <math>\Delta T</math></i>	<i>Average peak <math>\Delta T</math> starting temperature spread (°C)</i>
<i>700 nm sample: considering the three individual datasets</i>						
Eight alternative sets of predictions	2.03	82.4	38.67	1.31	63.8	25.70
Smoothly varying predictions	0.58	42.6	38.67	0.22	23.4	12.91

**Table 24. Peak  $\Delta T$  prediction variation. 700 nm PMN-PT.**

The above two tables follow the same format and meaning as established with the PZT results. It is clear from the peak  $\Delta T$  graphs how the predictions are far more dispersed, though one must take into account the much smaller values. In relative terms, the peak  $\Delta T$  values are far more varied, compared to the PZT results, whereas the starting temperature spreads are quite similar.

**Ignoring dubious  $\Delta T$  predictions, the analysis method alone accounts for a variation in peak  $\Delta T$  results that can represent up to 42.6% of its largest peak  $\Delta T$  prediction, over a 38.67 °C range of starting temperatures.**

	<i>Peak <math>\Delta T</math> spread (°C)</i>	<i>Peak <math>\Delta T</math> spread in % terms of its largest peak <math>\Delta T</math></i>	<i>Peak <math>\Delta T</math> starting temperature spread (°C)</i>
<i>225 nm sample: over all datasets.</i>			
Eight alternative sets of predictions	1.22	80.3	82.33
Smoothly varying predictions	0.57	64.8	40.33
<i>700 nm sample: over all datasets.</i>			
Eight alternative sets of predictions	2.68	90.5	38.67
Smoothly varying predictions	1.08	79.4	38.67

**Table 25. Peak  $\Delta T$  prediction variation. PMN-PT.**

**When considering all  $\Delta T$  predictions for each sample, over the same voltage range per sample, the reliable  $\Delta T$  results for the 225 nm sample can cover up to 64.8% of the largest  $\Delta T$  prediction, over a 40.33 °C range of starting temperatures, while for the 700 nm sample, that percentage rises to 79.4%, over a 38.67 °C range of starting temperatures.**

## 4. APPLICABILITY OF THERMODYNAMICS

### 4.1. THERMODYNAMIC BEHAVIOUR

The last chapter presented much  $P(E, T)$  data and many electrocaloric temperature change predictions using the indirect method, finding that much variation is possible just by the way one decides to treat the data and that when many datasets measured on the same, small sample of material are considered, predicted  $\Delta T$  can vary by up to 35%, for PZT.

The underlying and most important question from the point of view of this author, is whether or not it is justifiable to apply the thermodynamically based indirect method to electrocaloric predictions in ferroelectrics. The fundamental issues that precede the practical deduction of temperature changes via the indirect method, are whether or not the material passes through equilibrium points during loop measurement and the extent of the reversibility of that process. Dragan Damjanovic has done much to study the reversibility of ferroelectrics [63-66], but even if those questions were answered, it remains to be seen how well predictions from the indirect method fare against direct measurements. To date, far too little has been published on that topic for any conclusions to have been drawn.

Curiously, if one delves deeper into the indirect method, several further conditions are found, that a  $P(E, T)$  surface must meet in order for it to be thermodynamic, which can be tested just by looking at the data itself. This is where the four equivalent  $dT$  equations describing isentropic temperature changes due to the electrocaloric effect, derived at the end of chapter 2, become useful. They are presented again, below:

(4.1)

$$dT = - \left( \frac{T}{c} \right)_{E_0} \left( \frac{\partial P}{\partial T} \right)_{E_0} dE_0$$

(4.2)

$$dT = \left( \frac{T}{c} \right)_P \left( \frac{\partial E_0}{\partial T} \right)_P dP$$

(4.3)

$$dT = \left(\frac{T}{c}\right)_P \left(\frac{\partial E}{\partial T}\right)_P dP$$

(4.4)

$$dT = -\left(\frac{T}{c}\right)_E \left(\frac{\partial P}{\partial T}\right)_E dE$$

If the assumptions upon which the indirect method are based are correct, then these four  $dT$  equations are equivalent at each point on a thermodynamic  $P(E, T)$  surface. In the electrocaloric literature,  $c_E$ ,  $c_{E_0}$  and  $c_P$  have traditionally been taken as constant over isentropic temperature and field changes, but when one considers any given point on the  $P(E, T)$  surface, which represents a specific state of the system, the volumetric heat capacity, or any type of heat capacity, can only have one value for that state, so  $c_E$ ,  $c_{E_0}$  and  $c_P$  are identical at any given point on the  $P(E, T)$  surface. This simplifies the equivalence to the following:

(4.5)

$$-\left(\frac{\partial P}{\partial T}\right)_{E_0} dE_0 = \left(\frac{\partial E_0}{\partial T}\right)_P dP = \left(\frac{\partial E}{\partial T}\right)_P dP = -\left(\frac{\partial P}{\partial T}\right)_E dE$$

There is a very helpful illustration that can be used in this situation. In the infinite capacitor model implicit in the thermodynamic treatment,  $D = \epsilon_0 E_0 = \text{surface charge density on one electrode}$ . This surface charge density is made up of two other surface charge densities:  $\epsilon_0 E + P$ , which can be pictured as follows:

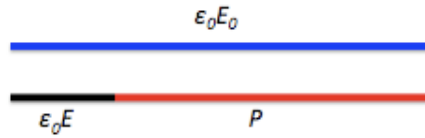


Figure 4-1. Relative charge densities on one capacitor electrode.

where the length of each line is proportional to the surface charge density that each quantity represents. So first of all, it can be seen from the above figure that:

(4.6)

$$\left(\frac{\partial E}{\partial T}\right)_P = \left(\frac{\partial E_0}{\partial T}\right)_P$$

As when one holds  $P$ , i.e. the length of the red line representing  $P$  remains unchanged, then any change in  $\varepsilon_0 E_0$  will be equal to the change in  $\varepsilon_0 E$  and the change in  $E_0$  will be the same as the change in  $E$ . So this can reduce equation 4.5 to:

(4.7)

$$\left(\frac{\partial E}{\partial T}\right)_P dP = -\left(\frac{\partial P}{\partial T}\right)_{E_0} dE_0 = -\left(\frac{\partial P}{\partial T}\right)_E dE$$

This expression can be simplified to:

(4.8)

$$ax = by = cz$$

where

$$a = \left(\frac{\partial E}{\partial T}\right)_P, x = dP, b = -\left(\frac{\partial P}{\partial T}\right)_{E_0}, y = dE_0, c = -\left(\frac{\partial P}{\partial T}\right)_E, z = dE$$

As  $\varepsilon_0 E_0 = \varepsilon_0 E + P$ , then  $E_0 = E + \frac{P}{\varepsilon_0}$ , so equation 4.7 can be rewritten:

(4.9)

$$\left(\frac{\partial E}{\partial T}\right)_P dP = -\left(\frac{\partial P}{\partial T}\right)_{E_0} d\left(E + \frac{P}{\varepsilon_0}\right) = -\left(\frac{\partial P}{\partial T}\right)_E dE$$

or

(4.10)

$$ax = bz + (bx/\varepsilon_0) = cz$$

Therefore:

(4.11)

$$z = \frac{ax}{c} = \left(\frac{a}{b} - \frac{1}{\varepsilon_0}\right)x$$

and

(4.12)

$$\frac{a}{c} = \frac{a}{b} - \frac{1}{\varepsilon_0}$$

or

(4.13)

$$\frac{1}{\varepsilon_0 a} = \frac{1}{b} - \frac{1}{c}$$

or

(4.14)

$$\frac{1}{\varepsilon_0} \left(\frac{\partial T}{\partial E}\right)_P = \left(\frac{\partial T}{\partial P}\right)_E - \left(\frac{\partial T}{\partial P}\right)_{E_0}$$

Any  $P(E, T)$  surface that is to be analysed by the indirect method, must comply with the above equation. Besides this, there are two things that can be deduced logically. The first is that  $\left(\frac{\partial P}{\partial T}\right)_{E_0}$  and  $\left(\frac{\partial P}{\partial T}\right)_E$  have the same sign. Whether one holds  $E_0$  or  $E$ ,  $P$  changes in the same direction with rising  $T$ . For example, if dealing with a dielectric or ferroelectric,  $P$  will decrease with temperature. If  $E_0$  is held by keeping the charge on the electrodes constant, for example by disconnecting a charged capacitor from the battery, or if  $E$  is kept constant by reducing the charge on the electrodes as  $T$  goes up and  $P$  goes down, either way,  $P$  decreases with temperature. In the case of PZT, for example, where there is a phase transition from antiferroelectric to ferroelectric with rising temperature for zinc concentrations above 90%, at around 180 °C,  $P$  can increase with temperature, but then again, it increases whether  $E_0$  or  $E$  is held constant. So  $\left(\frac{\partial P}{\partial T}\right)_{E_0}$  and  $\left(\frac{\partial P}{\partial T}\right)_E$  have the same sign.

The second thing to note is that  $\left(\frac{\partial E}{\partial T}\right)_P$  has the opposite sign to  $\left(\frac{\partial P}{\partial T}\right)_E$ . Taking a ferroelectric or dielectric again, consider  $\left(\frac{\partial E}{\partial T}\right)_P$ . As  $P$  drops with rising temperature, then in order to maintain  $P$  constant, one needs to raise  $E$  as the temperature rises, so this gradient is positive. The second gradient,  $\left(\frac{\partial P}{\partial T}\right)_E$ , as explained in the last paragraph, is negative under these conditions. It is straightforward to see that in the case where  $P$  increases with rising temperature, the same arguments apply, but the other way round. So the signs of  $\left(\frac{\partial P}{\partial T}\right)_E$  and  $\left(\frac{\partial E}{\partial T}\right)_P$  are always opposite.

Finally, coming back to equation 4.14, the two gradients on the right-hand side of the equation thus have the same sign, which is opposite to the sign of the gradient on the left-hand side of the equation. In order for this equation to be true, the magnitude of  $\left(\frac{\partial T}{\partial P}\right)_{E_0}$  must be larger than that of  $\left(\frac{\partial T}{\partial P}\right)_E$ .

These conditions can be exploited by evaluating whether or not they are met on any measured  $P(E, T)$  surface, indicating the suitability of a surface for  $\Delta T$  calculations.

## 4.2. A SEARCH FOR VALID DATASETS

The programming facility of the graphing and analysis software, Igor Pro, was used to define functions (see appendix D) that would go through a set of  $P(E, T)$  data, point by point, testing for these three conditions and whether or not equation 4.14 was satisfied.  $dT$  is the same for each point, being taken as next highest temperature, less the temperature of the point in question.  $dT$  can be cancelled through and  $(\partial P)_E$ ,  $(\partial P)_{E_0}$  and  $(\partial E)_P$  are then calculated over that temperature interval, in exactly the same way as  $\left(\frac{\partial P}{\partial T}\right)_E$  is assessed in indirect method calculations, i.e. forward-difference differentiation. Thus, the equation was put in the form:

(4.15)

$$(\partial P)_E = 1 / \left( \left( \frac{1}{\varepsilon_0 \partial E} \right)_P + \left( \frac{1}{\partial P} \right)_{E_0} \right)$$

and the results of the two sides were compared and deemed to be the same if they agreed within  $2 \times 10^{-6} \text{ C/m}^2$ .  $P$  is measured to a precision of  $\pm 5 \times 10^{-7} \text{ C/m}^2$ , so  $dP$  has a tolerance of  $\pm 10^{-6} \text{ C/m}^2$ , which would apply to the left-hand side. As for the right-hand side,  $\varepsilon_0$  reduces the measurement error of  $E$ , taking an exact film thickness and considering the voltage measurement precision of  $\pm 5 \times 10^{-5} \text{ V}$ , to a negligible level, even for the smallest  $(\partial E)_P$  and regardless of the relevant film thicknesses. This leaves the precision of  $dP$  as the only applicable tolerance and the comparison of the two sides of the equation was between two  $dP$  values, which could differ by up to  $2 \times 10^{-6} \text{ C/m}^2$ .

The results of these tests are shown in the table below:

	<i>Met three conditions?</i>					<i>Agreed with equation?</i>				
	<i>Raw</i>	<i>Poly</i>	<i>Smth</i>	<i>POIP</i>	<i>SOIP</i>	<i>Raw</i>	<i>Poly</i>	<i>Smth</i>	<i>POIP</i>	<i>SOIP</i>
<i>PZT 95/05</i>										
45-285 °C. 5 °C steps	Yes	Yes	Yes	Yes	Yes	Yes	Yes	Yes	Yes	Yes
45-285 °C. 20 °C steps	Yes	Yes	Yes	Yes	Yes	No	No	No	Yes	Yes
45-285 °C. 30 °C steps	Yes	Yes	Yes	Yes	Yes	No	No	No	Yes	Yes
211-275 °C. 1 °C steps	Yes	Yes	Yes	Yes	Yes	Yes	Yes	Yes	Yes	Yes
230-280 °C. 5 °C steps	No	No	No	No	No	No	No	No	No	No
275-215 °C. 3 °C steps	No	No	No	No	No	No	No	No	No	No
275-211 °C. 4 °C steps	Yes	Yes	Yes	Yes	Yes	Yes	Yes	Yes	Yes	Yes
285-45 °C. 20 °C steps	Yes	Yes	Yes	Yes	Yes	No	No	No	Yes	Yes
300-200 °C. 10 °C steps	Yes	Yes	Yes	Yes	Yes	No	No	Yes	Yes	Yes
1000 nm Slow Cool	Yes	Yes	Yes	Yes	Yes	No	No	No	Yes	Yes
1100 nm Fast Cool	No	Yes	Yes	Yes	Yes	No	Yes	Yes	Yes	Yes
<i>PMN-PT 225 nm</i>										
0-75 °C. 5 °C steps	No	No	No	No	No	No	No	No	No	No
0-75 °C. Hys 5 °C steps	No	No	No	No	No	No	No	No	No	No
-100-100 °C. 10 °C st	No	No	No	No	No	No	No	No	No	No
<i>PMN-PT 700 nm</i>										
75-45 °C 10kHz. 5°C st	Yes	Yes	Yes	Yes	Yes	Yes	Yes	Yes	Yes	Yes
75-45 °C 1kHz. 5°C st	No	No	No	No	No	No	No	No	No	No
100—100 °C. 10 °C st	No	No	No	No	No	No	No	No	No	No

**Table 26. Indirect method conditions test - pass or fail.**

The above table covers all the datasets presented in this thesis. The raw data of each was tested, along with the manipulated data, referred to by the column headings. “Raw” is obviously raw data, “Poly” and “Smth” refer to the raw data  $P(E, T)$  surface being adjusted by polynomial fits to and smoothing of the  $P(T)$  at different  $E$ , while “POIP” and “SOIP” refer to polynomial fits over intermediate  $P(T)$  points and smoothing over intermediate points, respectively.

For many datasets, the three conditions were met, but for the raw data and some adaptations of that, the data did not agree with the equation. The simplest way to deal with that is to ignore the  $\Delta T$  predictions from those sets of information. There are, however, many datasets that do not pass any of the tests and the one thing they have in common is that there are 250 points per second loop quadrant, i.e. the data that make up the  $P(E, T)$  surface, has 250 data points at each temperature, as opposed to 25 in all other datasets. This is because the data were taken more slowly. To clarify, a data point was measured once every microsecond in most cases, but for the 250 data point second loop quadrant data, an entire loop was measured in 1 or 10 ms, as opposed to 0.1 ms, for the 25 point data case. This means that one gains much more real information in the 250 point case. On inspection, it is clear why these datasets are failing the tests, as is shown in the following graphs:

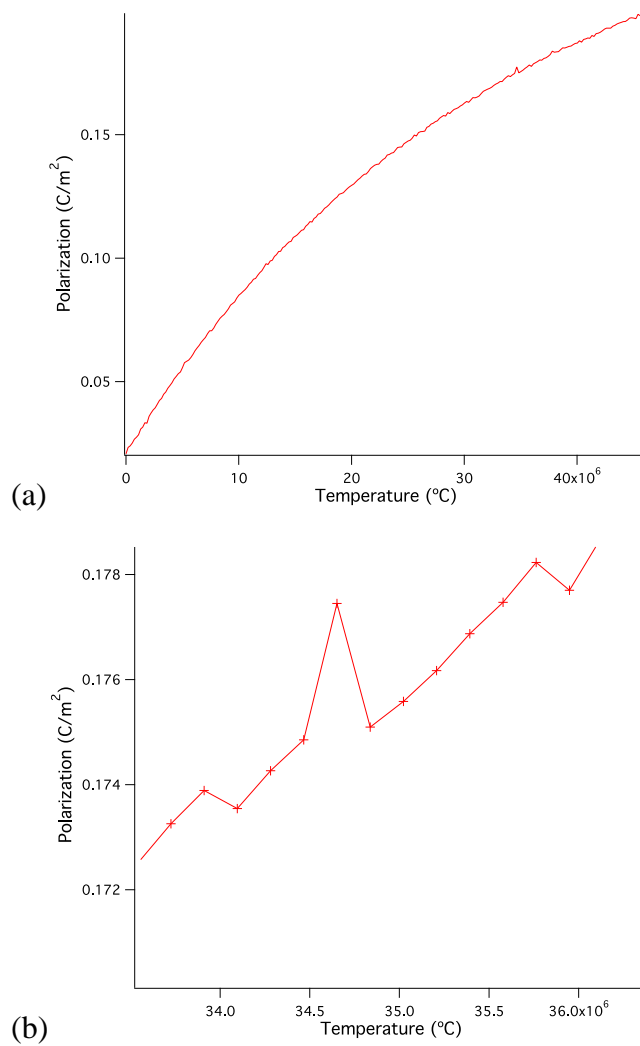


**Figure 4-2. (a)  $P(E)$  from 230-280 °C dataset. Branch taken at 270 °C. Data points are not marked by crosses, but only joined by lines, due to their quantity, that would obscure their progression. (b) Close-up of spurious data point.**

Graph (a), in the above figure, contains 250 measured points and though the shape of this second quadrant of the measured hysteresis loop is clear, the odd point is an outlier to the general shape, as shown in graph (b), where  $P$  values are measured as being higher than other  $P$  values at higher field. This will cause the  $P(E, T)$  surface to fail the conditions necessary for thermodynamic interpretation with the indirect method. Specifically, as  $E_0$  is calculated as a function of  $E$  and  $P$ , a spurious value of  $P$  can be large enough to cause

$E_0$  to be larger than  $E_0$  at higher  $E$  values, resulting in  $\left(\frac{\partial P}{\partial T}\right)_{E_0}$  being of opposite sign to  $\left(\frac{\partial P}{\partial T}\right)_E$ , failing the first three conditions and consequently not agreeing with the equation.

Why would there be these spurious values of  $P$ ? Is it a limitation of the ferroelectric tester, or perhaps just an accurate measure of reality, where the material varies in its polarization, over time, with  $P$  being occasionally measured at an extreme limit of oscillating values of  $P$ , which varies at the nanosecond scale?

A program was written that takes all the  $P$  values at one temperature and tries to adjust the  $P$  values at the next highest temperature and so on, to make all the points on the  $P(E, T)$  surface comply with equation 4.15. This, however, proved to be a very tricky task, as  $(\partial P)_E$ ,  $(\partial P)_{E_0}$  and  $(\partial E)_P$  all depend on ALL the  $P$  values at the next highest temperature. Recursive programs of many sorts were tried, but to no avail. In the end, by simply deleting some intermediate  $P(E)$  values, leaving a total of 25  $P(E)$ , roughly equally spread values, as with the other dataset branches, were the  $P(E, T)$  surfaces with 250 points per temperature branch able to be reduced to 25 points and agree with the necessary conditions and equality of the indirect method. The kind of improvement, in terms of the indirect method, in data, can be seen by looking at the same  $P(E)$  branch as presented in fig. 4-2, that has been reduced to 25 points, below:

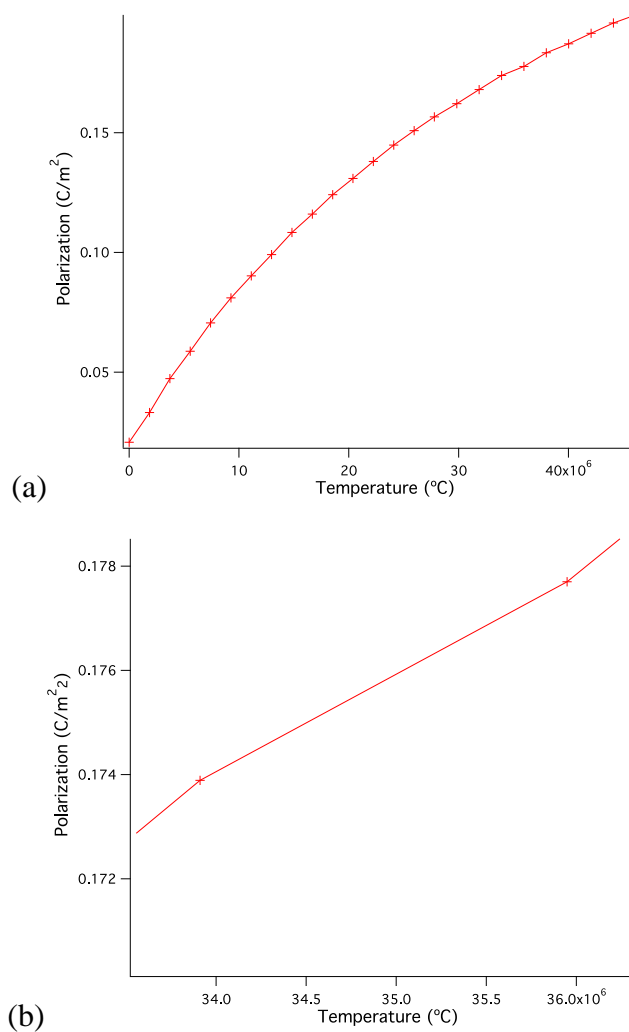


**Figure 4-3. (a) P(E) from 230-280 °C dataset. Branch taken at 270 °C. (b) Close-up of region shown in graph (b), fig. 4-2.**

In the above figure, one can see how  $P$  is always larger at higher  $E$ , thus not suffering from the same problems as the 250 point branch datasets, when being assessed for compliance with the indirect method conditions. In fact, when reassessing the 250 point branch datasets, when reduced to 25 points per branch, all except the raw data of the 230-280 °C dataset, passed the tests. This changes the spread of  $\Delta T$  predictions and their starting temperatures, most importantly for the comparisons across many datasets measured over the same voltage ranges. In terms of the 1000SC and 1100FC PZT 95/05 datasets, the 1000SC predictions are reduced to cooling between -25.38 °C and -27.38 °C

at 224.85 °C and 235.38 °C, respectively, or heating between 25.37 °C and 27.32 °C at 199.27 °C and 208.30 °C, respectively, while the 1100FC predictions are hardly affected.

The spread of the starting temperatures of the peak  $\Delta T$  predictions, when comparing the data across the 230-280 °C and 275-215 °C datasets, which were measured at the same electrode, on the same day, does not change, though the peak  $\Delta T$  values drop from being 21.5% of the maximum  $\Delta T$  prediction, to 19.0%. This change is relevant, but insignificant.

The new  $\Delta T$  curves, from the datasets reduced from 250 points per temperature branch to 25 points, are shown in the following figures:

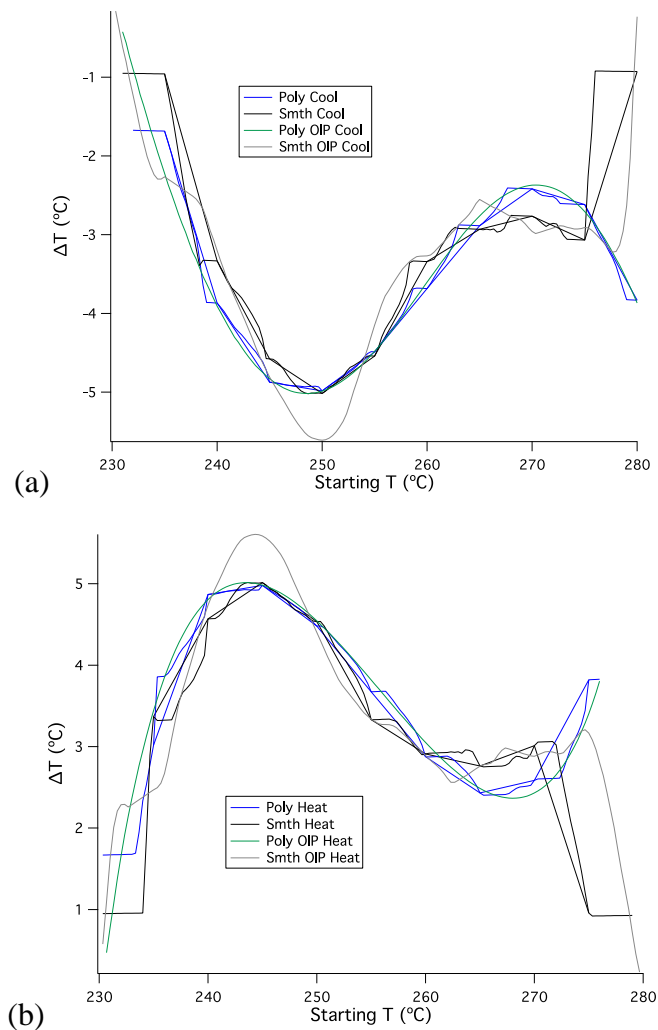


**Figure 4-4. (a) Cooling predictions and (b) Heating predictions for 230-280 °C dataset measured on PZT 95/05.**

The peak “Smth OIP” data sits noticeably outside the rest of the predictions, but nonetheless varies smoothly and is worthy of consideration for this reason.

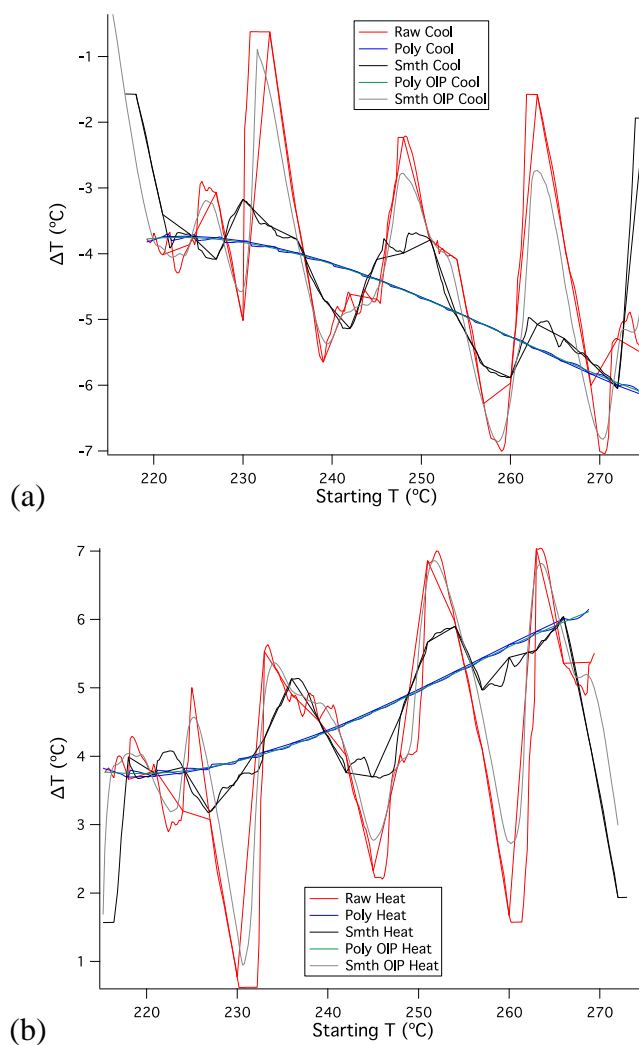


**Figure 4-5. (a) Cooling predictions and (b) Heating predictions for 275-215 °C dataset measured on PZT 95/05.**

Looking at the effect these re-calculated values have on the spread of peak  $\Delta T$  predictions for the 50 V PZT datasets, the following graph compares the more conservative assessments of such predictions before and after the improvement of the datasets, with respect to their validity for the indirect method.

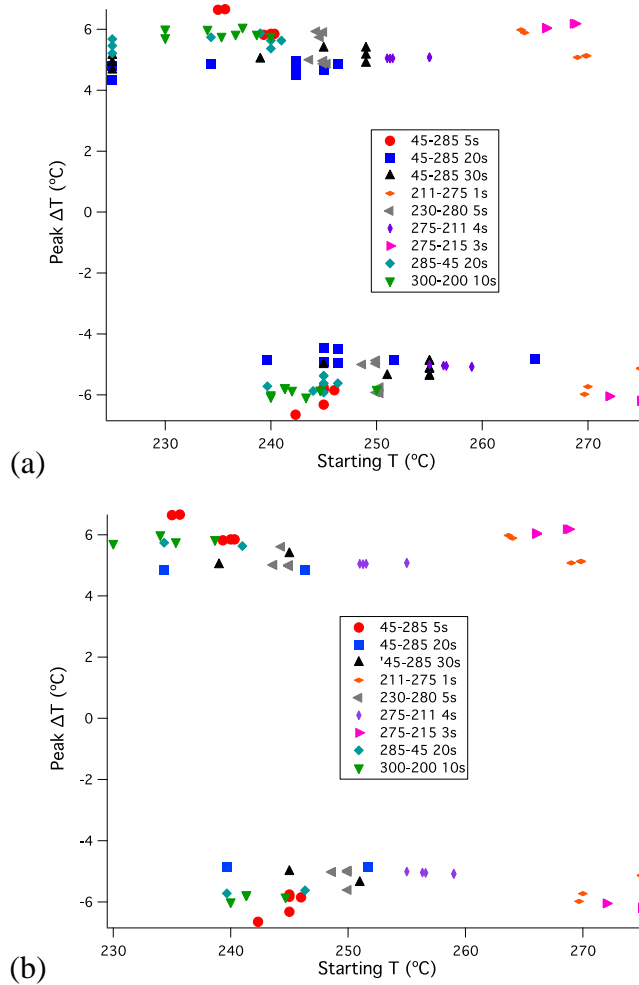


**Figure 4-6. (a) Original  $\Delta T$  prediction set for PZT 95/05, measured over 50 V, excluding erratic  $\Delta T$  curves. (b) New  $\Delta T$  prediction set that only includes predictions that comply with thermodynamic conditions.**

As with original  $\Delta T$  prediction set, the excluded, erratic  $\Delta T$  curves were deemed to be those determined from raw data and smoothed OIP data, for the ‘275-211 °C 4s’, ‘211-275 °C 1s’, ‘275-215 3s’ and ‘45-285 °C 20s’ datasets. Comparison between the above graphs shows seemingly little change, but the following table specifies the differences:

	<i>Peak <math>\Delta T</math> spread (<math>^{\circ}\text{C}</math>)</i>	<i>Peak <math>\Delta T</math> spread in % terms of its largest peak <math>\Delta T</math></i>	<i>Peak <math>\Delta T</math> starting temperature spread (<math>^{\circ}\text{C}</math>)</i>
<i>PZT 95/05, over all 50 V range calculations.</i>			
More smoothly varying predictions, BEFORE fixing datasets	2.33	35.0	44.87
More smoothly varying predictions, AFTER fixing datasets	1.80	27.0	39.87

**Table 27. Peak  $\Delta T$  prediction variation. PZT 95/05.**

The PMN-PT, 225 nm sample  $\Delta T$  predictions changed to the following:

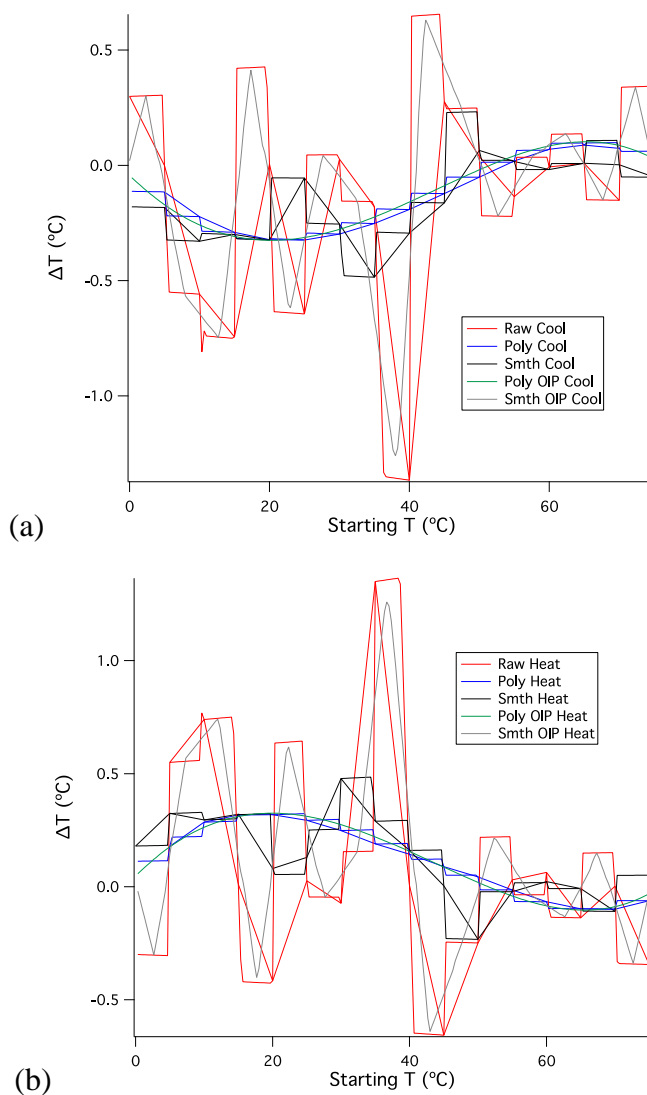


**Figure 4-7. (a) Cooling predictions and (b) Heating predictions for 0-75 °C dataset measured on PMN-PT 225 nm.**

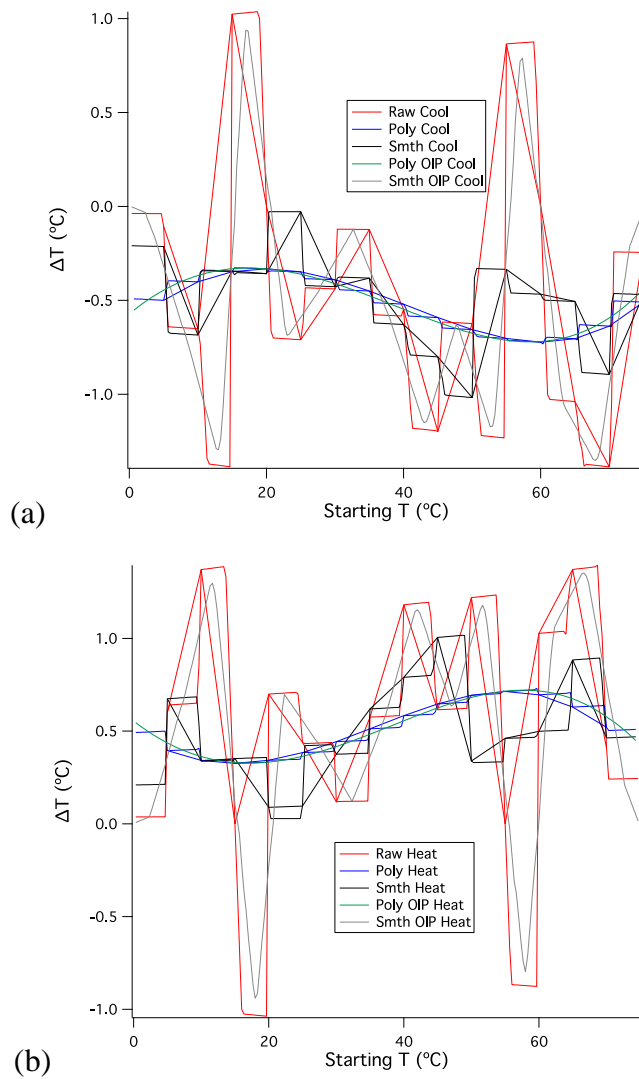


**Figure 4-8. (a) Cooling predictions and (b) Heating predictions for 0-75  $^{\circ}\text{C}$  (“Hysteresis removed”) dataset measured on PMN-PT 225 nm.**

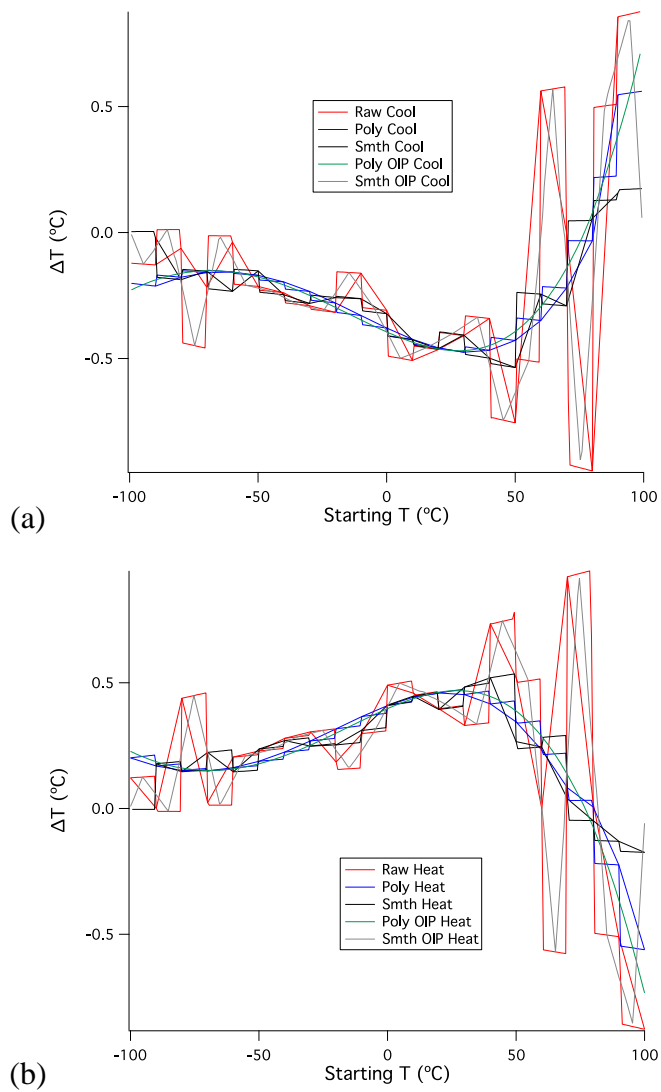


**Figure 4-9. (a) Cooling predictions and (b) Heating predictions for -100-100 °C dataset measured on PMN-PT 225 nm.**

The peak  $\Delta T$  predictions from the 250 point-per-branch and 25 point-per-branch data are shown in the following graphs:

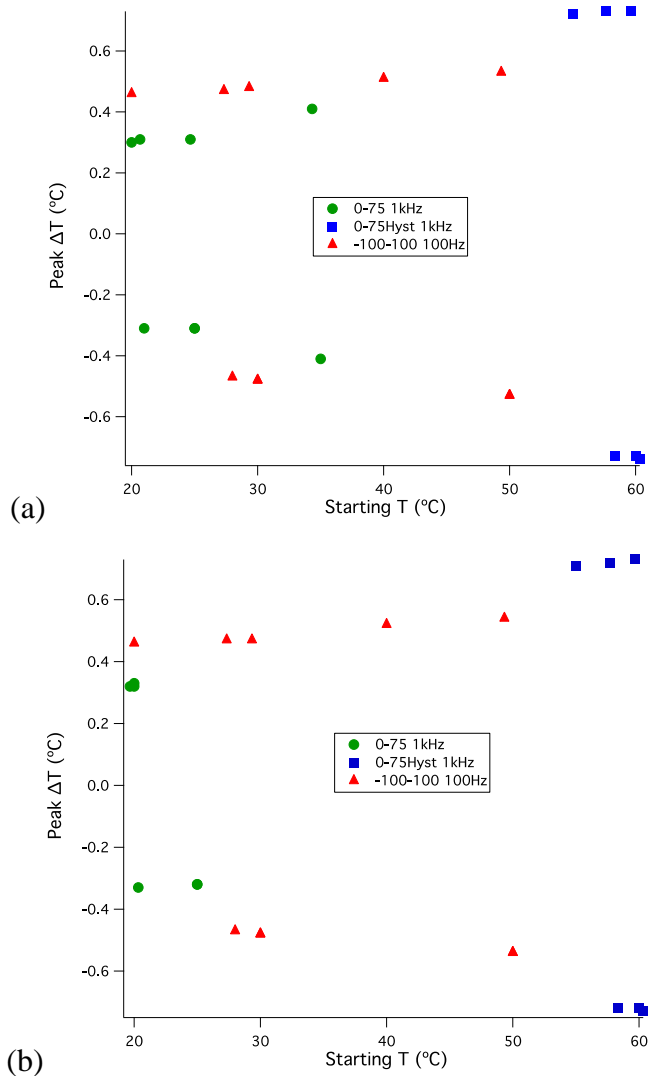


**Figure 4-10. (a) Original  $\Delta T$  prediction set for 225 nm thick PMN-PT, measured over 14 V, excluding erratic  $\Delta T$  curves. (b) New  $\Delta T$  prediction set that only includes predictions that comply with thermodynamic conditions.**

The excluded  $\Delta T$  curves were those determined from raw data and smoothed OIP data in all three datasets, plus the smoothed data in the two datasets measured between 0 °C and 75 °C. The change in the peak  $\Delta T$  variation is shown in the table below.

	<i>Peak <math>\Delta T</math> spread (<math>^{\circ}\text{C}</math>)</i>	<i>Peak <math>\Delta T</math> spread in % terms of its largest peak <math>\Delta T</math></i>	<i>Peak <math>\Delta T</math> starting temperature spread (<math>^{\circ}\text{C}</math>)</i>
<i>PMN-PT 225 nm: over all datasets</i>			
More smoothly varying predictions, BEFORE fixing datasets	0.57	64.8	40.33
More smoothly varying predictions, AFTER fixing datasets	0.41	56.2	40.00

**Table 28. Peak  $\Delta T$  prediction variation. 225 nm PMN-PT.**

Finally, two of the PMN-PT, 700 nm sample  $\Delta T$  predictions changed to the following:

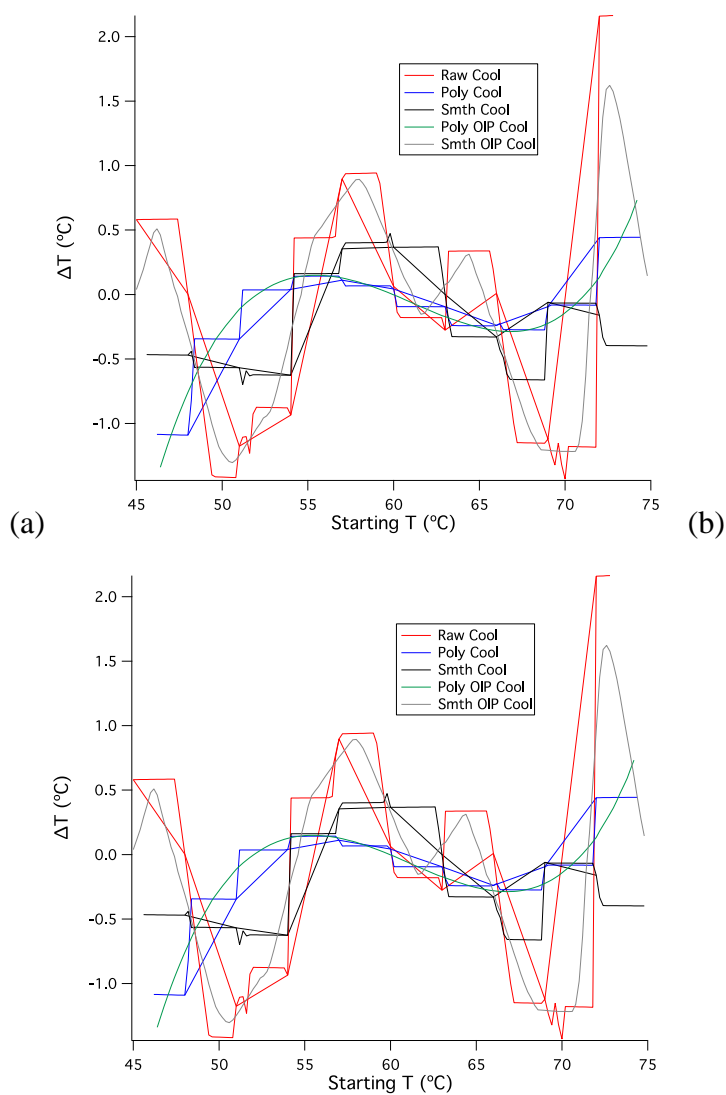


**Figure 4-11. (a) Cooling predictions and (b) Heating predictions for 75-45 °C, 1 kHz dataset measured on PMN-PT 700 nm.**

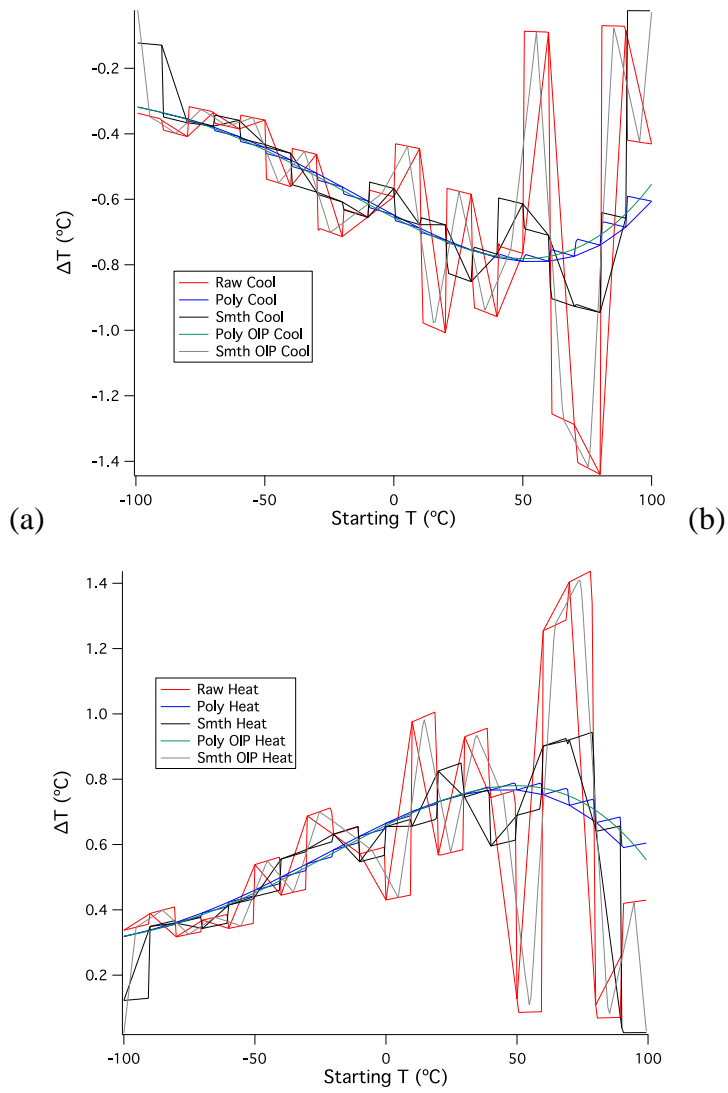


**Figure 4-12. (a) Cooling predictions and (b) Heating predictions for 100 - -100 °C, 1 kHz dataset measured on PMN-PT 700 nm.**

The peak  $\Delta T$  predictions from the original PMN-PT 700 nm datasets and those after exchanging 250 point-per-branch data for 25 point-per-branch data are compared by the following two graphs:

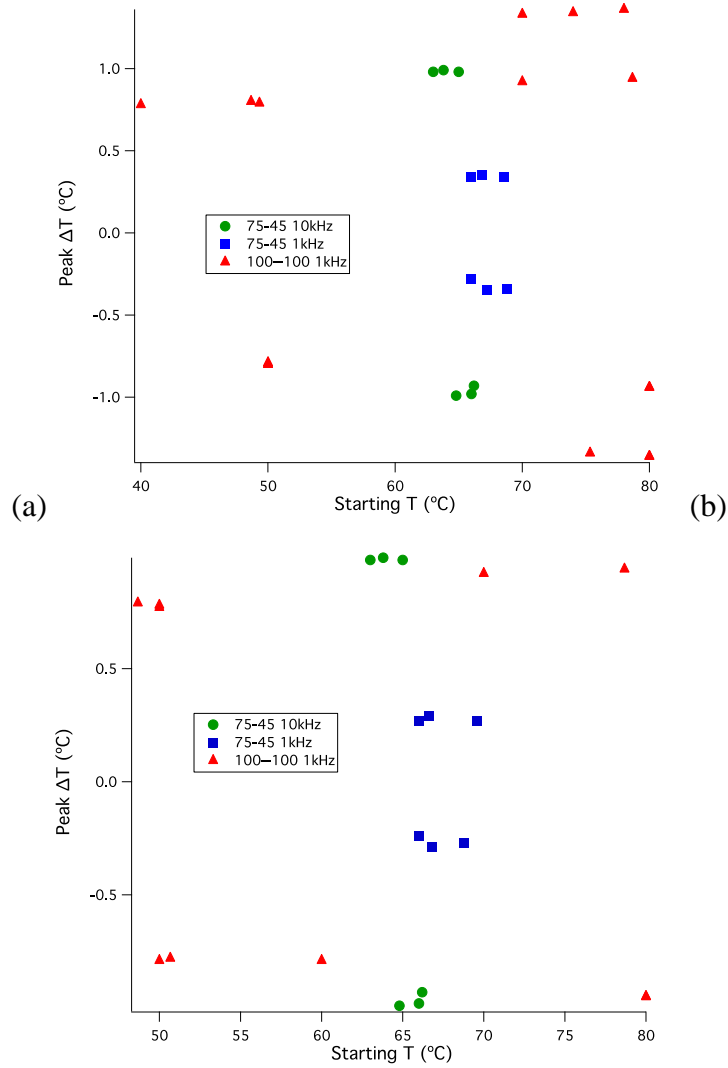


**Figure 4-13. (a) Original  $\Delta T$  prediction set for 700 nm thick PMN-PT, measured over 50 V, excluding erratic  $\Delta T$  curves. (b) New  $\Delta T$  prediction set that only includes predictions that comply with thermodynamic conditions.**

The excluded  $\Delta T$  curves were those determined from raw data and smoothed OIP data in all three datasets, plus the smoothed data in the two datasets measured between 75 °C and 45 °C. The change in the peak  $\Delta T$  variation is shown in the table below.

	<i>Peak <math>\Delta T</math> spread (<math>^{\circ}\text{C}</math>)</i>	<i>Peak <math>\Delta T</math> spread in % terms of its largest peak <math>\Delta T</math></i>	<i>Peak <math>\Delta T</math> starting temperature spread (<math>^{\circ}\text{C}</math>)</i>
<i>PMN-PT 700 nm: over all datasets</i>			
More smoothly varying predictions, BEFORE fixing datasets	1.08	79.4	38.67
More smoothly varying predictions, AFTER fixing datasets	0.75	75.8	30.00

**Table 29. Peak  $\Delta T$  prediction variation. 700 nm PMN-PT.**

In general, the reduction of the 250 point-per-branch data to 25 point per branch, allowing the dataset to comply with requirements of the indirect method, has resulted in a smaller spread of peak  $\Delta T$  predictions, though the change is small, but perhaps most notable in the PZT 95/05 results, where the spread expressed as a percentage of the largest peak  $\Delta T$  prediction drops from 35.0% to 27.0%.

By ignoring some of the measured polarization values, the new sets of  $\Delta T$  predictions, in some cases, are simply based on less information. However, **the data are consistent with conditions implicit to the indirect method.**

### **4.3. ISOTHERMAL OR ADIABATIC?**

When  $P(E, T)$  data contained in this thesis were measured at a given temperature, it was assumed that the material experiences an isothermal process. This has not just been the approach taken here, but applies to all the electrocaloric literature that employs the indirect method, where there is no mention of any tests or estimation of how isothermal the measurement process is. On the face of it, this seems to be intuitively reasonable. One takes the sample to a stable temperature and then applies a bipolar voltage to measure a hysteresis loop, during which time the material will attempt to cool and heat, twice, as its configurational entropy is altered. The process will be basically isothermal if the heat can enter and leave the material quickly enough. The volume of material that is

subject to electrocaloric changes is very small in these experiments with thin films, of the order of  $10^{-5} \text{ mm}^3$ . It also takes the form of a disc or square tile, the area of which is very much larger than its thickness. Given this, one might expect the measurement process to be isothermal. However, measurements were also performed rather quickly, as in the electrocaloric literature, where the most popular hysteresis loop frequency is 1 kHz, during which, 250 polarization and voltage values are measured in each second loop quadrant, as defined earlier. This means a polarization and voltage measurement is made once every microsecond. The assumption of isothermality is rather fundamental and is worthy of a decent estimation as to its veracity.

The experiments presented in this thesis were performed on two materials under different conditions and the volume of material, along with its geometry, would have affected the heat flow rate, which determines how isothermal one can maintain the material. If it can be estimated that the flow of heat into and out of the film, during electrocaloric changes, was fast enough to maintain the film essentially isothermal, under the most demanding conditions for isothermality, then one can assume that all other experiments experienced isothermal conditions. Such conditions would occur where the most amount of heat is required to move the most quickly.

One could consider either the heat flow out of the film as the field is applied, or take the film to be at ambient temperature and consider the heat flow into the film as the field is released. The latter is chosen here.

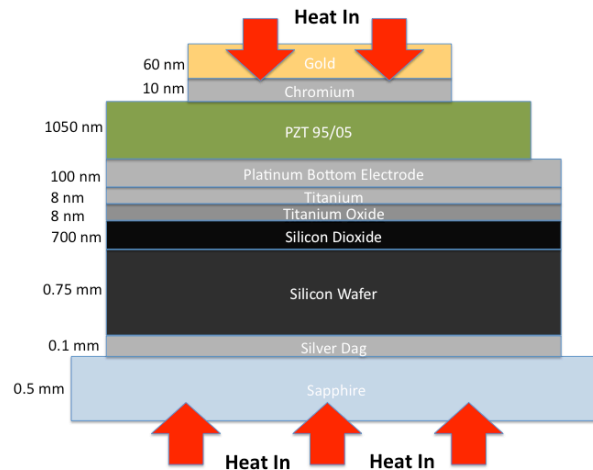


**Figure 4-14. Illustration of heat flow into PZT 95/05 sample as film cools electrocalorically.**

The above figure shows the component materials of the PZT 95/05 sample stuck to the sapphire mounting disc, as the PZT film is cooling electrocalorically in the cryostat, though the visual proportions are not representative. The Au/Cr electrodes are  $350\ \mu\text{m}$  square compared to the roughly  $1\ \mu\text{m}$  thick film that is cooling. This relationship between active film area and thickness means heat flow into the part of the film that is experiencing the electrocaloric effect, through the sides, will be negligible compared to that which passes through the top electrode and the equivalent area of the bottom platinum electrode. The 1000SC and 1100FC datasets were measured on a sample that differed slightly, apart from the obvious PZT film thickness difference, as the top electrodes were  $100\ \text{nm}$  thick, made of platinum and circular, covering nearly one quarter of the area of the  $350\ \mu\text{m}$  square Au/Cr electrodes. However, the diameter of these electrodes was  $200\ \mu\text{m}$  and the same argument of negligible heat flow through the sides of the film is applied here.

For samples measured in the cryostat, the sapphire disc was held tight against the copper block of the sample stage, which will be treated as a thermal bath. Measurements on the hotplate did not include the sapphire disc and the sample was held down on the centre of the hotplate, with Kapton tape. In this case, the hotplate is also treated as a thermal bath. Heat flow through this bottom face of the sample is by conduction, whereas heat flow through the opposite surface in both cases, is from the thermal bath of the surrounding air,

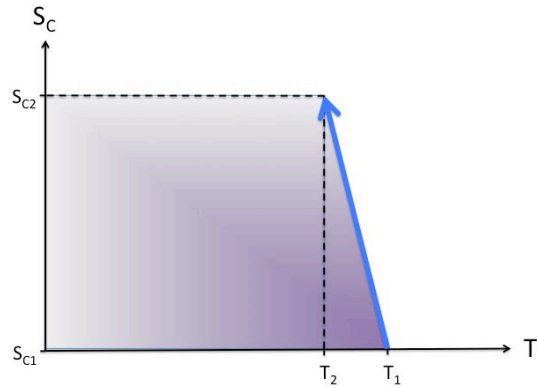
through the top electrode via convection. On the hotplate there is the free convection of the surrounding air in the laboratory, while in the cryostat, evacuation via a standard rotary pump can be expected, at most, to reduce the air pressure to  $10^{-3}$  mbar.

To estimate how much heat is required to move in each experiment, it will be assumed that the predicted electrocaloric temperature changes are correct. Under the required isentropic conditions for these predictions, there would be no heat flow in or out of the electrocalorically active section of film. There would be no change in its entropy, though its configurational entropy would change with the field, compensated for by the opposite change in entropy related to its temperature. That is:

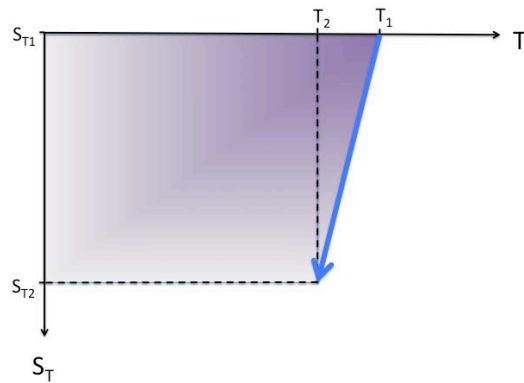
(4.16)

$$dS = dS_C + dS_T = 0$$

The overall change in entropy,  $dS$ , is zero under isentropic conditions and can be viewed as a compensating change,  $dS_T$ , as  $dS_C$  is effected by a changing field. This can be described graphically.



(a)



(b)

**Figure 4-15. (a) Configurational entropy,  $S_C$ , vs temperature and (b) Entropy associated with temperature,  $S_T$ , vs temperature for an isentropic field removal.**

In the above figure, the blue lines that stretch from  $T_1$  to  $T_2$  show how the material would approximately change temperature in relation to its configurational and temperature-related entropy, in an isentropic process of field removal. Regardless of the actual trajectory of these blue lines, the two graphs would always be a mirror image of each other, across the temperature axis. The purple-shaded area in graph (a) is equal to the integral of  $TdS_C$ , while the equivalent area in graph (b) is equal to the integral of  $TdS_T$ . The two areas are equal in size, but opposite in sign:

(4.17)

$$\text{Overall heat change} = \int_{S_{C1}}^{S_{C2}} T dS_C + \int_{S_{T1}}^{S_{T2}} T dS_T = \Delta q_1 + (-\Delta q_1) = 0$$

where  $\Delta q_1$  represents a heat change.

If, after performing such isentropic cooling, one removes the barrier to heat flow into or out of the system and the surroundings are a thermal bath at temperature,  $T_1$ , then heat will flow into the material until there is thermal equilibrium and its temperature returns to  $T_1$ . Taking the heat capacity of this section of material to be constant, as is done in all the indirect method literature predictions, the heat required to return the material to  $T_1$ , is  $C(T_1 - T_2)$ , where  $C$  is the heat capacity. With the field now removed,  $dS_C = 0$ , while  $S_T$  will increase as the temperature rises. The change will approximately follow the blue line of graph (b) in fig. 4-15, but in the opposite direction, from  $T_2$  to  $T_1$ .  $dS_T$  will be positive, whereas it was negative in the isentropic cooling example.

(4.18)

$$C(T_1 - T_2) = \int_{T_2}^{T_1} C dT \approx \int_{S_{T2}}^{S_{T1}} T dS_T = \Delta q_1$$

By taking the indirect method predictions for peak temperature changes and a value for the heat capacity, one has  $\Delta q_1$ . This is slightly less than the heat required to enter the material during an isothermal removal of the field, as illustrated below:

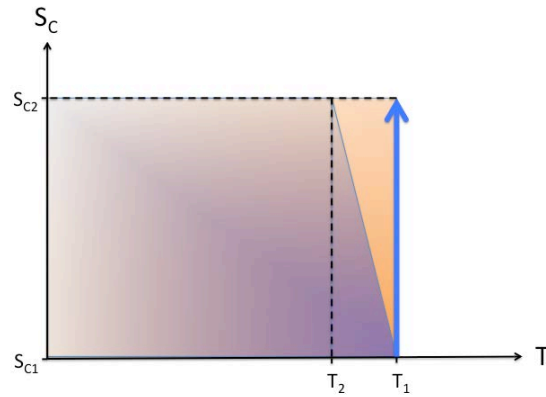


**Figure 4-16. Isothermal change of configurational entropy as a function of temperature. Orange rectangle behind the purple shape, represents heat required to maintain system isothermal, whereas the area of the purple shape is the integral of  $TdS_C$  during isentropic cooling.**

During the isothermal removal of a field,  $dS_T = 0$ , so all entropy change is configurational and the corresponding heat that must enter the material is equal to the area represented by the orange rectangle in the above figure. The rectangle is situated behind the purple area, which has been shown to be approximately the same as  $C(T_1 - T_2)$ , and stretches from  $T_1$  down to zero Kelvin. Hence, if the area of the purple shape is visualised as a rectangle of the same height as the orange rectangle, but reaching a temperature which is half way between  $T_2$  and  $T_1$ , then the amount of heat represented by the orange rectangle can be calculated as the area of the purple shape multiplied by the factor of  $T_1 / \left(T_1 - \frac{(T_1 - T_2)}{2}\right)$ . This is:

(4.19)

$$C(T_1 - T_2) \left( T_1 / \left( T_1 - \frac{(T_1 - T_2)}{2} \right) \right) \approx \Delta q_{ISO} = T_1 \Delta S$$

In this way, it is possible to see which of the datasets was measured under the most demanding conditions for isothermality, i.e. where the heat transfer rate was required to be highest.

<i>Dataset</i>	<i>Loop frequency (kHz)</i>	<i>Quarter loop duration (<math>\mu</math>s)</i>	<i>Film area (<math>10^{-8}m^2</math>)</i>	<i>Film thickness (nm)</i>	<i>Film volume (<math>10^{-14}m^3</math>)</i>	<i>Largest predicted peak cooling (<math>^{\circ}C</math>)</i>	<i>Peak starting temperature (<math>^{\circ}C</math>)</i>	<i>Heat per quarter loop (<math>\mu</math>J)</i>	<i>Average heat transfer rate (mW)</i>
<i>PZT 95/05</i>									
1000SC	10	25	3.14	1000	3.14	-25.79	228.00	2.28	91
1100FC	10	25	3.14	1100	3.45	-22.50	208.00	2.17	87
211-275 $^{\circ}C$ 1s, 275-211 $^{\circ}C$ 4s, 300-200 $^{\circ}C$ 10s, 45-285 $^{\circ}C$ 5s, 20s, 30s & 285- 45 $^{\circ}C$ 20s	10	25	12.3	1050	12.9	-6.32	245.00	2.25	90
230-280 $^{\circ}C$ 5s & 275-215 $^{\circ}C$ 3s	1	250	12.3	1050	12.9	-6.16	275.00	2.20	8.80
<i>PMN-PT</i>									
0-75 $^{\circ}C$ & 0- 75 $^{\circ}C$ Hyst	1	250	12.3	225	2.76	-0.73	60.00	0.06	0.242
-100-100 $^{\circ}C$	0.1	2500	12.3	225	2.76	-0.54	50.00	0.04	0.0179
75-45 $^{\circ}C$ (a)	10	25	12.3	700	8.56	-0.98	66.00	0.25	10
75-45 $^{\circ}C$ (b) & 100--100 $^{\circ}C$	1	250	12.3	700	8.56	-0.95	80.00	0.24	0.976

**Table 30. Experimental parameters by dataset determining maximum necessary average heat transfer rate in final column.**

The above table groups together datasets measured on the same film, using the same area electrode, subject to the same speed of loop measurement. The maximum  $\Delta T$  predictions by the indirect method for each group, considering only the measurement temperatures, are then recorded in the seventh and eighth columns. Only measurement temperatures are considered, of course, as the objective is to assess isothermality during measurement. The penultimate column shows how much heat energy was required to enter the electrocalorically active section of film, to keep it from cooling while the field was removed, i.e. during the second quadrant of the measured hysteresis loop. The final column takes this heat energy and divides it by the duration of this second quadrant to give the largest average heat transfer rate, required for isothermality during measurement of the datasets for each group.

The first three rows referring to PZT datasets show the highest heat transfer rates. Relevant differences to consider in comparing these three are the electrode areas and the temperature changes. The 1000SC and 1100FC datasets were both measured using the 200  $\mu\text{m}$  diameter circular electrodes, while the third group were all measured using 350  $\mu\text{m}$  square electrodes. Hence the area of the electrode of the third group is roughly four times larger, allowing for a potentially four-times-faster heat flow rate. However, the predicted temperature change is coincidentally roughly four times smaller than the 1000SC and 1100FC datasets, so one would expect actual heat transfer rates to be similar. Having said that, the third group of datasets were all measured in the cryostat, where heat transfer by convection, through the top electrode, will be considerably smaller in the reduced air pressure environment of the evacuated cryostat chamber. Nonetheless, one might expect most heat transfer to be through the bottom electrode, via conduction and perhaps this difference in air pressure is irrelevant. Finally, in the cryostat, the silicon substrate sits on a thin layer of silver dag, which sits on a sapphire disc. The thermal bath of the copper sample stage makes contact with the sapphire disc, whereas with the 1000SC and 1100FC measurements, the silicon substrate is in direct contact with the thermal bath of the hotplate. These issues may or may not be relevant, so isothermality of both the 1000SC dataset and the '45-285 °C 5s' dataset, where maximum cooling was predicted for the third group, will be investigated.

Both of these datasets were measured with a 10 kHz hysteresis loop, meaning that the second quadrant consists of 25 points measured at 1  $\mu$ s intervals, over a total of 24  $\mu$ s. Each point is defined as a polarization at a voltage, both of which are measured at the same time. It is known that the polarization response of a ferroelectric, to a changing field, takes place over the order of a nanosecond, so the electrocaloric cooling that takes place and the resulting heat flow into the film, is to be assessed nanosecond by nanosecond. The Radiant ferroelectric tester takes the maximum value of the required bipolar voltage, input by the user and calculates a voltage step value, as  $(4V_{max}) / (No. points - 1)$ . By looking at measured hysteresis loops where demands on the voltage ramp rate are high, one can see that the tester does not quite manage to reach  $V_{max}$  in some cases, such as when measuring a 10 kHz loop to a maximum of  $\pm 90$  V, which is right at the limit of its performance. In this case, there are 101 points recorded, so the voltage step is  $\pm 3.6$  V, depending on whether the voltage is being ramped up or down. It can be seen that the tester only reaches 95% of the 90 V specified when ramping up the voltage and this represents an average attainment of each voltage step. Over the microsecond between each loop-data-point measurement, the tester only manages to reach 95% of the prescribed voltage change. Hence, 1  $\mu$ s is equal to three RC time constants, or the RC time constant is  $1/3 \mu$ s. With this knowledge, one can determine the voltage reached at each nanosecond and translate that into a polarization change, by taking the change in polarization as linear between measured points.

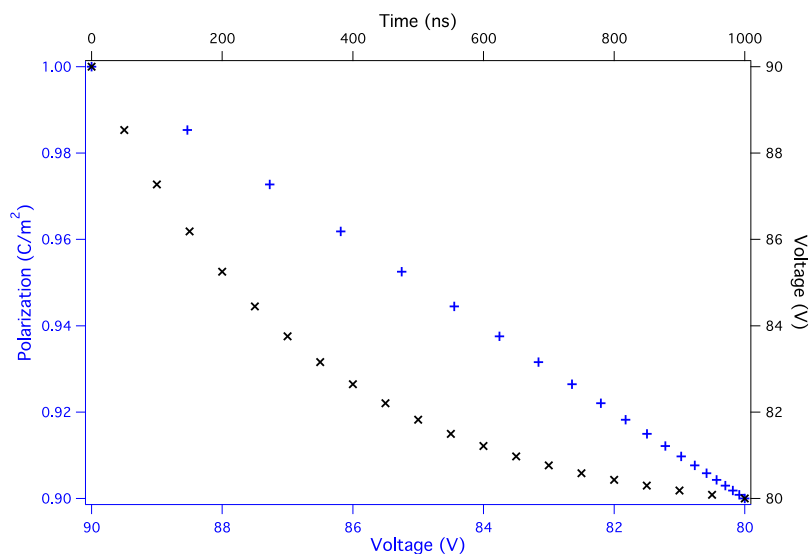


**Figure 4-17. Example of how voltage varies between measurement points and proportionally distributed polarization values.**

The above figure illustrates how the voltage changes between measurement points and a linear relationship between voltage and polarization over the same interval. The curve of black crosses is described by the top and right axes, showing the voltage to fall according to the RC time constant over the 1000 ns period between measurement points. For the purposes of this isothermality estimation, it is taken that the variation of polarization between measured points, is linear. Hence, as the voltage drops, so the polarization falls by the same proportion. In the above example, the voltage drops from 90 V to 80 V, while the polarization drops from 1.0 C/m<sup>2</sup> to 0.9 C/m<sup>2</sup> over the same microsecond. When the voltage falls by some proportion of that interval, say 40%, to 86 V, then the polarization is taken to have fallen by the same proportion, to 0.96 C/m<sup>2</sup>. This can be seen in the figure as corresponding black and blue crosses lie at the same height up the vertical axes. By applying this idea to real data, an estimation for intermediate polarization values between measured points is obtained.

Now if the increase in configurational entropy as the field is removed were proportional to the drop in polarization, the total changes in polarization and entropy over the second quadrant set of loop data points,  $\Delta P$  and  $\Delta S$  could be compared to ascertain the equivalent fractional changes.  $\Delta P$  is known from the measured data, while  $\Delta S$  can be taken from the estimated  $\Delta q_{ISO} = T_1 \Delta S$ . One of the Maxwell relations derived previously can be rewritten as:

(4.20)

$$\left(\frac{\partial E}{\partial T}\right)_P = -\left(\frac{\partial s}{\partial P}\right)_T$$

where small “s” represents entropy per unit volume, proportional to total entropy.

Looking at a typical graph of  $\left(\frac{\partial E}{\partial T}\right)_P$ :

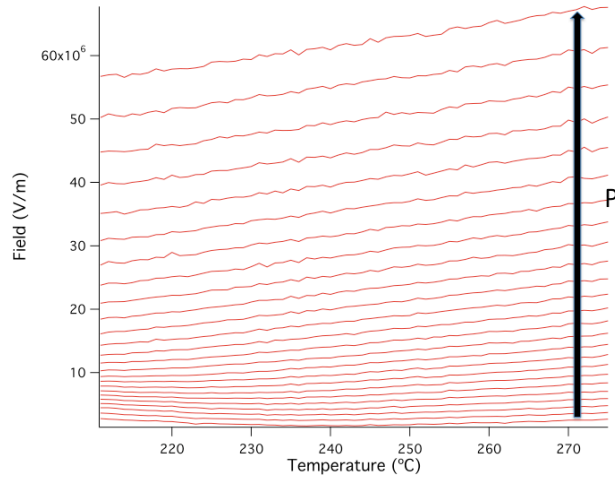


**Figure 4-18. Field vs temperature at different polarization for 211-275 °C 1s dataset.**

at higher polarization values,  $\left(\frac{\partial E}{\partial T}\right)_P$  is slightly larger than at lower polarization, but basically constant at each  $P$ , over wide temperature ranges. This is a feature that is common to all the datasets, at least around the peak  $\Delta T$  prediction starting temperatures. From this, one could say then, that  $-\left(\frac{\partial S}{\partial P}\right)_T$  is larger at higher  $P$  and this information can be used to weight the fractional changes in entropy over  $\Delta S$  according to fractional changes in  $\Delta P$ . The above graph is constructed by interpolating  $E(P)$  data at each temperature to a set of  $P$  values evenly distributed across the measured range.  $\left(\frac{\partial E}{\partial T}\right)_P$  is taken at the peak cooling starting temperature, for each  $P$ , plotted against  $P$  and the curve then interpolated to find  $\left(\frac{\partial E}{\partial T}\right)_P$  at the polarization values of the measured loop quadrant. These values are then used for weighting.

Before loop measurement, the sample and all constituent parts, including the film, will be at a constant temperature. By the time the tester has ramped up to the maximum voltage, the film may or may not have changed temperature relative to its starting value, but for the purposes of this isothermality estimation, the temperature at this point is taken to be equal to the starting temperature and constant throughout the sample. Then as one imagines the voltage reducing to zero volts over 25  $\mu$ s, the estimated entropy changes over each nanosecond period can be used to determine the electrocaloric cooling of the film, while heat moves into the film due to the temperature gradient induced.

As this is an example of transient, as opposed to steady-state, heat flow, a numerical, finite-element method is used. Heat will flow into the film through the top electrode via convection heat transfer, while conduction accounts for heat entering via the bottom electrode. Thermal resistance between sample layers is taken to be negligible. The finite-element method divides the sample materials into imaginary slices, in the sample plane and considers heat transfer across these elements. For the film and those materials below it, the conducted heat flowing into any finite element is equated with the sum of the change in its internal energy and the heat flowing out [67]. The differential equation that describes this is [68]:

(4.21)

$$\frac{\partial^2 T}{\partial x^2} = \frac{1}{\alpha} \frac{\partial T}{\partial t}$$

where  $x$  is distance in the direction of the heat flow,  $T$  is the temperature,  $t$  is time and  $\alpha$  is thermal diffusivity, equal to  $k/\rho c$ , where  $k$  is thermal conductivity,  $\rho$  is material density and  $c$ , its specific heat. If the thickness of a finite element of a given material is  $\Delta x$  and a series of three adjacent planes that sit between elements are denoted by (m-1), m and (m+1), then the left hand side of the above equation can be approximated by:

(4.22)

$$\frac{\partial^2 T}{\partial x^2} \approx \frac{1}{(\Delta x)^2} (T_{m+1} + T_{m-1} - 2T_m)$$

for plane, m [69]. Equation 4.21 can then be rewritten for this numerical method as:

(4.23)

$$\frac{(T_{m+1}^p + T_{m-1}^p - 2T_m^p)}{(\Delta x)^2} = \frac{1}{\alpha} \frac{(T_m^{p+1} - T_m^p)}{\Delta t}$$

where the subscript “p” refers to a given moment in time and “p+1”, a time  $\Delta t$  later. This can be rearranged to give:

(4.24)

$$T_m^{p+1} = \frac{\alpha \Delta t}{(\Delta x)^2} (T_{m+1}^p + T_{m-1}^p) + \left(1 - \frac{2\alpha \Delta t}{(\Delta x)^2}\right) T_m^p$$

If  $\frac{(\Delta x)^2}{\alpha \Delta t}$  is now set to be equal to 2, the above equation reduces to  $T_m^{p+1} = \frac{1}{2}(T_{m+1}^p + T_{m-1}^p)$  and the temperature across plane  $m$ , at time  $(p+1)$  is then equal to the average of the temperatures of the planes either side of it, at time  $p$  [70]. The time interval,  $\Delta t$  proposed for analysing temperature changes, is one nanosecond, resulting in a characteristic element thickness,  $\Delta x$  for each material in the sample.

For convection heat transfer through the top electrode, an energy balance at the convection boundary results in [71]:

(4.25)

$$T_{m+1}^{p+1} = \frac{T_m^{p+1} + \left(h \frac{\Delta x}{k}\right) T_\infty}{1 + \left(h \frac{\Delta x}{k}\right)}$$

where  $(m+1)$  refers to the convection boundary and  $m$ , the next plane down, i.e. that on the interior side of the finite element at the convection boundary.  $T_\infty$  is the temperature of the air well away from the electrode, which remains constant, at the starting temperature.  $h$  is the convection heat transfer coefficient, which depends on  $T_{m+1}^p$  and is calculated as:

(4.26)

$$h = 0.59 \left( \frac{T_\infty - T_{m+1}^p}{L} \right)^{0.25}$$

where  $L$  is the electrode area divided by its perimeter length. At reduced air pressures,  $h$  is modified by multiplying the result of the above equation by the factor,  $\left(\frac{\mathcal{P}}{101.32}\right)^{0.5}$ , where  $\mathcal{P}$  is the air pressure in kilopascals [72].

For a given sample, each material is divided into a specific number of finite elements according to the characteristic value of  $\Delta x$ , based on the analysis time interval of one nanosecond and the properties of the material. At time  $t=0$ , all planes between elements are set to the same starting temperature. For the base of the sample, against the thermal bath of the hotplate or cryostat sample stage, the boundary temperature is set to the starting temperature for all  $t$ . The following temperature, after one nanosecond, is determined for all planes between elements, as the average of the temperature of the two planes either side of each plane, at  $t=0$ . Equation 4.25 is then used to determine the temperature of the convection boundary. The cooling of the film is then calculated according to its polarization change after that nanosecond and the weighted, proportionally inferred entropy change. This lowers the temperatures associated with elements of the film. The process is repeated at nanosecond intervals, for the duration of the field removal and builds a picture of transient temperature changes throughout the sample.

The first case to be analysed is that where the 1000SC dataset loops were predicted to experience the largest heat change due to the electrocaloric effect. This corresponds to the loop measured at 228 °C, where it was predicted that a 25 °C drop in temperature would have occurred, were the removal of the field performed isentropically, i.e. adiabatically and reversibly. The properties of the materials in the sample and their  $\Delta x$  values for a 1 ns  $\Delta t$  are presented in the table below:

<i>Material</i>	<i>k</i> (W/m.K)	$\rho$ (kg/m <sup>3</sup> )	<i>c</i> (J/K.kg)	$\Delta x$ (nm)	<i>Material thickness</i> (nm)	<i>No. of finite elements</i>
Top platinum electrode	73 <sup>1</sup>	21400 <sup>2</sup>	141 <sup>1</sup>	220	100	1
PZT 95/05	1.25 <sup>5</sup>	8300 <sup>3</sup>	330 <sup>3</sup>	30.2	1000	33
Bottom platinum electrode	73 <sup>1</sup>	21400 <sup>2</sup>	141 <sup>1</sup>	220	100	1
Titanium	20 <sup>1</sup>	4500 <sup>2</sup>	586 <sup>1</sup>	120	8	0
Titanium Oxide	7.0 <sup>1</sup>	4000 <sup>4</sup>	711 <sup>4</sup>	70	8	0
Silicon Dioxide	1.9 <sup>1</sup>	2100 <sup>1</sup>	710 <sup>6</sup>	51	700	14
Silicon	78 <sup>1</sup>	2330 <sup>2</sup>	850 <sup>1</sup>	281	750000	2669

**Table 31. Material properties,  $\Delta x$  values and corresponding number of finite elements. Sources: 1. [73], 2. [74], 3. [5], 4. [75], 5. [76], 6. [77].**

The electrodes only really qualify for half an element and the thin layers of titania and titanium, around a tenth or less of an element. However, this method requires whole numbers of elements, so compromises have been made, evident in the table. The isothermality estimation should not suffer, given the large number of elements in the film and the sample base. The temperature evolution of the finite-element model was performed with Igor and the programming can be found in appendix E.

The modelled results for the temperature of each element within the PZT, as a function of the 24000 nanosecond steps (25 measured points – 1000 points per measured point interval), are shown in the following graph:

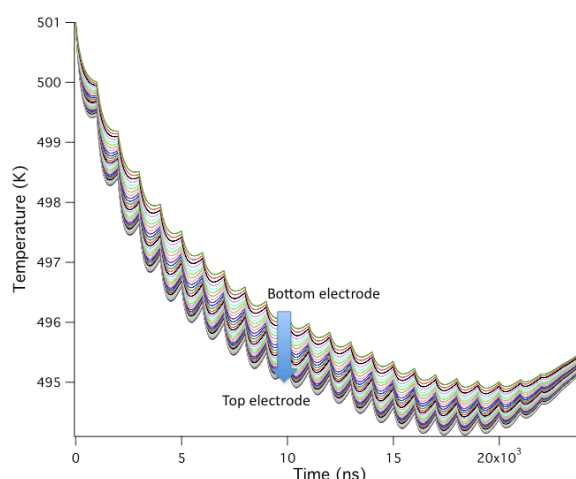


**Figure 4-19. Temperature evolution of 33 equidistant planes across 1 μm thickness of PZT 95/05, during second quadrant of 10 kHz hysteresis loop measurement. Sample on hotplate.**

The collection of multi-coloured curves in the above figure represent the temperature, as a function of time, of 33 equidistant planes in the PZT 95/05 being measured in the 1000SC dataset. All curves have this scalloped characteristic which reflects how the voltage changes and thus the polarization and entropy, between measured points. The uppermost, light-green-coloured curve, is associated with the element that makes contact with the bottom platinum electrode, while the lowermost curve shows the PZT temperature next to the top electrode. Hence, as the electrocaloric effect attempts to cool the film and heat flows in from both the top and bottom electrode sides, it is the heat transfer via conduction, through the bottom of the film, that most manages to stop the

film from cooling. Nonetheless, the top element of the film still cools by as much as 6.9 °C, which is 28% of the 25 °C predicted isentropic temperature change. Based on this information, the hysteresis loop cannot be considered an isothermal measurement.

It is also interesting to look at the temperatures across all 2718 elements at moments through the second quadrant measurement, as shown below:

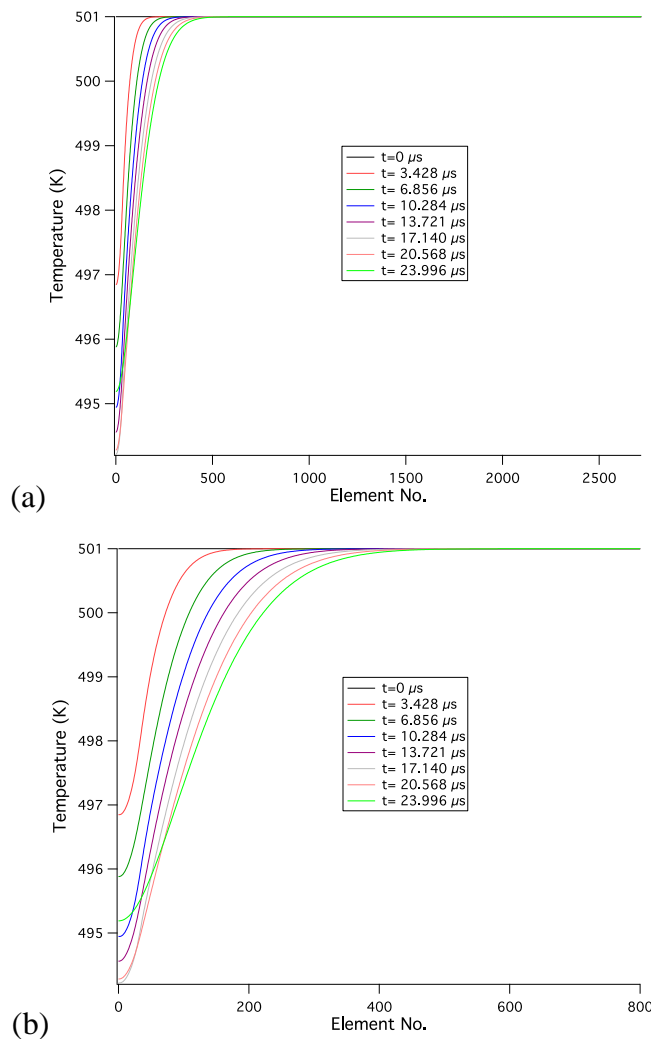


**Figure 4-20. (a) Element number vs associated temperature for entire sample thickness, at a range of times during field removal. (b) Close-up of same data on the horizontal axis.**

Graph (a) in the above figure shows how the whole sample is taken to begin the process at 501 K (228 °C) and how the drop in temperature in the film affects the temperature of the sample layers below it. Elements are numbered from zero to 2717, so elements 1-33

represent temperatures within the film. The elements from 49 upwards, are all associated with temperatures within the silicon substrate and the majority of the substrate is not affected at all by the electrocaloric change in temperature of the film. This means that were this measured in the cryostat, where the sample was stuck to a mounting disc made of sapphire, using silver dag, the conductive heat flow through those extra layers would have been irrelevant to the transient temperature changes in the sample and heat flow through the bottom of the film would have been identical.

The same analysis is now made for the relevant loop in the '45-285 5s' dataset. The degree to which this measurement was, or was not, isothermal is expected to be similar. The differences between this and the previous analysis are that the top electrode area is roughly four times larger here, while the predicted temperature change is roughly four times smaller. The finite element model of transient heat flow is, however, independent of the active film area, as an increase in area and thus rate of heat flow, is accompanied by proportionally more material needing warming. Also, for a larger attempted temperature change, the heat flow rate is increased proportionally. The air pressure in the cryostat is taken to be  $10^{-3}$  mbar, which will reduce the heat transfer rate through the top electrode due to free convection of the air above it, but it is expected that this will have little effect, as it was shown in the last estimation that heat transfer from the air was relatively unimportant compared to the conduction through the bottom electrode.

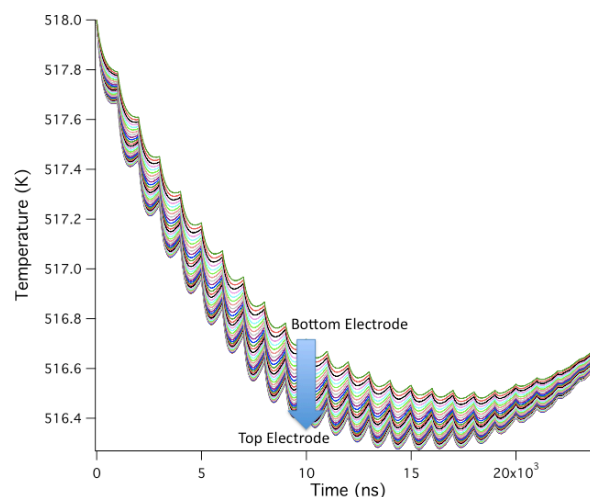


**Figure 4-21. Temperature evolution of 35 equidistant planes across 1.05  $\mu\text{m}$  thickness of PZT 95/05, during second quadrant of 10 kHz hysteresis loop measurement. Sample in cryostat.**

Here, the estimation has the top element falling in temperature by as much as 1.8 °C, which is 28% of the predicted cooling, on a par with the 1000SC case, as expected.

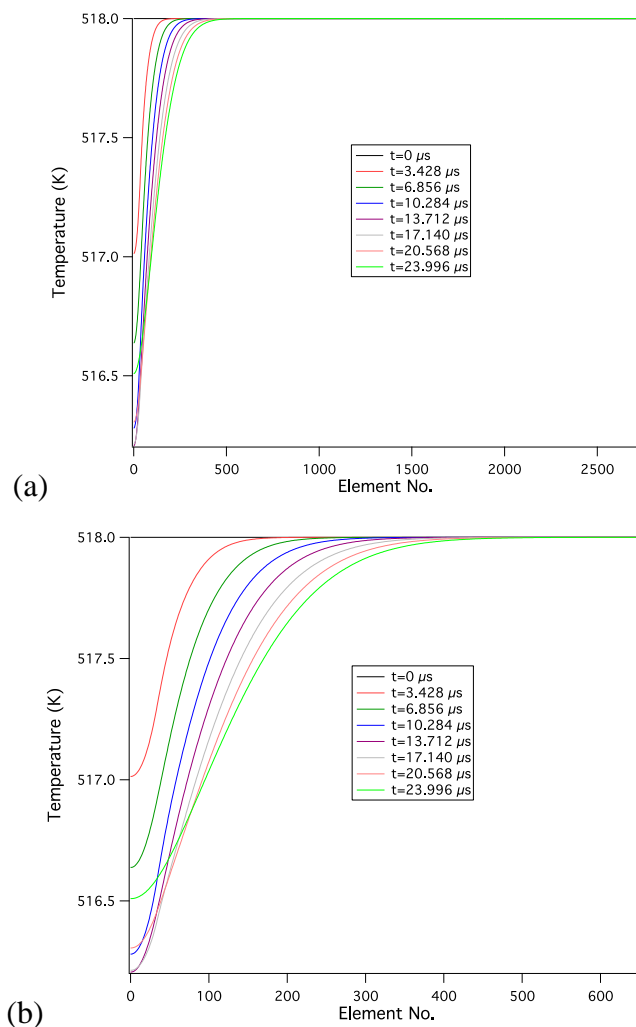


**Figure 4-22. (a) Element number vs associated temperature for entire sample thickness, at a range of times during field removal. (b) Close-up of same data on the horizontal axis.**

The temperature distribution through the sample is also very similar to the analysis of the 1000SC data. Here, the film is slightly thicker, giving an extra two finite elements to the PZT film, while the top electrode is thinner and mostly made of gold here, resulting in its exclusion due to the large  $\Delta x$  values, which were at least 29 times the material thicknesses. It seems the larger absolute temperature changes in the 1000SC film case affect the temperature of more of the silicon substrate, reaching as deeply as 190  $\mu m$  into the silicon substrate, whereas here, temperature changes only reach as far as 170  $\mu m$ .

Looking at the other material investigated, PMN-PT, the thermal conductivity of which is five times smaller than PZT [78], but at the same loop frequency, the following temperature versus time graph was obtained:

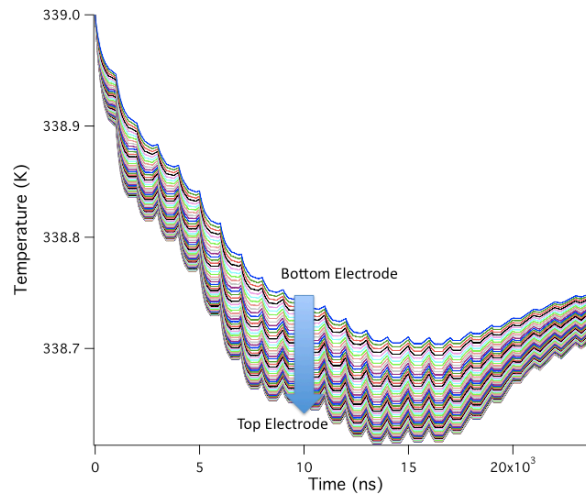


**Figure 4-23. Temperature evolution of 54 equidistant planes across 700 nm thickness of PMN-PT, during second quadrant of 10 kHz hysteresis loop measurement. Sample in cryostat. '75-45a 10kHz' dataset.**

The largest temperature change within this film, is 0.40 °C, which is 41% of the estimated 0.98 °C of isentropic cooling. This percentage is considerably larger than the 28% from the PZT estimations. The sample temperature distributions are shown below:

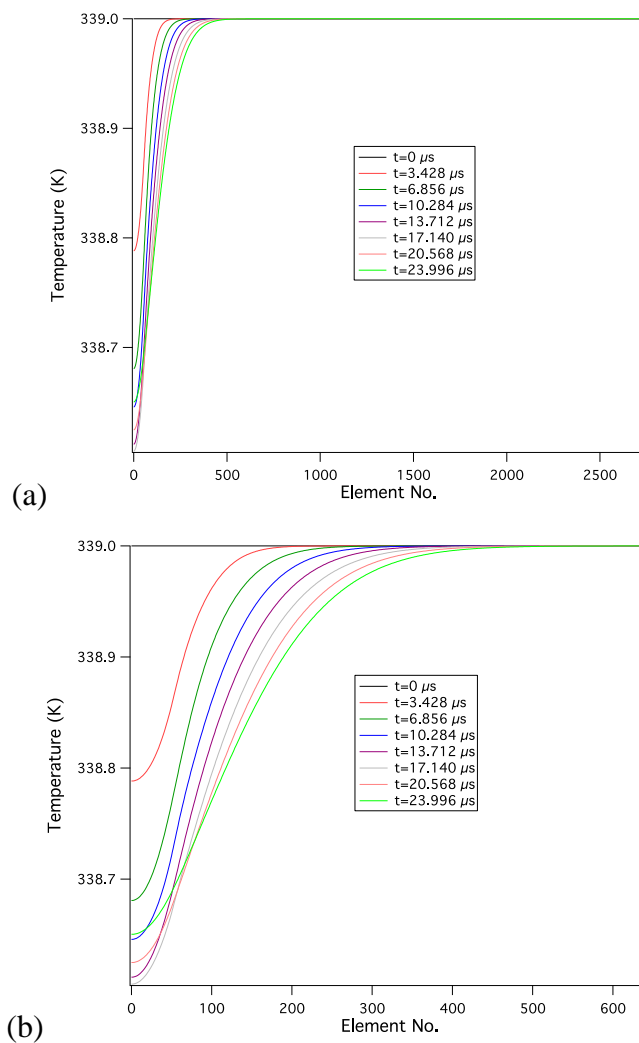


**Figure 4-24. (a) Element number vs associated temperature for entire sample thickness, at a range of times during field removal. (b) Close-up of same data on the horizontal axis.**

At the other end of the scale, the peak heat transfer required for isothermality in the ‘-100-100 °C’ dataset measured on the 225 nm thick sample of PMN-PT, was predicted to be much smaller, of the order of  $10^{-5}$  W, due to the 100 Hz hysteresis loop frequency and taking its peak cooling as  $-0.54$  °C. In order to set a number of calculations that the computer could handle for this estimation, the temperature of each element was assessed every 50 ns. A 100 Hz loop results in the ferroelectric tester measuring 250 points in the second loop quadrant, where the time interval between each measurement was  $10 \mu\text{s}$ , so temperatures were calculated for 200 intermediate point between those measured. Over a 250 point spread, the field removal time analysed is that of 249 intervals, or 2.49 ms. The

increased  $\Delta t$  interval for the finite element model, leads to larger  $\Delta x$  values and less elements. In this case, there were just two temperature points associated with the film and a total of 382 elements for the whole sample. It seems, however, that the much slower loop frequency results in temperature changes of material that is further from the film. Heat is conducted from beyond the base of the sample substrate, beyond the silver dag, from as far away as some point within the sapphire mounting disc. This called for extra finite elements for the model and the relevant properties of silver dag and sapphire [55, 79, 80]. In total, there were then 1060 finite elements accounting for all the material up to the copper sample stage in the cryostat. The film temperature distribution is shown here:

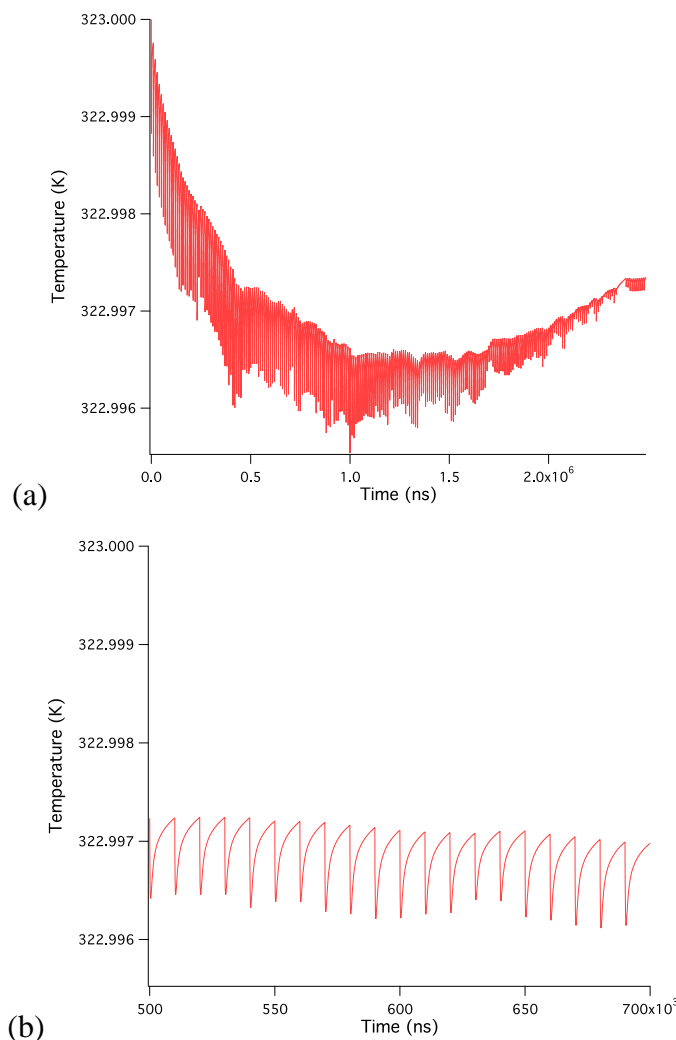


**Figure 4-25. (a) Temperature evolution of 2 equidistant planes across 225 nm thickness of PMN-PT, during second quadrant of 100 Hz hysteresis loop measurement. Sample in cryostat. (b) Close-up along time axis.**

Graph (a) is difficult to interpret at this scale, hence graph (b). In both graphs there are the two “curves” that represent the PMN-PT film. One is red, the other black, but since the two “curves” have virtually identical values and the red one was drawn last, this is the only visible data. The reason for this is that the model defines the temperature of the convection boundary, i.e. the plane between the surrounding air and the sample, in terms of the current temperature of the next finite element plane down, within the film. The convection boundary temperature is a modification of this adjacent temperature according to the heat transfer from the air and this contribution is tiny, hence a calculated difference of the order of merely  $10^{-12}$  K. In any case, the film temperature can be seen, by comparing graphs (a) and (b) in the above figure, to drop quickly as the voltage does, at the beginning of every interval between measured points. Then as the entropy changes become rapidly smaller over the  $10 \mu\text{s}$  interval between measurements, heat flow into the film brings its temperature up until the next dip down, after the following measurement.

The largest deviation from ambient temperature is much smaller than previous analyses, at  $-0.0045 \text{ }^\circ\text{C}$ , which is 0.83% of the estimated  $-0.54 \text{ }^\circ\text{C}$  of isentropic cooling. This is very arguably, an isothermal process. The sample temperature distribution is shown below:

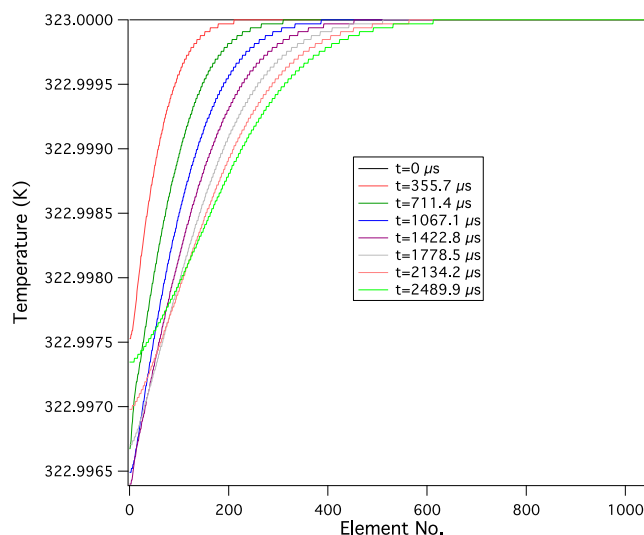


**Figure 4-26. Element number vs associated temperature for mounted sample thickness, at a range of times during field removal.**

Finally, the degree of isothermality of the ‘275-215 °C’ dataset is analysed where cooling was predicted to be at its highest at a measurement temperature. The equivalent loop frequency here is 1 kHz, i.e. 10 times slower than the estimated, non-isothermal processes, but 10 times faster than the estimated, isothermal process. There were 250 points measured during the second quadrant of the hysteresis loop, 1  $\mu$ s apart and the analysis required calculations every 10 ns to be manageable. A total of 859 finite elements were required to account for the entire sample, where the first 11 represented the film.

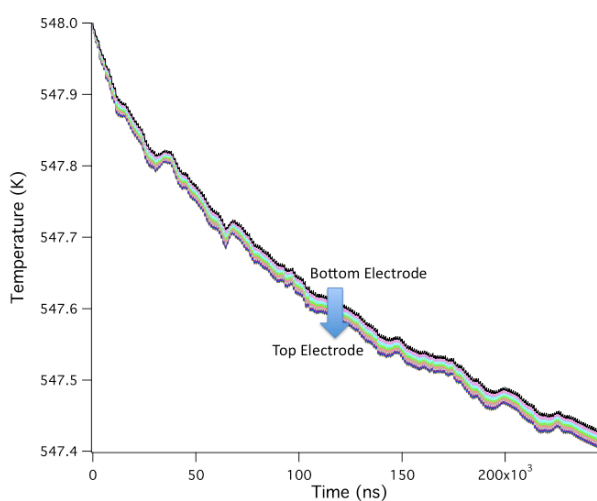


**Figure 4-27. . Temperature evolution of 11 equidistant planes across 1.05  $\mu$ m thickness of PZT 95/05, during second quadrant of 1 kHz hysteresis loop measurement. Sample in cryostat. ‘275-215 °C’ dataset.**

The largest deviation from ambient temperature is -0.6 °C, which is 9.7% of the estimated -6.16 °C of isentropic cooling. The sample temperature distribution is shown below:

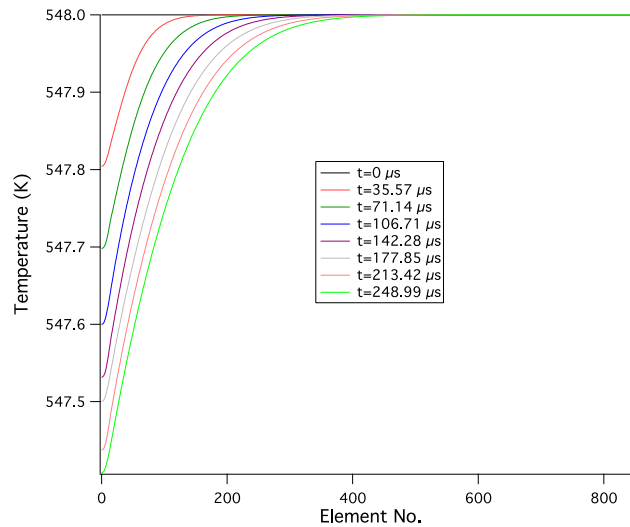


**Figure 4-28. Element number vs associated temperature for sample thickness, at a range of times during field removal.**

There are several noteworthy characteristics of these analyses. First and foremost, those measurements made in hysteresis loops of 10 kHz or 1 kHz, were not isothermal, whereas the 100 Hz measurements could well be considered so. This is significant for the  $\Delta T$  predictions from those faster datasets, which were the largest, reaching as much as 25 °C cooling. Earlier assumptions that passing through one of the two polarization states, for a given field in the ferroelectric films, could be a possible description of the measured points on the hysteresis loops and that these points could be deemed to be in thermodynamic equilibrium, thus possibly validating the indirect method for electrocaloric predictions, are considerably weakened in light of this lack of thermal equilibrium. In fact, the clear lack of thermal equilibrium means a categorical lack of thermodynamic equilibrium and for a classical definition, the entropy is not even well defined. One could still also argue, however, that the indirect method remains valid for “approximations” of electrocaloric behaviour and adjusting the temperature coordinate of the data points is all that is necessary, that it would be excessive to ignore the temperature change predictions completely.

Taking this view, one could say that as the hysteresis loops begin to be traced out and reach their peak field, before heading back to zero field along the second quadrant, they will have heated by the estimated 28% of the predicted electrocaloric temperature change. Then it could be said that the temperature coordinates of the data points along the second

quadrant follow a straight line back to the starting temperature. Redefining the temperature coordinates of all the data points on the  $P(E, T)$  surface in this way changes its character very little. Re-calculating  $\Delta T$  predictions using the ‘polynomial OIP’ and ‘smoothing OIP’ approaches to  $P(T)$  approximation produces the following:

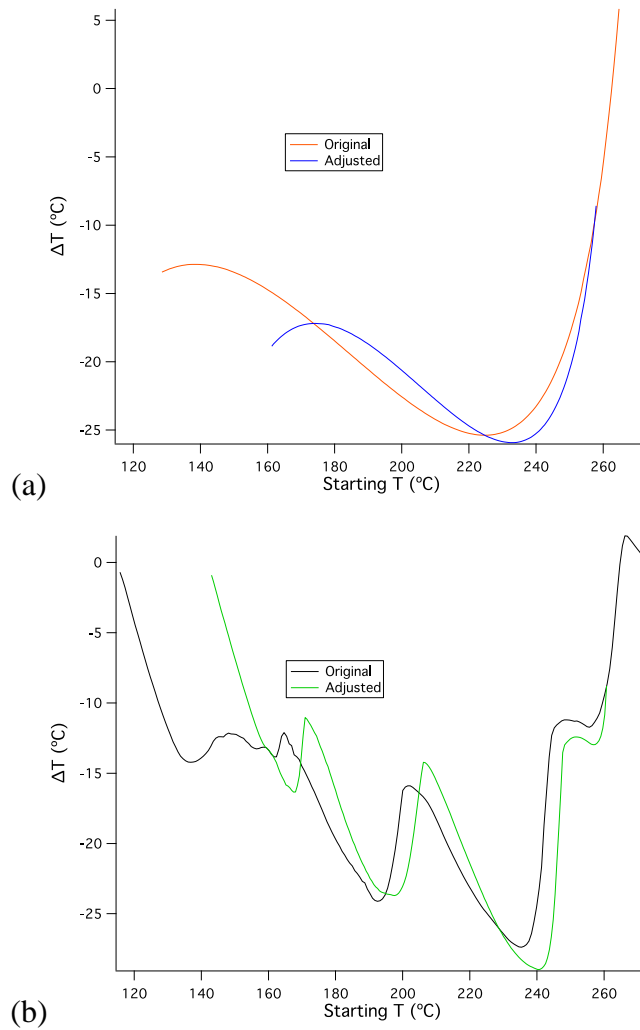


**Figure 4-29. (a) ‘Polynomial OIP’ predictions from original and adjusted P(E,T) data (b) As (a), for ‘Smoothing OIP’ approach.**

where the difference is very small, having slightly increased the peak predictions while shifting their starting temperatures up a little.

It is seen that the slower the measurement, the further away from the film there is heat movement. In the 100 Hz loop measurements, the temperature between finite elements

that represent parts of the cryostat mounting disc are affected, as far as 955  $\mu\text{m}$  below the film, whereas in the faster measurements, there is no modelled change in temperature beyond the sample substrate, which is stuck to the mounting disc. 1 kHz loop measurements also affect the temperature of elements further away from the film (up to 455  $\mu\text{m}$  below film) than those affected during 10 kHz loop measurements (up to 162-190  $\mu\text{m}$  below film).

Not only are the 100 Hz measurements more reliable in this sense, in terms of  $\Delta T$  predictions, but the loop frequency also seems to be the determining factor for thermal equilibrium for these analyses. That may sound superficially obvious, but there are other seemingly important considerations, such as film thickness, the thermal conductivity of the materials and the electrocaloric temperature change. If one increases film thickness, no change in polarization is expected, nor its change in polarization with temperature, hence no expected change in  $\Delta T$  predictions. For the difference in thickness of the films tested in this thesis, even considering large electrocaloric cooling by 25  $^{\circ}\text{C}$  in all cases, further estimations show the degree of isothermality to be unaffected. Nor are the differences in thermal conductivity anywhere as near as significant as the variation in isothermality due to measurement loop frequency.

**There are clear levels of the degree to which these processes are isothermal, according to the measurement loop frequency. For 100 Hz, the deviation from ambient temperature is less than 1% of the predicted electrocaloric temperature change, for 1 kHz, it is around 10%, while for 10 kHz, the figure is around 30-40%.**

## 5. FINAL THOUGHTS

Though many electrocaloric predictions have been presented here, the sentiment behind them has been a deep mistrust of their validity. Ferroelectrics nominally have two equilibrium states for every applied field and as such, do not lend themselves to thermodynamic treatments. It has been shown in the literature that certain materials, under certain conditions, experience an essentially reversible electrocaloric temperature change, when measured directly. This does not mean, however, that the material passes through the same states during field application as it does during field removal. We know it does not because when we measure polarization as a function of field, we get hysteresis loops. For this reason, thermodynamic analysis should have no place here. Despite this, when the indirect method has been applied alongside direct measurements, there have been similarities in the results to within as little as 15%. This is, however, one case of only eight, published since the study of electrocalorics began. In the other seven comparisons the larger of the values is 20%, 41%, 43%, 80%, 135%, 160% and over 300% bigger than the smaller value. This scant data and generally poor “agreement”, is not convincing.

It has been demonstrated in this thesis that even with good quality  $P(E, T)$  data, the application of the indirect method to raw data does not generally return useful results and that some manipulation of the raw data is necessary. In choosing the method for this manipulation, one finds several methods are arguably valid and hence electrocaloric predictions can vary considerably. When consideration of predictions has been extended to other measurement points on the same film, all within just half a centimetre of each other, that variation grows and results can easily be separated by a factor of 2.

A technique for testing data quality for use in the indirect method has also been put forward, showing how datasets can frequently be incompatible with the method and that the long assumed isothermality of measured data presented in the literature may well not exist, especially given the many commonalities between the experiments presented in this thesis and those of post-Mischenko literature.

As mentioned in the introduction, the recent advent of direct temperature measurement techniques in thin films may well mark the end of the indirect method, but this author urges against the use of the indirect method as an “easy” option. As a growing body of published data on directly measured electrocaloric effects appears in journals, it would be useful to accompany them with indirect results. Were this author both willing and in a position to continue in electrocalorics, the next step in this story would be to do just that – produce direct and indirect results, vary experimental and analytical parameters and perform hundreds of comparisons to see if a correlation can be established between direct/indirect agreement and experimental conditions and/or materials. Such an investigation could lead to a greater understanding of the reversibility of ferroelectrics.

The conclusions of this thesis are few and simple. In the view of this author, the most important are that the thermodynamic work performed on a capacitor medium during charging or discharging is not the commonly purported version and that it is made clear why two versions have arisen, the reason for mistaken derivation of the incorrect version and the correct meaning of the incorrect version. It is also important to note that the analogy generally drawn between the electrical work done on a polarizable medium and the magnetic work done on a magnetizable medium is false. The study of the implementation of the indirect method of measuring electrocaloric temperature change has shown that there are several important aspects of both measurement and analysis that have not been considered in the electrocalorics community, which should be taken into account when declaring the cooling potential of materials. With respect to guidelines for further, such indirect measurement of the electrocaloric effect, this author would urge checking the estimated isothermality of measured  $P(E)$  loops under the given conditions before attempting an experiment and the avoidance of smoothing  $P(T)$  data during analysis, by working only with raw data that results in non-erratic temperature change predictions over a starting-temperature range. This can be achieved by measuring isothermal  $P(E)$  loops at intervals of at least 20 °C and calculating temperature change predictions from starting temperatures that are the same as the  $P(E)$  loop measurement temperatures.

## 6. APPENDICES

### APPENDIX A – ELECTRICAL WORK WITHIN THE MODEL OF AN INFINITE-AREA CAPACITOR

After the general definition of the infinitesimal work by the battery in charging or discharging a capacitor:

(6.1)

$$\delta W_B = VdQ$$

a simplified model of the capacitor can be used where the capacitor is an imagined slab cut from a capacitor with electrodes of infinite area and finite thickness. The charge on the electrodes is then uniform, as opposed to the real case, where the charge is denser at electrode edges. This model, including the assumption of a homogeneous medium, results in a uniform field and polarization between the electrodes. In addition, the field is confined to the volume between the electrodes. There are no fringing fields and no fields on the battery side of the electrodes, as they cancel out there.

The work done by the battery continues by considering  $D$ , the magnitude of the displacement field normal to the plates, which is equivalent to the charge density on one plate [2] and is defined as:

(6.2)

$$D = \varepsilon_0 E_0 = \varepsilon_0 E + P$$

where  $\varepsilon_0$  is the permittivity of free space,  $E$  is the field magnitude across the capacitor and  $P$  is the magnitude of the polarization of the medium in the direction of the field, normal to the capacitor plates. As  $E = V/l$  between the plates, where  $l$  is the plate separation; and  $D = Q/A$ , where  $A$  is the plate area:

$$\delta W_B = VdQ = ElAdD = vEdD$$

where  $v$  is the volume between the plates.

$E_0$  describes the magnitude of the field between the electrodes of an empty capacitor for the same charge on the electrodes as in the filled capacitor case. That is to say, if one were to charge the filled capacitor, creating a field,  $E$ , across it and then all charges were frozen in their positions, then upon removal of the polarizable medium, there would be a larger field across the capacitor, represented by  $E_0$ . Experimentally, one measures the charge on one electrode and the voltage across the capacitor from which one can calculate  $D$  and  $E_0$  from the charge and  $E$  from the voltage.  $E$  is the resulting superposition of the field due to the charge on the electrodes ( $E_0$ ) and the field due to the polarized medium ( $E_M$ ).

For a capacitor with square or circular electrodes, where the length of one side of the square electrode, or the diameter of the circular electrode, is very much larger than the thickness of the medium filling the capacitor, the errors introduced by this model are considered to be small and the use of  $D = \epsilon_0 E_0 = \epsilon_0 E + P$  is usually justified.

In general,  $\mathbf{D}$  is not equal to  $\epsilon_0 \mathbf{E}_0$ , as the curl of  $\mathbf{D}$  is not zero everywhere, as it is for  $\mathbf{E}$ . As  $\mathbf{D} = \epsilon_0 \mathbf{E} + \mathbf{P}$  and the curl of  $\mathbf{P}$  is not zero everywhere, neither is the curl of  $\mathbf{D}$ . Hence  $\mathbf{D}$  cannot be described as the gradient of a scalar and thus does not have an equivalent to the potential of an electric field. The integral of  $\mathbf{D}$  from one point to another depends upon the path taken, so  $\mathbf{D} \neq \epsilon_0 \mathbf{E}_0$ . However, in the simplified model, not only is  $\mathbf{P}$  uniform throughout the medium, but all fields are confined to the volume of the medium, cancelling each other out above and below the plates, for the orientation shown in the above figures. The work done by the battery is then stored in the medium and the field, hence the reason why only the volume of the medium is necessary to determine the work done in the simplified model, apparent from equation 6.3 onwards. The curl of  $\mathbf{P}$  is zero everywhere in this volume, so  $\mathbf{D} = \epsilon_0 \mathbf{E}_0$  and  $D = \epsilon_0 E_0$ , for this model.  $D$  is equivalent to the total surface charge density of the free charge on either electrode, where  $P$  is that

due to the free charge per unit area compensating the adjacent charged surface of the polarized medium and  $\epsilon_0 E$  accounts for the rest of the free charge per unit area. If the capacitor were empty, this uniform surface charge density,  $\epsilon_0 E$ , would create the field,  $E$ , between the plates:

(6.4)

$$D = \epsilon_0 E_0 = \epsilon_0 E + P \quad \equiv \quad \sigma_{total} = \sigma_{total} = \sigma_{E \text{ in vacuum}} + \sigma_{compensating P}$$

where  $\sigma$  refers to the magnitude of surface charge density on either electrode. The work done by the battery continues from equation 6.3:

(6.5)

$$\delta W_B = v E dD = v \epsilon_0 E dE_0 = v(\epsilon_0 E_0 - P) dE_0 = v \epsilon_0 E_0 dE_0 - v P dE_0$$

and hence:

(6.6)

$$W_B = v \epsilon_0 \int_{E_{01}}^{E_{02}} E_0 dE_0 - \int_{E_{01}}^{E_{02}} P_m dE_0 = \int_{Q_1}^{Q_2} V dQ$$

When looked at from this point of view, the first term (middle expression) is the same in the cases of both the empty and filled capacitor, so the difference, the work done on the medium by the battery, is equal to the second term,  $-\int_{E_{01}}^{E_{02}} P_m dE_0$ . This clarifies an important point. When a capacitor is charged, the medium does work on its surroundings and not the other way around, as claimed by the more common  $\int_{E_1}^{E_2} E dP_m$ . As more charged is placed on the electrodes, the medium polarizes and bound charge within the medium, of opposite sign to that on a given electrode, moves towards the electrode and effectively reduces the potential at that electrode as seen by the approaching charge in the wire. Thus the battery does less work on the filled capacitor, compared with an empty capacitor, for the same change of charge on the electrodes. The reduction in work is due

to the presence of the medium and the work done by the medium is logically equal to this reduction,  $\int_{E_{01}}^{E_{02}} P_m dE_0$ .

## APPENDIX B – THE LOCATION OF THE ENERGY OF A CHARGE CONFIGURATION

The energy of a charge configuration can be expressed in two ways:

(6.7)

$$\mathcal{E}_F = \int \frac{1}{2} \epsilon_0 \mathbf{E}^2 dv = \int \frac{1}{2} \rho \phi dv$$

where  $\rho$  is the charge density and  $\phi$ , the potential at the charge. This equality is explained below. As  $\rho = \epsilon_0 \nabla \cdot \mathbf{E}$ , then:

(6.8)

$$\int \frac{1}{2} \rho \phi dv = \frac{\epsilon_0}{2} \int (\nabla \cdot \mathbf{E}) \phi dv$$

By integrating the expression  $\int \nabla \cdot (\mathbf{E} \phi) dv$  by parts, the right hand side can be turned into:

(6.9)

$$\frac{\epsilon_0}{2} \int (\nabla \cdot \mathbf{E}) \phi dv = \frac{\epsilon_0}{2} \int \nabla \cdot (\mathbf{E} \phi) dv - \frac{\epsilon_0}{2} \int \mathbf{E} \cdot (\nabla \phi) dv$$

and as  $\nabla \phi = -\mathbf{E}$ , this becomes:

(6.10)

$$\frac{\epsilon_0}{2} \int (\nabla \cdot \mathbf{E}) \phi dv = \frac{\epsilon_0}{2} \int \nabla \cdot (\mathbf{E} \phi) dv + \int \frac{1}{2} \epsilon_0 \mathbf{E}^2 dv$$



```

LoadWave /A/G/D/W/K=0 FilePath

Temperature=StartT+((i-1)*Tint)
Npoints=numpts(Point)

Rename Point, $("T"+num2str(i))
Killwaves Date_Time
Rename Drive_Voltage, $("E"+num2str(i))
Rename Measured_Polarization,$("D"+num2str(i))

//Create list of temperatures for P(T) later
If (i==1)
Make/D/N=1 Templist
Templist[0]=Temperature
else
InsertPoints (i-1),1,Templist
Templist[i-1]=Temperature
endif

//Create waves full of same temperature values for each loop
j=0
do
WAVE x=$("T"+num2str(i))
x[j]=Temperature
j+=1
while (j<Npoints)

//Calculate field
WAVE y=$("E"+num2str(i))
y=y/(ThicknessFactor*1E-9)

//Surface charge density correction, due to incorrect electrode area, if necessary
WAVE z=$("D"+num2str(i))
z=z*Psf*0.01
Duplicate z, $("P"+num2str(i))

//Calculate P values
WAVE x=$("P"+num2str(i))
WAVE y=$("D"+num2str(i))
WAVE z=$("E"+num2str(i))
x=y-(z*eps)

WAVE k=$("T"+num2str(i))
WAVE l=$("E"+num2str(i))
WAVE m=$("P"+num2str(i))
WAVE n=$("D"+num2str(i))

Duplicate/D k, $("UplT"+num2str(i))
Duplicate/D l, $("UplE"+num2str(i))
Duplicate/D m, $("UplP"+num2str(i))
Duplicate/D n, $("UplD"+num2str(i))

WAVE a=$("UplT"+num2str(i))
WAVE b=$("UplE"+num2str(i))
WAVE c=$("UplP"+num2str(i))
WAVE d=$("UplD"+num2str(i))

```

```

//Cut out second quadrant
If (mod(Npoints,2)>0)
DeletePoints 0,1, a,b,c,d
Npoints=Npoints-1
Reset=1
endif
DeletePoints 0,(Npoints/4), a,b,c,d
DeletePoints (Npoints/4),(Npoints/2),a,b,c,d
pts=numpts(a)
If (Reset==1)
Npoints=Npoints+1
Reset=0
endif

//For each loop
i+=1
while (i<(Ntemps+1))

// Change T,E,P and D wave names
i=0
do
Rename $("UplT"+num2str(i+1)),$("wave"+num2str((i*3)+1))
Rename $("UplE"+num2str(i+1)),$("wave"+num2str((i*3)+2))
Rename $("UplP"+num2str(i+1)),$("wave"+num2str((i*3)+3))
Rename $("UplD"+num2str(i+1)),$("Dwave"+num2str((i*3)+3))
i+=1
while (i<Ntemps)

// Find MaxField and MinField of all second quadrant data together
i=2
do
    WAVE m = $("wave" + num2str(i))
    tmp1=WaveMax(m)
    tmp2=WaveMin(m)
    if (tmp1<MaxField)
        MaxField=tmp1
    endif
    if (tmp2>MinField)
        MinField=tmp2
    endif
    i+=3
while (i<(Ntemps*3))
Print "MaxEField is",MaxField
Print "MinEField is", MinField

// Create universal, evenly spaced, E wave
i=0
Make/D/N=(pts) waveptsfields
do
    waveptsfields[i]=MinField+(i*((MaxField-MinField)/(pts-1)))
    i+=1
while (i<pts)
Edit waveptsfields

// Interpolate P(E) at each T to match universal E wave values
i=0
do
WAVE E=$("wave"+num2str(2+(i*3)))

```

```

WAVE P=$(("wave"+num2str(3+(i*3)))
String interped=("Intwave"+num2str(3+(i*3)))
XYToWaveJam(E,P, interped,pts, MaxField,MinField)
i+=1
while (i<Ntemps)

// Replace P(E) with new interpolated set
i=0
do
WAVE E=$(("wave"+num2str(2+(i*3)))
WAVE P=$(("wave"+num2str(3+(i*3)))
Killwaves E,P
Duplicate/D waveptsfields, $("wave"+num2str(2+(i*3)))
Rename $("Intwave"+num2str(3+(i*3))), $("wave"+num2str(3+(i*3)))
i+=1
while (i<Ntemps)

//P(T)@E. Make table of all interpolated P data for transpose
i=3
Edit
do
WAVE p = $("wave" + num2str(i))
AppendToTable p
i+=3
while (i<((Ntemps*3)+1))

// Transpose P(E) at T to give P(T) at E. Ntemp points on each curve.
WMTransposeWavesInTable("", "OrigPT")

//Display P(T)
Display
j=0
do
WAVE PT2 = $("OrigPT_" + num2str(j))
AppendToGraph PT2 vs wave0
j+=1
while (j<pts)

End

```

## P(T) APPROXIMATIONS

### *POLYNOMIAL FITTING*

```

//P=Polynomial fit order+1 (No. of coefficients)
Function PolyNW(Ntemp,Nfields,P)
Variable Ntemp,Nfields,P
Variable j=0, pts=Ntemp
String basename="OrigPT_"

// Combine P(T) into one wave
j=0
do
WAVE PT = (basename + num2str(j))
String PT_solo=(basename + num2str(j)+"_solo")
XYToWaveJambee(wave0,PT,PT_solo,pts)

```

```

j+=1
while (j<Nfields)

// Polynomial fitting
j=0
do
WAVE PT1=$(basename + num2str(j)+"_solo")
CurveFit/L=(Ntemp)/Q poly P, PT1/D
j+=1
while (j<Nfields)

//Display fit curves
Display
Variable jump=(Nfields/25)
j=0
do
WAVE PT1=$(basename + num2str(j)+"_solo")
WAVE PT2=$( "fit_" + basename + num2str(j) + "_solo" )
AppendToGraph PT1
ModifyGraph mode($(basename + num2str(j)+"_solo")=3,rgb($(basename + num2str(j)+"_solo"))=(0,0,0)
AppendToGraph PT2
j+=(jump)
while (j<Nfields)

End

```

### *SMOOTHING*

```

//Smth=Odd number of data points over which to average
Function SmoothNW(Smth, Ntemp,Nfields)
Variable Smth, Ntemp, Nfields
Variable pts=Ntemp, j
String basename="OrigPT_"

// Combine P(T) into one wave
j=0
do
WAVE PT = $(basename + num2str(j))
String PT_solo=(basename + num2str(j)+"_solo")
XYToWaveJambee(wave0,PT,PT_solo,pts)
j+=1
while (j<Nfields)

//Duplicate P(T) single waves and plot 25 of them for ease of interpretation
j=0
do
WAVE PT2 = $(basename + num2str(j)+"_solo")
Duplicate/D PT2, $("PT2_Orig_" + num2str(j))
j+=1
while (j<Nfields)
j=0
Variable jump=(Nfields/25)
do
WAVE PT2_Orig=$( "PT2_Orig_" + num2str(j) )
AppendToGraph PT2_Orig
j+=(jump)
while (j<Nfields)

```

```

//Smooth all P(T) single waves
j=0
do
WAVE PT2 = $(basename + num2str(j)+"_solo")
Smooth/B=1 Smth, PT2
Rename PT2, $("Ready_" + num2str(j))
j+=1
while (j<Nfields)

//Plot 25 smoothed waves along with originals
j=0
do
WAVE PT2 = $("Ready_" + num2str(j))
AppendToGraph PT2
j+=1
while (j<Nfields)

```

End

### *POLYNOMIAL FIT OVER INTERMEDIATE P(T) VALUES*

```

//P=Polynomial fit order+1 (No. of coefficients)
Function PolySNW(Ntemp,Nfields,P)
Variable Ntemp,Nfields,P
Variable j=0, pts=Ntemp, split=15, i
String basename="OrigPT_"

Ntemp=(((Ntemp-1)*split)+1)
Print "Spoly Ntemps is",Ntemp

// Combine P(T) into one wave
j=0
do
WAVE PT = $(basename + num2str(j))
String PT_solo=$(basename + num2str(j)+"_solo")
XYToWaveJambee(wave0,PT,PT_solo,pts)
j+=1
while (j<Nfields)

//Polynomial fitting to many points, adding intermediate values
j=0
Edit
do
WAVE PT1=$(basename + num2str(j)+"_solo")
CurveFit/L=(Ntemp)/Q poly P, PT1/D
WAVE PT2=$( "fit_" + basename + num2str(j) + "_solo" )
AppendToTable PT2
j+=1
while (j<Nfields)

//Create wave of new set of temperature values
i=0
Variable MaxTemp=wavemax(wave0), MinTemp=wavemin(wave0)
Make/N=(Ntemp) waveptstemp
do
waveptstemp[i]=MinTemp+i*((MaxTemp-MinTemp)/(Ntemp-1))
i+=1
while (i<Ntemp)

```

```

Edit waveptstemp
Duplicate/O waveptstemp, wave0
Redimension/Y=4 wave0

//Plot original P(T) data and fit data on same graph
Display
Variable jump=(Nfields/25)
j=0
do
WAVE PT1=$(basename + num2str(j)+"_solo")
WAVE PT2=("fit_" + basename + num2str(j)+"_solo")
AppendToGraph PT1
ModifyGraph mode($(basename + num2str(j)+"_solo")=3,rgb($(basename + num2str(j)+"_solo")=(0,0,0)
AppendToGraph PT2
j+=jump)
while (j<Nfields)

```

End

### *SMOOTHING OVER INTERMEDIATE P(T) VALUES*

```

//Smth=Odd number of data points over which to average, normally 15
Function SmoothSNW(Smth, Ntemp,Nfields)
Variable Smth, Ntemp, Nfields
Variable pts=Ntemp, j, i, split=15
String basename="OrigPT_"

Ntemp=(((Ntemp-1)*split)+1)
Print "SmthS Ntemp is",Ntemp

// Combine P(T) into one wave
j=0
do
WAVE PT = $(basename + num2str(j))
String PT_solo=(basename + num2str(j)+"_solo")
XYToWaveJambee(wave0,PT,PT_solo,Ntemp)
j+=1
while (j<Nfields)

//Create wave of new set of temperature values
i=0
Variable MaxTemp=wavemax(wave0), MinTemp=wavemin(wave0)
Make/N=(Ntemp) waveptstemp
do
    waveptstemp[i]=MinTemp+i*((MaxTemp-MinTemp)/(Ntemp-1))
    i+=1
    while (i<Ntemp)

Edit waveptstemp
Duplicate wave0, wave02
Duplicate/O waveptstemp, wave0
Redimension/Y=4 wave0

//Plot original P(T) data and fit data on same graph
Display
Variable jump=(Nfields/25)
j=0
do

```

```

WAVE PT1 = $(basename + num2str(j))
WAVE PT2 = $(basename + num2str(j)+"_solo")
AppendToGraph PT1 vs wave02
AppendToGraph PT2
ModifyGraph mode($(basename + num2str(j)))=3,rgb($(basename + num2str(j)))=(0,0,0)
j+=jump
while (j<Nfields)

```

```

//Smoothing of all points, including new intermediate values
j=0
do
WAVE PT2 = $(basename + num2str(j)+"_solo")
Smooth/B=1 Smth, PT2
Rename PT2, $("Ready_" + num2str(j))
j+=1
while (j<Nfields)

```

End

*RESET MODIFIED P(T) DATA WAVES TO BE CALLED ORIGPT\_ FOR NEXT STEP*

```

Function Orig(Nfields)
Variable Nfields
Variable j

```

```

j=0
do
//Choose following line or the one after, appropriately
//WAVE PT = $("fit_FieldCv_" + num2str(j) + "_solo")
WAVE PT = $("Ready_" + num2str(j))
Duplicate/O PT, $("OrigPT_" + num2str(j))
Killwaves PT
j+=1
while (j<Nfields)

```

End

PREPARE FINAL GRAPH FROM WHICH TO CALCULATE TEMPERATURE  
CHANGES

(i.e.  $\left(\frac{\partial P}{\partial T}\right)_E$  vs.  $E$ , at many  $T$ )

```

// HC=Heat Capacity per unit volume
Function TruCoolorHeat(Ntemps,Nfields,HC)
Variable Ntemps,Nfields,HC
Variable i=0, j,MaxField=wavemax(waveptsfields), MinField=wavemin(waveptsfields)
String basewave="wave"
String basewave3="OrigPT_"
String basewave4="_DIF"

```

```

//Forward-difference differentiate P(T) waves
If (wavetype(OrigPT_0)==2)
Redimension/Y=2 wave0

```

```

endif
do
WAVE w = $(basename3 + num2str(i))
Differentiate/METH=1 w/X=wave0/D=$(basename3 + num2str(i)+basename4)
i+=1
while (i<Nfields)

// Produce table of dPdT curves for transposing
Edit
i=0
do
WAVE p = $(basewave3 + num2str(i) + basewave4)
AppendToTable p
i+=1
while (i<Nfields)

// Transpose dPdT(T) at E to give dPdT(E) at T. Ntemp temperature curves for dPdT(E) graph.
// Nfields points on each curve. Produce table and graph.
i=0
WMTransposeWavesInTable("", "Final")
Edit
Display
do
WAVE p = $("Final_" + num2str(i))
AppendToTable p
AppendToGraph p
i+=1
while (i<Ntemps)
Print MaxField
Print MinField

//Create single waves to work from in  $\Delta T$  calculation
j=0
do
WAVE PT = $("Final_" + num2str(j))
String PT2_solo=("$Final_" + num2str(j) + "_solo")
XYToWaveJambee(waveptsfields,PT,PT2_solo,Nfields)
WAVE PT2=("$Final_" + num2str(j) + "_solo")
Duplicate/O PT2, $("Final_" + num2str(j))
Killwaves PT2
j+=1
while (j<Ntemps)

// Calculate and display dT vs T for specified field range
TruFinalC(Maxfield, MinField, Ntemps, HC)
//TruFinalH(Maxfield, MinField, Ntemps, HC)

End

```

## STEPWISE CALCULATION OF $\Delta T$ (COOLING)

(there is an equivalent function for heating)

```

Function TruFinalC(Maxfield, MinField, Ntemps, HC)
Variable MaxField, MinField, Ntemps, HC
String rt="Final_"

```

Variable i, j, k, curve, strtE, CT, IT, inc=(Maxfield/1000000), integral, biggstchange  
 Variable tchange, bfld, Mintemp, Maxtemp

```
//Make waves to store results
Make/O/N=(Ntemps) dTresults
Make/O/N=(Ntemps) Errors
```

```
//Maxfield=45585710
//MinField=2470700
```

```
WAVE Twave=wave0
  Maxtemp=wavemax(Twave)
  Mintemp=wavemin(Twave)
  Print "Maxtemp",Maxtemp
  Print "Mintemp",Mintemp
```

```
i=0
do
  // Set starting field=highest field (initial top integral limit)
  strtE=MaxField
  // IT is initial temperature, starting at temperature of curve
  IT=Twave[i]
  Print "IT is",IT
  // CT is current temperature
  CT=IT
```

```
// Work out T changes
```

```
k=0
tchange=0
biggstchange=0
```

```
do
```

```
j=0
do
```

```
// Find curve to integrate with. Each curve covers its temperature and all above it,
// up to next temperature curve, in accordance with forward-difference differentiation.
  If (CT>=Twave[j])
    curve=j
  endif
```

```
j+=1
while (j<Ntemps)
```

```
WAVE currentT=$(rt+num2str(curve))
```

```
  // Set lower integral limit. Very small interval.
  bfld=(strtE-(inc+(inc*k)))
```

```
  // If move beyond lowest field, break loop
  If (bfld<MinField)
    break
  endif
```

```
  // Calculate area under curve
  integral=area(currentT,strtE,bfld)
```

```
  // Calculate dT
  tchange=((CT+273.15)/HC)*integral*-1
```

```

// Keep track of largest dT to watch for non-negligible error in calculation
  If (abs(tchange)>biggstchange)
    biggstchange=abs(tchange)
  endif

// Set new temperature
CT=CT+tchange

// For next integral, lower limit is now top limit
strE=bfld

// If stepwise calculation moves beyond temperature limits of data, it is nulled.
  If (CT>Maxtemp || CT<Mintemp)
    break
  endif

// Next dT to calculate
k+=1
while(1)

// If calculation moves beyond temperature limits, no ΔT is recorded.
  If (CT>Maxtemp || CT<Mintemp)
    dTresults[i]=NaN
  else
// ΔT over max and min set field limits recorded in results wave.
    dTresults[i]=CT-IT
    Errors[i]=biggstchange
    Print "dT is", (CT-IT)
    Print "Biggstchange is", biggstchange
  endif

// Repeat process starting from next temperature curve
i+=1
while (i<Ntemps)

Display dTresults vs Twave
//ErrorBars dTresults,Y wave=(Errors,Errors)

End

```

## SUPPLEMENTAL FUNCTIONS

(called during the above functions)

```

// Modified from Wavemetrics built-in function
Function XYToWaveJam(xWave, yWave, wWaveName, numPoints,MaxF,MinF)
  Wave xWave // x wave in the XY pair
  Wave yWave // y wave in the XY pair
  String wWaveName // name to use for new waveform
wave
  Variable numPoints // number of points for waveform
  Variable MaxF, MinF

  Make/D/O/N=(numPoints) $wWaveName // make waveform
  Wave wWave= $wWaveName
  SetScale/I x MinF, MaxF, wWave // set X scaling for waveform
  wWave = interp(x, xWave, yWave) // do the interpolation

```

```

End

// // Modified from Wavemetrics built-in function
Function XYToWaveJambee(xWave, yWave, wWaveName, numPoints)
    Wave xWave // x wave in the XY pair
    Wave yWave // y wave in the XY pair
    String wWaveName // name to use for new waveform
wave
    Variable numPoints // number of points for waveform

    Interpolate2/T=1/N=(numPoints)/Y=$wWaveName xWave, yWave
End

// Wavemetrics built-in function
Function/S WMTransposeWavesInTable(TableName, OutBase)
    String TableName // can be "" for top table
    String OutBase

    OutBase= OutBase[0,26] // leave room for _ and 3 digits

    if( strlen(TableName) == 0 )
        TableName=WinName(0,2) // ensure we get the top TABLE (if any)
    endif

    String ListofWaves=WMTransposeGetTableWaveList(TableName,1,";")

    String OutputWaveList = ""

    WAVE/Z w= $StringFromList(0,listofWaves)
    if( !WaveExists(w) )
        return ""
    endif

    String ThisWaveName = NameOfWave(w)
    Variable NumRows=numpts(w)

    Variable i = 0
    do
        WAVE/Z w= $StringFromList(i,listofWaves)
        if( !WaveExists(w) )
            break
        endif
        if( numpts(w) != NumRows )
            DoAlert 0, "Waves must all have same length"
            return ""
        endif
        i += 1
    while(1)

    Variable NumCols=i

    if (NumCols < 2)
        DoAlert 0, "Must have at least two input waves"
        return ""
    endif

    i = 0
    do
        ThisWaveName = CleanupName(OutBase+"_"+num2istr(i),1)

```

```

        Make/O/N=(NumCols) $ThisWaveName
        OutputWaveList += PossiblyQuoteName(ThisWaveName)+","
        i += 1
    while (i < NumRows)

    i = 0
    do
        WAVE wIn= $StringFromList(i,listofWaves)

        Variable j = 0
        do
            ThisWaveName = CleanupName(OutBase+"_"+num2istr(j),1)
            WAVE wOut = $ThisWaveName
            wOut[i] = wIn[j]
            j += 1
        while (j < NumRows)

        i += 1
    while (i < NumCols)

    // remove trailing comma, which would be bad for an Edit command
    OutputWaveList = OutputWaveList[0, strlen(OutputWaveList)-2]
    return OutputWaveList
End

```

## APPENDIX D - IGOR FUNCTIONS FOR TESTING P(E,T) SURFACES FOR COMPLIANCE WITH INDIRECT METHOD CONDITIONS

### MAIN FUNCTION

```

Function ThermoConditionsTest(Ntemps, pts)
Variable Ntemps,pts
Variable i, j, k, eps=8.85418781762E-12, a1, b1, c1, tol, x, health

// Make table of P(T) data for transpose
i=0
Edit
do
    WAVE p = $("OrigPT_" + num2str(i))
    AppendToTable p
    i+=1
while (i<pts)

// Transpose P(T) at E to give P(E) at T, i.e. makes P waves.
WMTransposeWavesInTable("", "CPwaveP")

//Make E waves
i=0
do
    WAVE g=waveptsfields
    Duplicate g, $("CPwaveE_" + num2str(i))
    WAVE f=$("CPwaveE_" + num2str(i))
    i+=1

```

```

while (i<Ntemps)

//Make E0 waves
i=0
do
WAVE g=waveptsfields
Duplicate g, $("CPwaveE0_" + num2str(i))
WAVE a=$("CPwaveE0_" + num2str(i))
WAVE b=$("CPwaveE_" + num2str(i))
WAVE c=$("CPwaveP_" + num2str(i))
a=b+(c/eps)
i+=1
while (i<Ntemps)

//Check them out in graphs
i=0
Display
do
WAVE b=$("CPwaveE_" + num2str(i))
WAVE c=$("CPwaveP_" + num2str(i))
AppendToGraph c vs b
i+=1
while (i<Ntemps)

i=0
Display
do
WAVE a=$("CPwaveE0_" + num2str(i))
WAVE c=$("CPwaveP_" + num2str(i))
AppendToGraph c vs a
i+=1
while (i<Ntemps)

// Go through, temp by temp, point by point, check to see if 3 conditions are met
i=0
do

//Set E, E0 and P waves, plus equivalents at next temperature up
WAVE E=$("CPwaveE_" + num2str(i))
WAVE E0=$("CPwaveE0_" + num2str(i))
WAVE P=$("CPwaveP_" + num2str(i))
WAVE Epl=$("CPwaveE_" + num2str(i+1))
WAVE E0pl=$("CPwaveE0_" + num2str(i+1))
WAVE Ppl=$("CPwaveP_" + num2str(i+1))

j=0
do

//dT is equal for a1, b1 and c1, so can be ignored
a1=dE(E,P,Epl,Ppl,j)
b1= dPE0(E0,P,E0pl,Ppl,j)
c1=dPE(E,P,Epl,Ppl,j)

//See if 3 conditions are met
health=HealthCheck(a1,b1,c1)

//If not, notify
If (health==0)
Print "i=",i,"j=",j
Print "Bad dates!"

```

```

endif

//Do for all data points at this T
j+=1
while (j<pts)

//Repeat at each temperature except last
i+=1
while (i<(Ntemps-1))

Print "Checkpoint 1. Tested first 3 conditions."

// Tolerance of following calculations based on x function and measurement limits
tol=0.000002

//Repeat above analysis of all data points, seeing if thermo conditions equation is satisfied
i=0
do

WAVE E=$( "CPwaveE_" + num2str(i) )
WAVE E0=$( "CPwaveE0_" + num2str(i) )
WAVE P=$( "CPwaveP_" + num2str(i) )
WAVE Epl=$( "CPwaveE_" + num2str(i+1) )
WAVE E0pl=$( "CPwaveE0_" + num2str(i+1) )
WAVE Ppl=$( "CPwaveP_" + num2str(i+1) )

j=0
do

a1=dE(E,P,Epl,Ppl,j)
b1= dPE0(E0,P,E0pl,Ppl,j)
c1=dPE(E,P,Epl,Ppl,j)

// Thermo equality
x=1/((1/(a1*eps))+(1/b1))

If (abs(c1-x)>tol)
Print "i=",i,"j=",j
Print "Doesn't comply with equality"
Abort
else
endif

j+=1
while (j<pts)

i+=1
while (i<(Ntemps-1))

Print "Success!!! Points on surface comply with thermodynamics."

End

```

## SUPPLEMENTAL FUNCTIONS

(called during main function)

//Functions to calculate forward-going (i.e., rising temp) changes in E or P with P,E and E0 held

```

Function dE(E,P,Epl,Ppl,index)
    Wave E,P,Epl,Ppl
    Variable index
    Variable dEpl
    dEpl=interp(P[index],Ppl,Epl)-E[index]
    return dEpl
End

Function dPE(E,P,Epl,Ppl,index)
    Wave E,P,Epl,Ppl
    Variable index
    Variable dPEpl
    dPEpl=Ppl[index]-P[index]
    return dPEpl
End

Function dPE0(E0,P,E0pl,Ppl,index)
    Wave E0,P,E0pl,Ppl
    Variable index
    Variable dPE0pl
    dPE0pl=interp(E0[index],E0pl,Ppl)-P[index]
    return dPE0pl
End

// Health Check

Function HealthCheck(a1,b1,c1)
    Variable a1,b1,c1

    If (abs(c1) < abs(b1))
        Print "dPdTatE is less than dPdTat E0"
        return 0
    elseif ((c1<0 && b1>0) || (c1>0 && b1<0))
        Print "dPdTatE and dPdTatE0 differ in sign"
        return 0
    elseif ((c1<0 && a1<0) || (c1>0 && a1>0))
        Print "dEdTatP same sign as other two"
        return 0
    else
        return 1
    endif
End

```

## APPENDIX E - IGOR FUNCTIONS FOR FINITE-ELEMENT MODEL OF TEMPERATURE EVOLUTION IN SAMPLE

### *PLOT E(T) DATA TO EXTRACT WEIGHTING INFO*

```

Function ET(Ntemps,pts)
    Variable Ntemps, pts
    Variable i,j,tmpy1,tmpy2,MaxField=9E20,MinField=0

    //E(T)@P

```

```

//Find MaxP and MinP of polarization data
Variable MaxP=10, MinP=0
i=3
do
    WAVE m = $("wave" + num2str(i))
    tmp1=WaveMax(m)
    tmp2=WaveMin(m)
    if (tmp1<MaxP)
        MaxP=tmp1
    endif
    if (tmp2>MinP)
        MinP=tmp2
    endif
    i+=3
while (i<=(Ntemps*3))
Print "MaxP is",MaxP
Print "MinP is", MinP

//Create universal, evenly spaced, P wave
i=0
Make/N=(pts) waveptsP
do
    waveptsP[i]=MinP+(i*((MaxP-MinP)/(pts-1)))
    i+=1
while (i<pts)
Edit waveptsP

//Interpolate E(P) at each T to match universal P wave values
i=2
do
    Wave x=$("wave" + num2str(i+1))
    Wave y=$("wave" + num2str(i))
    String ww1=("OrigwaveETintp" + num2str(i+1))
    XYToWaveJam(x, y, ww1, pts,MaxP,MinP)
    i+=3
while(i<(Ntemps*3))

//Make table of all interpolated E data for transpose
i=3
Edit
do
    WAVE p = $("OrigwaveETintp" + num2str(i))
    AppendToTable p
    i+=3
while (i<=(Ntemps*3))

// Transpose E(P) at T to give E(T) at P. Ntemp points on each curve.
WMTransposeWavesInTable("", "OrigET")

//Display E(T)
Display
j=0
do
    WAVE ET = $("OrigET_" + num2str(j))
    AppendToGraph ET vs wave0
    j+=1
while (j<pts)

End

```

### *CREATE A WAVE FOR EACH FINITE ELEMENT PLANE*

```
Function Iso1()
Variable i

i=0
do
Make/D/O/N=24000 $("Slice_" + num2str(i))
i+=1
while (i<2719)

End
```

### *EXTRACT WEIGHTING FOR POLARIZATION OF LOOP DATA POINTS*

```
Function Iso2()
Variable i

Duplicate Pol, Weight
Wave polari=Pol

i=0
do
Weight[i]=interp(polari[i],waveptsPol,Weight_Orig)
i+=1
while (i<25)

i=1
Variable totalweight=0
do
totalweight=totalweight+Weight[i]
i+=1
while (i<25)
Print "totalweight=",totalweight

Edit Weight
Display Weight_Orig vs waveptsPol
AppendToGraph Weight vs Pol

End
```

### *PERFORM TRANSIENT TEMPERATURE CALCULATIONS*

```
(set initial data in function)

Function Iso3()
Variable T1=518, Thickness=1050, AdiabT=-6.32, Volume=12.25E-8*Thickness*1E-9
Variable C=2739000*Volume, fact=1/(1-((1-((T1+AdiabT)/T1))/2))
Variable i,j, k, totaldeltaSIso, totaldeltaSAd, totalweight=39070133
Variable RC=0.3333E-6, Fc, Polr, dS, DELS, LastDELS, dT, row

totaldeltaSIso=((C*AdiabT)/T1)*-1*fact
totaldeltaSAd=((C*AdiabT)/T1)*-1
Print "Adiabatic Entropy Change",totaldeltaSAd,"Isothermal Entropy Change", totaldeltaSIso

// Set up entropy values to coincide with measured points
Killwaves/Z Ent
i=1
Duplicate Pol, Ent
wave s=Ent
```

```

wave wt=Weight
s[0]=0
Variable stdint=totaldeltaSIso/24
do
s[i]=s[i-1]+(stdint*(wt[i]/(totalweight/24)))
i+=1
while (i<25)

// Check entropy totals are OK
Print "Total entropy of Ent wave is", Ent[24]
Print "totaldeltaSIso=", totaldeltaSIso

// Set all planes to T1 at time=0, i.e. row=0
i=0
do
Wave a=$( "Slice_" + num2str(i) )
a[0]=T1
i+=1
while (i<2719)

// Establish wave id
Wave a=Fld
Wave b=Pol
Wave r=Ent

// i corresponds to measured point number
i=0
LastDELS=0
CurrentT=T1
do

// j corresponds to times of intermediate points between measured points
j=1

// Move on 1 nanosecond for first calculation, as row 0 is already done
If (i==0 && j==1)
j=2
endif

// Sort one row at a time, i.e. temperatures at one nanosecond later. Time =(j-1)+(i*1000)
do
// Find field at Time
Fc=a[i]+((100/95.022787)*(a[i+1]-a[i])*(1-(exp(-(j-1)*1E-9)/RC))))

// Find P, assuming it to have changed proportionally to the change in V, between measured points.
Polr=b[i]+(((Fc-a[i])/(a[i+1]-a[i]))*(b[i+1]-b[i]))

// Find change in entropy since last measured point
DELS=r[i]+(((Polr-b[i])/(b[i+1]-b[i]))*(r[i+1]-r[i]))

// Get change in entropy since last iteration and set change in entropy since last measured point
dS=DELS-LastDELS
LastDELS=DELS

// Establish the row to determine, i.e. that of time.
row=((j-1)+(i*1000))

// Set temperature for plane next to conductive heat source
Wave m=Slice_2718
m[row]=T1

```

```

// Calculate temperatures at new time for other planes, excluding entropy change influence.
k=1
do
Wave l=$( "Slice_" + num2str(k) )
Wave f=$( "Slice_" + num2str(k+1) )
Wave d=$( "Slice_" + num2str(k-1) )
l[row]=(f[row-1]+d[row-1])/2
k+=1
while (k<2718)

// Calculate temperature for plane at convection boundary
Wave n=Slice_0
Wave o=Slice_1
Variable lowpressfac=(1E-4/101.32)^0.5,hconvect, lengthL=87.5E-6, delxtopelec=3.02E-8, ktopelec=1.25,
term=hconvect*delxtopelec/ktopelec
hconvect=0.59*(((T1-n[row-1])/lengthL)^0.25)*lowpressfac
n[row]=(o[row]+(term*T1))/(1+term)

// Add change in temperature to all planes in film due to electrocaloric effect
k=0
do
Wave g=$( "Slice_" + num2str(k) )
dT=((g[row-1]*dS)*-1)/C
g[row]=g[row]+dT
k+=1
while (k<35)

j+=1
while (j<=1000)

i+=1
while (i<24)

End

```

*PLOT TEMPERATURE EVOLUTION OF PLANES IN FILM AND AT VARIOUS TIMES  
ACROSS SAMPLE*

```

Function Iso4()
Variable i

// Graph all film planes' temperature evolution with time
Display
i=0
do
Wave h=$( "Slice_" + num2str(i) )
AppendToGraph h
i+=1
while (i<35)

End

Function Iso5()
Variable i,k

//Plot temp distribution waves at 7 moments during process
i=0
Display

```

```
do
Make/O/N=2719 $("TD_"+num2str(i))
Wave v=$("TD_"+num2str(i))
k=0
do
Wave theone=$("Slice_"+num2str(k))
v[k]=theone[i]
k+=1
while (k<2719)
AppendToGraph v
i+=3428
while (i<24000)

End
```

## BIBLIOGRAPHY

- [1] ISIF, Cambridge, UK, Aug 1-4, 2011; *Integrated Ferroelectrics* (2011, in press)
- [2] R.P. Feynman, R.B. Leighton, and M.L. Sands, *The Feynman lectures on physics*. Vol. 2 p.10-3-10-4, Addison-Wesley Pub. Co. (1963).
- [3] P. Kobeko and J. Kurtschatov, *Zeitschrift für Physik A Hadrons and Nuclei* **66**, 192 (1930).
- [4] B. Tuttle and D. Payne, *Ferroelectrics* **37**(1-4), 603 (1981).
- [5] A. Mischenko *et al.*, *Science* **311**(5765), 1270 (2006).
- [6] G. Wiseman and J. Kuebler, *Physical Review* **131**(5), 2023 (1963).
- [7] R. Olsen *et al.*, *Physical Review Letters* **45**(17), 1436 (1980).
- [8] S. Lu *et al.*, *Applied Physics Letters* **98**, 122906 (2011).
- [9] X. Li *et al.*, *Applied Physics Letters* **99**, 052907 (2011).
- [10] S. Lu *et al.*, *Applied Physics Letters* **97**(20), 202901 (2010).
- [11] S. Lu *et al.*, *Applied Physics Letters* **97**, 162904 (2010).
- [12] L. Luo *et al.*, *Journal of Alloys and Compounds* **509**(32), 8149 (2011).
- [13] Z. Feng *et al.*, *Thin Solid Films* **519**(16), 5433 (2011).
- [14] T. Correia *et al.*, *Journal of Physics D: Applied Physics* **44**, 165407 (2011).
- [15] Y. He *et al.*, *Functional Materials Letters* **04**(01), 45 (2011).
- [16] B. Rozic *et al.*, *Ferroelectrics* **416**(1), 139 (2011).
- [17] Z. Feng, D. Shi, and S. Dou, *Solid State Communications* **151**, 123 (2011).
- [18] Y. Bai, G. Zheng, and S. Shi, *Applied Physics Letters* **96**, 192902 (2010).
- [19] P. Liu *et al.*, *New Journal of Physics* **12**, 023035 (2010).
- [20] S. Kar-Narayan and N. Mathur, *Journal of Physics D: Applied Physics* **43**, 032002 (2010).
- [21] T.M. Correia *et al.*, *Applied Physics Letters* **95**(18), 182904 (2009).
- [22] D. Saranya *et al.*, *Bulletin of Materials Science* **32**(3), 259 (2009).
- [23] H. Chen *et al.*, *Applied Physics Letters* **94**, 182902 (2009).
- [24] B. Neese *et al.*, *Applied Physics Letters* **94**(4), 042910 (2009).
- [25] B. Neese *et al.*, *Science* **321**(5890), 821 (2008).
- [26] J. Parui and S.B. Krupanidhi, *Physica Status Solidi-Rapid Research Letters* **2**(5), 230 (2008).

- [27] G. Sebald *et al.*, *Journal of the European Ceramic Society* **27**(13-15), 4021 (2007).
- [28] A. Mischenko *et al.*, *Applied Physics Letters* **89**(24), 242912 (2006).
- [29] G. Sebald *et al.*, *Journal of Applied Physics* **100**(12), 4112 (2006).
- [30] D. Guyomar *et al.*, *J. Phys. D: Appl. Phys* **39**(20), 4491 (2006).
- [31] C.J. Adkins, *Equilibrium thermodynamics* p.39-40, Cambridge University Press (1983).
- [32] W.G. Cady, *Piezoelectricity; an introduction to the theory and applications of electromechanical phenomena in crystals* p.709, McGraw-Hill Book Company, inc. (1946).
- [33] Y.-C. Cheng, *Macroscopic and statistical thermodynamics* p.13, World Scientific (2006).
- [34] C. Kittel and H. Kroemer, *Thermal physics* p.364, W. H. Freeman (1980).
- [35] J.F. Nye, *Physical properties of crystals, their representation by tensors and matrices* Chap.10, Clarendon Press (1957).
- [36] M.W. Zemansky and R. Dittman, *Heat and thermodynamics : an intermediate textbook* p.62-63, McGraw-Hill (1997).
- [37] C.J.F. Böttcher *et al.*, *Theory of electric polarization* p.108, Elsevier Scientific Pub. Co. (1973).
- [38] G. Carrington, *Basic thermodynamics* p.162-163, Oxford University Press (1994).
- [39] L.D. Landau and E.M. Lifshitz, *Electrodynamics of continuous media* p.52-53, Pergamon Press (1960).
- [40] J.R. Waldram, *The theory of thermodynamics* p.182, Cambridge University Press (1985).
- [41] V. Heine, *Mathematical Proceedings of the Cambridge Philosophical Society* **52**(03), 546 (1956).
- [42] H. Leupold, *American Journal of Physics* **39**(9), 1099 (1971).
- [43] R. Howard, *Foundations of Physics* **10**(1), 109 (1980).
- [44] D.J. Griffiths, *Introduction to electrodynamics* p.191-192, Prentice Hall (1999).
- [45] A.B. Pippard, *Elements of classical thermodynamics for advanced students of physics* p.26, University Press (1957).
- [46] G. Carrington, *Basic thermodynamics* p.162, Oxford University Press (1994).
- [47] C. Kittel, *Elementary statistical physics* p.77-80, Wiley (1958).

- [48] D.J. Griffiths, *Introduction to electrodynamics* p.96, Prentice Hall (1999).
- [49] A. Schilling *et al.*, *Nano letters* **7**(12), 3787 (2007).
- [50] A. Schilling *et al.*, *Applied Physics Letters* **89**, 212902 (2006).
- [51] A.B. Pippard, *Elements of classical thermodynamics for advanced students of physics* p.24-27, University Press (1957).
- [52] H.B. Callen, *Thermodynamics; an introduction to the physical theories of equilibrium thermostatics and irreversible thermodynamics* p.243-244, Wiley (1960).
- [53] C.J. Adkins, *Equilibrium thermodynamics* p.40-42, Cambridge University Press (1983).
- [54] P. Thacher, *Journal of Applied Physics* **39**(4), 1996 (1968).
- [55] R. Floyd. *Cyrostat supplier data (Janis)*. Private Communication (2010)
- [56] J.P. Holman, *Heat transfer* p.651, McGraw Hill Higher Education (2010).
- [57] W.J. Merz, *Physical Review* **91**(3), 513 (1953).
- [58] M. Grossmann *et al.*, *Applied Physics Letters* **77**(12), 1894 (2000).
- [59] J.F. Scott, *Ferroelectric memories* p.76, Springer (2000).
- [60] J. Scott, *Journal of Physics: Condensed Matter* **18**, 7123 (2006).
- [61] L.K. Chao *et al.*, *Physical Review B* **72**(13) (2005).
- [62] U. Voelker *et al.*, *Journal of Applied Physics* **102**(11) (2007).
- [63] D. Damjanovic, *Reports on Progress in Physics* **61**(9), 1267 (1998).
- [64] D. Damjanovic and M. Demartin, *Journal of Physics D: Applied Physics* **29**, 2057 (1996).
- [65] M. Davis, D. Damjanovic, and N. Setter, *Journal of Applied Physics* **100**, 084103 (2006).
- [66] N.B. Gharb, S. Trolier-Mckinstry, and D. Damjanovic, *Journal of Applied Physics* **100**, 044107 (2006).
- [67] J.P. Holman, *Heat transfer* p.2-3, McGraw Hill Higher Education (2010).
- [68] J.P. Holman, *Heat transfer* p.139, McGraw Hill Higher Education (2010).
- [69] J.P. Holman, *Heat transfer* p.89, McGraw Hill Higher Education (2010).
- [70] J.P. Holman, *Heat transfer* p.168-169, McGraw Hill Higher Education (2010).
- [71] J.P. Holman, *Heat transfer* p.170-171, McGraw Hill Higher Education (2010).
- [72] J.P. Holman, *Heat transfer* p.345-346, McGraw Hill Higher Education (2010).
- [73] <http://www.kayelaby.npl.co.uk/>
- [74] Periodic Table X, v4.0.7, B. Thornton, *Synergy Creations* (2007)

- [75] [http://www.china-raremetal.com/product/Titanium\\_Dioxide\\_TiO2.htm](http://www.china-raremetal.com/product/Titanium_Dioxide_TiO2.htm)
- [76] S. Sherrit *et al.*, *Ultrasonics Symposium, 2001 IEEE* **2**, 1097 (2001).
- [77] <http://www.diracdelta.co.uk/science/source/q/u/quartz/source.html>
- [78] [http://www.hcmat.com/Pmn\\_Properties.html](http://www.hcmat.com/Pmn_Properties.html)
- [79] [http://www.2spi.com/catalog/spec\\_prep/cured\\_silver\\_film.html](http://www.2spi.com/catalog/spec_prep/cured_silver_film.html)
- [80] <http://www.silmid.com/getattachment/d69cfcfc-97b2-45a0-bf3d-df8b96f9fc0b/Electrodag-1415M-Tech-Data.aspx>
- [81] G. Akcay *et al.*, *Applied Physics Letters* **90**, 252909 (2007).